Departamento de Química Física y Termodinámica Aplicada

DISEÑO DE INTERFASES FUNCIONALES: ESTUDIO DE PROCESOS DE TRANSFERENCIA ELECTRÓNICA A TRAVÉS DE MONOCAPAS MOLECULARES AUTOENSAMBLADAS SOBRE ORO

Tesis Doctoral
Alain Rafael Puente Santiago

Córdoba, Julio 2017

TITULO: *Diseño de interfases funcionales: Estudio de procesos de transferencia electrónica a través de monocapas moleculares autoensambladas sobre oro*

AUTOR: *Alain Rafael Puente Santiago*

TÍTULO DE LA TESIS: DISEÑO DE INTERFASES FUNCIONALES: ESTUDIO DE PROCESOS DE TRANSFERENCIA ELECTRÓNICA A TRAVÉS DE MONOCAPAS MOLECULARES AUTOENSAMBLADAS SOBRE ORO

DOCTORANDO/A: Alain Rafael Puente Santiago

INFORME RAZONADO DEL/DE LOS DIRECTOR/ES DE LA TESIS

El trabajo presentado como Tesis Doctoral por D. Alain Rafael Puente Santiago ha sido realizado bajo nuestra dirección en los laboratorios del Departamento de Química Física y Termodinámica Aplicada de la Universidad de Córdoba, así como en el Materials Chemistry Group en la School of Chemistry of the University of Bristol, Reino Unido, y reúne las condiciones exigidas según la legislación vigente.

El trabajo realizado en esta Tesis ha dado lugar a 1 publicación como primer autor en la revista *J. Phys. Chem. C (2016), 120(16), 8595-8606*, indexada en el Journal Citation Reports en el primer cuartil de la categoría, Chemistry Physical, así como a 4 comucaciones a congresos internacionales, 1 nacional y 2 regionales. La estancia de tres meses realizada por el doctorando en la Universidad de Bristol dentro del grupo de electroquímica liderado por el Profesor David Fermín ha contribuido de manera muy satisfactoria en su formación y en la discusión científica establecida para el desarrollo de una parte de esta Tesis.

Por todo ello, se autoriza la presentación de la tesis doctoral.

Córdoba, 25 de junio de 2017

Firma del director/es

Fdo.: Rafael Madueño Jiménez   Fdo.: María Teresa Pineda Rodrígue

TRABAJO PARA OPTAR AL GRADO DE DOCTOR EN QUÍMICA

Fdo.: Alain Rafael Puente Santiago
Licenciado en Radioquímica

TÍTULO DE LA TESIS:

DISEÑO DE INTERFASES FUNCIONALES: ESTUDIO DE PROCESOS DE TRANSFERENCIA ELECTRÓNICA A TRAVÉS DE MONOCAPAS MOLECULARES AUTOENSAMBLADAS SOBRE ORO

LOS DIRECTORES DEL TRABAJO

Fdo.: Rafael Madueño Jiménez
Profesor Titular del Departamento de
Química Física y Termodinámica Aplicada
de la Universidad de Córdoba

Fdo.: María Teresa Pineda Rodríguez
Profesor Titular del Departamento de
Química Física y Termodinámica Aplicada
de la Universidad de Córdoba

Mediante la defensa de esta memoria se pretende optar a la mención de "Doctorado Internacional", habida cuenta que el doctorando reúne los requisitos exigidos por dicha mención:

- Se cuenta con los informes favorables de dos doctores expertos internacionales, con experiencia investigadora acreditada, pertenecientes a instituciones de educación o de investigación extranjeras.

- Existe un miembro en el Tribunal, que ha de evaluar la Tesis, perteneciente a una institución de educación superior o instituto de investigación del extranjero.

- Parte de la redacción y defensa de esta Memoria se realizará en una de las lenguas habituales para la comunicación científica y distinta a cualquiera de las lenguas oficiales en España.

- El doctorando ha realizado una estancia de investigación en la School of Chemistry of the University of Bristol (UK, Reino Unido), gracias a la concesión de una ayuda para la movilidad con objeto de obtener el Doctorado con Mención Internacional, concedida por la Universidad de Córdoba.

"Lo que sabemos es una gota, lo que ignoramos es un océano. La admirable disposición y armonía del universo no ha podido sino salir del plan de un Ser omnisciente y omnipotente"

Isaac Newton

TABLE OF CONTENTS

Index

OBJETIVOS

Motivations and Objectives of the Thesis

0. Objectives

This doctoral thesis aims to study the interfacial and chemical properties of 2D molecular organic structures at surfaces as model systems to evaluate their influence in the electron transfer (ET) of anchored redox proteins, such as myoglobin (Mb). The motivation is building up electrochemical biointerfaces whose properties can be tailored to tune a wide landscape of hydrophobic and hydrophilic interactions between Mb and functionalized surfaces by mimicking some basic features of ET at membranes or protein domains. The adsorption of building blocks constituted by ω-substituted alkanethiols that self-organize into molecular layers (SAMs) at gold surfaces exposing –COOH and –CH3 terminal groups at the solution interface is hypothesized to meet such requirement. The following ob jectives have been set:

1.- The formation of functional interfaces formed by 11-mercaptoundecanoic (MUA) and decanethiol (DT) molecules assembled onto Au substrates.

2.- To test deposition procedures for the spontaneous or potentially-driven molecular assembly of MUA and DT under different experimental conditions (e.g. modification time, solvent and pH) in order to select those yielding well-organized structures of pure and homogeneously mixed SAMs with reproducible interfacial properties. The selection would be based on the proper control of the surface composition gradients of the MUA and DT components spatially distributed into nanopatterns at the SAMs, while their acid-base interfacial properties are modulated by the solution pH.

3.- The replacement of surface patches of negatively charged residues at native Mb (n-Mb) by positively ones at cationized Mb (c-Mb) upon chemical modification.

4.- The immobilization of n-Mb and c-Mb onto gold substrates modified with pure and mixed SAMs to get insight into the relationship between their function to directly shuttling electrons or to catalyze redox reactions and their structural/conformational rearrangements at the electrochemical interfaces depending on the underlying surface interactions.

5.- The characterization of the 2D surface assemblies and protein complexes by using different mass analysis, electrochemical and spectroscopic techniques.

0. Objetivos

Esta tesis doctoral pretende estudiar las propiedades interfaciales de estructuras moleculares orgánicas 2D formadas sobre superficies, y que sirvan como sistemas modelo para evaluar su influencia en la transferencia electrónica (TE) de proteínas redox inmovilizadas, como es el caso de la mioglobina (Mb). La principal motivación consiste en construir interfases electroquímicas cuyas propiedades puedan adaptarse a un amplio paisaje de interacciones hidrófobas e hidrofílicas entre la superficie y la Mb, y que permitan imitar algunas de las características básicas de la TE de proteínas que tiene lugar en membranas o entre dominios de éstas. La hipótesis de partida se basa en que la adsorción y ensamblaje de alcanotioles ω-sustituidos (SAMs) sobre superficies de oro para formar capas moleculares (SAMs) que exponen grupos -COOH y -CH$_3$ hacia la interfase de la disolución pueden cumplir con tales requisitos. Para ello se han fijado los siguientes objetivos:

1.- La formación de interfases funcionales formadas por moléculas de ácido 11-mercaptoundecanoico (MUA) y decanotiol (DT) ensambladas sobre substratos de Au.

2.- Ensayar procedimientos de deposición para llevar a cabo el ensamblaje molecular espontáneo o bajo control de potencial de MUA y DT bajo diferentes condiciones experimentales (ej.: tiempo de modificación, disolvente y pH) con el objeto de seleccionar aquellos que conducen a estructuras bien organizadas de SAM puras y mezcladas homogéneamente con propiedades interfaciales reproducibles. La selección se basaría en aquellas condiciones que permitan el control adecuado de la composición superficial de los componentes, MUA y DT, que se distribuyan en patrones superficiales nanométricos en las SAMs, a la vez que sus propiedades ácido-base interfaciales son moduladas por el pH de la solución.

3.- La sustitución de cargas negativas de residuos situados en la superficie de la Mb nativa (n-Mb) por positivas en la Mb cationizada (c-Mb) tras su modificación química.

4.- La inmovilización de n-Mb y c-Mb en sustratos de oro modificados con SAMs puras y mixtas con el objeto de conocer la relación entre la función de transferencia directa de electrones o la capacidad de catálisis reacciones redox con su reordenamiento estructural/conformacional en interfaces electroquímicas en función de las interacciones superficiales subyacentes.

5.- La caracterización de los ensamblajes formados por SAMs y proteínas mediante el uso de diferentes técnicas de análisis masa, electroquímicas y espectroscópicas.

CHAPTER 1

Introduction

1. Introduction

1.1. Self-Assembly: A bottom-up strategy in molecular nanotechnology

Self-assembly is defined as the spontaneous organization of components into higher hierarchically-ordered patterns or complex structures.[1] The most characteristic features of the process are the following:

(I) – The system has higher order (lower entropy) than its isolated components (*i.e. surroundings become more disordered - higher entropy*).

(II) – The building blocks span a wide range of typologies such as atoms or molecules, nano- or mesoscopic structures with different compositions, shapes and functionalities.

(III) – Interactions between the components (*e.g. covalent, van der Waals, hydrogen bonding, electrostatic,* π-π interactions*, etc.*). This fact enables stable and flexible structures to withstand minor perturbations (ability of reversibility).

The self-assembling processes occurring in Nature, as well as in technology, can be classified as static or dynamic (Figure 1). On one hand, the systems formed by static self-assembly don´t dissipate energy as far as a global or local equilibrium is achieved. However, the formation of stable or ordered structures requires energy to trigger the assembly process. Some examples of this kind are represented by atomic, ionic, molecular, liquid or colloidal crystals, polymers, self-assembled monolayers (SAMs), lipid bilayers, folded proteins, etc. Templated/Directed self-assembly is a variant where the interactions between building blocks and regular features (*e.g. surfaces, optical fields, etc.*) determine the final structure.
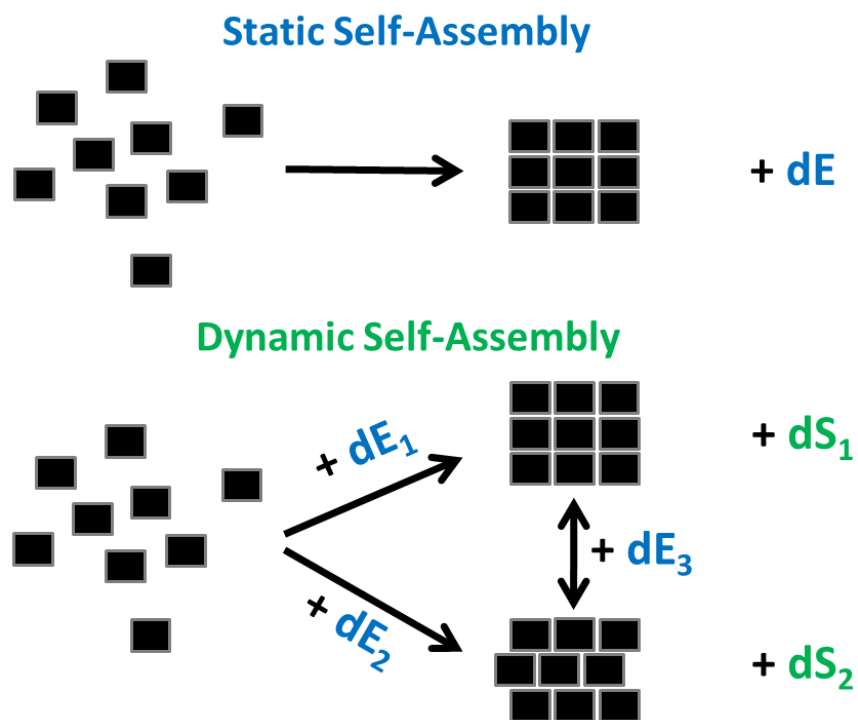
Figure 1. Static vs dynamic self-assembly (E=energy and S=entropy of the system).

14

On the other hand, dynamic self-assembly implies that the systems are dissipating energy which allows the formation of patterns or structures by their components interacting under non-equilibrium conditions. This definition is closer to that of self-organization. While self-assembly arrives at an equilibrium configuration, self-organization drives the system off the equilibrium which requires energy to maintain. Such situation is created by small fluctuations that are amplified by a positive feed-back loop where entropy decreases evoking emergent phenomena. The open thermodynamic systems may move from ordered, to near chaotic and far from equilibrium states (Figure 2). As energy consumption increases, systems pass through transition states between order and chaos. Live systems meet these requirements as a self-sustained chemical system over a period of time being able to undergo biological evolution by gathering energy and molecules from its surroundings, self-replicating and mutating. Thus, life is adaptive and dynamic and, when the energy flux stops through the living entities/systems they collapse.

The most common example of these complex and adaptive systems is the biological cell whose patterns are due to oscillating chemical reactions (i.e. competition between diffusion and reaction). The characteristic of biological self-assembly is the diversity and complexity of functions produced. *How does life emerge from chemical reactions?* It seems that self-organization play a *central role in life,* connecting the simplicity of chemical reactions to the complexity of cell division and self-replication by a hierarchy of self-assembling processes that are fundamental to their operation. Such chemical reactions are usually confined in a space delimited by membranes - thin walls

of self-assembled molecules - keeping complex molecules inside but allowing pass through the smaller ones that are related to the waste and nutrition cycles. Then, the study of the interfacial and chemical properties of these molecular assemblies is interesting from the surface and colloidal chemistry points of view. Although, the study of dynamic systems is still in its infancy, it offers great challenges and opportunities. Thus, most of the research and understanding of self-assembly has focused in the examination of static systems. This will be essentially the case for the work presented in this doctoral thesis which is focused on functional interfaces formed by SAMs.
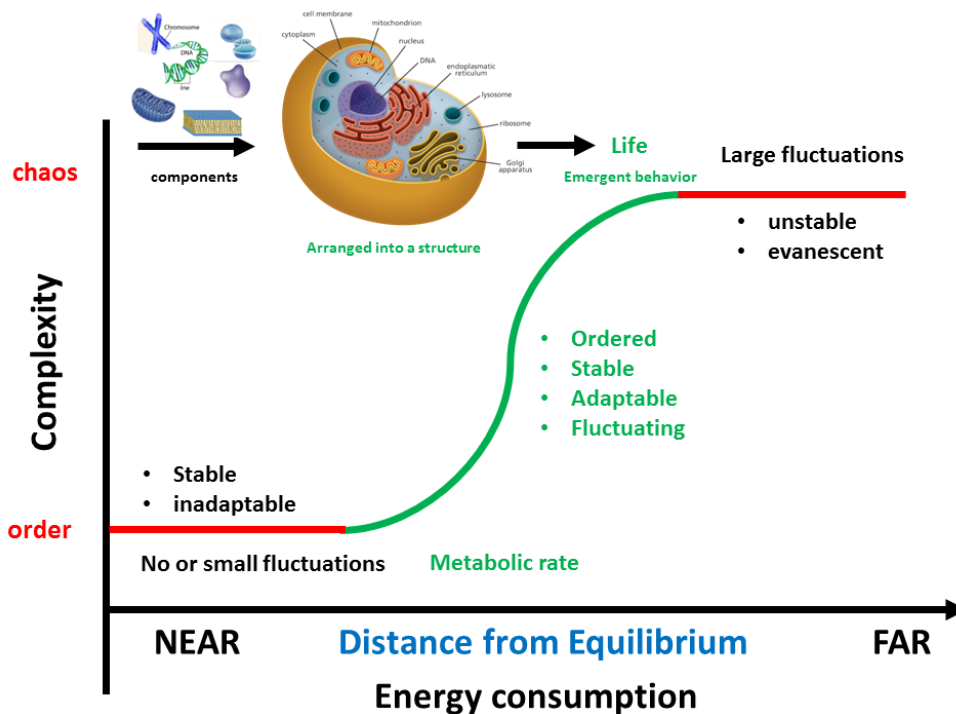
Figure 2. Concept of self-organization: Illustration of the continuum of open thermodynamic systems from ordered, near-to-chaotic, to far-from-equilibrium states (Source: Review of the Universe: universe-review.ca).

Self-assembly represents a practical "bottom-up" strategy for the construction and design of materials and devices with nanoscale dimensions.[2] Nanoscience deals with the study, construction, imaging, measuring or manipulation of objects with one dimension below 100 nm (Figure 3a), whose new physical, chemical and/or biological properties are of interest in the development of added-value industrial and market products for technological applications, Nanotechnology.[3-5] Nanoscience is an emerging highly interdisciplinary research field integrating chemistry, materials and surface science, applied physics, biology and engineering disciplines. [4, 5]

The assembly of entirely molecular building blocks into functional devices is usually named *molecular nanotechnology* to differentiate it from nanotechnology where devices are fabricated using other constituents (Figure 3b).[6] The fabrication of these nanostructured materials has been driven by the development of synthetic methods and advances in supramolecular chemistry.[7] They have been developed not only from organic and organometallic components but also integrated with nanomaterials and biomolecules.[8-10] Thus, nanomaterials have been designed with control over size, morphology and functionality by tailoring their properties. Additionally, advances in surface science have allowed building up 2D nanoscale molecularly assembled structures – *2D ultrathin films* – in a simple and reproducible way with a plethora of functional groups, which can be chemically modified, onto a wide variety of conducting, semiconducting or insulating substrates.

(A)		NANOMATERIALS CLASSES		
		(1) Discrete nano-objects	(2) Surface nano-featured	(3) Bulk nanostructured
Dimensionality	0-D	Nanoparticles Dots Clusters	Nanocrystalline Films	Nanocrystalline Materials Nanoparticle composites
	1-D	Nanorods Nanotubes	Nano interconnects	Nanorods/tubes Reinforced-composites
	2-D	Nanofilms foils	Nano surface layers Thin films	Multilayer Structures
	3-D	Nanowires Nanotubes	Multi layers	Multilayer Structures

Figure 3. General classification of: (a) Nanomaterials classes and dimensionality and (b) Molecular nanotechnology, nanotools and nanodevices. Red highlighted parts of the schemes relate to the specific areas where this doctoral thesis would be included.

The 2D films with nanoscale thickness (<<100 nm) can be classified as follows [7]:

(I)   Self-assembled monolayers (SAMs)

(II)   Langmuir-Blodgett films (LBFs)

(III)   Two-dimensional supramolecular assemblies

Therefore, the combination of the concepts of self-assembly and molecular recognition provides an efficient tool for surface functionalization. Like Nature, artificial constructs may response to external stimuli (*e.g. electrical, chemical/biochemical, temperature, electromagnetic radiation, etc.*) or interact with other isolated monomers to form functional materials.[11, 12] Then, the fabrication of functionalized surfaces can be used for designing 2D nanodevices, such as sensor/biosensors and for electronic applications, with either improved performance or new attributes (Figure 3b). The detection principle in nanosensor is simply based on monitoring changes in physicochemical properties (*e.g. electrical, optical, magnetic, mass, pH, etc.)* from the specific interaction of a target molecule with the molecular device.

1.2.   Self-Assembled Monolayers (SAMs) on surfaces

1.2.1. General Concepts and Historical Background

SAMs represent ordered molecular superstructures that are formed by the spontaneous adsorption of functional organic molecules from a liquid or gas phase through the attachment of a high-affinity head group onto a substrate. The balance of the intermolecular and surface interactions determines the final organization, sometimes into crystalline or

19

semicrystalline structures epitaxially grown (Figure 4).[6, 13-17] They are the most elementary form of 2D organic thin-film nanomaterials showing thicknesses between 1 to 4 nm, which can be incremented for multi-layered assemblies. An advantage of SAMs over LBFs is that more flexibility is provided in the molecular design because the molecules required do not need to be exclusively amphiphilic.
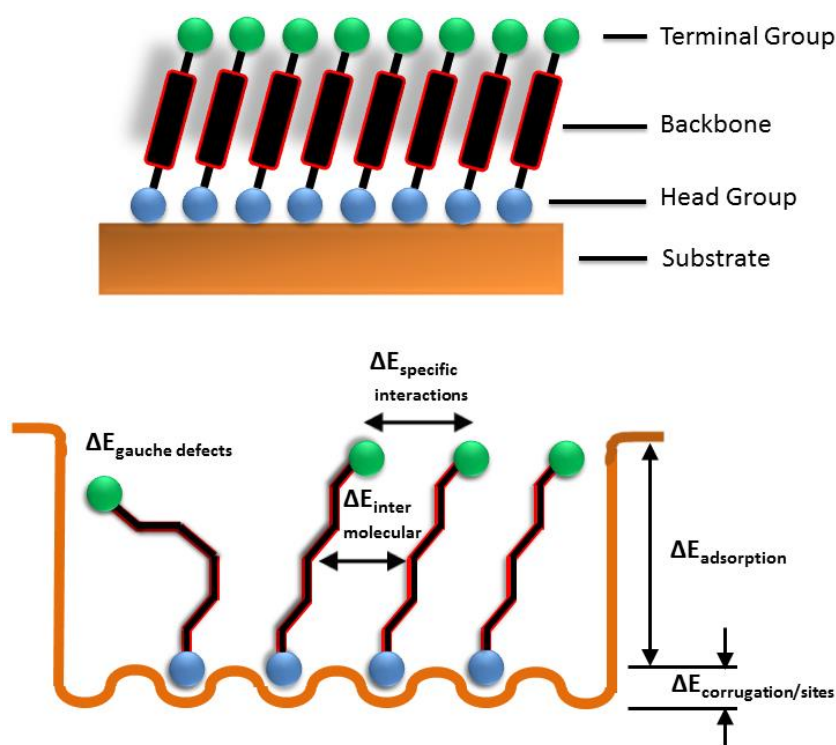
Figure 4. SAM general organization scheme and energy balance on surfaces.

The molecular structure of the adsorbate building blocks can be divided into three main parts: [14]
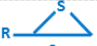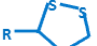
(I) – *Head group*. It is constituted by chemical moieties placed at one end of the molecule having a high affinity for the substrate surface. The head group is usually grafted to the substrate by covalent bonding with surface atoms (c*hemisorption)*. Some groups that have been mainly used are (Table 1): *-SH, -S-S-, -S-, -SOCH$_3$, xanthate, thiocarbamate, -SeH, -Se-Se-, -COOH, -PO$_3$H, -OH, -H, -SiCl$_3$, -Si-(OCH$_3$)$_3$, -N$_3$ or diazonium salts, etc.*

(II) – *Backbone*. This is a spacer part linking the head and terminal groups of the molecule. It is usually composed by alkyl chains *(saturated bonds)* and/or aromatic rings *(unsaturated bonds)*. Weak and short range backbone intermolecular interactions (*e.g. Van der Waals, dipolar,* п-п*, etc.)* play a crucial role in the final ordering/packing of the monolayer. Some examples of spacers used in the backbone are the following:

-(CH$_2$)$_n$-, -(CF$_2$)-(CH=CH)$_n$-, -(C≡C)$_n$-, -(C=C)$_n$-, -(CH$_2$-O)$_n$-, -CO$_2$-CH$_2$-, -CO-NH-, -SO$_2$-, -(-CH$_2$-CH$_2$-O)$_n$-, aryl, biphenyl, alkylbiphenyl, azobenzene, oligo(phenylenen-ethynylene, etc).

(III) - *Terminal/Tail group*. It is the distal moiety exposed to the SAM/environment interfacial area defining the chemical functionality of the surface. A rich surface chemistry has been exploited thanks to the wide range of terminal functionalities available in SAMs (*e.g. –COOH, -CH$_3$, –OH, -SH, -NH$_2$. -NO$_2$, -CH=CH$_2$,-C≡CH, -CF$_3$, -CN, -O-CH$_3$, -CO$_2$CH$_3$, -CO-NH$_2$, -Cl, -SO$_3$H, -B(OH)$_2$, -N$_3$, epoxide, aryl, pyrrole, ferrocene, etc.)*

The formation of a monolayer of adsorbed molecules diminishes the interfacial free energy between the substrate and the environment. Consequently, interfacial properties are altered by acting the organic material as a physical or electrostatic barrier changing the electronic and/or optical

21

properties, by decreasing the reactivity of surface atoms and modifying the electronic states, by acting as an electrically conducting or insulating film or even by introducing changes in the surface chemistry and reactivity through different terminal groups. That is, a hydrophobic terminal moiety will make a low energy hydrophobic surface, while polar or ionisable moieties will produce high energy ones. Hence, the plethora of molecular structure combinations and substrates available for SAMs formation (Table 1) provides a convenient and versatile system to tailor interfacial or tribological properties of surfaces, such as conductivity, corrosion, wettability and adhesion among others.[14, 15, 18]

Then, the reason that makes SAMs attractive for building molecular devices is that well-defined surface packing and density of specific molecules can be obtained. Another reason is the possibility to build multifunctional surfaces by incorporating molecules with different terminal groups into SAMs (*mixed SAMs*) to finely tune chemistry at the top of the layers with precision down to the nanoscale or molecular level. Multifunctional surfaces can be designed to contain components that allow coupling further functionality, spacing components apart or aiding to control surface interactions with the environment. Thus, SAMs provide excellent models for studying electron transfer processes,[19-21] controlling interfacial reactions and tailoring surface properties.[6, 14, 15, 22, 23] SAM-based platforms have been widely applied in many fields such as biomaterials and biosensing,[9, 10, 24, 25] fuel cells,[26] molecular electronics and photovoltaics [17, 26, 27] (Figure 5).

Table 1. Chemical systems of adsorbates and substrates that form SAMs

Absorbate	Substrate	Thin Films Bulk Material	Nanoparticles Nanostructures
Organosulfur			
RSH	**Metals**		
	Au	✓	✓
	Ag	✓	✓
	Pt	✓	✓
	Pd	✓	✓
	Cu	✓	✓
	Hg	✓	
	Ir		✓
	Ni	✓	
	Ru		✓
	Zn	✓	
	AuAg		✓
	AuCu		✓
	Au_xPd_{1-x}		✓
	Ag_9Ni	✓	
	FePt		✓
	PdAg		✓
	Semiconductors		
	Ge	✓	
	GaAs	✓	
	InP	✓	
	CdTe		✓
	CdSe		✓
	CdS		✓
	ZnSe		
	ZnS	✓	✓
	PbS		✓
	HgTe		✓
	Ag_2S		✓
	Oxides		
	Stainless Steel	✓	
	ITO	✓	
	Tl-Ba-Ca-Cu-O	✓	
	$YBa_2Cu_3O_7$-δ	✓	
RSSR'	**Metals**		
	Au	✓	✓
	Ag	✓	✓
	Pd	✓	
	Semiconductors		
	CdS		✓
RSR'	**Metals**		
	Au	✓	
RSOCH$_3$	Au	✓	
R (S–S triangle)	Au		✓
R (S–S pentagon)	Au	✓	
RS_2O_3Na	Au	✓	✓
	Cu	✓	
RCSSH	Au	✓	
	Semiconductors		
	CdSe		✓

Absorbate	Substrate	Thin Films Bulk Material	Nanoparticles Nanostructures
Organoselenide			
RSeH	**Metals/Semiconductors**		
	Au	✓	
	Ag	✓	
	CdS		✓
	CdSe		✓
RSeSeR'	Au	✓	
Organophosphorous (III-IV)			
R_3P	**Metals/Semiconductors**		
	Au		✓
	FeS_2	✓	
	CdS / CdSe / CdTe		✓
$R_3P=O$	Co		✓
	CdS / CdSe / CdTe		✓
RPO_3^{2-} $RP(O)(OH)_2$	**Oxides/Semiconductors**		
	Al	✓	
	Al-OH	✓	
	$Ca_{10}(PO_4CO_3)_6(OH)_2$	✓	
	ITO	✓	
	Mica	✓	
	TiO_2	✓	
	ZrO_2	✓	
	GaAs / GaN	✓	
	CdSe / CdTe		✓
RPO_4^{2-}	**Oxides**		
	Al_2O_3 / TiO_2	✓	
	Nb_2O_3 / Ta_2O_3	✓	
Fatty acids / Alcohols			
ROH	**Oxides/Semiconductors**		
	Fe_xO_y		✓
	Si / Si-H	✓	
$RCOO^-/RCOOH$	**Metals/Oxides**		
	Ni		✓
	Ti/TiO_2	✓	
	Al_2O_3	✓	
	Fe_xO_y		✓
RCOO-OOCR	**Semiconductors**		
	Si (111):H / Si (100):H	✓	
Ene-diol	Fe_2O_3	✓	
Organosilanes			
$RSiX_3$ (X=H, Cl, OCH$_2$CH$_3$)	**Oxides**		
	$HfO_2 / ZrO_2 / TiO_2 / SiO_2$	✓	
	ITO	✓	
	PtO	✓	
Nitrogen and Carbon Derivatives			
RNH_2	**Metals/Semiconductors**		
	Stainless Steel	✓	
	Mica	✓	
	$YBa_2Cu_3O_7$-δ	✓	
	FeS_2 / CdSe	✓	✓
RC≡N / RN≡C	Au / Ag / Pt	✓	✓
RC≡CH / RHC=CH$_2$	Si (111):H / Si	✓	

In 1983, Nuzzo and Allara reported a new methodology for preparing organic monolayers with different terminal functional groups by adsorbing disulphide compounds from solution into gold surfaces.[28] In the next decade (1983-1993), this fact extended dramatically the previous approaches to a wide variety of functional SAMs mainly formed by chemisorption of organosulfur compounds from solution or vapour phases onto Au and Ag surfaces.[29, 30]

Among organosulfur compounds, the studies were mainly focused on ω-substituted alkanethiols ($HS(CH_2)_nX$), dialkyl disulfides ($X(CH_2)_mS\text{-}S(CH_2)_nX$) and dialkyl sulphides ($X(CH_2)_mS(CH_2)_nX$) SAMs, where n and m represent the number of methylene units and X the tail group of the alkyl chain. In this period, much effort is dedicated to elucidate the structure, preparation protocols and some details governing thermodynamics and kinetics of the assembly process in these kinds of SAMs.

Since early-1990s, research on organosulfur and ω-substituted alkanethiol SAMs on Au and Ag continued to get insight into the aspects commented above but also expanded to some degree the type of molecules used to build them and to other metallic and semiconductor flat surfaces (Table 1).[31-38] During this period, this kind of monolayers also started to be employed in the stabilization, synthesis of nanoparticles (3D-SAMs) and, design of nanostructured materials.[38]
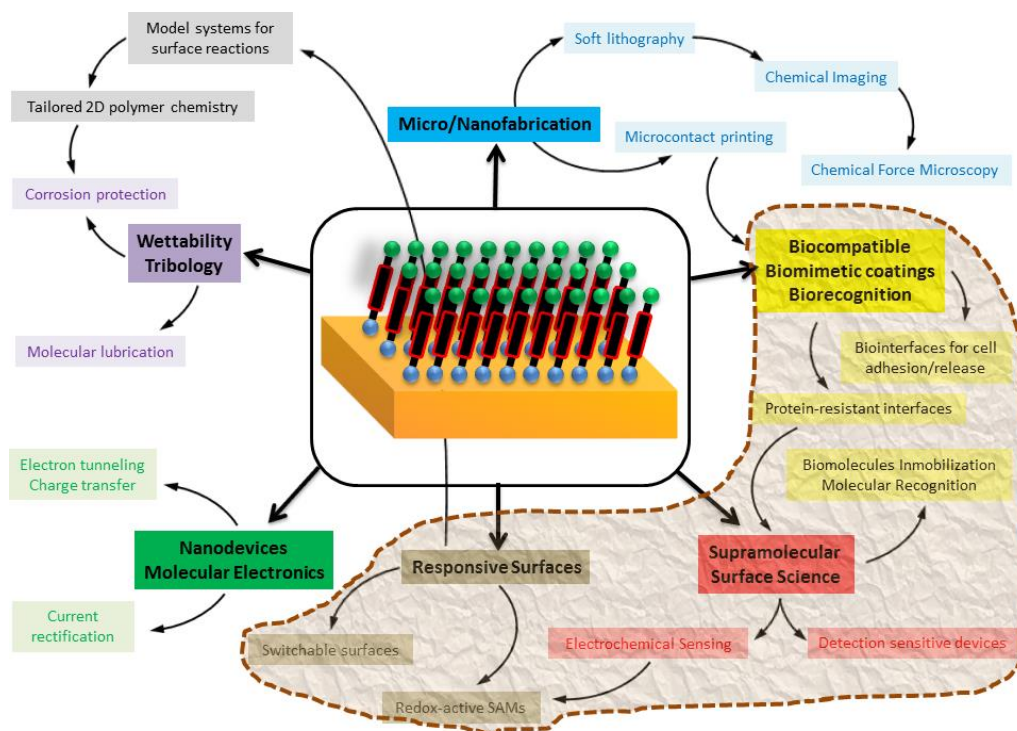
Figure 5. Diagram of SAMs applications. The work presented in this doctoral thesis would be ascribed to the research fields and applications included in the shaded-area.

In the last decade, the research interest in ω-terminated alkanethiols has grown on: (i) reactive surfaces by adding functionality, biocompatibility and implementing surface chemical gradients to pure and mixed 2D-SAMs in a controllable manner (*e.g. click chemistry*),[39, 40] (ii) electron/charge transport across molecular and nanoscale junctions (*Metal-SAM-Metal or Metal-SAM-semiconductor interfaces*) [40-42] and, specially (iii) the design of biocompatible nanoparticles and nanostructured materials in prospect of applications in Nanotechnology.[10, 43, 44]

1.2.2. Organosulfur SAMs: Alkanethiols on Gold

Why alkanethiol SAMs are the most popular and studied 2D assemblies?

They are considered model systems in 2D thin solid films for understanding of the self-assembly process at surfaces, which is essentially based on: (i) the ease of forming a structurally well-defined organic surface and (ii) providing unprecedented control over the monolayers formed at the molecular level with the possibility of further surface derivatization. However, the real challenge comes in making stable SAMs and almost defect-free in a reproducible way for different applications.

Why is Gold the standard surface for alkanethiol SAMs?

Although for some applications gold may not be the best substrate, several characteristics make it the best choice for studying alkanethiol SAMs:

(I) – Unlike other metals, gold is reasonably inert with most chemicals and does not readily form surface oxides under atmospheric conditions. This makes possible to manipulate samples and conduct experiments without need of using complicated and expensive UHV equipment.

(II) – It is a biocompatible material without evidence of toxicity for macromolecules or cells that can adhere and function on the modified surface. SAMs formed on gold are stable from days to weeks in contact with biological media when required.[14]

(III) - The gold is easy to obtain either as a 15-1000 nm thick film deposited on Si, glass and mica, sometimes attached to the underlying substrate by a 1-5 nm adhesion interlayer of Cr or Ti, or as a colloid. Highly organized and packed SAMs with low density of defects and well-defined interfacial properties

usually require the use of large atomically smooth terraces and single crystalline-textured gold surfaces.

The use of commercial or "home-made" gold single crystals is more expensive and with a more reduced applicability for their easy implementation in conventional techniques for SAM´s characterization. However, they offer a unique possibility to unravel the role of the S-Au chemistry at different surface coordination sites and crystallographic orientations *(e.g. low index Au(111), Au(100) and Au(110) surfaces)* on the SAM organization and their interfacial properties.[30] The use of polyfaceted gold surfaces is an intermediate lower cost solution compared to that of single crystals and deposited thin films.

(IV)   – The development of accepted methodologies to obtain reliably clean, either by wet chemical or flame annealing procedures, and well-defined single crystalline or polyoriented gold surfaces is another important reason for its use.[45] This fact allows improving reproducibility in the SAMs formation and characterization, as well as a more satisfactory comparison of results between laboratories. However, polycrystalline films are sufficient for many applications on planar substrates and inexpensive in comparison to single crystals. Then, the criteria for selecting the type of substrate and preparation method will depend on the SAM´s applications.

1.2.2.1. Protocols for the formation of alkanethiol-based SAMs on gold

The spontaneous formation of alkanethiol monolayers on gold can be performed from either the liquid or vapour phase. Assembly from solution is a convenient method for the gold surface modification and sufficient for most

applications of SAMs where subsequent contact with liquid phases is required (Figure 6a). The spontaneous adsorption of thiols to the gold surface takes place by a chemisorption process where a pseudo-covalent thiolate-gold bond (*referred as S-Au for sake of simplicity*) is formed *($\sim$40-50 kcal/mol*): [30]

$$X\text{-}(CH_2)_n\text{-}SH + Au_n^0 \rightarrow X\text{-}(CH_2)_n\text{-}S^-Au^+ \cdot Au_n^0 + \frac{1}{2}\,H_2 \qquad (1)$$
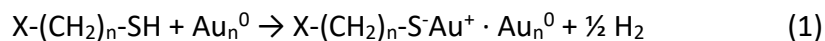
The proposed reaction (1) and the nature of the S-Au interface are still controversial and under debate as it will be commented later. The energy related to other parts of the molecule has a different order of magnitude compared to the S-Au bond. In this sense, 1–2 kcal/mol energy values are involved per methylene unit for the van der Waals interactions between hydrocarbon chains, and only a few kT values relate to the terminal groups.[14, 30] However, all three parts of the molecule contribute to the structure and to the physico-chemical properties of the SAMs.

1.2.2.2. Deposition from solution phase

SAMs are easily prepared by immersing a freshly prepared and clean gold surface into a dilute (*0.01-10 mM*) ethanolic solution of the alkanethiol compound for an adequate period (*from minutes to 24 h*) at room temperature (Figure 6a). The most common procedure described in literature is the use of 1-10 mM ethanolic solution of thiols for a 12-18 h immersion time period.[14, 46] This fact comes from early studies designed to optimize reproducibility of the SAMs produced and convenience. The widespread use of ethanol is due to several reasons: (i) the solvation of different alkanethiols

with variable degrees of polarity and chain length, (ii) low-cost, (iii) high purity and (iv) low toxicity.[46]

Although, high surface coverage of alkanethiols can be quickly obtained within milliseconds to minutes, a slow reorganization process is usually required over a period of time of several hours to maximize the packing and ordering of the monolayer while minimizing the structural defects in the SAM (Figure 6).[13, 46, 47]

It is generally accepted that SAMs are formed following a multistep process: (I) the molecules that are physisorbed on the surface in lying-flat configuration, (II) they subsequently chemisorb, reorient and, (III) become densely packed into islands or domains of molecules that start to nucleate and spread across the surface with time, while thiol molecules continue to adsorb at domain boundaries and, (IV) finally at longer times and high surface coverages, the growing domains merge to form a quasi-defect free monolayer (Figure 6b).
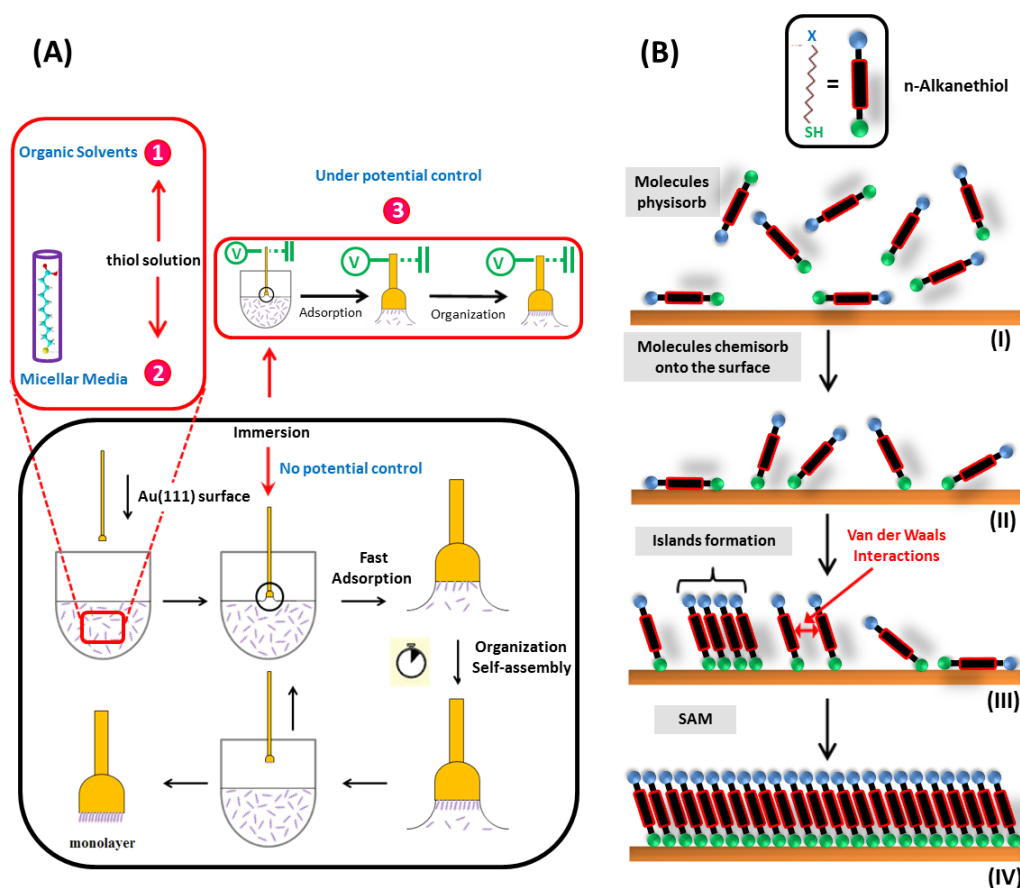
Figure 6. (a) Diagram showing the steps in the formation of a SAM deposited on a Au(111) surface upon immersion in alkanethiols solution or micellar medium either under potential control or in its absence, and (b) representation of the assembly process: (I) physisorption, (II) chemisorption, (III) island and (IV) SAM formation.

The assembly process is determined from thermodynamics and kinetics for the adsorption of the SAM (Figure 4).[13, 14] The order and the final structure of the SAM is mainly derived from the van der Waals (*v.d.W.*) intermolecular interactions between neighbouring alkyl chains as long as efficient molecular packing is not disrupted by tail groups that are bulkier than the footprint of

the alkyl backbone (~20 Å). [13, 14, 29, 30] Then, the specific protocol selected will depend on the compound structure and the purpose for the SAM formation.

Therefore, any experimental parameter that influences v.d.W. intermolecular interactions will affect the rate of formation and the resulting organization of the SAM.[14] In practice, most experimental conditions yield SAMs with desirable functional behaviours which are acceptable for some applications. However, fundamental studies of interfacial properties usually require minimize defects in the final structure.[18, 40] If a more ordered monolayer is required then, longer times of immersion, longer alkyl chains, more concentrated thiol solutions, small amount of dissolved impurities of other sulphur compounds, smoother, clean and well-defined surfaces would be recommended. However, the effects of other parameters as *choice of solvent and temperature* are less known.

The thermodynamics and kinetics of the assembly process can be affected by the solvent structure and polarity used for the SAM deposition because of the balance of the solvent-substrate and solvent-adsorbate interactions in the dynamic equilibrium governing the thiol adsorption.[48, 49] Stronger solvent-substrate interactions may slow down the adsorption rate of the thiols from solution as they must compete for the displacement of the solvent molecules from the surface.[50] Hydrocarbon non-polar solvents may improve the adsorption kinetics but, stronger solvent-adsorbate interactions lead to less-organized alkanethiol SAMs to that formed from polar solvents.[48, 51] It seems that poor solvents for n-alkanethiols (*low solubility and heat of adsorption*) reduce SAM conformational and pinhole defects by promoting densely packed layers but, in some cases, at the cost of the physisorption or

intercalation of thiol molecules on the monolayer.[48, 51] Therefore, the solvent is an important parameter for determining the quality of the SAM. However, there remains a challenge to understand in detail the complex and dynamic interactions that takes place between solvent, surface and adsorbates in the assembly process.

1.2.2.3. Deposition under potential control

Gold substrates are metallic conductors that can act as electrodes. The adsorption of alkanethiols and the SAM organization process can be altered by changing the external potential applied to the metal. The studies focusing on the potential-controlled formation of the SAMs was firstly demonstrated by Porter and coworkers.[52, 53] This fact is evidenced by the presence of oxidative readsorption peaks (*electrochemical S-Au chemisorption reaction in alkaline media:* $Au + X\text{-}(CH_2)_n\text{-}S^- \rightarrow X\text{-}(CH_2)_n\text{-}S\text{-}Au + e^-$) in cyclic voltammograms once the potential is swept back to anodic values after the SAM formed has been reductively desorbed from gold at cathodic potentials.

More recently, control on the deposition kinetics of SAMs on gold is effectively achieved by changing the electrode potentials.[54] When holding the electrode potential positive to the *potential of zero charge* of gold, the thiol molecules are covalently attached while, at cathodic potentials, chemisorption and reorganization processes are significantly slowdown. This potential-assisted deposition method usually leads to the formation of complete, free of pinhole defects and highly-ordered thiol SAMs faster, over time scales of a few minutes, than the common deposition process under open circuit potential (OCP) conditions.[54, 55] However, this behaviour seems not prevail in the case of thiol SAMs with the shorter chains.[56] Additionally,

this method is especially effective to: (i) tune surface composition to the molecular level in mixed SAMs, (ii) create surface gradients by switching off/on the SAM formation under soft conditions, (iii) control surface coverage in the submonolayer range or even the formation of monolayers or bilayers otherwise inaccessible using OCP deposition.[54, 57-59]

1.2.2.4. Deposition from micellar medium

SAM formation based on deposition from aqueous micellar media is a less explored method, but represents an interesting approach to build almost defect-free alkanethiolate monolayers. The study of this micelle-assisted deposition method was firstly reported by Kaifer et. al. [60] and examined in detail by Jennings et. at. [61-64] Self-assembly process of thiols from aqueous micellar solutions has been investigated by using Triton X-100,[60, 65, 66] olygoethylene glycol monodecyl ethers (C_nE_6),[61-63] sodium dodecylsulfate (SDS),[60] and n-alkytrimethylammonium bromides (C_nTAB) [63] as representative nonionic, anionic, and cationic surfactants, respectively.

The interactions of the micelles with alkanethiols influence the thermodynamics and kinetics of the adsorption process.[62, 63, 65, 66] In this sense, the hydrophobic interactions between neighbouring alkyl chains are usually facilitated during the self-assembly process in hydrophobic micellar environments, while adsorption kinetics are slow down exponentially upon increasing the alkanethiols chain length.[62, 63] Therefore, the formation of high quality monolayers with even improved packing density and excellent electron transfer blocking properties can be achieved as compared to SAMs prepared from organic solvents under similar experimental conditions.[61, 65, 66]

Interestingly, micelles have been suggested to act as vehicles transporting and delivering the thiols to the metal surface (Figure 7). The general mechanism proposed to explain the micelle-assisted monolayer formation consists of several steps (Figure 7a): (1) the micelles containing the alkanethiols diffuse to the proximity of the Au surfaces, (2) the release of the alkanethiols from the micelles adsorbed at the metal surface (admicelles) and, (3) alkanethiols chemisorb on the surface after admicelles removal. Yan et.al. have also proposed that thiols are likely to be transferred between micelles in solution and, to admicelles in metal surfaces at low surface coverages, through a collision induced activated diffusion process (Figure 7b).[62, 63] At high surface coverages, the alkanethiols must be released atop the growing SAM by forming surfactant bilayers.
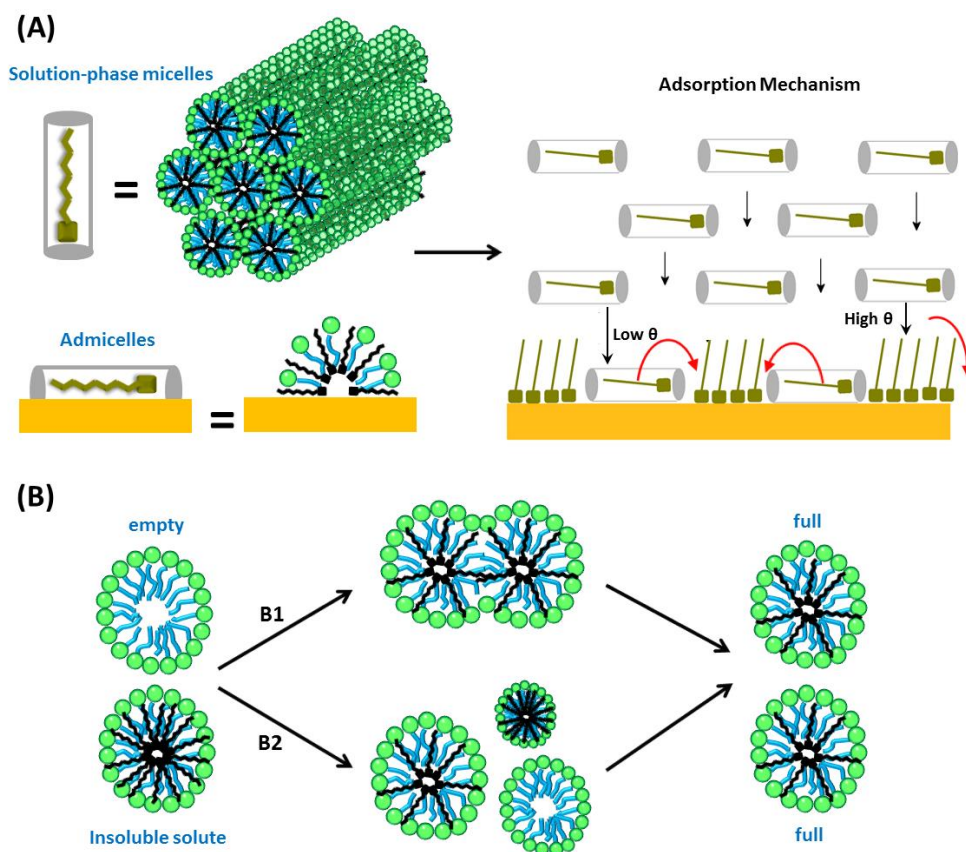
Figure 7. (a) Proposed scheme for the transfer to the surface of alkanethiols dissolved in a hexagonal liquid crystalline micellar phase of Triton X-100 (non-ionic surfactant) and water. (b) Possible pathways for exchanging insoluble alkanethiols in micellar solutions: B1 - collision-driven fusion-fragmentation and B2 – fragmentation-growth mechanism, where either solute-dissolved sub-micelles separate from a normal-sized micelles to grow or become incorporated into empty micelles.

1.2.3. Alkanethiol-based mixed self-assembled monolayers

Multicomponent SAMs, so-called mixed SAMs, are comprised by a well-defined mixture of 2D molecular structures. The simplest case is a mixture of two components leading to binary SAMs with defined gradients of

interfatial composition and surface nanopatterns.[67, 68] As already commented, molecular level control over the density and spatial distribution of functional groups in surfaces is important for a wide variety of applications, and in particular, for the design of biomaterials, biosensors and molecular electronics devices.[17, 24, 69, 70] At present, mixed SAMs offers the best option for controlling the density and spatial distribution of biomolecules on surfaces while preserving their biological activity in many cases. Morever, such SAM surfaces may be stimuli responsive (*e.g. electrical, chemical/biochemical, optical, temperature, etc.*), where their surface properties are manipulated providing the possibility to switch "on-off" states that modulate, for example, the biomolecule activity and function, protein immobilization and cell adhesion.[7, 11, 12] These interfaces are also usually referred as "switchable" SAM surfaces.

Mixed SAMs can be produced by spontaneous coadsorption from solutions containing mixtures of thiols in which the substrate is immersed. The formation of ω-terminated alkanethiol binary SAMs with widely varying surface compositions of functional groups can be controlled by changing the mole fraction of the adsorbates in solution – but does not necessarily coincide with their surface fraction usually due to the preferential adsorption of one component - for different concentration ranges.[71, 72] Analytical techniques, such as X ray photoelectron (XPS)[73-77] and infrared (IR) [74-76] spectroscopies, contact angle (CA),[73, 76-78] ellipsometry,[74, 79] cyclic voltammetry (CV)[58, 75, 77, 79, 80] and scanning probe microscopies (SPMs)[75-77, 81] have been used to characterize the phase separation of components and determine the average surface composition of binary monolayers. SPMs are a powerful tool that

meets the requirement of molecular resolution for direct imaging of nanometer scale patterned mixed SAMs.[75-77, 81] Then, macroscopic techniques can be used not only to elucidate the phase behaviour in mixed SAMs but also to relate the information provided with nanopatterns schemes of monolayer´s organization already supported by SPMs.
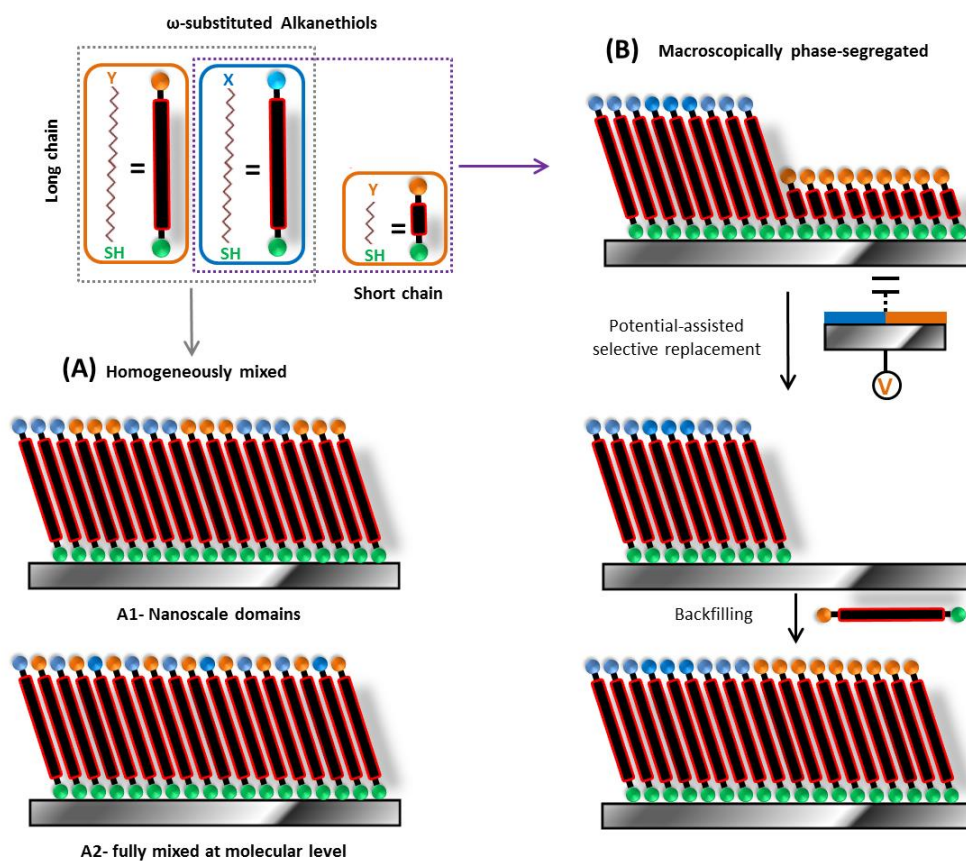
Figure 8. Schematic illustration of mixing phases in binary SAMs and selective replacement by partial electrochemical desorption. X (*blue*) and Y (*orange*) represents the end-group of the alkyl chain (-CH$_3$, -COOH, -OH, etc.) of the ω-substituted thiols.

ω-terminated alkanethiols having similar molecular features and hydrocarbon chain lengths lead to <u>homogeneously mixed</u> SAMs formed either by nanoscale phase-separated domains of each component (*macroscopically mixing*)[58, 75, 76] or uniformly distributed individual components (*molecular level mixing*) (Figure 8).[58] The tendency of mixed binary SAMs whose components are markedly different in the hydrocarbon chain length and in the ω-terminal group is to <u>phase-segregate</u> into bigger size domains of each molecule (*macroscopically phase-segregated*) (Figure 8).[79] When deposition is carried out under near-to-equilibrium conditions, such mixing phase behaviours can be explained by thermodynamics and the prevalence of homo- or heteromolecular interactions between neighbouring molecules would be the main factor determining the final phase composition. However, kinetics may play a crucial role in obtaining metastable trapped states under non-equilibrium conditions. Some examples are the following: (i) binary SAMs formed by short and long ω-substituted alkanethiols may behave as an intermediate state between completely mixed (*homogeneous mixing*) and fully phase-segregated (*macroscopically phase-separated*)[73] and (ii) binary SAMs formed by ω-terminated alkanethiols with the same chain length that form nanoscale phase-separated islands (*homogeneous macroscopically mixing*) at room temperature may either behave as uniformly distributed at the molecular level or macroscopically phase-separated when increasing the temperature.

As in the case of pure SAMs, potential-assisted deposition of mixed SAMs allows the formation of highly-ordered films faster than the common deposition process under OCP conditions. Additionally, post-adsorption

processing of mixed SAMs under potential control offers unprecedented control over surface patterning, otherwise non-accessible by the conventional method of spontaneous deposition (Figure 8). Thus, different surface gradients can be created by selective replacement of the SAM components (*e.g. electrochemical partial reductive or oxidative desorption*) and backfilling with new functional molecules. Regarding to the deposition of mixed SAMs from micellar medium, the firstly reported example in literature will be described in the present doctoral thesis.

1.2.4. Structural characterization of alkanethiolate SAMs

A plethora of techniques for surface analysis and physico-chemical characterization (*RAIRS, Raman, XPS, SFG, HREELS, NEXAFS, XRD, SPMs, ellipsometry, contact angle, mass spectrometries, etc.*) have contributed to elucidate structural organization (*orientation, organization and surface structure*) and in the understanding of the self-assembly mechanisms at molecular scale in alkanethiolate SAMs (Table 2). Most of the studies have been carried out on Au(111) surfaces as a model system and in fact, still today there is only limited information about self-assembly of these molecules on other gold single crystalline surfaces.

Table 1. Summary of SAM properties collected by different analytical techniques

SAM properties		EC	XPS	SPM	XRD	ellipsometry	IR	Raman	SFG	UPS	LEED	NEXAFS	SIMS	SEM	RBS	ISS
Coverage	Overall coverage/thickness	✓	✓	✓	✓	✓	✓					✓				
	Pinholes	✓	✓	✓							✓	✓	✓	✓	✓	✓
Composition	Average		✓									✓		✓	✓	
	Surface		✓									✓				✓
	Conc. Profile		✓									✓			✓	✓
Functional Groups	Bonding	✓	✓				✓	✓	✓	✓		✓	✓			
	Valence		✓							✓		✓				
	Orientation		✓	✓		✓	✓	✓	✓	✓		✓				
	Conformation						✓	✓	✓	✓						
	Average composition	✓	✓				✓	✓	✓	✓		✓	✓			
	Depth profile	✓	✓			✓	✓	✓	✓	✓		✓	✓		✓	✓
Ordering	Pinholes	✓	✓									✓	✓	✓	✓	✓
	Long-range dislocation	✓	✓	✓			✓	✓	✓	✓	✓	✓	✓	✓	✓	
	Orientation			✓	✓	✓	✓	✓	✓	✓		✓		✓		
	Interface ordering	✓	✓	✓	✓						✓		✓			
Substrate	Bonding	✓	✓			✓	✓	✓	✓	✓		✓	✓			
SAM interface	Pinhole	✓		✓							✓			✓		

Note: EC = *Electrochemical* , **XPS** = *X-ray photoelectron spectroscopy*, **SPM** = *Surface probe microscopy*, **XRD** = *X-ray diffraction*, **IR** = *Infrared*, **SFG** = *Sum frequency generation spectroscopy*, **UPS** = *Ultraviolet photoelectron spectroscopy*, **LEED** = *Low energy electron diffraction*, **NEXAFS** = *Near-edge X-ray absorption fine structure spectroscopy* , **SIMS** = *Secondary ion mass spectroscopy*, **RBS** = *Rutherford backscattering spectroscopy*, **ISS** = *Ion scattering spectroscopy*

SAMs are generally accepted as well-defined phases of organic groups laterally organized on the underlying substrate. However, SAMs are dynamic materials with significant forms of structural complexies and embed extrinsic and intrinsic defects, specially when inmersed in fluids. Some of these dynamic aspects keep still opened discussions and controversial of SAM structure about phase transitions, conformational isomerism, lateral diffusion, the metal-sulphur bonding and environmentally responsive reconstructions of their surfaces.

1.2.4.1. Gold-sulphur interface

Knowledge of the S-Au bond is imperative in molecular electronics and the design of novel optoelectronic devices. The reaction (1) for the thiolate-gold bond formation is generally accepted. However, chemistry involved in its mechanism of formation and nature of S-Au interface are still under debate in search of a unified model.

In general, the ordering and the final structure of an alkanethiolate monolayer on single crystalline gold surfaces is esentially determined by the energy balance (Figure 4) of two factors:

(I) - The periodicity arrangment of surface atoms in the gold lattice and the presence of different coordination sites for the adsorbate molecules that leads to different adsorbate-substrate lateral corrugation and adsorption energies (Figure 9).

(II) – The V.d.W. intermolecular interactions between alkyl chains that determine the adsorbate ordering in the absence of substrate corrugation.
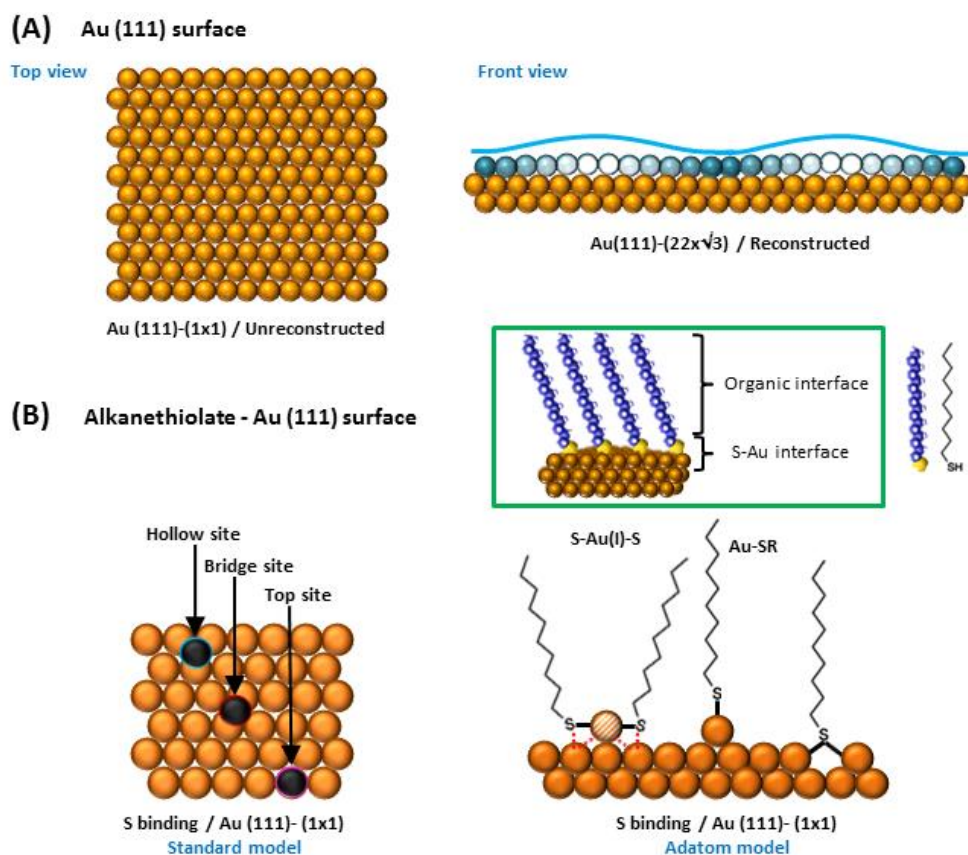
Figure 9. (a) Top and front view of simplified models of the un-reconstructed and reconstructed Au(111) surface. Different shades emphasize the corrugation of the outer-most layer due to misfits between surface and the bulk atomic structure. (b) Schematics of bonding motifs between thiolates and unreconstructed Au(111) for the standard model, describing sulphur binding atop, bridge or hollow sites and, the adatom model, describing binding of dithiolate (RS-Au(I)-RS) and thiolate (RS-Au) with Au adatoms.

A common motif at metal-gold interfaces is that the SAM structure tends to arrange similarly to a simple adlayer structure of elemental sulphur does on gold. Then, most of the long-range ordered alkanethiolate monolayers are

commensurate with the gold surface lattice. The substrate corrugation plays an important role in SAM ordering and intermolecular interactions also clearly influence the lateral spacing within neighboring hydrocarbon chains. This fact has been implicitly assumed by the standard model tradicionally accepted for the S-Au interfacial bonding where molecular ordering would take place on an unreconstructed surface (Figure 9). In this sense, the unreconstructed Au(111)-(1x1) surface would provide a rigid chequer-board of one, two and three-fold symmetry surface sites (*i.e. atop, brigde and hollow sites*) on which alkylthiolate molecules pin and assemble into different ordered structures depending on the thiolate surface coverage achieved (Figure 9b).

However, flame-annealed clean Au(111) adopts a uniaxially-compressed hexagonal close-packing in the outer-most atomic layer with a gold interatomic distance smaller than the underlying bulk gold (Figure 9a). The larger atomic density of 4.4 % compared to the bulk layers below originates a $(23 \times \sqrt{3})$ rectangular commensurate mesh with the substrate and a "herring-bone" corrugation pattern.

The Au(111)- $(23 \times \sqrt{3})$ surface reconstruction is lifted to a unreconstructed surface termination as the thiolate coverage increases.[82] This fact must lead to an atomic surface motion with the release of the excess of Au atoms in the outer-most layer, and indeed the formation of surface "pits", identified by STM technique as vacancy islands whose depth is equivalent to one or two gold atoms in height. The nature of these vacancies and the origin of the c(4 x 2) molecular superstructure, systematically observed in alkanethiol SAMs, has been a long-time controversial issue. For that reason, despite the classical view of static and unreconstructed Au(111) surface with

adsorbates occupying a specific surface site, different and dynamic bonding models have emerged for the S-Au interface, the so-called adatom models (Figure 9b). This new picture for the S-Au interface is based on the formation of surface thiolate species attached to Au adatoms, the most important being the RS-Au and RS-Au-RS complexes, whose surface movement allows to order the SAM structure and gives a reasonable explanation for the existance of vacancy islands. In fact, it is accepted that a certain amount of the gold atoms removed from the topmost layers forms gold-thiolate complexes that leave monoatomic vacancies yield to larger ones by Ostwald ripening.

Among the different adatom models, that proposed by Grönbeck et. al., which involves RS-Au-SR complexes in a cis configuration, is the most widely accepted (*(RS)₂Au model*). In the RS-Au-SR moieties, the central Au atom is linearly coordinated by surface-paralell bonds to the thiolates, bridging sulphurs to two Au atoms of the underlying surface on top sites. The formation of these complexes satisfactoraly explains the behavior of low-coverage striped phases of alkanethiolates on Au(111), and also the possibility to construct a full monolayer coverage with c (4 x 2) superstructure consisting only of trans- or cis-RS-Au-SR units without any disorder (Figure 10). At present is unclear how low-coverage striped phases evolve to intermediate coverage or full monolayers. It can be speculated that favoured cis-trans isomeration of RS-Au-SR complexes, their mobility, steric interactions and other S-Au complexes may play a role.

1.2.4.2. SAM surface structure and organization on Au(111)

Alkanethiols yield different long-range ordered structural phases and commensurated lattices on Au(111). In the general, there are three main unit

meshes of $(m \times \sqrt{3})$rect., $(\sqrt{3}\times\sqrt{3})$R30^o and $(2\sqrt{3} \times 3)$rect. The $(m \times \sqrt{3})$ rect. structures correspond to the so-called striped phases where molecules are lying-down on the surface (*m value represents the number of molecules per surface unit mesh*). At higher surface coverages of alkanethiolates on Au(111), the $(\sqrt{3}\times\sqrt{3})$R30^o and $(2\sqrt{3} \times 3)$rect. overlayers both correspond to standing-up phases. The basic structural motif and prototypical example of a full-coverage thiol monolayer on Au(111) is a $(\sqrt{3}\times\sqrt{3})$R30^o lattice, as expected by simple packing arguments based on the balance between the adlayer structure and lateral interactions. In this case, the tilt angle (α) of the hydrocarbon chains from the surface normal is around 30°, which is associated with a hexagonal packing with the nearest neighbour sulphur moieties on 3-fold hollow or bridge sites (*Standard structural* model) separated by 0.5 nm, and a thiolate surface coverage of θ_{RS}=0.33 (Figure 10).

Spectroscopic, diffraction, SPM and density functional theory (DFT) simulation techniques have unravelled an orthorhombic c(4 x 2) superlattice structure of the $(\sqrt{3}\times\sqrt{3})$R30^o adlayer. Such c(4 x 2) superstructure corresponds to a secondary ordering of the alkyl chains promoted by attractive lateral interactions (*~1 kcal/mol per methylene group in the chain*) which leads to the backbone rotation (β angle) about the long axis of the molecule (Figure 10) . The stability of thiolate SAMs is sensitive to the alkyl chain length, being the longer ones more robust in their applications (*e.g. thermal, chemical, etc.*) than shorter ones for reasons that are probably both thermodynamic and kinetic. In addition to methyl terminated SAMs, this

structure has been also observed by STM for ω-functionalized alkanethiols with other functional groups like –COOH, –OH or –NH$_2$.

Minimizing the intermolecular forces between alkanethiolates molecules implies the reorganization of the backbone hydrocarbon chains to adopt a quasi-crystalline structure with the alkyl chains in an all-trans configuration. The variation in the orientation of the organic molecules within the monolayers can be described by a simple single-chain model (figure 10b) consisting in two angles: (i) the tilt angle (α) of the alkanethiolate backbone respect to the surface normal, and (ii) the rotation angle (β) about the long axis of the alkyl chain.
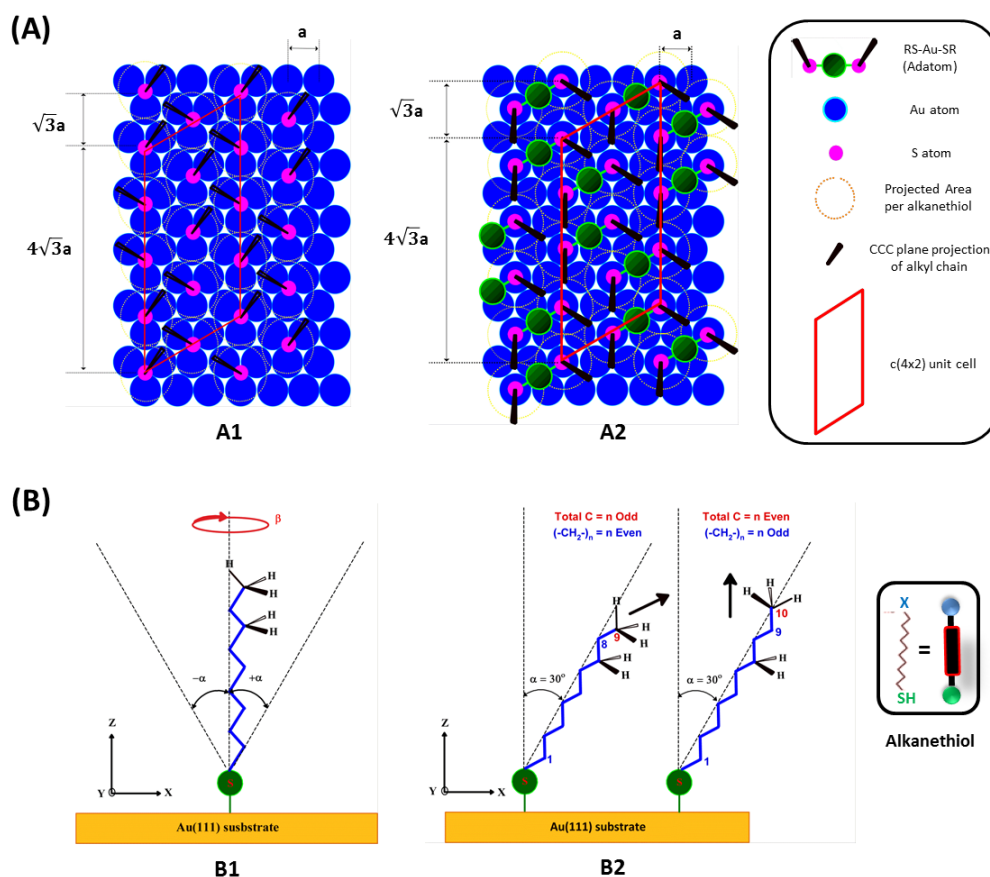
Figure 10. (a) Scheme showing alkanethiolates arrangement on the unreconstructed Au(111) lattice for a complete surface coverage: (a1) Standard structural model of a commensurate adlayer of adsorbed thiols in a $\left(\sqrt{3}\times\sqrt{3}\right)R30^{o}$ hexagonal structure where sulphur atoms are positioned in 3-fold hollow sites of Au(111) (a=2.88Å), and (a2) equivalent adatom $(RS)_2Au$ model. Note the alternating orientation of the alkane chains to define a c(4x2) superlattice structure by tilting in the direction of their next-nearest neighbours. (b) Representation of alkanethiolate adsorbed in an up-right configuration at the gold surface: (b1) including the angular degrees of freedom of the all-trans alkyl chain conformation, tilt (α) and twist (β) angles, and (b2) the schematic diagram of the orientation of the terminal group depending on the odd-even numbers of methylene groups in the alkyl chain.

For gold substrates, α and β values are close to 30° and 50°, respectively, while SAMs organized on silver and mercury exhibit lower cant angles of 10° and 0°, respectively, and β values near to 45°.[14] Other ordered phases have also been observed for longer alkyl chains, where intermediate α values of ~50° were found at intermediate coverages to those of lying-down and standing-up tilted SAM configurations. [83]

The value of α for 2D crystalline alkanethiolate SAMs on Au(111) is characteristic regardless of the number of carbons in the chain. This fact leads to a different surface projection of the terminal groups for SAMs depending on the odd and even numbers of methylene units in their backbones (Figure 10b), which correlates with the observed odd-even effects in wetting, tunnelling junctions, friction, field-effect transistors and molecular diodes related interfacial properties. [84-88] In general, such effect describes a zigzag oscillation in material structure and/or its physicochemical interfacial properties (*e.g. chemical reactivity, electronic, friction and electrochemical properties*). However, based on the structure of an ideal SAM, an odd-even effect in wetting or other interface-dependent properties should be expected for atomically flat gold surfaces with molecules in an all-trans extended conformation without gauche defects.[85, 86]

The wetting behaviour of SAMs with an odd number of $-CH_2-$ groups correlates systematically with surfaces of larger free energy (*i.e. lower wettability and higher contact angles*) than those with an even number of $-CH_2-$. All these aspects evidenced the different orientation of the $-CH_3$ end-group in $CH_3-(CH_2)_n-SH$ SAMs as demonstrated by vibrational spectroscopies, such as IR and high-resolution electron energy loss (HREELS) .[84, 89] For CH_3-

$(CH_2)_n$-SH SAMs with n = odd or even, the dipolar transition moment for the terminal $-CH_2-CH_3$ tends to be parallel or tilted to the surface normal, respectively (Figure 10b), largely enhancing or weakening alternatively the vibrational features of the symmetric ($\upsilon_s^{CH_3}$) or asymmetric ($\upsilon_{as}^{CH_3}$) stretching modes.

1.2.4.3. Defects in alkanethiolate SAMs

The control of the structural organization of the self-assembled monolayers is a key point to solve many technological issues. Despite the high degree of order that alkanethiolate SAMs can achieve there are different kinds of structural defects that might limit their applications. Numerous factors can cause defects in the monolayer structure (Figure 11). Among the extrinsic factors are found the cleanliness and preparation of the substrate, and purity of the thiol solution that can complicate kinetics of the formation and final structure of the SAM. On the other hand, intrinsic factors for some defects in SAMs are simply based on its dynamic nature involving complex phase behaviours.

The surface structure of substrates can directly determine structural defects in monolayers. All metal substrates, including the low-index surfaces have a large number of topographic irregularities such as misalignments, atomic steps, grain boundaries, faceting, twins, dislocations, etc. which directly impact the density of defects in SAMs as confirmed by STM. [82, 90, 91] One type of defect, which is typical of monolayers on gold, is the monoatomic vacancy islands. [16, 82, 92] These pit-like defect-structures are induced by the lifting of the reconstructed gold surface due to the adsorption of thiols, where

relaxation of the surface stress results in the formation of single atom vacancies that nucleate and grow into larger islands.
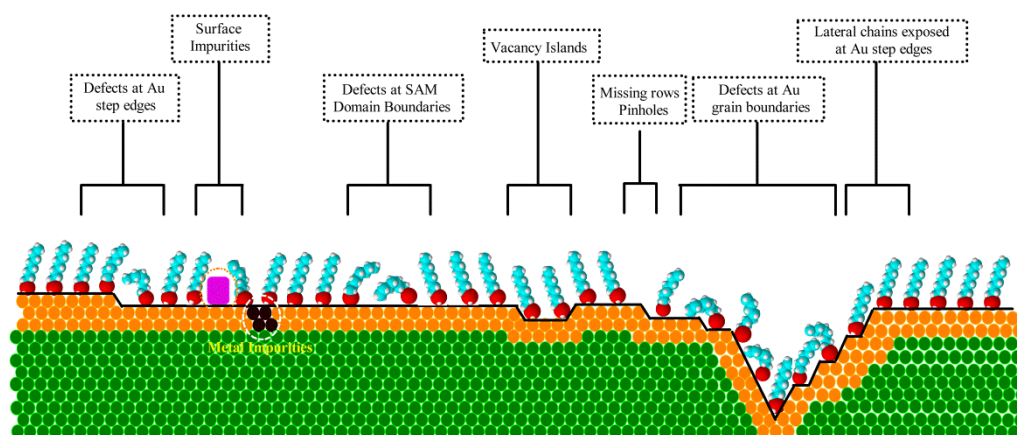
Figure 11. Diagram showing intrinsic and extrinsic defects in SAMs formed on flat and/or roughen surfaces.

The intrinsic defects are related to the dynamic nature of the SAM structure. Once the SAM is formed it may be kinetically stable in the absence of adsorbate flux, as the rate of desorption is not rigorously zero. Then it becomes thermodynamically unstable to resist the competitive exchange or displacement from the surface by other species. The chain dynamics of alkanethiolate SAMs are subject of a variety of energy barrier-driven gauche conformers and tilt-order complex phase transitions.[14, 16, 93-95] Therefore, molecular defects are present even in well-ordered crystalline alkanethiolate domains, such as missing molecules or pinholes and regions with some degree of molecular disorder (Figure 11). The rows of missing molecules, either in a straight or zig-zag configuration, are usually found for short alkanethiols with

smaller intermolecular interactions. Other type of defects is related to disordered liquid-like molecular domains coexisting crystalline ones, which either have different tilt angles or the hydrocarbon chains are not fully extended. Similar defective regions are found at step edges or domain boundaries or step edges, the latter due to a mistmach (or simply missing) of molecules between adjacent domains of different or same ordered lattices that coalesce at terraces.[16, 82, 92]

1.2.4.4. Electron transfer blocking properties of SAMs

Alkanethiols SAMs provide interfaces with well-defined thicknesses that can be varied by changing their chain length. Highly compact and sufficiently pinhole-free monolayers can effectively block the ionic permeation and electron transfer (ET) between electroactive redox species present in solution and the gold electrode, where the dominant ET mechanism is electron tunnelling through the film (Figure 12 - bottom).[96] In this long-range ET mechanism, the apparent heterogeneous rate constant (k_{ET}) of a redox reaction is strongly dependent on the thickness of the insulating layer, which is described by an exponential decay of k_{ET} with the barrier distance according to the following expression: [40, 96, 97]

$$k_{ET} = k_{ET}^0 \cdot e^{-\beta d} \qquad\qquad (2)$$

where k_{ET}^0 is the ET rate in absence of the insulating barrier, β is the structure-dependent attenuation factor or electron tunnelling constant, describing the decay of electronic coupling between the redox species and the electrode as

the distance separating them increases, and d is the thickness of the monolayer.

Electrochemical studies have allowed determining k_{ET} and putting forward the influence of SAM structure (*e.g. backbone and terminal groups*) on ET as demonstrated by cyclic voltammetry (CV) and electrochemical impedance spectroscopy (EIS) techniques.[96, 98-105] This has been carried out by quantitative analysis of either the CV faradic response by constructing Tafel plots (*log i vs overpotential*), or the impedance (Z) response, by obtaining the charge transfer resistance (R_{CT}) from fitting of the experimental Nyquist plots (*-Z_{imag} vs Z_{real}*) to an equivalent Randles circuit (Figure 12). When k_{ET} followed the relation in equation (2), the β values reported for alkanethiol SAMs on metallic surfaces are usually ranging from 0.8-1.2 $Å^{-1}$.[40, 97]

However, the presence of SAM defects or pinholes allows the electroactive species in solution penetrating into the layer to be either at a closer distance or even into contact with the surface electrode, respectively. Then, short-range ET pathways can compete with electron tunnelling, either by permeation and/or diffusion/mass transfer of the redox species through the monolayer defects to the electrode surface (Figure 12). [98, 99] Consequently, when the degree of structural integrity of the SAM decreases, k_{ET} strongly increases as monitored by CV [99, 101-105] and EIS [101, 102, 104, 105] measurements. The limiting case would be that where k_{ET} takes the value for a bare electrode. In certain cases, the degree of integrity of the structure can be calculated semi-quantitatively as a function of the fractional coverage of defects (1-θ) with theoretical relationships for partially blocked microelectrodes.[106]

52
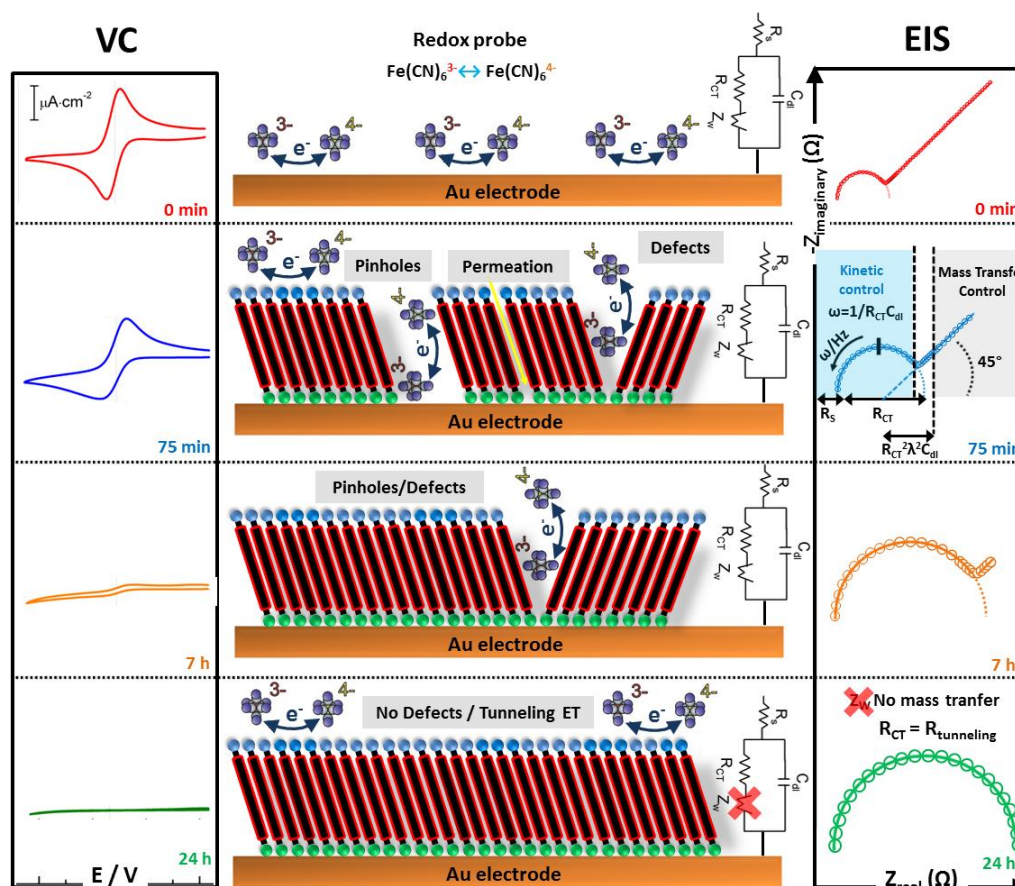
Figure 12. Schematic representation of electron transfer (ET) mechanisms for a redox probe on bare and SAM modified gold electrodes with a decreasingly number of defects (from top to bottom): (i) direct ET of the redox probe at the surface by a diffusion-controlled (mass transfer) process, (ii)-(iii) ET at SAM pinholes (surface), defects (surface vicinity) and by permeation, and (iv) ET by tunnelling mechanism at a defect-free SAM interface (on top of the layer at a defined distance from the surface). Alkanethiol SAMs acts as an ET barrier for diffusion-controlled redox reactions. From top to bottom, this is shown by further inhibition of the CVs faradic response (*Left side*) and the increasingly charge transfer resistance (R_{CT}) values determined by EIS (*Right side*. *Nyquist plots are described by a Randles equivalent circuit*) until reaction heterogeneous kinetics are controlled by electron tunnelling.

In such a case, the apparent k_{ET} at defective-SAMs can be expressed as:

$$k_{ET}^{app} = k_{ET}^{0} \cdot (1-\theta) \qquad\qquad (3)$$

where k_{ET}^{app} and k_{ET}^{0} are the ET heterogeneous rate constants in the presence and absence of the SAM, respectively. Therefore, the number, size and distribution of defects in SAMs can be determined by monitoring changes in the ET kinetics. [101, 102, 104, 105]

1.2.4.5. Electrochemical desorption of alkanethiolate SAMs on Au

Reductive desorption (RD) of alkanethiol SAMs occurs when a sufficiently negative potential is applied to the metallic substrate upon immersion in electrolyte aqueous or ethanolic solutions at a neutral or basic pH.[107] In this sense, conventional electrochemical techniques, such as CV and EIS, are employed to get insight into the SAM organization and packing by means of the study of its desorption process. Figure 13 shows a typical cyclic voltammogram profile for the reductive desorption of an alkanethiol SAM coated Au(111) electrode in 0.1 KOH.

A characteristic behaviour, before thiol adsorbates are electrochemically desorbed, is that alkanethiolate SAM coated electrodes drastically decrease the interfacial capacitance (*1-5 µF/cm²)* compared to the bare surface.[52, 66, 96, 98, 108, 109] This fact is manifested at the CV profiles by an important decrease of the capacitive current density in a wide range of potentials at the SAM's stability region (Figure 13). When the current remains almost constant in the double layer region independently of the potential, this is indicative of an ideal capacitance interfacial behaviour of the SAM (C_{dl}^{SAM}). Thus, C_{dl}^{SAM} values

of alkanethiols with different chain length can be determined from CV and EIS measurements, by assuming a simple capacitor model. [141, 212, 214,66] The validity of this model has been demonstrated by the linear relationship of $1/C_{dl}^{SAM}$ versus the number of methylene units (n) in different electrolyte solutions. [141, 212, 214]
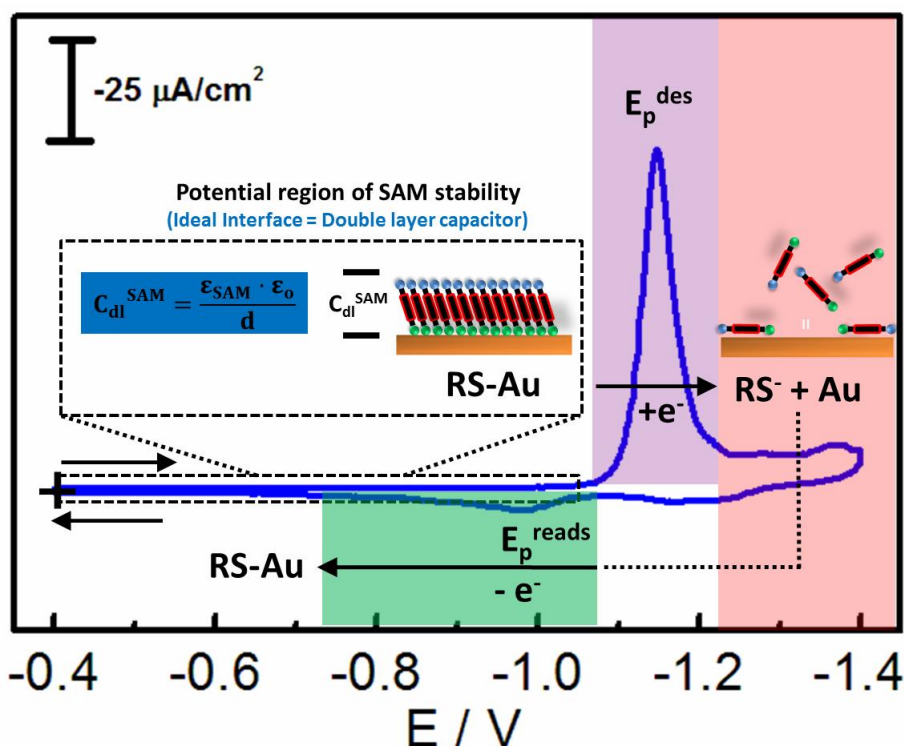
Figure 13. Representative cyclic voltammogram of the electrochemical reductive desorption and oxidative readsorption processes in 0.1M KOH solution of an alkanethiolate SAM coated Au(111) electrode. Scan rate (v) 0.1 V/s.

The SAM dielectric constant value, ε_m, calculated from the slope of the $1/C_{dl}^{SAM}$ vs n plots is around 2.6, which is in good agreement with the

expected value for a saturated hydrocarbon chain in an all trans configuration and α=30º. In some cases, the higher values found for ε_m are probably indicative of the presence of SAM defects and ionic permeation, which can be induced by the influence of the terminal groups in the SAM structure or by potential values approaching to those delimiting the SAM stability and desorption regions. [52, 108]

Once sufficiently negative potentials are applied to the alkanethiol SAM modified electrodes (X-$(CH_2)_n$-S-M), a one-electron faradic electrochemical half-reaction of desorption takes places on gold (M) in alkaline medium as follows: [52, 55, 107, 110-112]

$$X\text{-}(CH_2)_n\text{-}S\text{-}M + e^- \leftrightarrow M + X\text{-}(CH_2)_n\text{-}S^- \quad (4)$$
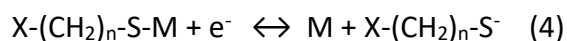
SAMs formed on Au(111) crystalline surfaces show usually the presence of a narrow desorption peak, E_p, (*sometimes appearing a second peak as a shoulder of the main one*) which corresponds to the reduction of the S-Au bond of the thiolates adsorbed (Figure 13). The reduction of the S-Au bond provokes that both, thiolates and bare metal electrode to become solvated, and that the thiolate diffuses away from the surface to solution.[113, 114] The RD process for alkanethiolates is suggested to proceed through the following steps: [114]

(I) - At the onset potential of the RD peak (E_p). A partial desorption occurs resulting in the formation of lying-down domains of molecules that coexist with aggregates of physisorbed molecules in a random configuration.

(II) – Shifting potential to the RD peak (E_p). The thiol desorption is accelerated while molecules remain close to the surface forming bigger aggregates (*bilayers to micelles*) in a random distribution.

(III) - At potential much more negative than E_p. Individual molecules and aggregates may diffuse away the surface.

The process is reversible and removing the applied negative potential can result in the readsorption of thiolates onto the surface. However, the reverse potential (*surface charge of the* metal) and the scan rate (*time* scale) of the CV experiment will determine the amount of surface material readsorbed. It is also worth mentioning that the higher interactions among alkyl chains (*longer alkanethiols*) are the higher order is maintained as a standing-up configuration in the molecules during the desorption-readsorption process. It is also accepted that the kinetics of the desorption process occurs first at defect sites and grain boundaries in the SAM and then, at apparently random distributed sites in SAM terraces where molecules are well-organized into crystalline phases. [115] Therefore, the electric-field induced rate of desorption seems to be the highest for molecules adsorbed at edges and defects.

E_p at which RD of alkanethiolates occurs depends on a number of factors, including chain length, degree of ordering and type of intermolecular interactions within the film (*e.g. hydrogen* bonding), even when a single crystalline surface is used as substrate. For example, increasing the chain length of n-alkanethiols in the SAMs formed results in a monotonically displacement of E_p to the negative direction of potential. This is in agreement with the energy stabilization due to additional -(CH$_2$)- intermolecular

interactions in the longer SAMs structures.[52, 111, 116] A similar behaviour is obtained for the evolution of E_p with the modification time, where longer times leads E_p to displace to negative values until a well-ordered and packed SAM structure is finally achieved.[55] Nevertheless, it is also necessary to consider the possible influence of the terminal groups of ω-substituted SAMs in the E_p values of the RD, as additional effects, such as the potential and pH-dependent ionization of the terminal groups, may be present.[117]

On the other hand, the desorption charge (Q_{des}) of the process, determined by the integrated area of the RD peak, does not appreciably change by increasing the alkanethiols chain length once the charging current due to non-faradic processes in the RD process are eliminated.[52, 110-112] Q_{des} values between 70-80 $\mu C/cm^2$ have been reported for alkanethiol SAMs on Au. This leads to alkanethiol surface coverages, Γ, considering a one-electron process, close to $7.5 \cdot 10^{-10}$ mol/cm^2 ($Q_{des}^c = n \cdot F \cdot \Gamma$), which is in nice agreement with a θ_{RS}=0.33, typical of $\left(\sqrt{3}x\sqrt{3}\right)$R30^o adlayer of thiolates with the alkyl chains in an all-trans up-right configuration. Finally, crystallinity of the substrate also plays a role in E_p values and the number of peaks obtained in the RD multiresponse obtained by CV,[33, 113, 118-121] which can help to selective replacement of adsorbates under potential control.[80]

1.3. The importance of electron transfer (ET) reactions and proteins

Since processes in life are highly non-equilibrium, constant energy input (energy flow) is required to maintain the structures and to support the functions.[122] The main metabolic and photosynthetic pathways for energy

transformation and dissipation are referred to redox and potential gradients, where redox potential (E^0) is a measure of the tendency of compounds to deliver electrons.[122-125] In this sense, proteins are basically essential for these purposes as they constitute the most versatile macromolecules in living systems and serve crucial functions in all biological processes. In fact, they can catalyse reactions, transport and store other molecules, provide mechanical support and immune protection, generate movement, transmit nerve impulses and control growth and differentiation.

Enzymes (*biological catalysts*) are probably the most important proteins as they are required to accelerate the chemical reactions necessary for organizing the random population of molecules into self-sustaining metabolic cycles in a highly specific way. The high specificity of enzymes is related to their structure and complementarity of interactions with other proteins or substrates that regulate the enzymatic activity. Their binding ability can be contributed to their tertiary structure that creates binding or active sites together with the chemical properties of the amino acids side chains constituting it. Therefore, proteins are also essential for cell signalling, molecular and electron transport pathways. A classic example is haemoglobin which binds O_2 and transports it from the lungs, through the blood to all the essential body organs and tissues.

Biological processes are essential for life, especially those catalysing redox reactions and shuttling electrons in a specific way.[122-125] In this sense, redox proteins, such as metalloproteins, play a crucial role either in electrocatalytic processes or as biochemical electron shuttles in enzymatic reactions.[126] In particular, long-range electron transfer (ET) reactions of redox

59

proteins occur at/or in heterogeneous membrane/solution interfaces, either by docking or specific recognition interactions. Therefore, important considerations arise:

(I)   - Protein mobility is restricted for integral proteins embedded in membranes or, for soluble ones, because of their specific binding either to surface or solvent-exposed parts of membrane-bound reaction partners.

(II)   – Dielectric constants may vary substantially along the ET pathways.

(III)   – Gradient concentrations of ions outside and inside of the membranes originate a potential drop and an inhomogeneous charge distribution within these organic thin layers and proteins which leads to high electrical fields.

However, the protein environment can adjust the redox potential (E^0) over a large range of values and its structure be altered to ensure rapid and efficient electron transfer (ET) from the redox center (heme or metal clusters) to distances located at several even to tens of nanometers.[127] Then, protein orientation and structural dynamics could be also necessary for shuttling electrons through efficient ET pathways. When the dynamics of charge transfer processes and protein structure are altered by local changes in chemical and potential gradients at protein-protein complexes and membrane-protein interfaces, this may also affect the ET processes and consequently, to the regulatory functions and reaction mechanisms involved. Addressing these questions is of fundamental interest to find relationships between function and structural properties of proteins under external stimuli at interfaces.

In this respect, this doctoral thesis aims to study electrochemical biointerfaces formed by hemeproteins adsorbed on biocompatible SAMs coated electrodes as a model system, where ET takes place across organic thin layers that mimic some basic features of membranes or protein domains.

1.4. References

1.   Whitesides, G. M.; Grzybowski, B., Self-Assembly at All Scales. *Science* **2002,** *295* (5564), 2418-2421.

2.   *Self-Assembly and Nanotechnology: A Force Balance Approach*. John Wiley & Sons: New Jersey, **2008**; p 344.

3.   *Fundamentals of Nanotechnology*. CRC Press, Taylor & Francis Group: Boca Raton, London, New York, **2009**.

4.   *Handbook of Nanoscience, Engineering and Technology*. Third ed.; CRC Press, Taylor & Francis Group: Boca Raton, London, New York, **2012**.

5.   Nano on Reflection. *Nat Nano* **2016,** *11* (10), 828-834.

6.   Gooding, J. J.; Ciampi, S., The Molecular Level Modification of Surfaces: from Self-Assembled Monolayers to Complex Molecular Assemblies. *Chem. Soc. Rev.* **2011,** *40* (5), 2704-2718.

7.   *Supramolecular Chemistry: From Molecules to Nanomaterials*. John Wiley & Sons, Inc.: **2012**; p 4014.

8.   Zhang, S. G., Fabrication of Novel Biomaterials through Molecular Self-Assembly. *Nature Biotechnol.* **2003,** *21* (10), 1171-1178.

9.   Sapsford, K. E.; Algar, W. R.; Berti, L.; Gemmill, K. B.; Casey, B. J.; Oh, E.; Stewart, M. H.; Medintz, I. L., Functionalizing Nanoparticles with Biological Molecules: Developing Chemistries that Facilitate Nanotechnology. *Chem. Rev.* **2013,** *113* (3), 1904-2074.

10.   Biju, V., Chemical Modifications and Bioconjugate Reactions of Nanomaterials for Sensing, Imaging, Drug Delivery and Therapy. *Chem. Soc. Rev.* **2014,** *43* (3), 744-764.

11.   Yang, H.; Yuan, B.; Zhang, X.; Scherman, O. A., Supramolecular Chemistry at Interfaces: Host-Guest Interactions for Fabricating Multifunctional Biointerfaces. *Acc. Chem. Res.* **2014,** *47* (7), 2106-2115.

12.   Mendes, P. M., Stimuli-Responsive Surfaces for Bio-Applications. *Chem. Soc. Rev.* **2008,** *37* (11), 2512-2529.

13.   Schreiber, F., Structure and Growth of Self-Assembling Monolayers. *Prog. Surf. Sci.* **2000,** *65* (5-8), 151-256.

14.   Love, J. C.; Estroff, L. A.; Kriebel, J. K.; Nuzzo, R. G.; Whitesides, G. M., Self-Assembled Monolayers of Thiolates on Metals as a Form of Nanotechnology. *Chem. Rev.* **2005,** *105* (4), 1103-1169.

15.   Kind, M.; Woell, C., Organic Surfaces Exposed by Self-Assembled Organothiol Monolayers: Preparation, Characterization, and Application. *Prog. Surf. Sci.* **2009,** *84* (7-8), 230-278.

16.   Vericat, C.; Vela, M. E.; Benitez, G.; Carro, P.; Salvarezza, R. C., Self-Assembled Monolayers of Thiols and Dithiols on Gold: New Challenges for a Well-Known System. *Chem. Soc. Rev.* **2010,** *39* (5), 1805-1834.

17.   Casalini, S.; Bortolotti, C. A.; Leonardi, F.; Biscarini, F., Self-Assembled Monolayers in Organic Electronics. *Chem. Soc. Rev.* **2017,** *46* (1), 40-71.

18.   Watson, S.; Nie, M.; Wang, L.; Stokes, K., Challenges and Developments of Self-Assembled Monolayers and Polymer Brushes As a Green Lubrication Solution for Tribological Applications. *Rsc Advances* **2015,** *5* (109), 89698-89730.

19.   Rampi, M. A.; Whitesides, G. M., A Versatile Experimental Approach for Understanding Electron Transport Through Organic Materials. *Chem. Phys.* **2002,** *281* (2-3), 373-391.

20.   Adams, D. M.; Brus, L.; Chidsey, C. E. D.; Creager, S.; Creutz, C.; Kagan, C. R.; Kamat, P. V.; Lieberman, M.; Lindsay, S.; Marcus, R. A.; Metzger, R. M.; Michel-Beyerle, M. E.; Miller, J. R.; Newton, M. D.; Rolison, D. R.; Sankey, O.; Schanze, K. S.;

Yardley, J.; Zhu, X., Charge Transfer on the Nanoscale: Current Status. *J. Phys. Chem. B* **2003,** *107* (28), 6668-6697.

21.   Waldeck, D. H.; Khoshtariya, D. E., Fundamental Studies of Long- And Short-Range Electron Exchange Mechanisms between Electrodes and Proteins. *Mod. Aspects Electrochem.* **2011,** *52* (Applications of Electrochemistry and Nanotechnology in Biology and Medicine I), 105-238.

22.   Eckermann, A. L.; Feld, D. J.; Shaw, J. A.; Meade, T. J., Electrochemistry of Redox-Active Self-Assembled Monolayers. *Coord. Chem. Rev.* **2010,** *254* (15-16), 1769-1802.

23.   Chechik, V.; Crooks, R. M.; Stirling, C. J. M., Reactions and Reactivity in Self-Assembled Monolayers. *Adv. Mater.* **2000,** *12* (16), 1161-1171.

24.   Prime, K. L.; Whitesides, G. M., Self-Assembled Organic Monolayers: Model Systems for Studying Adsorption of Proteins at Surfaces. *Science* **1991,** *252* (5009), 1164.

25.   Vaisocherova, H.; Brynda, E.; Homola, J., Functionalizable Low-Fouling Coatings for Label-Free Biosensing in Complex Biological Media: Advances and Applications. *Anal. Bioanal. Chem.* **2015,** *407* (14), 3927-3953.

26.   Jonkheijm, P.; Weinrich, D.; Schroeder, H.; Niemeyer, C. M.; Waldmann, H., Chemical Strategies for Generating Protein Biochips. *Angew. Chem., Int. Ed.* **2008,** *47* (50), 9618-9647.

27.   Arya, S. K.; Solanki, P. R.; Datta, M.; Malhotra, B. D., Recent Advances in Self-Assembled Monolayers Based Biomolecular Electronic Devices. *Biosens. Bioelectron.* **2009,** *24* (9), 2810-2817.

28.   Nuzzo, R. G.; Allara, D. L., Adsorption of Bifunctional Organic Disulfides on Gold Surfaces. *J. Am. Chem. Soc.* **1983,** *105* (13), 4481-4483.

29.   Dubois, L. H.; Nuzzo, R. G., Synthesis, Structure, and Properties of Model Organic Surfaces. *Annu. Rev. Phys. Chem* **1992,** *43* (1), 437-463.

30.   Ulman, A., Formation and Structure of Self-Assembled Monolayers. *Chem. Rev. (Washington, D. C.)* **1996,** *96* (4), 1533-1554.

31.   Tour, J. M.; Jones, L.; Pearson, D. L.; Lamba, J. J. S.; Burgin, T. P.; Whitesides, G. M.; Allara, D. L.; Parikh, A. N.; Atre, S., Self-Assembled Monolayers and Multilayers of Conjugated Thiols, alpha, omega-Dithiols, and Thioacetyl-Containing Adsorbates. Understanding Attachments between Potential Molecular Wires and Gold Surfaces. *J. Am. Chem. Soc.* **1995,** *117* (37), 9529-9534.

32.   Harder, P.; Grunze, M.; Dahint, R.; Whitesides, G. M.; Laibinis, P. E., Molecular Conformation in Oligo(Ethylene Glycol)-Terminated Self-Assembled Monolayers on Gold and Silver Surfaces Determines their Ability to Resist Protein Adsorption. *J. Phys. Chem. B* **1998,** *102* (2), 426-436.

33.   Madueno, R.; Sevilla, J. M.; Pineda, T.; Roman, A. J.; Blazquez, M., A Voltammetric Study of 6-Mercaptopurine Monolayers on Polycrystalline Gold Electrodes. *J. Electroanal. Chem.* **2001,** *506* (2), 92-98.

34.   Laibinis, P. E.; Whitesides, G. M.; Allara, D. L.; Tao, Y. T.; Parikh, A. N.; Nuzzo, R. G., Comparison of the Structures and Wetting Properties of Self-Assembled Monolayers of n-Alkanethiols on the Coinage Metal Surfaces, Copper, Silver, and Gold. *J. Am. Chem. Soc.* **1991,** *113* (19), 7152-67.

35.   Love, J. C.; Wolfe, D. B.; Haasch, R.; Chabinyc, M. L.; Paul, K. E.; Whitesides, G. M.; Nuzzo, R. G., Formation and Structure of Self-Assembled Monolayers of Alkanethiolates on Palladium. *J. Am. Chem. Soc.* **2003,** *125* (9), 2597-2609.

36.   Petrovykh, D. Y.; Kimura-Suda, H.; Opdahl, A.; Richter, L. J.; Tarlov, M. J.; Whitman, L. J., Alkanethiols on Platinum: Multicomponent Self-Assembled Monolayers. *Langmuir* **2006,** *22* (6), 2578-2587.

37.   Sevilla, J. M.; Pineda, T.; Madueno, R.; Roman, A. J.; Blazquez, M., Characterization of 6-Mercaptopurine Monolayers On Hg Surfaces. *J. Electroanal. Chem.* **1998,** *442* (1-2), 107-112.

38.   Brust, M.; Walker, M.; Bethell, D.; Schiffrin, D. J.; Whyman, R., Synthesis of Thiol-Derivatized Gold Nanoparticles in a 2-Phase Liquid-Liquid System. *J. Chem. Soc., Chem. Commun.* **1994,** (7), 801-802.

39.   Decreau, R. A.; Collman, J. P.; Hosseini, A., Electrochemical Applications. How Click Chemistry Brought Biomimetic Models to the Next Level: Electrocatalysis under Controlled Rate of Electron Transfer. *Chem. Soc. Rev.* **2010,** *39* (4), 1291-1301.

40.   Holmlin, R. E.; Haag, R.; Chabinyc, M. L.; Ismagilov, R. F.; Cohen, A. E.; Terfort, A.; Rampi, M. A.; Whitesides, G. M., Electron Transport through Thin Organic Films in Metal-Insulator-Metal Junctions Based on Self-Assembled Monolayers. *J. Am. Chem. Soc.* **2001,** *123* (21), 5075-5085.

41.   Xie, Z.; Baldea, I.; Smith, C. E.; Wu, Y.; Frisbie, C. D., Experimental and Theoretical Analysis of Nanotransport in Oligophenylene Dithiol Junctions as a Function of Molecular Length and Contact Work Function. *ACS Nano* **2015,** *9* (8), 8022-8036.

42.   Majumdar, S.; Malen, J. A.; McGaughey, A. J. H., Cooperative Molecular Behavior Enhances the Thermal Conductance of Binary Self-Assembled Monolayer Junctions. *Nano Lett.* **2017,** *17* (1), 220-227.

43.   Saha, K.; Agasti, S. S.; Kim, C.; Li, X.; Rotello, V. M., Gold Nanoparticles in Chemical and Biological Sensing. *Chem. Rev.* **2012,** *112* (5), 2739-2779.
44.   Dreaden, E. C.; Alkilany, A. M.; Huang, X.; Murphy, C. J.; El-Sayed, M. A., The Golden Age: Gold Nanoparticles for Biomedicine. *Chem. Soc. Rev.* **2012,** *41* (7), 2740-2779.

45.   Clavilier, J.; Faure, R.; Guinet, G.; Durand, R., Preparation of Mono-Crystalline Pt Microelectrodes and Electrochemical Study of the Plane Surfaces Cut in the Direction of the (111) and (110) Planes. *J. Electroanal. Chem.* **1980,** *107* (1), 205-209.

46.   Bain, C. D.; Troughton, E. B.; Tao, Y. T.; Evall, J.; Whitesides, G. M.; Nuzzo, R. G., Formation of Monolayer Films by the Spontaneous Assembly of Organic Thiols from Solution onto Gold. *J. Am. Chem. Soc.* **1989,** *111* (1), 321-335.

47.   Poirier, G. E.; Pylant, E. D., The Self-Assembly Mechanism of Alkanethiols on Au(111). *Science* **1996,** *272* (5265), 1145-1148.

48.   Yamada, R.; Sakai, H.; Uosaki, K., Solvent Effect on the Structure of the Self-Assembled Monolayer of Alkanethiol. *Chem. Lett.* **1999,** (7), 667-668.

49.   Sur, U. K.; Lakshminarayanan, V., A Study of the Hydrophobic Properties of Alkanethiol Self-Assembled Monolayers Prepared in Different Solvents. *J. Electroanal. Chem.* **2004,** *565* (2), 343-350.

50.   Dannenberger, O.; Buck, M.; Grunze, M., Self-assembly of n-alkanethiols: A kinetic study by second harmonic generation. *J. Phys. Chem. B* **1999,** *103* (12), 2202-2213.

51.   Bain, C. D.; Whitesides, G. M., Modeling Organic Surfaces with Self-Assembled Monolayers. *Angew. Chem.* **1989,** *101* (4), 522-8.

52.   Widrig, C. A.; Chung, C.; Porter, M. D., The Electrochemical Desorption of n-alkanethiol Monolayers from Polycrystalline Gold and Silver Electrodes. *J. Electroanal. Chem.* **1991,** *310* (1-2), 335-59.

53.   Weisshaar, D. E.; Lamp, B. D.; Porter, M. D., Thermodynamically Controlled Electrochemical Formation of Thiolate Monolayers at Gold: Characterization and Comparison to Self-Assembled Analogs. *J. Am. Chem. Soc.* **1992,** *114* (14), 5860-5862.

54.   Ma, F. Y.; Lennox, R. B., Potential-Assisted Deposition of Alkanethiols on Au: Controlled Preparation of Single- and Mixed-Component SAMs. *Langmuir* **2000,** *16* (15), 6188-6190.

55.   Sumi, T.; Uosaki, K., Electrochemical Oxidative Formation and Reductive Desorption of a Self-Assembled Monolayer of Decanethiol on a Au(111) Surface in KOH Ethanol Solution. *J. Phys. Chem. B* **2004,** *108* (20), 6422-6428.

56.   Li, Z.; Niu, T.; Zhang, Z.; Bi, S., Potential Control Characteristics of Short-Chain Thiols of Thioctic Acid and Mercaptohexanol Self-Assembled on Gold. *Electrochim. Acta* **2010,** *55* (22), 6907-6916.

57.   Haag, A.-L.; Toader, V.; Lennox, R. B.; Grutter, P., Selective in Situ Potential-Assisted SAM Formation on Multi Electrode Arrays. *Nanotechnology* **2016,** *27* (45), 455501.

58.   Gonzalez-Granados, Z.; Sanchez-Obrero, G.; Madueno, R.; Sevilla, J. M.; Blazquez, M.; Pineda, T., Formation of Mixed Mono layers from 11-Mercaptoundecanoic Acid and Octanethiol on Au(111) Single Crystal Electrode under Electrochemical Control. *J. Phys. Chem. C* **2013,** *117* (46), 24307-24316.

59.   Garcia-Raya, D.; Madueno, R.; Blazquez, M.; Pineda, T., Formation of 1,8-Octanedithiol Mono- and Bilayers under Electrochemical Control. *J. Phys. Chem. C* **2010,** *114* (8), 3568-3574.

60.   Liu, J.; Kaifer, A. E., Preparation of Self-Assembled Monolayer from Micellar Solutions. *Isr. J. Chem.* **1997,** *37* (2-3), 235-239.

61.   Yan, D.; Saunders, J. A.; Jennings, G. K., Enhanced Chain Densities of n-Alkanethiolate Self-Assembled Monolayers on Gold from Aqueous Micellar Solutions. *Langmuir* **2000,** *16* (20), 7562-7565.

62.   Yan, D.; Saunders, J. A.; Jennings, G. K., Kinetics of Formation for n-Alkanethiolate Self-Assembled Monolayers onto Gold in Aqueous Micellar Solutions of C12E6 and C12E7. *Langmuir* **2002,** *18* (26), 10202-10212.

63.   Yan, D.; Jordan, J. L.; Burapatana, V.; Jennings, G. K., Formation of n-Alkanethiolate Self-Assembled Monolayers onto Gold in Aqueous Micellar Solutions of n-Alkyltrimethylammonium Bromides. *Langmuir* **2003,** *19* (8), 3357-3364.

64.   Yan, D.; Saunders, J. A.; Jennings, G. K., Formation and Stability of Hexadecanethiolate SAMs Prepared in Aqueous Micellar Solutions of C12E6. *Langmuir* **2003,** *19* (22), 9290-9296.

65.   Ganesh, V.; Lakshminarayanan, V., Self-Assembled Monolayers of Alkanethiols on Gold Prepared in a Hexagonal Lyotropic Liquid Crystalline Phase of Triton X-100/Water System. *Langmuir* **2006,** *22* (4), 1561-1570.

66.   García Raya, D.; Madueno, R.; Blazquez, M.; Pineda, T., Formation of a 1,8-Octanedithiol Self-Assembled Monolayer on Au(111) Prepared in a Lyotropic Liquid-Crystalline Medium. *Langmuir* **2010,** *26* (14), 11790-11796.

67.   Pace, G.; Petitjean, A.; Lalloz-Vogel, M.-N.; Harrowfield, J.; Lehn, J.-M.; Samori, P., Subnanometer-Resolved Patterning of Bicomponent Self-Assembled Monolayers on Au(111). *Angew. Chem., Int. Ed.* **2008,** *47* (13), 2484-2488.

68.   Liedberg, B.; Tengvall, P., Molecular Gradients of ω-Substituted Alkanethiols on Gold: Preparation and Characterization. *Langmuir* **1995,** *11* (10), 3821-7.
69.   Ghanghoria, R.; Kesharwani, P.; Tekade, R. K.; Jain, N. K., Targeting Luteinizing Hormone-Releasing Hormone: A Potential Therapeutics to Treat Gynecological and Other Cancers. *Journal of Controlled Release*.

70.   Gooding, J. J.; Darwish, N., The Rise of Self-Assembled Monolayers for Fabricating Electrochemical Biosensors-An Interfacial Perspective. *Chem. Record* **2012,** *12* (1), 92-105.

71. Bain, C. D.; Whitesides, G. M., Formation of 2-Component Surfaces by the Spontaneous Assembly of Monolayers on Gold from Solutions Containing Mixtures of Organic Thiols. *J. Am. Chem. Soc.* **1988,** *110* (19), 6560-6561.

72. Laibinis, P. E.; Fox, M. A.; Folkers, J. P.; Whitesides, G. M., Comparisons of Self-Assembled Monolayers on Silver and Gold: Mixed Monolayers Derived from $HS(CH_2)_{21}X$ and $HS(CH_2)_{10}Y$ (X, Y = CH_3, CH_2OH) Have Similar Properties. *Langmuir* **1991,** *7* (12), 3167-73.

73. Folkers, J. P.; Laibinis, P. E.; Whitesides, G. M., Self-Assembled Monolayers of Alkanethiols on Gold - Comparisons of Monolayers Containing Mixtures of Short-Chain and Long-Chain Constituents with CH_3 and CH_2OH Terminal Groups. *Langmuir* **1992,** *8* (5), 1330-1341.

74. Laibinis, P. E.; Nuzzo, R. G.; Whitesides, G. M., Structure of Monolayers Formed by Coadsorption of 2-N-Alkanethiols of Different Chain Lengths on Gold and its Relation to Wetting. *J. Phys. Chem.* **1992,** *96* (12), 5097-5105.
75. Kakiuchi, T.; Iida, M.; Gon, N.; Hobara, D.; Imabayashi, S.; Niki, K., Miscibility of Adsorbed 1-Undecanethiol and 11-Mercaptoundecanoic Acid Species in Binary Self-Assembled Monolayers on Au(111). *Langmuir* **2001,** *17* (5), 1599-1603.

76. Stranick, S. J.; Parikh, A. N.; Tao, Y. T.; Allara, D. L.; Weiss, P. S., Phase Separation of Mixed-Composition Self-Assembled Monolayers into Nanometer Scale Molecular Domains. *J. Phys. Chem.* **1994,** *98* (31), 7636-46.

77. Besharat, Z.; Wakeham, D.; Johnson, C. M.; Odnevall, W. I.; Luengo, G. S.; Greaves, A.; Gothelid, M.; Rutland, M. W., Mixed Monolayers of Alkane Thiols with Polar Terminal Group on Gold: Investigation of Structure Dependent Surface Properties. *J Colloid Interface Sci* **2016,** *484*, 279-290.

78. Laibinis, P. E.; Nuzzo, R. G.; Whitesides, G. M., Structure of Monolayers Formed by Coadsorption of Two N-Alkanethiols of Different Chain Lengths on Gold and its Relation to Wetting. *J. Phys. Chem.* **1992,** *96* (12), 5097-105.

79. Meunier-Prest, R.; Legay, G.; Raveau, S.; Chiffot, N.; Finot, E., Potential-Assisted Deposition of Mixed Alkanethiol Self-Assembled Monolayers. *Electrochim. Acta* **2010,** *55* (8), 2712-2720.

80.   Imabayashi, S.; Hobara, D.; Kakiuchi, T.; Knoll, W., Selective Replacement of Adsorbed Alkanethiols in Phase-Separated Binary Self-Assembled Monolayers by Electrochemical Partial Desorption. *Langmuir* **1997,** *13* (17), 4502-4504.

81.   Hobara, D.; Ota, M.; Imabayashi, S.; Niki, K.; Kakiuchi, T., Phase Separation of Binary Self-Assembled Thiol Monolayers Composed of 1-Hexadecanethiol and 3-Mercaptopropionic Acid on Au(111) Studied by Scanning Tunneling Microscopy and Cyclic Voltammetry. *J. Electroanal. Chem.* **1998,** *444* (1), 113-119.

82.   Poirier, G. E., Characterization of Organosulfur Molecular Monolayers on Au(111) using Scanning Tunneling Microscopy. *Chem. Rev. (Washington, D. C.)* **1997,** *97* (4), 1117-1127.

83.   Barrena, E.; Palacios-Lidon, E.; Munuera, C.; Torrelles, X.; Ferrer, S.; Jonas, U.; Salmeron, M.; Ocal, C., The Role of Intermolecular and Molecule-Substrate Interactions in the Stability of Alkanethiol Nonsaturated Phases on Au(111). *J. Am. Chem. Soc.* **2004,** *126* (1), 385-395.

84.   Tao, F.; Bernasek, S. L., Understanding Odd-Even Effects in Organic Self-Assembled Monolayers. *Chem. Rev.* **2007,** *107* (5), 1408-1453.
85.   Newcomb, L. B.; Tevis, I. D.; Atkinson, M. B. J.; Gathiaka, S. M.; Luna, R. E.; Thuo, M., Odd-Even Effect in the Hydrophobicity of n-Alkanethiolate Self-Assembled Monolayers Depends upon the Roughness of the Substrate and the Orientation of the Terminal Moiety. *Langmuir* **2014,** *30* (40), 11985-11992.

86.   Wang, Z.; Chen, J.; Gathiaka, S. M.; Oyola-Reynoso, S.; Thuo, M., Effect of Substrate Morphology on the Odd-Even Effect in Hydrophobicity of Self-Assembled Monolayers. *Langmuir* **2016,** *32* (40), 10358-10367.

87.   Jiang, L.; Sangeeth, C. S. S.; Nijhuis, C. A., The Origin of the Odd-Even Effect in the Tunneling Rates across EGaIn Junctions with Self-Assembled Monolayers (SAMs) of n-Alkanethiolates. *J. Am. Chem. Soc.* **2015,** *137* (33), 10659-10667.
88.   Yuan, L.; Thompson, D.; Cao, L.; Nerngchangnong, N.; Nijhuis, C. A., One Carbon Matters: The Origin and Reversal of Odd-Even Effects in Molecular Diodes with Self-Assembled Monolayers of Ferrocenyl-Alkanethiolates. *J. Phys. Chem. C* **2015,** *119* (31), 17910-17919.

89.   Chang, S.-C.; Chao, I.; Tao, Y.-T., Structure of Self-Assembled Monolayers of Aromatic-Derivatized Thiols on Evaporated Gold and Silver Surfaces: Implication on Packing Mechanism. *J. Am. Chem. Soc.* **1994,** *116* (15), 6792-805.

90.   O'Dwyer, C.; Gay, G.; de Lesegno, B. V.; Weiner, J., The Nature of Alkanethiol Self-Assembled Monolayer Adsorption on Sputtered Gold Substrates. *Langmuir* **2004,** *20* (19), 8172-8182.

91.   Silien, C.; Buck, M., On the Role of Extrinsic and Intrinsic Defects in the Underpotential Deposition of Cu on Thiol-Modified Au(111) Electrodes. *J. Phys. Chem. C* **2008,** *112* (10), 3881-3890.

92.   Yang, G.; Liu, G.-Y., New Insights for Self-Assembled Monolayers of Organothiols on Au(111) Revealed by Scanning Tunneling Microscopy. *J. Phys. Chem. B* **2003,** *107* (34), 8746-8759.

93.   Guo, Q.; Li, F., Self-Assembled Alkanethiol Monolayers on Gold Surfaces: Resolving the Complex Structure at the Interface by STM. *Phys. Chem. Chem. Phys.* **2014,** *16* (36), 19074-19090.

94.   Touzov, I.; Gorman, C. B., Tip-Induced Structural Rearrangements of Alkanethiolate Self-Assembled Monolayers on Gold. *J. Phys. Chem. B* **1997,** *101* (27), 5263-5276.

95.   Gannon, G.; Greer, J. C.; Larsson, J. A.; Thompson, D., Molecular Dynamics Study of Naturally Occurring Defects in Self-Assembled Monolayer Formation. *ACS Nano* **2010,** *4* (2), 921-932.

96.   Miller, C.; Cuendet, P.; Gratzel, M., Adsorbed Omega-Hydroxy Thiol Monolayers on Gold Electrodes - Evidence for Electron-Tunneling to Redox Species in Solution. *J. Phys. Chem.* **1991,** *95* (2), 877-886.

97.   Holmlin, R. E.; Ismagilov, R. F.; Haag, R.; Mujica, V.; Ratner, M. A.; Rampi, M. A.; Whitesides, G. M., Correlating Electron Transport and Molecular Structure in Organic Thin Films. *Angew. Chem., Int. Ed.* **2001,** *40* (12), 2316-2320.

98.   Porter, M. D.; Bright, T. B.; Allara, D. L.; Chidsey, C. E. D., Spontaneously Organized Molecular Assemblies. 4. Structural Characterization of Normal-Alkyl Thiol Monolayers on Gold by Optical Ellipsometry, Infrared-Spectroscopy, and Electrochemistry. *J. Am. Chem. Soc.* **1987,** *109* (12), 3559-3568.

99.   Cannes, C.; Kanoufi, F.; Bard, A. J., Cyclic Voltammetry and Scanning Electrochemical Microscopy of Ferrocenemethanol at Monolayer and Bilayer-Modified Gold Electrodes. *J. Electroanal. Chem.* **2003,** *547* (1), 83-91.

100.   Molinero, V.; Calvo, E. J., Electrostatic Interactions at Self Assembled Molecular Films of Charged Thiols on Gold. *J. Electroanal. Chem.* **1998,** *445* (1-2), 17-25.

101.   Finklea, H. O.; Snider, D. A.; Fedyk, J.; Sabatani, E.; Gafni, Y.; Rubinstein, I., Characterization of Octadecanethiol-Coated Gold Electrodes as Microarray Electrodes by Cyclic Voltammetry and Ac-Impedance Spectroscopy. *Langmuir* **1993,** *9* (12), 3660-3667.

102.   Janek, R. P.; Fawcett, W. R.; Ulman, A., Impedance Spectroscopy of Self-Assembled Monolayers on Au(111): Sodium Ferrocyanide Charge Transfer at Modified Electrodes. *Langmuir* **1998,** *14* (11), 3011-3018.

103.   Che, G. L.; Li, Z. L.; Zhang, H. Q.; Cabrera, C. R., Voltammetry of Defect Sites at a Self-Assembled Monolayer on a Gold Surface. *J. Electroanal. Chem.* **1998,** *453* (1-2), 9-17.

104.   Brito, R.; Tremont, R.; Cabrera, C. R., Electron Transfer Kinetics Across Derivatized Self-Assembled Monolayers on Platinum: A Cyclic Voltammetry and Electrochemical Impedance Spectroscopy Study. *J. Electroanal. Chem.* **2004,** *574* (1), 15-22.

105.   Garcia-Raya, D.; Madueno, R.; Manuel Sevilla, J.; Blazquez, M.; Pineda, T., Electrochemical Characterization of A 1,8-Octanedithiol Self-Assembled Monolayer (ODT-SAM) on a Au(111) Single Crystal Electrode. *Electrochim. Acta* **2008,** *53* (27), 8026-8033.

106.   Amatore, C.; Saveant, J. M.; Tessier, D., Charge-Transfer at Partially Blocked Surfaces - A Model for the Case of Microscopic Active and Inactive Sites. *J. Electroanal. Chem.* **1983,** *147* (1-2), 39-51.

107.   Finklea, H. O., Electrochemistry of Organized Monolayers of Thiols and Related Molecules on Electrodes. *Electroanal. Chem.* **1996,** *19*, 109-335.

108.   Boubour, E.; Lennox, R. B., Stability of ω-Functionalized Self-Assembled Monolayers as a Function of Applied Potential. *Langmuir* **2000,** *16* (19), 7464-7470.

109.   Agonafer, D. D.; Chainani, E.; Oruc, M. E.; Lee, K. S.; Shannon, M. A., Study of Insulating Properties of Alkanethiol Self-Assembled Monolayers Formed under

Prolonged Incubation Using Electrochemical Impedance Spectroscopy. *J. Nanotechnol. Eng. Med.* **2012,** *3* (3), 031006/1-031006/8.

110.   Schneider, T. W.; Buttry, D. A., Electrochemical Quartz Crystal Microbalance Studies of Adsorption and Desorption of Self-Assembled Monolayers of Alkyl Thiols on Gold. *J. Am. Chem. Soc.* **1993,** *115* (26), 12391-7.

111.   Kakiuchi, T.; Usui, H.; Hobara, D.; Yamamoto, M., Voltammetric Properties of the Reductive Desorption of Alkanethiol Self-Assembled Monolayers from a Metal Surface. *Langmuir* **2002,** *18* (13), 5231-5238.

112.   Kawaguchi, T.; Yasuda, H.; Shimazu, K.; Porter, M. D., Electrochemical Quartz Crystal Microbalance Investigation of the Reductive Desorption of Self-Assembled Monolayers of Alkanethiols and Mercaptoalkanoic Acids on Au. *Langmuir* **2000,** *16* (25), 9830-9840.

113.   Shepherd, J. L.; Kell, A.; Chung, E.; Sinclar, C. W.; Workentin, M. S.; Bizzotto, D., Selective Reductive Desorption of a SAM-Coated Gold Electrode Revealed Using Fluorescence Microscopy. *J. Am. Chem. Soc.* **2004,** *126* (26), 8329-8335.

114.   Pensa, E.; Vericat, C.; Grumelli, D.; Salvarezza, R. C.; Park, S. H.; Longo, G. S.; Szleifer, I.; Mendez De Leo, L. P., New Insight into the Electrochemical Desorption of Alkanethiol SAMs on Gold. *Phys. Chem. Chem. Phys.* **2012,** *14* (35), 12355-12367.

115.   Mulder, W. H.; Calvente, J. J.; Andreu, R., A Kinetic Model for the Reductive Desorption of Self-Assembled Thiol Monolayers. *Langmuir* **2001,** *17* (11), 3273-3280.

116.   Cometto, F. P.; Calderon, C. A.; Berdakin, M.; Paredes-Olivera, P.; Macagno, V. A.; Patrito, E. M., Electrochemical Detection of the Thermal Stability of N-Alkanethiolate Monolayers on Au(1 1 1). *Electrochim. Acta* **2012,** *61*, 132-139.

117.   Munakata, H.; Oyamatsu, D.; Kuwabata, S., Effects of ω-Functional Groups on pH-Dependent Reductive Desorption of Alkanethiol Self-Assembled Monolayers. *Langmuir* **2004,** *20* (23), 10123-10128.

118.   Yu, Z. L.; Casanova-Moreno, J.; Guryanov, I.; Maran, F.; Bizzotto, D., Influence of Surface Structure on Single or Mixed Component Self-Assembled Monolayers via in Situ Spectroelectrochemical Fluorescence Imaging of the Complete Stereographic Triangle on a Single Crystal Au Bead Electrode. *J. Am. Chem. Soc.* **2015,** *137* (1), 276-288.

119.	Arihara, K.; Ariga, T.; Takashima, N.; Okajima, T.; Kitamura, F.; Tokuda, K.; Ohsaka, T., Multiple Voltammetric Waves for Reductive Desorption of Cysteine and 4-Mercaptobenzoic Acid Monolayers Self-Assembled on Gold Substrates. *Phys. Chem. Chem. Phys.* **2003,** *5* (17), 3758-3761.

120.	Strutwolf, J.; O'Sullivan, C. K., Microstructures by Selective Desorption of Self-Assembled Monolayer from Polycrystalline Gold Electrodes. *Electroanalysis* **2007,** *19* (14), 1467-1475.

121.	Doneux, T.; Steichen, M.; De Rache, A.; Buess-Herman, C., Influence of the Crystallographic Orientation on the Reductive Desorption of Self-Assembled Monolayers on Gold Electrodes. *J. Electroanal. Chem.* **2010,** *649* (1-2), 164-170.

122.	Falkowski, P. G.; Fenchel, T.; Delong, E. F., The Microbial Engines That Drive Earth's Biogeochemical Cycles. *Science (Washington, DC, U. S.)* **2008,** *320* (5879), 1034-1039.

123.	Lill, R., Function and Biogenesis of Iron-Sulfur Proteins. *Nature (London, U. K.)* **2009,** *460* (7257), 831-838.

124.	Rutherford, A. W.; Osyczka, A.; Rappaport, F., Back-Reactions, Short-Circuits, Leaks and other Energy Wasteful Reactions in Biological Electron Transfer: Redox Tuning to Survive Life in O_2. *FEBS Letters* **2012,** *586* (5), 603-616.

125.	Harel, A.; Bromberg, Y.; Falkowski, P. G.; Bhattacharya, D., Evolutionary History of Redox Metal-Binding Domains Across the Tree of Life. *Proc. Natl. Acad. Sci. U. S. A.* **2014,** *111* (19), 7042-7047.

126.	Williams, R. J. P.; Begley, T. P., Metallo-Enzymes and Metallo-Proteins, Chemistry of. In *Wiley Encyclopedia of Chemical Biology*, John Wiley & Sons, Inc.: **2007**.

127.	Skourtis, S. S., Review Probing Protein Electron Transfer Mechanisms from the Molecular to the Cellular Length Scales. *Biopolymers* **2013,** *100* (1), 82-92.

CHAPTER 2

Experimental and Methods

2. Experimental and methods

2.1. Chemical reagents

11-mercaptoundecanoic acid (COOH-$(CH_2)_{10}$-SH, MUA), 1-decanethiol (CH_3-$(CH_2)_9$-SH, DT), Triton X-100, potassium ferrocyanide ($Fe(CN)_6^{4-}$) , potassium ferricyanide ($Fe(CN)_6^{3-}$), myoglobin from horse heart (Mb), 3-dimethylamino propylamine (DMAPA), N-(3-dymethylaminopropyl)-N-ethylcarbodiimide hydrochloride (EDC) and semiconductor grade purity potassium hydroxide (KOH) were purchased from Aldrich-Sigma (purity ≥ 99%). The rest of the reagents, ethanol (CH_3CH_2OH), phosphoric acid (H_3PO_4), hydrochloric acid (HCl), perchloric acid ($HClO_4$), hydrogen peroxide (H_2O_2), potassium chloride (KCl) and potassium nitrate (KNO_3) were from Merck analytical grade. Aqueous solutions were prepared with deionized ultrapure water produced by a Millipore system (18.2 MΩ with an organic content < 4 ppb).

2.2. Substrates/Electrodes

Electrochemical experiments were carried out with a conventional three electrodes cell comprising a platinum wire as the counter electrode, a calomel electrode with 50 mM of KCl as the reference electrode (E = +0.353 V vs E^o_{NHE}), unless otherwise stated, and gold as working electrode (Figure 1).

Figure 1. Conventional electrochemical cell of three electrodes.

The spectroscopic and electrochemical experiments were carried out using different kinds of gold substrates:

(I) <u>Polyfaceted Au bead</u>. This substrate is prepared by the flame-annealing method developed by Clavilier et. al..[1] A gold wire of 0.5 mm diameter (Goodfellow, 99.998 %) was melted into approximately 2.5 mm diameter sphere and after slowly cooling; it was quickly immersed in deoxygenated

ultrapure water. After this treatment, several facets were visible on the bead surface indicating its monocrystalline structure.

Figure 2. Flame annealing procedure of a polyfaceted gold bead.

(II) Au (111) single crystal. This was an approximately 3 mm in diameter and 2 mm thick cylinder with a flat polished side oriented in the (111) low-index crystallographic direction (Metal Crystals and Oxides Ltd. - Cambridge, England). A gold wire is mounted at its far tip which allows easier handling of the crystal for the electrochemical experiments (Figure 3a).

(III) Au (111) textured flat surface. This surface consisted on a 250 nm thick Au layer adhered to a 2.5 nm thin chromium layer deposited on a Borosilicate glass 11x11 mm flat surface were used as Au(111) coated substrates (Gold Arrandee^{TM}) for the Infrared Reflection-Absorption Spectroscopy (IRRAS) and electrochemical measurements. Similar substrates were employed for Quartz Crystal Microbalance (QCM) experiments, where gold was deposited on an AT quartz crystal.
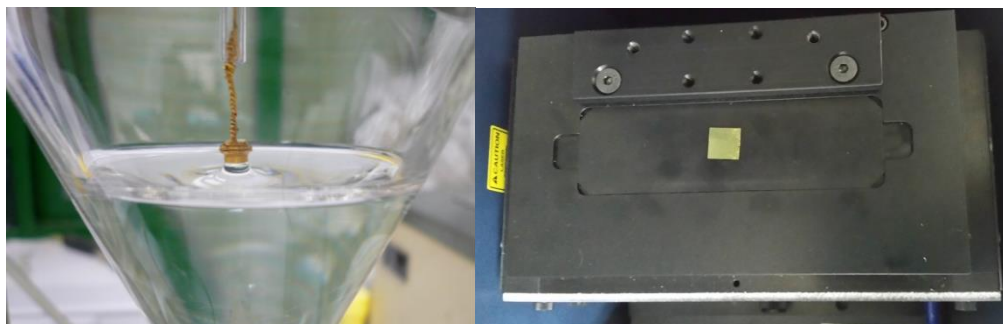
Figure 3. (a) Au(111) single crystal transferred into the electrochemical cell in contact with a solution by the meniscus method and (b) Au(111) textured substrate placed on the mask platform of IRRAS equipment.

2.3. Methodologies

2.3.1. Substrates cleaning. Determination of the real surface area.

Before each electrochemical measurement, the gold substrates (Section 2.2) were annealed in a natural gas flame to light red melt for about 20 s and, after a short period of cooling in air, the electrode was then transferred into the electrochemical cell. The surface condition was then checked by recording a cyclic voltammogram in 0.01 M HClO$_4$ that showed the well-known characteristic profile for an Au(111) single crystal or poliorientated gold faces (Figure 4).[2] This surface treatment protocol was the most appropriate to produce a surface that was clean, ordered and highly reproducible (Figure 4). The substrates electrochemically cleaned and transformed in their respective unreconstructed surface states (e.g. Au(111)-(22x $\sqrt{3}$ → Au(111)-(1x1)) were used for further experiments (Introduction -Section 1.2.5.1). The real surface area was determined from the integrated area of the reduction peak of

oxygen adsorption on the Au electrode ($AuO + 2H^+ + 2e^- \leftrightarrow Au + H_2O$), assuming in the case of Au(111) and polyfaceted surfaces that the gold atomic density was $1.35 \cdot 10^{15}$ (432 µC/cm^2) and $1.2 \cdot 10^{15}$ atoms/cm^2 (390 µC/cm^2), respectively.[3] The areas determined for the gold bead electrodes ranged from 0.175 to 0.238 cm^2, meanwhile, the Au(111) single crystal and textured surface areas were 0.099 and 1.4 cm^2, respectively.

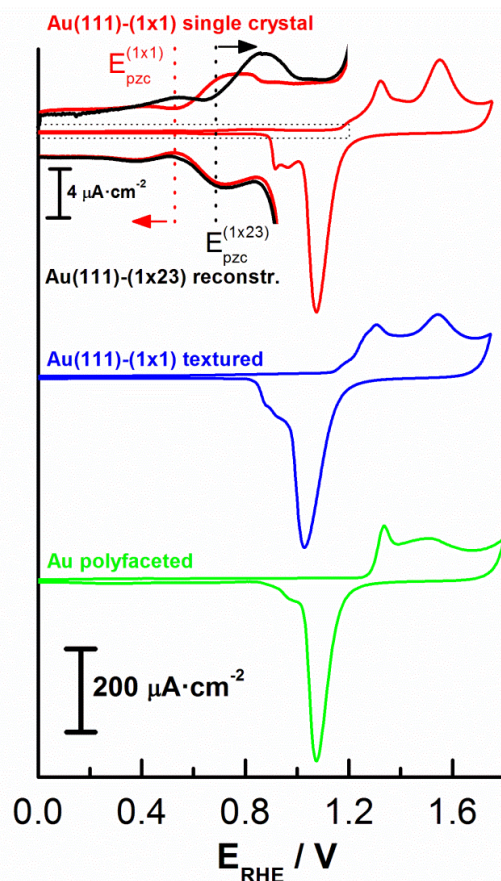**Figure 4.** Cyclic voltammograms of electrochemically clean gold substrates obtained in HClO$_4$ 0.01 M . Scan rate, v = 100 mV/s. Au(111)-(1x1) surface is obtained by lifting of the Au(111)-(22x $\sqrt{3}$) surface reconstruction one upon applying sufficiently anodic potentials, which is reflected by a change of approximately +0.09 V in the potential of zero charge (E$_{pzc}$) of the unreconstructed surface.[4]

## 2.3.2. Substrates modification. Formation of SAMs.

The SAMs were formed spontaneously or under potential control by contacting the electrochemically clean unreconstructed gold substrates with solutions containing the thiols, either by the hanging meniscus method or direct immersion (Section 2.2). Pure SAMs were prepared by using 1 mM solutions of 1-decanethiol (CH_3-$(CH_2)_9$-SH (DT) or 11-mercaptoundecanoic acid ($COOH$-$(CH_2)_{10}$-SH, MUA). Mixed SAMs were obtained from solutions containing both MUA and DT at different concentration ratios and a final concentration of 1mM. Ethanolic and micellar solutions were used to prepare SAMs spontaneously adsorbed on the substrates under open circuit potential (OCP) conditions. In this particular case, the adsorption times assayed were from 15 min to 24 hours at a controlled temperature ranging from 25 to 35 °C. Meanwhile, SAMs were prepared under potential control by substrate immersion in 0.1 M KOH solutions of the thiols at -0.4 V during 15 minutes.

The micellar medium was composed by a mixture of Triton X-100 (42 wt %) and water (58 wt %) to which MUA and/or DT were added. After heating to 40-45 °C under stirring, an isotropic phase containing a hexagonal phase was obtained upon cooling as already described in literature.[5, 6]

Once the SAMs were formed, if necessary, before their characterization by electrochemical (e.g. CV and EIS) and/or spectroscopic (FT-IRRAS) techniques, they were thoroughly rinsed with solvent and dried with nitrogen gas. In the case of pH titration experiments, the samples were previously stabilized in aqueous solutions at the corresponding pH during 20 minutes and then, if necessary, dried with nitrogen for further characterization.

2.2.3. Chemical modification of myoglobin. Protein cationization

Native myoglobin (n-Mb) was cationized by carbodiimide-activated coupling (EDC) reaction of the surface-accessible glutamic and aspartic acid residues to covalently attach DMAPA molecules (Scheme 1) as similar procedures elsewhere described.[7, 8]
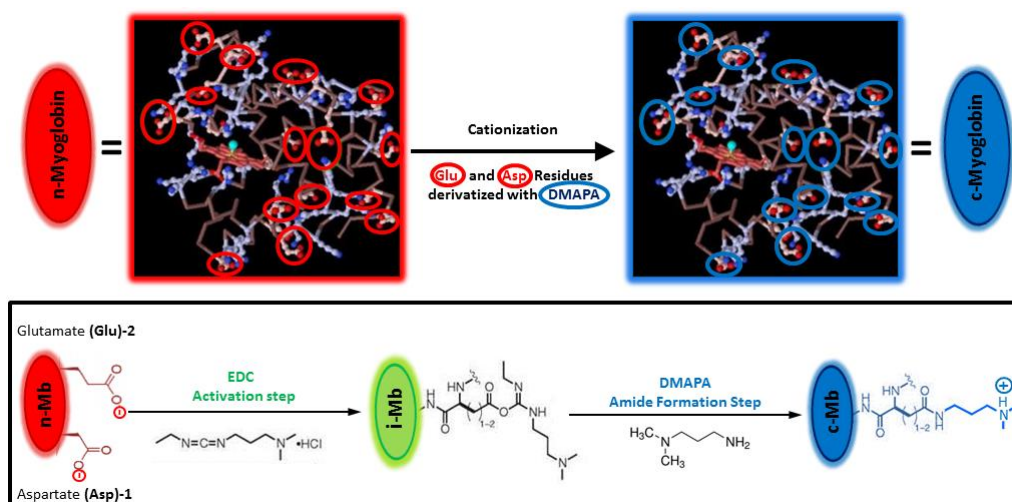
Scheme 1. Graphic shows the chemical derivatization of surface-exposed glutamate and aspartate side-chain residues at the native myoglobin (n-Mb) structure by the insertion of 3-dimethylamino propylamine (DMAPA) molecules via amide bond formation. Negatively charged patches of n-Mb are transformed into positively charged ones to yield cationized Mb (c-Mb), as indicated by the reaction steps.

Typically, 5 ml of an aqueous solution of Mb (5 mg/mL, pH 6.5) was purified by centrifugation and extensive dialysis (Visking tubing, 7 kDa MWCO). Subsequently, a 0.65 M DMAPA solution adjusted to pH 6.5 was added drop wise to the native met-Mb purified solution (5 mg/ml) with continuous stirring until a 50:1 excess of DMAPA per acidic residue was

achieved. The coupling reaction was initiated by the addition of solid N-(3-dimethylaminopropyl)-N'-ethylcarbodiimide hydrochloride (EDC) to the solution in an excess of 20:1 per acidic residue. The reaction mixture was kept stirring at pH 6.5 with controlled additions of HCl, while another batch of solid EDC was added after 1 h. The resultant solution was left to stir for 24 h and then, centrifuged, filtered (Millex Millipore 0.22 micron), and dialyzed (7 kDa MWCO) against ultrapure water for 48 h (with water changes every 12 h) to obtain a stable solution of DMAPA-cationized Mb (c-Mb).

2.3.4. Characterization of cationized myoglobin (c-Mb)

The cationization efficiencies were evaluated by using matrix-assisted laser desorption ionization time-of-flight mass spectrometry (MALDI-TOF MS) and UV-visible spectroscopy of both native (n-Mb) and cationized myoglobin (c-Mb) samples. The sample preparation was the following:

- MALDI-TOF MS samples were obtained by combining a 3:1 (v/v) solution of 20 mg/ml 2,5-dihydroxy acetophenone: 18 mg/ml ammonium citrate dibasic with an equal volume of 2% trifluoroacetic acid, then adding an equal volume of sample approximately 1 mg/ml in 0.02 M phosphate buffer, before spotting onto the MS plate and drying at 40 ºC.

- UV-visible samples were 3 mg/ml in 0.01 M phosphate buffer at pH 7.

Typical MALDI-TOF spectra corresponding to n-Mb and c-Mb are shown in the Figure 5a.

(A) MALDI-TOF MS

(B) UV-Visible Spectroscopy
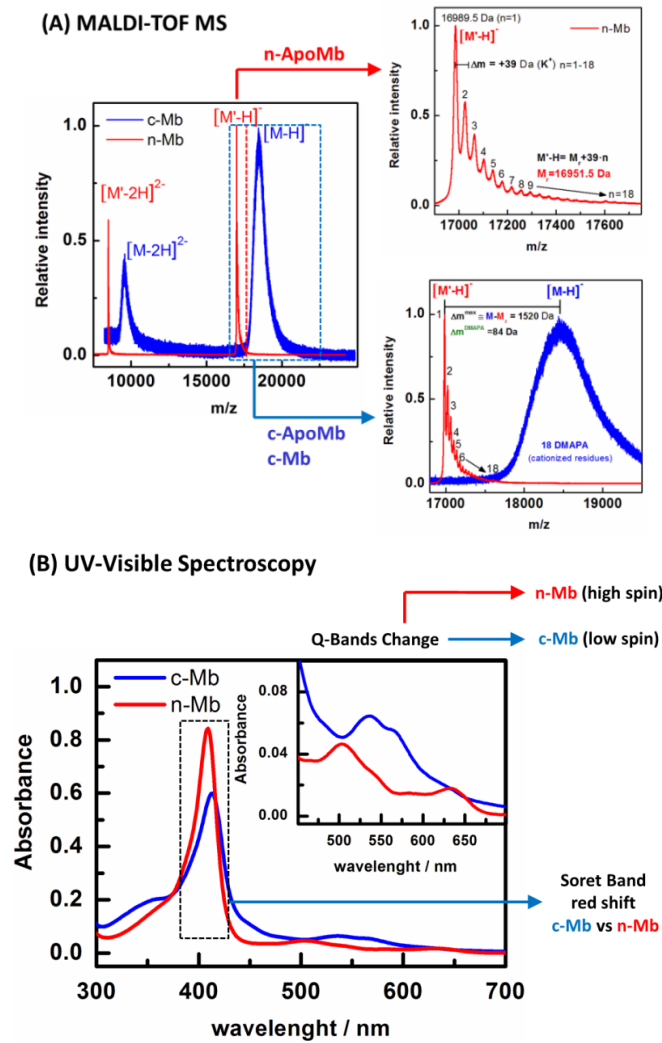
Figure 5. (a) MALDI-TOF MS of equine n-Mb and c-Mb show both single (z=1) and double charged (z=2) protein peak adducts. **(zoomed area-top)** The MS of the n-Mb gives a multiple peaks adducts response (discernible until n=18) associated with an incremental mass of K^+ to the average molecular weight of n-Mb, which is determined to be 16951.5 Da. **(zoomed area-bottom)** MS of c-Mb gives a broader distribution of cationized products with the highest abundance centred at approximately 18470 Da confirming the covalent conjugation of ca. 18 DMAPA molecules to all the accessible surface-exposed residues of n-Mb. **(b)** UV-visible spectra of n-Mb and c-Mb in aqueous solution are shown highlighting the differences.

85

An average molecular weight (MW) of 16951 Da is determined for n-Mb corresponding to the apomyoglobin form, as expected for the denatured state of heart and muscle equine myoglobins.[9] Thus, sample preparation conditions induced n-Mb to unfold while the labile heme (type b, MW= 616 Da) separates from the whole protein structure (MW=17.567 Da), which is only preserved when dissolved in an aqueous buffered solution (5–10 mM NH_4CH_3COO).[10] Then, buried amino acids become available and, at a sufficiently low pH, the histidine residues, acting as binding sites to heme moiety, become fully protonated. As a consequence, the heme-myoglobin interaction is disrupted and the heme group separates from the globin. The absence of the heme-myoglobin complex is characterized by a relatively higher charge state distribution.

The c-Mb sample shows a broader mass distribution of cationized products with the highest abundance at approximately 18470 Da and, a mass increase respect to n-Mb equivalent to the binding of 18 DMAPA molecules (Figure 5a). This would be indicative of a complete cationization of the exposed residues of n-Mb by the carbodiimide condensation reaction. Cationization has an important effect on the secondary structure of n-Mb due to changes in its electrostatic stabilization and the disruption of internal salt bridges.[8, 11] This fact strongly affects the heme environment, which is manifested by a red shift in the Soret band and changes in the Q-bands of the UV-visible absorption spectra of c-Mb compared to n-Mb (Figure 5b). Such spectral changes, together with the remarkable similarity of the absorption spectra of c-Mb with those reported for Mb-mutants with proximal and distal histidine-coordinated heme moieties, are consistent with a shift from high to

low spin-state of the iron in the heme.[8, 12] In conclusion, the results obtained are in good agreement with those previously reported for c-Mb. [7, 8]

2.3.5. Inmobilization of c-Mb onto SAMs.

Pure and mixed SAMs prepared on Au(111) substrates according to the procedures described in the section 2.3.2, unless otherwise stated, were used to immobilize c-Mb by electrostatic and/or hydrophobic interactions. Different immersion times for the SAM modified surfaces were tested in aqueous solutions of c-Mb or n-Mb (0.5 mg/ml). Finally, a time of immersion of 1 hour was chosen as the optimum to achieve the maximum protein surface coverage. Subsequently, the samples were thoroughly rinsed with water and dry with nitrogen prior to their characterization by electrochemical (e.g. CV) and spectroscopic (e.g. IRRAS and Resonance Raman-SERRS) techniques.

2.4. Instrumentation

2.4.1. Electrochemical Techniques

2.4.1.1. General Concepts

Cyclic voltammetry (CV) is an important and widely used technique in many areas of electrochemistry, such as the study of redox processes and understanding of reaction intermediates and products.[13] It is based on varying the applied potential (E) at a working electrode (WE) in both forward and reverse directions while monitoring the current (i) at a scan rate (v). Depending on the analysis, one full cycle, a partial cycle, or a series of cycles

can be performed to obtain i-E voltammetric profiles of the electrochemical processes occurring at the WE interface.

Electrochemical Impedance Spectroscopy (EIS) is a powerful technique that provides a perturbative characterization of the dynamics of an electrochemical process. It is exploits the Faraday´s and Ohm´s law (R=E/I) to characterize a chemical process in terms of electrical measurements. Like resistance (R), impedance (Z) is a measure of the ability of a circuit to resist the flow of electrical current. The fundamental approach of ESI methods is to measure impedance (Z) by applying an AC potential (*i.e.* small amplitude sinusoidal potential excitation signal of ∼ 5-10 mV) ripple on top a fixed DC potential to an electrochemical cell while a linear or pseudo-linear AC current response is monitored phase-shifted. The associated AC current signal can be analysed as a sum of sinusoidal functions (Fourier series).
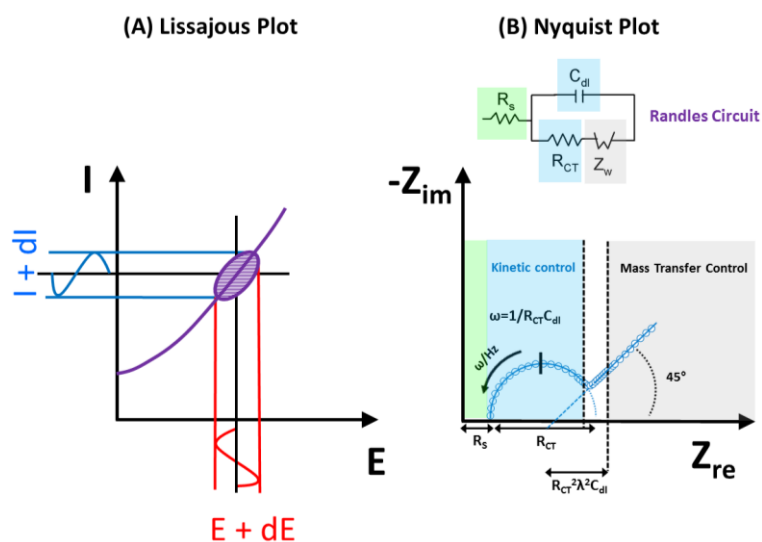

Figure 6. Lissajous and Nyquist plots representation.

Then, an expression analogous to the Ohm´s law can be obtained for Z:

$$Z(\omega) = \frac{E_t}{I_t} = \frac{E_0 \cdot \sin(\omega t)}{I_0 \cdot \sin(\omega t + \emptyset)} = Z_0 \cdot \frac{\sin(\omega t)}{\sin(\omega t + \emptyset)} \qquad (1)$$

where ϕ is the phase shift. By representing I_t vs E_t is obtained an oval in the classical Lissajous plot (Figure 6a). If the AC potential applied is a complex function (Euler relationship: $E_t = E_0 \cdot e^{j\omega t}$), impedance is represented as a complex number similarly to expression 1 ($Z(\omega) = Z_0 \cdot e^{j\omega\emptyset}$).

Therefore, $Z(\omega)$ is composed of a real and an imaginary part. When, the imaginary part ($-Z_{im}$) is plotted versus the real part (Z_{re}) is obtained a point in the Nyquist plot for a particular frequency (ω). However, $Z(\omega)$ is usually a complex quantity with a magnitude and a phase shift which depends on the frequency of the signal ($Z(\omega) = |Z(\omega)| \cdot e^{\omega\emptyset}$). Therefore, a wide range of frequencies (ω) can be selected for the applied AC potential perturbation in order to obtain an impedance-frequency spectrum (Nyquist plot $-Z_{im}$ vs Z_{re} for different ω) that can interrogate the electrochemical response of a system for extremely different time scales (Figure 6b).[13] Typically in electrochemistry, a frequency range of 100 kHz – 0.1 Hz is used.

By analysing the dependence of $Z(\omega)$ with ω for an applied potential is possible to isolate and distinguish the influence of different governing physical (e.g. capacitive, mass transfer or diffusion processes) and chemical (e.g. electron transfer or ionic charge transfer processes) phenomena in the electrochemical interface (*See Chapter 1 – Section 1.2.9 and Figure 12*).[13] The interpretation can be carried out by fitting EIS data to an equivalent circuit model, whose elements represent a physical basis of the processes modelled in the electrochemical interface. The Randles circuit is the most common and

simple model to represent a diffusion-controlled ET electrochemical reaction on a bare electrode (Figure 6b). In some cases, simplified Randles circuits can be used when ET or charge transfer reactions are blocked or inhibited by modified surfaces with SAMs (*Chapter 1-Section 1.2.9*).

2.4.1.2. Specifications and working conditions

CV and EIS measurements were recorded on Autolab (EcoChemie models Pgstat20 and Pgstat30) instruments attached to a PC with proper software for total control of the experiments and data acquisition (Figure 7).

The system is able to measure impedances from 1 mΩ up to 100 GΩ and capacitances from 0.1 pF up to 5000 F, which can be used in corrosion, bio-electrochemistry, battery, and supercapacitor research areas, among others. The following modules were also available for expanded capabilities (Figure 7):

- *BOOSTER*. BSTR10A allows for experiments at higher currents up to 10A.

- *ECD*. It provides two additional lowest current ranges of 1 nA and 100 pA, giving a minimum current resolution of 0.3 fA, as compared to the standard lowest current range of 10 nA with a current resolution of 30 fA.

-*SCAN-GEN/ADC 750*. This analog sweep generator combined with a fast sampling ADC module allows getting data points every 1.5 µs and increasing CV scan rates up to 10000 V/s.

-*FI20*. This filter (Sallen-Key type) and integrator module gives the possibility to measure charge in CV and potential step experiments, together with selectable RC times up to 500 ms to filter out noise.
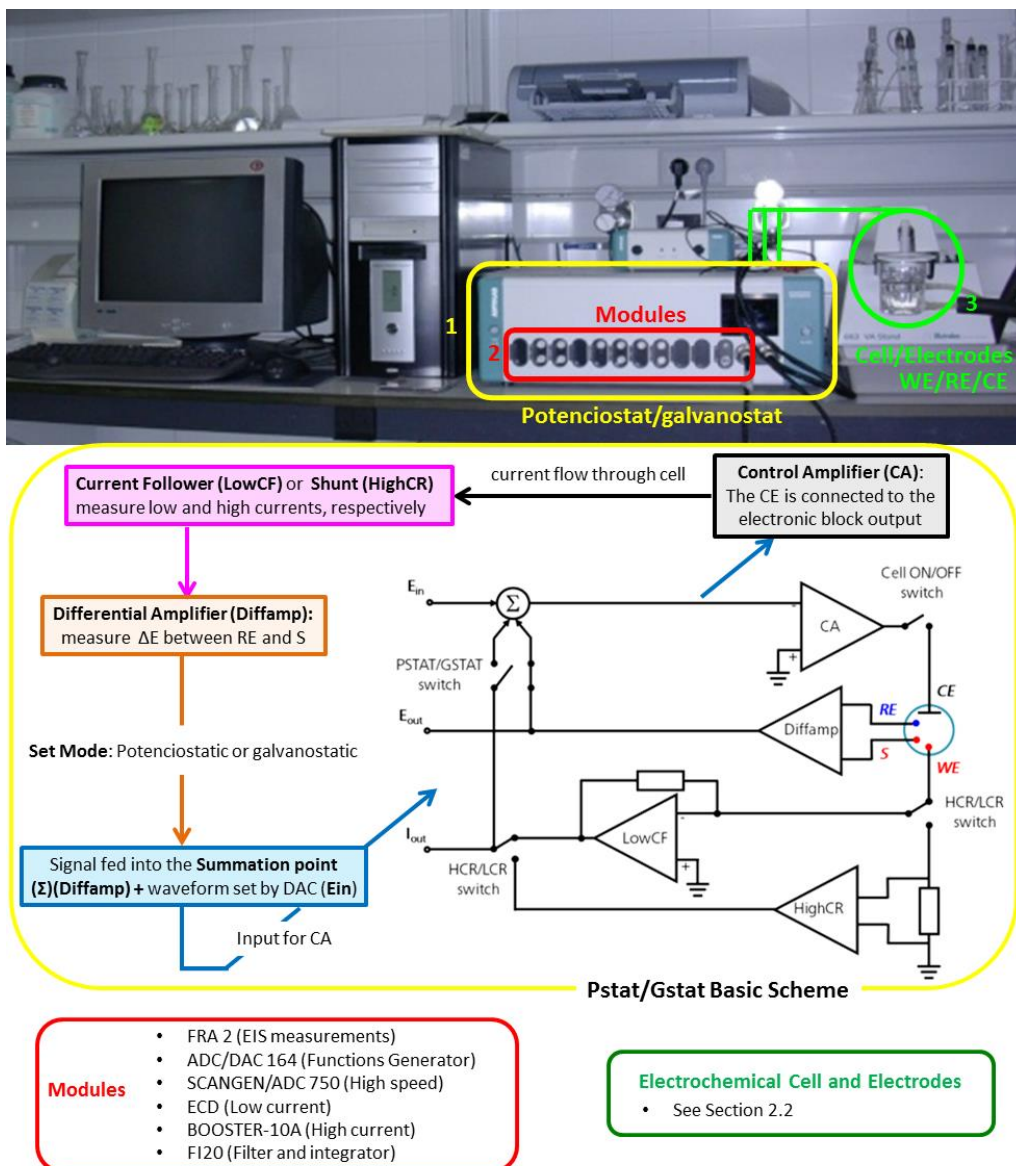
Figure 7. Instrument configuration of PGSTAT 20 and 30 models with additional modules. A basic scheme of a potenciostat/galvanostat is included.[13]

Before the electrochemical measurements, electrolyte solutions were purged with nitrogen gas (99.999 %) at least during 20-30 minutes to displace

dissolved oxygen. The solution contained in the electrochemical cell was kept under nitrogen atmosphere during the CV and EIS experiments. CV (i-E) profiles were recorded using scan rates ranging from 0.01 to 50 V/s. EIS spectra (Niquist Plots) were obtained in the potentiostatic mode by applying an AC sinusoidal potential excitation signal of 5 mV to a fixed DC potential in a frequency range (ω) from 100 kHz to 0.1 Hz.

CV and EIS data were further analyzed by using the supported software package (GPES 4.9, FRA and NOVA). Different parameters of the CV electrochemical profiles could be determined, such as peak potential (E_p), charge (Q), current (I_p), half-width (FWHM), etc. Similarly, EIS data were fitted to different equivalent circuits (*e.g. Randles circuit or simplified ones*) allowing to determine their constituent elements values (R_s, R_{CT}, C_{dl}, etc.) and their related physical and chemical parameters of the systems studied (e.g. heterogeneous electron transfer rate constants, double layer capacitance, etc.).[13]

2.4.2. Spectroscopic Techniques

2.4.2.1. Infrared reflection-absorption spectroscopy (IRRAS)

<u>General Concepts</u>

The reflection process at a surface can be analysed as the behaviour of s- and p- polarized components, whose electrical fields are parallel to the surface and perpendicular to the direction of propagation, for the s-component, and perpendicular to both the s component and the direction of propagation, for the p- component (Figure 8a). A molecule in the vicinity of the surface will experiment a combination (*i.e. the vector sum*) of the fields

due to the incident and reflected beams. In metals with high reflectivity in the IR region, the direction of the s component is almost exactly reversed on reflection and its magnitude is hardly changed. Therefore, electric vector E_S and E'_S nearly cancel. [14]

On the other hand, the behaviour of the p component depends somewhat on the incidence angle, θ, and when approaches to 90°, the fields combine to give a large component perpendicular to the surface ($E_\perp$) and a much smaller parallel to it ($E_{||}$) (Figure 8b). As the absorption intensity is proportional to the square the amplitude of the electric field vector, at $\theta = 0°$ there will be a significant field $E_{||}$, but an enhanced maximum field perpendicular, $E_\perp$, to the surface will arise from the p component at angles close to grazing (75-80°). This fact has two important consequences: (i) the sensitivity is maximized at high θ and, in this regard, field enhancement is also increased by a geometric factor due to that larger areas are covered by the beam and hence more molecules and, (ii) metal surface selection rules (MSSR) states that only those vibrational modes that have a component of their dipole change perpendicular to the metal surface will have measurable intensities and be detected.[14]

(A) Reflection process

(B) Electric fields vs incidence angle θ

θ ~ 75-80° (Grazing angle)
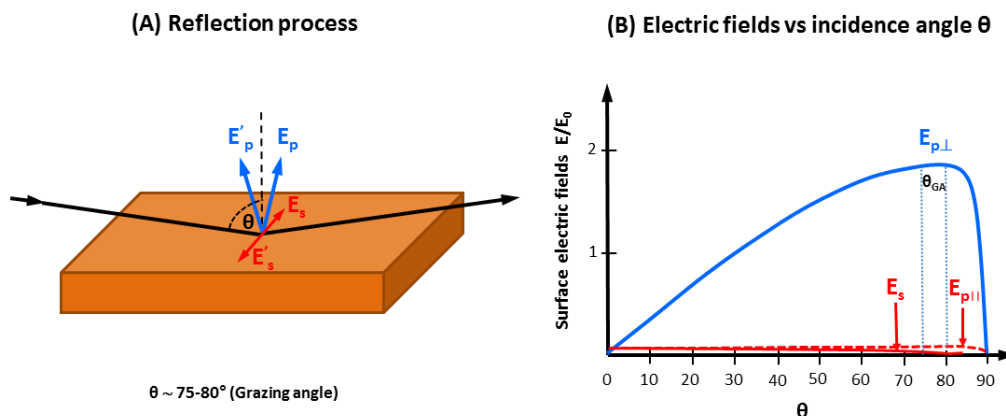
Figure 8. (a) Electric vectors of s- and p-polarized incident radiation on a metal surface at an angle θ to the normal. (b) Resultant electric fields (E) relative to the incident (E_0) for IR on a metal versus the incident angle θ, for perpendicular and parallel components to the surface arising from initially p-polarized radiation (Guided to eye).

Therefore, IRRAS is an especially adequate optical technique to study thin films adsorbed on reflective surfaces such as metals and, that often yields to important information about adsorption geometry. Other advantages of this technique are its high sensitivity ($<10^{-1}$-10^{-2} for monolayers in favourable cases) and the easiness to correlate its results with other surface- and bulk-sensitive vibrational spectroscopies.[14] Thus, IRRAS spectra monitor changes of reflectance (ΔR/R), where analytical solutions have been proposed for an adlayer of thickness, d, and complex refractive index, n, overlying a metal surface. Making approximations valid for low coverages of an adsorbate, the following simple expression is derived for the reflectance change of p-polarized radiation of wavelength λ:

$$\frac{\Delta R}{R} = -\left(\frac{4\pi k d}{\lambda}\right) \cdot \left(\frac{4\sin\theta\tan\theta}{n^3}\right) \tag{2}$$

94

where the first factor relates to the attenuation ε·C·l in the Beer-Lambert law, while the second corresponds to the field and geometrical enhancements previously commented. However, deviations from this simple behaviour are usually present, and recent work has favoured the use of numerical simulation for both reflection and transmission spectra of anisotropic systems.

Regarding to the comparison of IRRAS measurements with those from other non-surface IR spectroscopies, it is convenient to express the experimental intensities in terms of the dynamic dipole magnitude involved in the oscillation. Although, experimental measure of intensity for an dipole may be complicated, for a submonolayer film with dipoles oriented perpendicular to the surface it can be deduced the following equation:[14]

$$A = \frac{1}{4\pi\varepsilon_0} \cdot \frac{8\pi^3 n_s \breve{\upsilon}_p \mu^2 \sin\theta \tan\theta}{c \cdot h} \tag{3}$$

where n_s is the adlayer density (i.e. molecules per unit area), $\breve{\upsilon}_p$ the wavelength of the peak absorbance and μ the dynamic dipole.

Specifications and working conditions
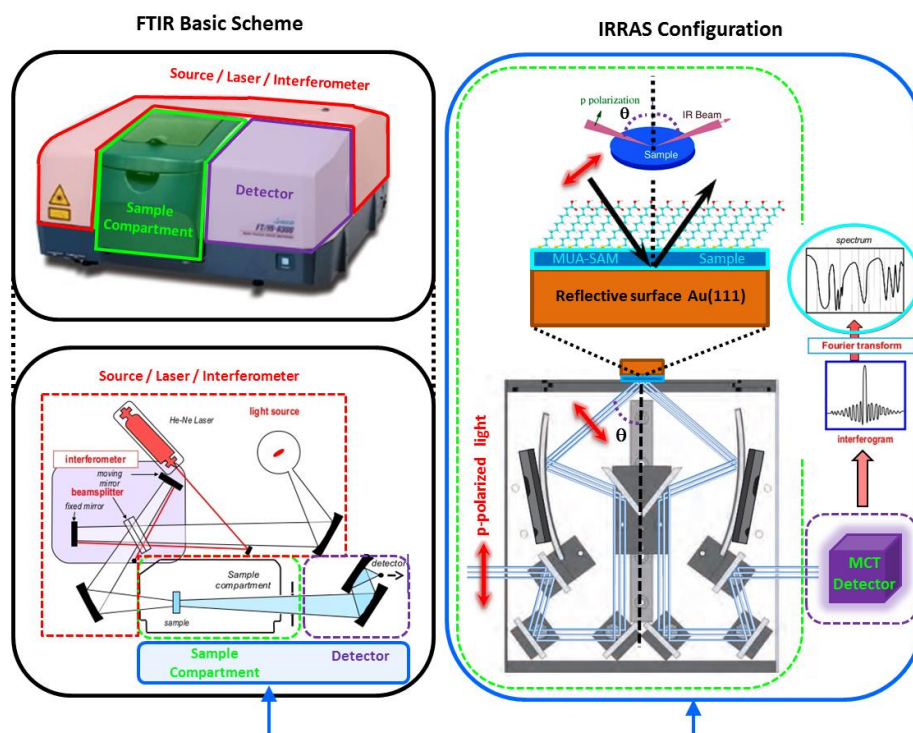
Figure 9. Basic scheme of the configuration of a JASCO 6300 FTIR spectrometer with a sample compartment adapted to a variable angle specular reflectance accessory for IRRAS measurements.

Reflectance-absorption infrared measurements were recorded on a JASCO 6300 FTIR single (He-Ne) laser beam spectrometer in the 400-400 cm^{-1} wavenumbers range at a resolution of 2 or 4 cm^{-1} (Figure 9). The data were acquired by the software integrated in the equipment (Spectra Manager). A variable angle specular reflectance accessory (Pike Technologies-VeeMAXTM) assembled in the FTIR spectrometer compartment enabled the samples to be analysed by a p-polarized beam at a grazing angle of 80º.

Prior to the measurements, the interferometer and sample compartments were purged with a dry and free CO2 air flux of 8 l/min supplied by a compressed air adsorption dryer (K-MT LAB, Parker/Zandet GmbH & Co.KG). Then, the samples dried with N_2 were placed face downwards on a mask platform with an aperture (10 mm in diameter) to define the position and sampling dimensions where the incident beam spot was collimated (Figure 9). The IR signals were collected by a liquid nitrogen cooled mercury cadmium telluride (MCT) detector which improves the dynamic range performance over a wide wavenumber range.[14]

2.4.2.2.   Resonance Raman spectroscopy (RRS) at surfaces

General Concepts for the analysis of biomolecules

Resonance Raman (RR) scattering occurs when the exciting line is chosen that its energy intercepts the electronic excited state (Figure 10a). [15] The depolarization ratios of Raman bands provide valuable information about the symmetry of a vibration , making possible band assigments. Figure 10 b shows Raman scattering geometries that allows to measuring intensities $I_{||}$ and $I_{\perp}$ using an analyzer and obtaining the depolarization ration, ρ_p. In this sense, if the molecule is performing a totally symmetric vibration, the molecules is polarized equally in every direction. Under this circumstance, $I_{\perp} =$ 0, since the oscillating dipole emitting the radiation is confined in the xz-plane (Figure 10b) and thus, $\rho_p = 0$. Such vibration is called ***polarized (p)***. On the other hand, if the molecule is performing a non-totally symmetric vibration, the polarizability changes from a spherical to an ellipsoidal shape during the

vibration. Then, the induced dipole would be the largest along the minor axis of the ellipsoid and, $\rho_p \neq 0$. Such vibration is called ***depolarized (dp)***.
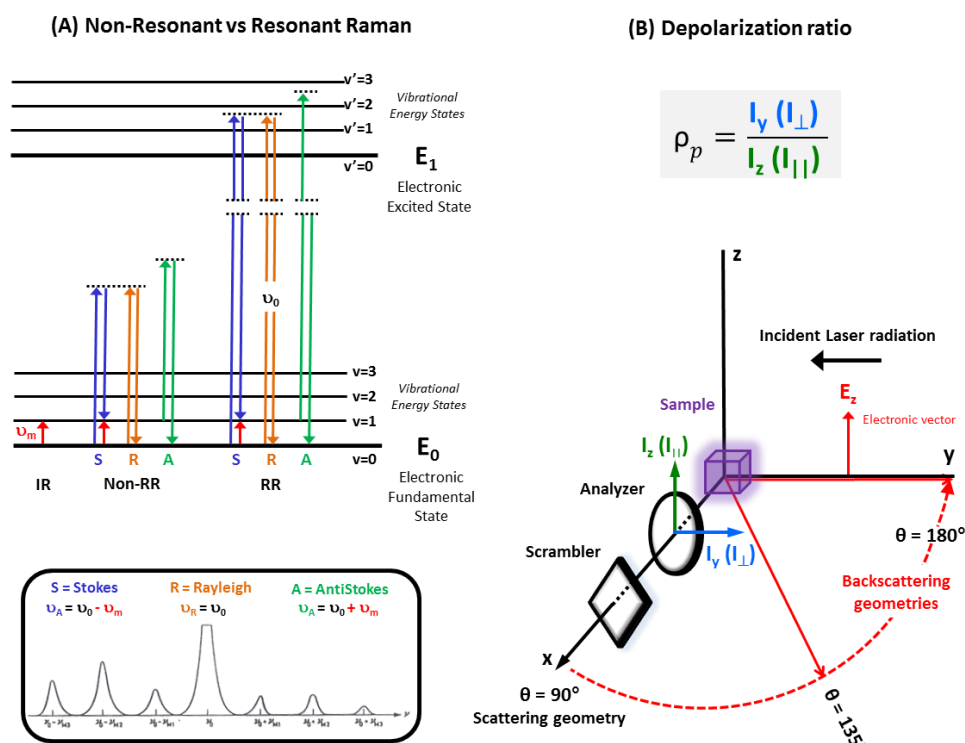
Figure 10. (a) Scheme showing differences between IR absorption, non-resonant and Resonant Raman (RR) scattering. (b) Scattering geometries and depolarization ratio.

        One of the main advantages to use RR effect for the analysis of biomolecules is that vibrations of a particular chromophoric group can be selectively and considerably enhanced (up to 10^6). Then, it is especially recommended for the study of hemeproteins because of the possibility to probe the vibrational spectra of the prosthetic group solely and, thus, affords detailed information on the redox site structure. However other important structural subunits, such as aromatic residues and peptide bonds can be also

explored by tuning the excitation frequency (υ_{ext}) into the electronic band of certain structural elements of the proteins. Such approach allows overcoming the difficulty of Raman spectra interpretation due to overlapping of multiple bands (Figure 11).[15, 16] In summary, the main electronic transitions regions for absorption in RR are the following ones (Figure 11):

- Heme charge transfer (CT) and Q (α and β, Q_0 and Q_v, respectively) transitions at the 520-650 nm range involving the metal ion (heme-in plane ring vibrations) and the axial ligands vibrations (**type B bands**).

- Soret band (B) due to a strong $\pi \rightarrow \pi^*$ transition in the heme group at 400 nm involving the heme in-plane ring vibrations (**type A bands**).

- The absorption of aromatic amino acid residues (Tryptophan and Tyrosine) in the 220-260 nm range

- The peptide backbone amide $\pi \rightarrow \pi^*$ transition below 220 nm.

Therefore, information can be obtained on the binding of the ligand to the metal ion, the spin and redox states of the heme group, the state of Trp and Tyr residues, and the secondary structure of the protein. Because of the coordination of N atoms from the porhyrin ring to the central metal ion influences the macrocycle structure, the observed RR enhanced vibrational spectrum contains unique information on the state of the central ion. Then, vibrations of axial ligands can be also studied due to coupling with the $\pi \rightarrow \pi^*$ electronic transitions. Excitation within the CT transition also results in enhancement of the axial ligand modes.
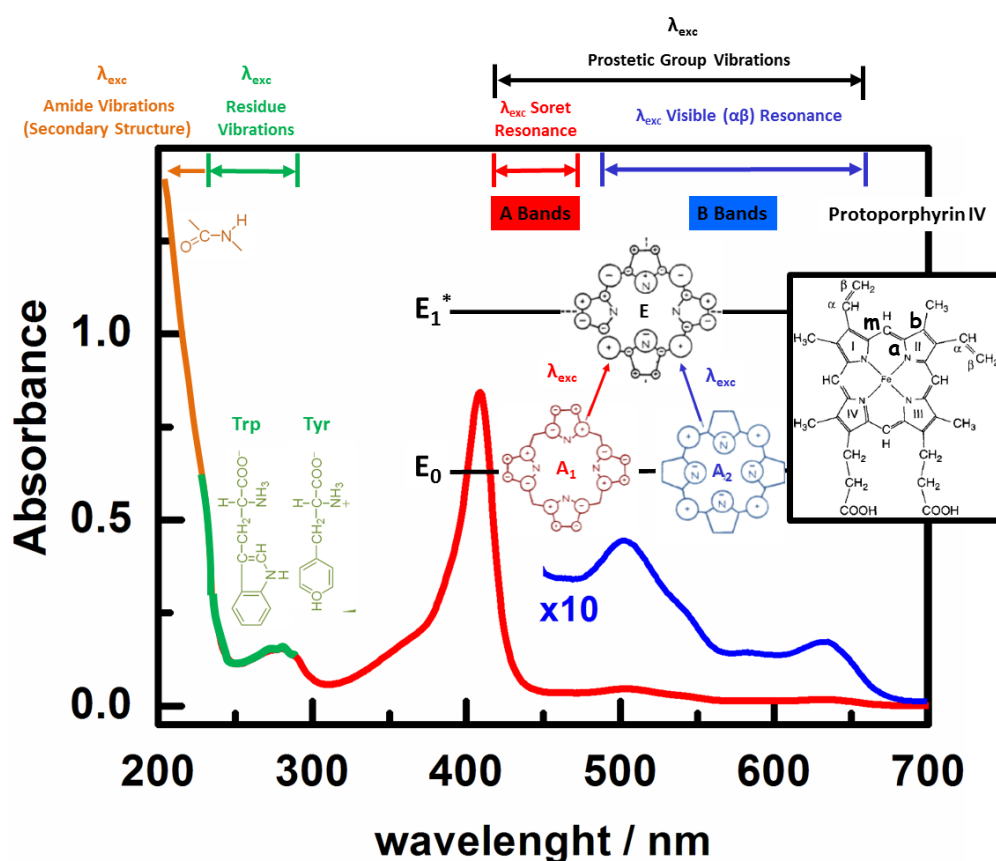
Figure 11. UV-visible spectrum of native myoglobin showing selected absorption spectral regions for excitation in RR scattering. Structure of heme group (protoporphyrin IV) and C assignments are included. Vibronic bands, type A and B, are associated to Soret and charge transfer electronic excitation, respectively. The electron density distributions of the Soret and visible molecular orbitals (groups symmetry) giving rise to the electronic transitions ($E_0 \rightarrow E_1^*$) are included.

The heme group can be considered in the first approximation as a planar structure with a D_{4h} symmetry. Further, if the substituents are treated as point masses, the *in-plane* and *out-of-plane* vibrational modes can be represented according to the following equations:

$$\Gamma_{\text{in-plane}} = 9A_{1g} + 8A_{2g} + 9B_{1g} + 9B_{2g} + 18E_u \tag{4}$$

$$\Gamma_{\text{out-of-plane}} = 3A_{1u} + 6A_{2u} + 5B_{1u} + 4B_{2g} + 8E_g \tag{5}$$

In an idealized heme group, the presence of a symmetry center operates the Raman selection rules where only "gerade" (g) modes are Raman-active. The allowed Raman modes can be recognized by the following polarization properties: (i) *polarized* (A_{1g}), (ii) *depolarized* (B_{1g} and B_{2g}), and (iii) *anomausly polarized* (A_{2g}). The observed spectral pattern depends on λ_{ex}. There is a relationship between symmetry of resonantly enhanced vibrational modes and the nature of the electronic transition. The Raman intensity, I_R, is proportional to the square of the polarizability tensor component for the k transition $[(\alpha_{p\sigma})_k]$. For RR scattering, the polarizability tensor can be approximately described as the sum of two terms A and B ($[(\alpha_{p\sigma})_k \approx A + B)$. Depending on the nature of the electronic transition, term A or B dominates, originating two varieties of RR vibrational modes:[15, 16]

- *Term **type A*** is associated with vibrational modes connecting the ground state to the excited state through Frank-Condon overlap, or which change the energy of the resonant excited state, and usually leading contribution to I_R. Fundamentals, overtones and combination bands of <u>totally symmetric modes dominate the spectra</u>. For the heme group this resembles excitation in the **Soret (B) band** and resonance enhancement of **A_{1g} modes**.

- *Term **type B*** is associated with the vibronic coupling of one resonantly excited state to another excited state of higher energy. Fundamental
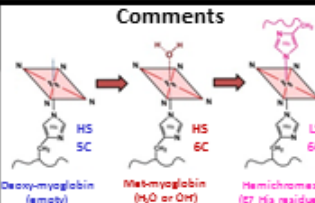
transitions of <u>non-totally symmetric vibrations</u> are resonantly enhanced. This is the case for a excitation within a weakly allowed electronic transition which is vibronically coupled with a strong one. For the heme group this corresponds to the **excitation within Q bands** and resonant enhancenment of **B_{1g}, B_{2g}** and **A_{2g}** modes.

Resonance with the Q_0 (α band) might be expected to enhance type A modes, but they are not observed because of their too low intensity. Rather, the type B modes are observed, which mix Q_0 and Q_v (α and β band, respectively) electronic transitions and give rise to the β band with the allowed symmetries, $E_u \times E_u = A_{1g} + A_{2g} + B_{1g} + B_{2g}$. However, as commented, the polarized symmetric A_{1g} modes show ineffective vibronic mixing and the depolarized B_{1g} and B_{2g} modes appears as observed Raman bands. The antisymmetric A_{2g} modes, which are inactive in normal Raman scattering, become active in the resonance region, giving rise to *inversely or anomaly polarized* RR bands.

The idealized D_{4h} symmetry of the heme group can be distorted by asymmetric substitutions (*axial ligands*) and deformation of its planar structure. In fact, in-plane inactive E_u and out-of-plane deformation modes are observed in hemeproteins when heme interactions with the protein matrix destroy the effective symmetry center of the chromophore. RR spectrum is mainly dominated by in-plane modes, inasmuch as the dominant $\pi \rightarrow \pi^*$ transitions are polarized in the plane. Most of the strong RR bands lie between 1000-1650 cm^{-1} and are expected to involve primarily C-C, C-N stretching and C_m-H bending vibrations of the porphyrin ring, with their

frequencies attending to their bond orders (*e.g.* C_b-C_b > C_a-C_m > C_a-N > C_a-C_b).
Usually the fingerprint region is in the 1000-1300 cm^{-1} wavenumber region.
Table 1 summarizes the unique information of the state of the heme metal
ion by analyzing certain oxidation and core size **marker bands**, which are
usually encountered between 1350-1650 cm^{-1}.[16]

Table 1. Oxidation state and spin marker bands of heme group (mode and frequency
assignments). Examples of different heme coordination states of myoglobin.[16-19]

Mode	Approximate interpretation	Fe³⁺ LS 6C	Fe³⁺ HS 5C	Fe³⁺ HS 6C	Fe²⁺ LS 6C	Fe²⁺ HS 5C	Fe²⁺ HS 6C	Comments
A_{1g} (υ_4)	υ_s (C-N) Pyr half-ring breath	1373	1373	1370	1359	1357	1355	Porphyrin π* e⁻ density marker: (1) Oxidation state marker band (υ_4 ↓ upon reduction) (2) Axial ligation marker band (υ_4 ↑ upon ligation)
A_{1g} (υ_3)	υ_s (C-C)	1502	1491	1480	1493	1471	1463	Porphyrin core size maker: (1) Spin marker band (LS → HS ↑υ) (2) CN marker band (6C → 5C ↑υ)
A_{2g} (υ_{19})	υ_a (C-C)	1586	1571	1560	1583	1550		
B_{1g} (υ_{10})	υ_a (C-C)	1640	1626	1610	1617	1604		

CN=Coordination number ; LS=Low Spin; HS=High Spin; 6C=Six Coordinated; 5C=Five Coordinated; **Pyr**=Pyrrole

There are three main reasons for the frequency of the modes to be displaced:

- <u>The electron density on the antibonding π* orbitals of the porphyrin ring</u>.
 Higher electron density weakens C-C and C-N bonds and frequency
decreases. This is the case for the transition from Fe^{3+} to Fe^{2+} due to the
increase in occupation of π* orbitals. On the contrary, electron withdrawal

from π^* orbitals, such as axial ligation by CO, NO and O_2, leads to a frequency increase (Table 1).

-        <u>The core size of the porphyrin ring</u>. The core size depends on two factors: (i) the spin state of Fe and, (ii) the coordination number (CN). In the high-spin (HS) state two antibonding d orbitals of the Fe contains an electron and, the porphyrin cavity is expanded, as compared to the low-spin (LS) state where these orbitals are empty. Expanding the core size decreases stretching frequencies. Similarly, the CN of the central Fe influences the core size. In the 6C state, Fe is located in the heme plane, while in the 5C state, Fe is dislocated from the heme plane towards the proximal fifth ligand. Such a dislocation decreases the core size and stretching frequencies increase (Table 1).

-        <u>Twisting/tilting of Pyr rings from the idealized heme planar structure.</u> This fact is usually due to interactions with the protein matrix.

Finally, the limitations of the RR technique must also be considered. First, a laser source is needed to observe weak Raman scattering, which causes local heating and/or photodescomposition of the active center in the biomolecule, especially in RR studies, where the radiation frequency is tuned within the electronic adsorption band. To avoid such problems, low laser powers, defocusing of the laser beam, cooling and rotating samples, and independent inspection of the sample integrity are employed. Another inconvenient is that many active centers in biomolecules or impurities intensely fluoresce when irradiated by the laser beam. In this sense, the backscattering geometry (135º or 180º) has several advantages over the

common 90º geometry. A simple and versatile design that allows rotation and cooling of the sample simultaneously.

Specifications and working conditions

Raman spectra were collected in back-scattering geometry using a Renishaw Raman instrument (InVia Raman Microscope) equipped with a Leica microscope furnished with various lenses, monochromators and filters in addition to a CCD camera (Figure 12a). An 1800 l/mm grating was used in the spectrograph. Spectra were obtain by excitation with green laser light (532 nm) from 150 cm^{-1} to 1500 cm^{-1}. A total of 15 scans were done in order to improve the signal-to-noise ratio. For RR measurements, a 20x microscope objective was used to focus the laser. RR spectra were acquired in 30 s using a laser power of 10 mW at the sample. RR measurements were conducted on samples of myoglobin immobilized on pure and mixed MUA/DT SAMs on gold, either dried or by contacting them with a drop of buffer solution at pH 7.5. Each experiment was repeated several times to check reproducibility.

(A) Instrument configuration

Research grade Leica microscope

Auto view/Raman changeover

Auto calibration

Auto performance verification

Auto excitation wavelength switching

Auto confocality control

Ultra-high precision multiple grating stage

CCD

UV capability

Raman imaging capability

Near-excitation filter capability

Wavelength optimized laser beam control

Auto alignment optimization

Class 1 laser safe enclosure

Sample handling

Safety interlock control

(B) RR Basic Scheme

180°   RR Backscattered

135°

Reflective surface Au(111)

Microscope   Notch filter   Focusing optics   Entrance slit

Grating

CCD-Camera

Imaging Setup

Entrance mirror

Laser beam

Mirror   Line filter   Beam shaping
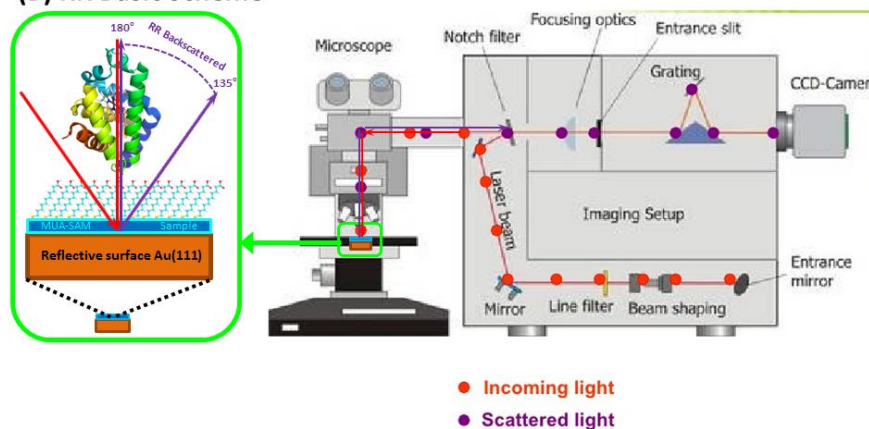
● Incoming light
● Scattered light

Figure 12. Basic scheme is shown for the configuration of a Renishaw Raman instrument (InVia Raman Microscope) with a sample compartment to perform measurements in backscattering geometry.

106

2.4.3. Mass Techniques

### 2.4.3.1.   Matrix-Assisted Laser-Desorption Ionization (MALDI-TOF)

General Concepts

MALDI is a leading soft ionization technique used in mass spectrometry (MS) for protein sequencing, proteomic research, DNA, lipids and glycoconjugates or polymers (*e.g. dendrimers*) analysis, and is commonly used together with electrospray ionization (ESI) technology. The main features of MALDI-TOF MS are: (I) The broad mass range allows analysing a wide variety of biomolecules, (II) it is relatively tolerant to buffers and salts, (III) Data acquisition is fast, and (IV) mass resolution, accuracy and sensitivity are very high.

In MALDI, the sample is first dissolved in a suitable solvent and mixed with an appropriate matrix before is spotted on a metal plate and air-dried. Then, the sample is co-crystallized with the matrix. The choice of a specific matrix is mainly experimental and can be influenced by the ionization mode, whether positive or negative. Secondly, the mixture is irradiated with a pulsed laser (*usually of nitrogen, λ = 337 nm*) which triggers the desorption of the matrix material by adsorption of energy of the laser. Finally, under these circumstances, the ionization of the analytes in the sample takes place (Figure 13a).[20]

Then, the ionized biomolecules enter to the mass analyzer sector, where ions are separated based on their *m/z* (mass to charge) values. In MS, the isolation of ions is usually electrically driven, although traditional analyzers employed magnetic fields that influenced ion separation.

107
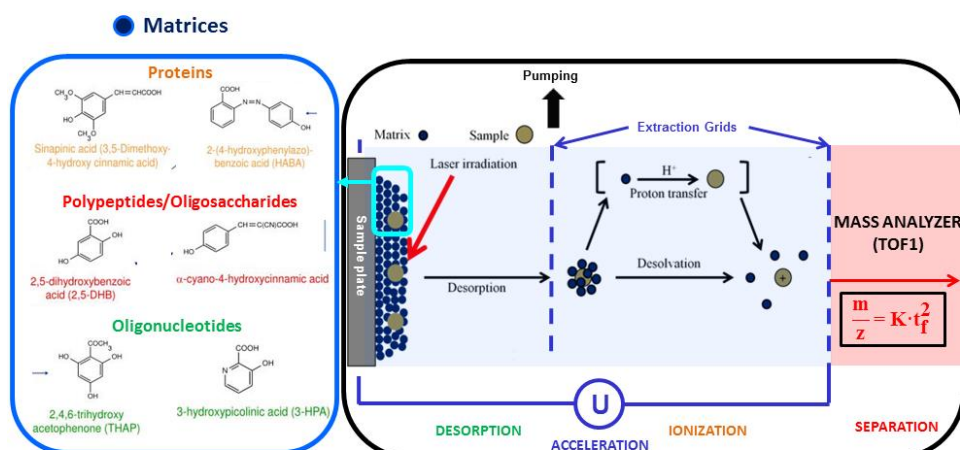
(A) Ion Source (MALDI)

(B) MALDI-TOF/TOF Basic Scheme
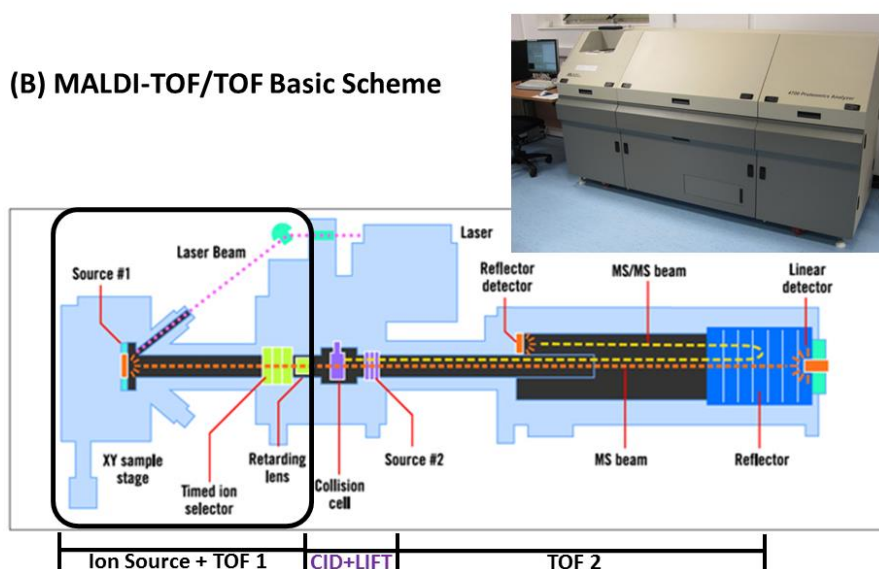
Figure 13. (a) Graphic representation of the MALDI ion source sector of a MS. (b) Basic scheme is shown for the configuration of an Applied Biosystems 4700 MALDI TOF/TOF spectrometer of the Facility Services of the University of Bristol (UK).

The Time of Flight (TOF) analyzer is based on a simple ion separation methodology, which relies on the free flight of the ionized molecules in a long tube (L=1-2 m) before reaching the detector. Then, two ions formed at the

same time and with the same charge but different mass will reach the detector at different times, which is due to their different kinetic energy (KE) upon being accelerated by a voltage (U) in a previous sector. The equation that correlates the *m/z* ratio with the total time of flight (t$_f$) is expressed as follows:

$$\frac{m}{z} = t_f^2 \cdot \frac{2U \cdot s}{(2s+L)} = K \cdot t_f^2 \tag{6}$$

where m is the mass, z is the charge, U is the acceleration voltage, s is the length of the acceleration region, L is the path length of the free flight region, t is the time of flight and e is the elementary charge. Theoretically, U, s, and x are fixed and included in K, the calibration factor of the instrument. TOF analyzer has the advandtage to detect a very high mass range and individual ions m/z at improved resolution thanks to the reflector electrostatic ion mirror.

In tandem mass spectrometry (MS/MS), MALDI-MS can provide not only valuable information about non-fragmented molecular ions, but also structural information when fragmentation is induced. Therefore, MS/MS relies on the isolation of a specific m/z, i.e. precursor ion, that is subjected to dissociation and production of product ions. The task consists to solve the fragmentation patterns created by the MS/MS spectrum to reveal information about the analyte sequentiation or structure. To achieve this goal, mass analyzers can be connected in series (e.g. TOF/TOF), so that ion isolation is performed in the first analyzer (TOF1) followed by ion fragmentation in the

collision cell (CID), whereas the final analizer (TOF2) separates fragment ions based on their m/z (Figure 13b).

Specifications and working conditions

Protein mass measurements of n-Mb and c-Mb were determined by MS performed by an Applied Biosystems instrument (Figure 13b). As indicated in section 2.3.3.1 (Experimental and Methods), MALDI-TOF MS samples were obtained by combining a 3:1 (v/v) solution of 20 mg/ml 2,5-dihydroxy acetophenone: 18 mg/ml ammonium citrate dibasic with an equal volume of 2% trifluoroacetic acid, then adding an equal volume of protein´s samples approximately 1 mg/ml in 0.02 M phosphate buffer, before spotting onto the MS plate and drying at 40 ºC.

2.4.3.2. Quartz Microbalance (QCM) Technique
General concepts

The quartz crystal microbalance (QCM) technique has found wide acceptance as an analytical technique. This is because of its sub-nanogram (ng) detection capabilities, is label-free, affordable, and QCM surfaces can be readily modified with a rich surface chemistry (*e.g. SAMs, polymerized films, sensing ionic liquids, etc.*) to detect and characterize diverse interactions (*e.g. hydrophobic, electrostatic and hydrogen bonding*), for example as a tool for biomolecular recognition, and detection of carbohydrates, nucleic acids, non-enzymatic proteins, cells, drugs, antigens and antibodies, among others.[21]

The signal transduction mechanism of QCM is based on the converse piezoelectric effect, investigated initially in quartz crystals. Piezoelectric effect is described by the generation of electrical charge on opposite surfaces of a crystalline material upon mechanical deformation (e.g. pressure or torsion) of the crystal along a given direction (Figure 14a). The converse piezoelectric effect takes place when the quartz crystal produces acoustic waves upon the application of an alternating current (AC) voltage by an oscillator circuit to a pair of metallic electrodes (e.g. Au, Ag, Pt, Al or Ni) where quartz is sandwiched. Then, mechanical oscillations are generated that cause shear displacements/deformations of the quartz-and any mass bound to its surface-at a particular frequency (Figure 14a).

Therefore, nanogram mass changes (Δm) that occur on the surface of a quartz crystal can be correlated with changes of the resonant frequency oscillation (Δf) at the quartz crystals surface. Quartz crystals are cut so that a particular mode of vibration dominates, being the AT-cut the most commonly used for QCM applications. The resonant frequency is governed by the thickness of crystal. Then, an increase of the material thickness produces a decrease of its resonant frequency. The Sauerbrey equation reports the principle postulate of this technique that relates the linear change in mass with frequency:[21]

$$\Delta f = - \frac{2f_0^2}{A\sqrt{\mu_q \rho_q}} \cdot \Delta m = -C_f \cdot \Delta m \qquad (7)$$

111

Here, Δf represents the measured frequency change (Hz), f_0 the fundamental frequency (Hz) of an AT-cut quartz crystal, Δm the change in mass (g) deposited elastically (*i.e., without energy loss*) as a thin, rigid and uniform film, A the area of the electrode (cm^2), μ_q the shear modulus of an AT-cut quartz crystal (2.947·10^{11} g·cm^{-1}·s^{-2}), and ρ_q the density of quartz crystal (2.648 g·cm^{-3}). C_f is the integrated QCM/mass sensitivity or Sauerbrey constant, which depends on f_0 and increases proportionally with the overtone number. This equation applies only when the mass layer has the same density as quartz does and is not greater than approximately 2% of the mass of the crystal.

(A) QCM Sensor

$$\Delta f = -\frac{2 f_0^{\,2}}{A \sqrt{\rho_q \mu_q}} \Delta m$$
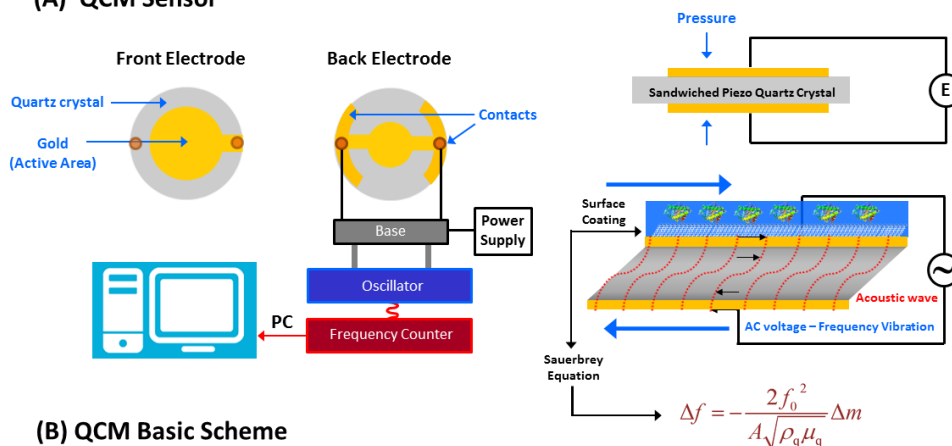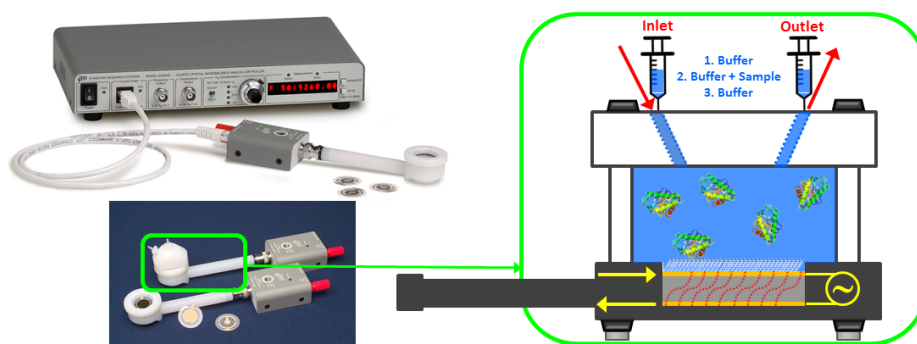
(B) QCM Basic Scheme

Figure 14. (a) Schematic representation of a QCM sensor and its fundamental principles of operation. (b) Basic scheme for the configuration of an SRS-QCM200 sensor used at the Electrochemistry Group of the School of Chemistry of the University of Bristol (UK).

Specifications and working conditions

QCM measurements were performed using a Stanford Research Systems (SRS) QCM200 at the University of Bristol, UK (Figure 14b). The frequency output of the SRS QCM200 was connected to the auxiliary analogue-to-digital converter (ADC) input of a PGSTAT30 controlled with GPES software. 5 MHz QCM crystals covered with gold, and functionalized with SAMs, were first mounted onto the QCM crystal holder using a retainer ring. Background electrochemical measurements were performed in solution as described below:

- The SAM modified gold surfaces were rinsed with 0.01 M pH 7.6 phosphate buffer solution (PBS). A flow cell attachment was connected to the crystal holder, and three injections of different solutions were made while recording the oscillation frequency, allowing the system to stabilize between each stage. The solutions injected were 0.01 M pH 6.5 PBS, 10 µM native or cationized protein in PBS, and finally a rinsing stage using only PBS. The crystal was immersed in solution during the whole QCM experiments (Figure 14b).

- Manual syringes were used to inject solution. A suspended waste syringe open to atmosphere was connected to the cell outlet to minimize pressure effects upon the oscillation frequency of the crystal. This was clamped at a constant height, and the waste solution left in it, kept at a constant level to

ensure the pressure remained constant within the cell during the experiment (Figure 14b). This setup also allowed removing bubbles in the system via gentle pumping. During the initial and final buffer stages, the parasitic capacitance (C_0) was nulled to ensure the Δf (Hz) due to adsorption processes could be accurately measured.

2.4.4. Other equipment

The solution pH was measured and adjusted by using CRISON Basic-20 and 20+ pH meters for carrying out CV or IRRAS titration experiments of modified gold surfaces with SAMs. The equipment was calibrated with pH 4, 7 and 9.21 standard solutions.

UV-visible spectra were acquired with a JASCO V-670 vis-NIR spectrophotometer and 0.2 and 1 cm path length cuvettes in order to characterize the protein aqueous solutions.

2.5.   Data Processing

As previously commented in Section 2.4.1.2, electrochemical data, and including those obtained from QCM measurements (Section 2.4.3.2.2), were analyzed with GPES, FRA and NOVA software packages, and electrochemical parameters determined. The data curve fitting is performed by the least squares of Marquardt method used for non-linear functions. The convergence criteria are based on the value of χ^2 test, Σ $(Y-Y_{fit})^2$, and its change during the last iteration, as well as the accuracy in the adjusted parameters. In the particular case of EIS spectra, those were analyzed a nonlinear adjustment

114

method (CNLS), Equivcrt[22] included in the FRA software configuration of the Autolab instrument.

The baseline correction, second-derivative and deconvolution analysis of the FT-IRRAS spectra were carried out by the Spectra Manager software package included in the configuration of the JASCO 6300 instrument. Similarly, the baseline of RR spectra was corrected with the software included in the Renishaw Raman instrument (In Via Microscope).

2.6. References

1.   Clavilier, J.; Faure, R.; Guinet, G.; Durand, R., Preparation of Mono-crystalline Pt Microelectroes and Electrochemical Study of the Plane Surfaces Cut in the Direction of the (111) and (110) Planes. *J. Electroanal. Chem.* **1980,** *107* (1), 205-209.

2.   Hamelin, A., Cyclic Voltammetry at Gold Single-Crystal Surfaces. Part 1. Behavior at Low-Index Faces. *J. Electroanal. Chem.* **1996,** *407* (1-2), 1-11.

3.   Trasatti, S.; Petrii, O. A., Real Surface-Area Measurements in Electrochemistry. *Pure and Applied Chemistry* **1991,** *63* (5), 711-734.

4.   Kolb, D. M.; Schneider, J., Surface reconstruction in electrochemistry: gold(100)-(5 x 20), gold(111)-(1 x 23) and gold(110)-(1 x 2). *Electrochim. Acta* **1986,** *31* (8), 929-36.

5.   Ganesh, V.; Lakshminarayanan, V., Self-Assembled Monolayers of Alkanethiols on Gold Prepared in a Hexagonal Lyotropic Liquid Crystalline Phase of Triton X-100/Water System. *Langmuir* **2006,** *22* (4), 1561-1570.

6.   Raya, D. G.; Madueno, R.; Blazquez, M.; Pineda, T., Formation of a 1,8-Octanedithiol Self-Assembled Monolayer on Au(111) Prepared in a Lyotropic Liquid-Crystalline Medium. *Langmuir* **2010,** *26* (14), 11790-11796.

7.   Perriman, A. W.; Brogan, A. P. S.; Coelfen, H.; Tsoureas, N.; Owen, G. R.; Mann, S., Reversible Dioxygen Binding in Solvent-Free Liquid Myoglobin. *Nature Chemistry* **2010,** *2* (8), 622-626.

115

8. Risbridger, T. A. G.; Watkins, D. W.; Armstrong, J. P. K.; Perriman, A. W.; Anderson, J. L. R.; Fermin, D. J., Effect of Bioconjugation on the Reduction Potential of Heme Proteins. *Biomacromolecules* **2016,** *17* (11), 3485-3492.

9. Dosi, R.; Carusone, A.; Chambery, A.; Severino, V.; Parente, A.; Di Maro, A., Rapid Primary Structure Determination Of Myoglobins by a Complementary Approach Based on Mass Spectrometry and Edman Degradation. *Food Chem.* **2012,** *133* (4), 1646-1652.

10. Strupat, K., Molecular Weight Determination of Peptides And Proteins by ESI and MALDI. *Methods Enzymol.* **2005,** *405* (Mass Spectrometry: Modified Proteins and Glycoconjugates), 1-36.

11. Brogan, A. P. S.; Siligardi, G.; Hussain, R.; Perriman, A. W.; Mann, S., Hyper-Thermal Stability and Unprecedented Re-Folding of Solvent-Free Liquid Myoglobin. *Chemical Science* **2012,** *3* (6), 1839-1846.

12. Nakanishi, N.; Takeuchi, F.; Park, S.-Y.; Hori, H.; Kiyota, K.; Uno, T.; Tsubaki, M., Characterization of Heme-Coordinating Histidyl Residues of an Engineered Six-Coordinated Myoglobin Mutant Based on the Reactivity with Diethylpyrocarbonate, Mass Spectrometry, and Electron Paramagnetic Resonance Spectroscopy. *Journal of Bioscience and Bioengineering* **2008,** *105* (6), 604-613.

13. Allen J. Bard, L. R. F., *Electrochemical Methods: Fundamentals and Applications, 2nd Edition*. John Wiley & Sons: New York (United States of America), **2001**; p 864.

14. Hollins, P., Infrared Reflection–Absorption Spectroscopy. In *Encyclopedia of Analytical Chemistry*, John Wiley & Sons, Ltd: **2006**.

15. Ferraro, J., Introductory Raman Spectroscopy. **2003,** *2*, 434.

16. Niaura, G., Raman Spectroscopy in Analysis of Biomolecules. In *Encyclopedia of Analytical Chemistry*, John Wiley & Sons, Ltd: **2006**.

17. Antonini, E.; Brunori, M., *Hemoglobin and Myoglobin in their Reactions with Ligands*. North-Holland: **1971**; Vol. 21.

18.   Spiro, T. G.; Strekas, T. C., Resonance Raman Spectra of Heme Proteins. Effects of Oxidation and Spin State. *Journal of the American Chemical Society* **1974,** *96* (2), 338-345.

19.   Abe, M.; Kitagawa, T.; Kyogoku, Y., Resonance Raman Spectra of Octaethylporphyrinato-Ni(II) and Meso-Deuterated and 15N Substituted Derivatives. II. A Normal Coordinate Analysis. *The Journal of Chemical Physics* **1978,** *69* (10), 4526-4534.

20.   El-Aneed, A.; Cohen, A.; Banoub, J., Mass Spectrometry, Review of the Basics: Electrospray, MALDI, and Commonly Used Mass Analyzers. *Appl. Spectrosc. Rev.* **2009,** *44* (3), 210-230.

21.   Cheng, C. I.; Chang, Y.-P.; Chu, Y.-H., Biomolecular Interactions and Tools for Their Recognition: Focus on the Quartz Crystal Microbalance and its Diverse Surface Chemistries and Applications. *Chem. Soc. Rev.* **2012,** *41* (5), 1947-1971.

22.   Boukamp, B. A., A Nonlinear Least-Squares Fit Procedure for Analysis of Immittance Data of Electrochemical Systems. *Solid State Ionics* **1986,** *20* (1), 31-44.

CHAPTER 3

MUA SAMs Formed on Au(111) by Different Methodologies

3. MUA SAMs formed on Au(111) by different methodologies

3.1. Introduction

The self-assembly processes of organic molecules in metallic substrates have been widely investigated due to their potential applications in different fields.[1-8] Specially, the interfacial behavior of nanofilms based on the self-assembly of ω-alkanethiols on gold surfaces have attracted a lot of attention opening a bottom-up strategy to build supramolecular assemblies through the attachment of different kind of biomolecules and cells by non-covalent interaction or via conjugation covalent chemistry.[8] To achieve this objective, the study of the quality and the interfacial properties of ω-

functionalized SAMs formed following different strategies results of great interest.

The most common method for preparing alkanethiols self-assembled monolayers is by immersion of a metal substrate into the assembly solution containing the thiols at room temperature.[1] The changes on the nature of the organic solvents used to prepare the formation solutions as well as the use of potential control, may direct the assembly mechanism of the self-assembled monolayers and in turn, their interfacial properties (*Chapter 1-Section 1.2.3.*) .[9, 10] Many researchers have studied the thiol-monolayers formed on Au surfaces in different solvents by immersion processes, but the mechanism that governs the solvent effects on the assembly step has not been elucidated. Bain et al.[11] have assessed the effect of various solvents (DMF, THF, ethanol, CCl_4, acetonitrile, hexadecane, cyclooctane and toluene) on the formation of nanofilms on Au substrates. It has been found that the hexadecanethiol monolayers adsorbed on Au from hexadecane, exhibited low contact angles when reached the expected thickness, which is most likely attributed to the incorporation of hexadecane into the monolayer. Bensebaa et al.[12] have characterised by infrared reflexion-absorption spectroscopy (IRRAS) the kinetics of the assembly processes of the C_{22}-thiol monolayer. The results showed that an ordered film was rapidly obtained in ethanol and, that the monolayers formed in CCl_4 were more disordered. Likewise, Sur et al.[13] using cyclic voltammetry (CV) and electrochemical impedance spectroscopy (EIS), have measured the interfacial capacitance of alkanethiol SAMs in Au electrodes in non-aqueous solvents, such as n-hexane, chloroform, toluene,

ethanol, DMF, acetonitrile and hexadecane. They concluded that the nanofilms formed from hexane and chloroform/hexane presented the best structural organization.

The assembly mechanism of self-assembled monolayers deposited over metallic substrates under potentiodynamic conditions are regulated by deposition kinetics and the surfaces coverages of the resulting films are often slightly lower than the theoretical surface coverage value for a full monolayer (*i.e. submonolayer coverage*).[14, 15] Porter et al.[16] have found that the monolayers formed under electrochemical control show similar structures and interfacial properties to those obtained by traditional routes.

A number of techniques have been employed to determine the acid-basic interfacial behaviour of surface confined carboxylic acids such as contact angle titration,[17] quartz crystal microbalance measurements,[18] amperometry,[19] FTIR-ATR,[20] laser-induced temperature jump studies, double layer capacitance titration,[21] impedance spectroscopic studies,[22] and chemical force microscopy measurements.[23-25]

Herein, the relationship between the structure and the interfacial acid-base properties of 11-mercaptoundecanoic-acid (MUA) self-assembled monolayers formed by three different methodologies is studied by means of electrochemical and IRRAS techniques.

3.2. Material and methods

Chemical reagents*.* 11-mercaptoundecanoic acid (MUA), Triton X-100, potassium ferrocyanide ($Fe(CN)_6^{4-}$), potassium ferricyanide ($Fe(CN)_6^{3-}$), and KOH were purchased from Aldrich-Sigma (purity ≥ 99%). The rest of the reagents (ethanol and HCl) were from Merck analytical grade. All solutions were prepared with deionized ultrapure water produced by Millipore system.

Methods*.* A conventional three electrode cell comprising a platinum coil as the counter electrode, a 50 mM KCl calomel electrode as the reference electrode and an Au(111) single crystal as the working electrode were used. Au(111) single crystal and (111) textured surfaces (Gold Arrandee^{TM}) were cleaned and modified with MUA as indicated in the protocols described in the Chapter 2 (Sections 2.3.1 and 2.3.2). The adsorption time assayed in the lyotropic medium was 15 minutes.

In the pH titration experiments, samples were immersed either in 5 mM HCl or KOH aqueous solutions at the adjusted pH, and allowed to equilibrate during 20 minutes (i.e. non-reactive spreading protocol).[26] Then, the modified substrates were dried with nitrogen for further characterization by FT-IRRAS. Titrations were performed from alkaline to acidic direction, and vice versa, by changing the pH solution upon addition of KOH or HCl. At least three freshly prepared samples were titrated for each deposition protocol by FT-IRRAS methodology.

Electrochemical and FT-IRRAS characterization of the samples was carried out accordingly to the specifications and working conditions included, unless otherwise stated, in the Chapter 2 (*Sections 2.4.1. and 2.4.2.1*). In the

particular case of FT-IRRAS analysis, the relative surface coverage of –COOH ($1-\theta$) and –COO$^-$ (θ) was determined from the integrated area of the νC=O vibrational bands corresponding to the stretching modes characteristic of carboxylic (1700-1750 cm^{-1}) and carboxylate (1400-1445 cm^{-1}) groups.

3.3. Results and discussion

The knowledge of the interfacial properties of ω-terminated SAMs is very important for the application of these layers as platforms to build more complex molecular architectures. As the final properties are entirely dependent on the preparation strategy, in this chapter, a comparison of the MUA-SAMs formed by different methods is carried out.

The first strategy is the classical spontaneous method that is performed by contacting the clean gold electrode with an ethanolic solution of the mercaptoderivative molecule. It is well known that this methodology is good for obtaining well organized SAMs upon long modification times (> 24 h). Under these conditions, it is believed that a dense and well organized monolayer of MUA is obtained.
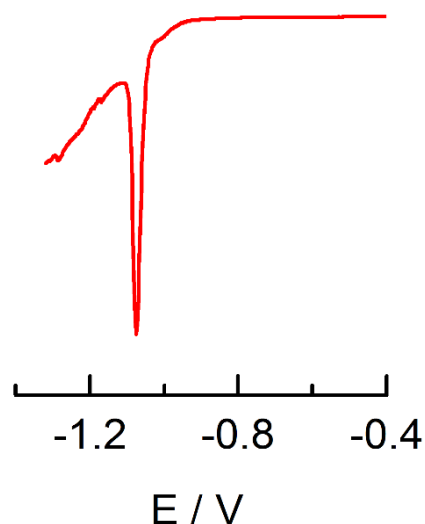
Figure 1. Cyclic voltammogram for the reductive desorption process of MUA-SAM in KOH 0.1 M formed by immersion of an Au(111) single crystal surface into a 1 mM MUA ethanol solution during 24 hours. Scan rate: 20 mV/s.

To get some information about the quality of the SAM, cyclic voltammetry of the reductive desorption (RD) process is carried out. Figure 1 shows the RD profile obtained in KOH 0.1 M for the MUA-SAM formed after 24 h of modification time in an ethanolic solution. Starting at -0.4 V and scanning to cathodic potentials, a low and constant current density is obtained in a wide potential region (~400 mV) until suddenly a very sharp peak at -1.07 V appears. This peak corresponds to the surface desorption of the monolayer by breaking the S-Au bonds as indicated in the following reaction:

$$R\text{-}S\text{-}Au + 1\,e \rightarrow R\text{-}S^- + Au^o \qquad (1)$$

The half-width measured for this peak (FWHM) is of 22 mV, suggesting a cooperative RD process due to long-range attractive interactions between the

126

molecules in the layer. The charge density involved in the RD process, determined by the area integrated under the reduction peak, is near 71 $\mu C/cm^2$ which gives rise to a thiol surface coverage of $7.35 \cdot 10^{-10}$ mol/cm^2, in good agreement with a ($\sqrt{3}x\sqrt{3}$) R30° overlayer structure of molecules organized in an up-right configuration on Au (111).[27]

The second method chosen for the formation of the MUA-SAM also consists of the spontaneous adsorption of the molecules on the metal substrate but, in this case, a new strategy has been employed. We have used the deposition from a lyotropic medium where the mercaptoderivative molecules are inserted. Under these experimental conditions a lower modification time is used to evidence the appropriateness of this micellar medium to prepare well-organized SAMs. In fact, by examining the formed layer by the RD process, a sharp peak, quite similar to that recorded for the SAM prepared from ethanolic solution is obtained (Figure 2). If the potential for the reduction peak is taken as a way to measure SAM energetics, it can be seen that, both layers, are reduced at the same potential and, therefore, their structural organization must be rather similar. Moreover, the charge density involved is both cases is almost coincident, which means that the compactness must be also closely similar.
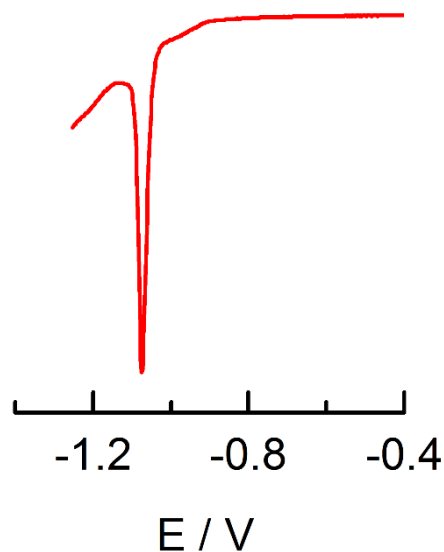
Figure 2. Cyclic voltammogram for the reductive desorption process of MUA-SAM in KOH 0.1 M formed by immersion of an Au(111) single crystal surface into a 1 mM MUA crystalline lyotropic mixture during 15 minutes. Scan rate: 20 mV/s.

Finally, a methodology based on potential control for the SAM formation has been developed. To perform this experiment it is necessary to know the characteristics of the electrochemical adsorption behavior of MUA on the gold electrode. Figure 3 shows the cyclic voltammogram recorded for a clean Au(111) substrate immerse into a solution containing 1 mM MUA in KOH 0.1 M. The electrochemical response is obtained by starting at a potential E_o, chosen as a sufficiently negative one that the thiol derivatives are not expected to bind to the gold surface. After stabilization of the electrode current intensity, the potential is scanned in the positive direction (at 20 mV/s) up to reach the potential E_m, where it was reversed (Figure 3, Inset).
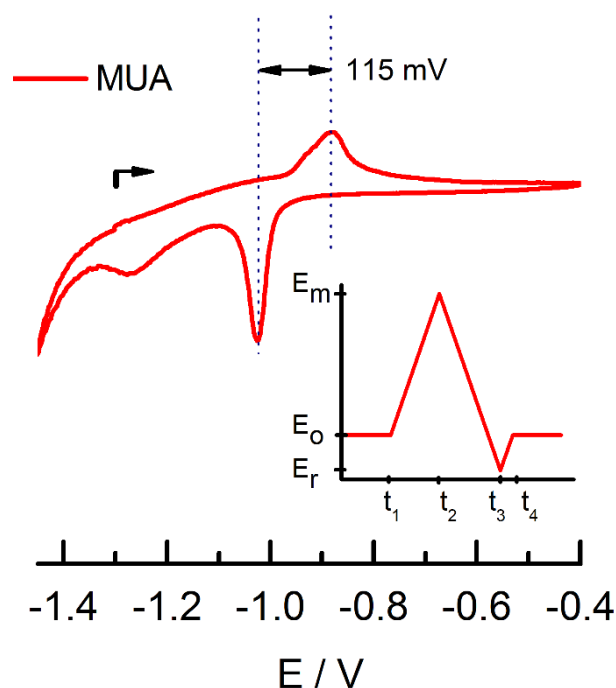
Figure 3. Cyclic voltammetry of an Au(111) single-crystal electrode in a 1 mM MUA in 0.1 M KOH solutions; scan rate = 20 mV/s. Inset: scan program. The arrows in the voltammetric curves indicate the position of E_o and the scan direction.

The characteristic features of this voltammetric curve are the appearance of an oxidation and a reduction peak that corresponds to the adsorption of the molecules through the formation of an S-Au bond and its subsequent desorption by bond breakage, respectively. The adsorption potential of MUA is -0.87 V. As the anodic formation reaction is taking place in alkaline medium, the terminal carboxylic group of MUA contributes to the destabilization of the layer. In fact, the charge density involved under potentially-driven adsorption is of 45 μC/cm^2, that is lower than that necessary for the formation of a complete monolayer of standing-up molecules on the surface.[28] It is

interesting to note that even if the scan rate is lowered to 2 mV/s (the lower scan rate used in our experimental conditions), the charge density corresponding to a complete monolayer is not attained. The reason for this can be found in the presence of a second functional endgroup in the molecule that should compete with the thiolate head-group for the interaction with the surface.[14] Moreover, the occurrence of certain anodic current at potentials positive to the adsorption peak can be explained by the reorganization of molecules on the surface from a lying-down to a standing-up orientation giving place to some adsorption events and, in this way, a higher charge density in the subsequent reductive peak ($\sim$ 65 μC/cm^2) in comparison to the oxidative one.

The way to build up the molecular layer by using a potentiostatic method consisted of using the potential program included in Figure 4. Firstly, the potential is stepped from a negative value compared to the anodic peak (E_o = -1.35 V; t = 120 s), where no adsorption of molecules occurs, to an anodic value in the region of S-Au formation (E_{form} = -0.4 V; t = 600 s) where it is maintained for a time that it is considered enough for a stable layer formation. After this time (black arrow in the Inset of Figure 4), the electrode is removed from the solution and transferred to an electrochemical cell containing only KOH 0.1 M. After equilibration at the initial potential (-0.4 V), the potential is scanned in the negative direction. Figure 4 shows the typical voltammetric response obtained under these conditions. The analysis of the parameters of the CV profiles obtained by this methodology evidences that the SAM formed under these experimental conditions is of apparently similar

quality to those formed either from ethanolic solutions, at much longer times, or from a lyotropic medium, only upon 15 min of modification time.
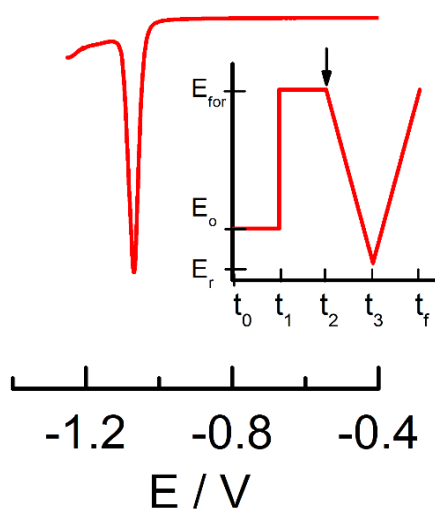
Figure 4. Voltammetric curve for the reductive desorption of a MUA-SAM formed by using the potential program shown in the inset, in the presence of 1 mM MUA in 0.1 M KOH solution. The arrow points the transfer to the solution without MUA; scan rate = 20 mV/s.

A deeper understanding of the structural details of these films was obtained by IRRAS measurements. Figure 5 displays the spectra obtained for the MUA SAMs prepared by each deposition method. In the high wavenumber region, the bands at 2918 and 2850 cm^{-1} are attributed to the C-H stretching asymmetric (ν_{as}) and symmetric (ν_s) vibrational modes of the -CH_2 groups, respectively, belonging to hydrocarbon chains arranged into crystalline-like structure. Then, it can be assumed that the monolayers formed from a micellar environment and under electrochemical control possess

predominantly an all-trans configuration of the alkyl chain with few gauche defects.[29, 30] Interestingly, a small shift to higher values of the v_{as} peak was observed for the MUA SAM formed from ethanol, suggesting a lower organization of these 2D-arrays. This fact is ascribed to the influence of the attractive interactions between the ethanol solvent molecules and the carboxyl groups on the assembly mechanism.

In the low frequency region, the spectra show the typical bands for the carboxyl groups region (1300-1800 cm^{-1}). Bands at 1741 and 1717 cm^{-1} are assigned to the non-hydrogen and hydrogen bonding interactions of the carboxylic groups, respectively,[31, 32] whereas the band at 1468 cm^{-1} is linked to CH$_2$ scissors deformation. The other low frequency features are ascribed to asymmetric (1440 cm^{-1}) and symmetric (1421cm^{-1}) stretching modes of carboxylates groups (COO$^-$).[33]
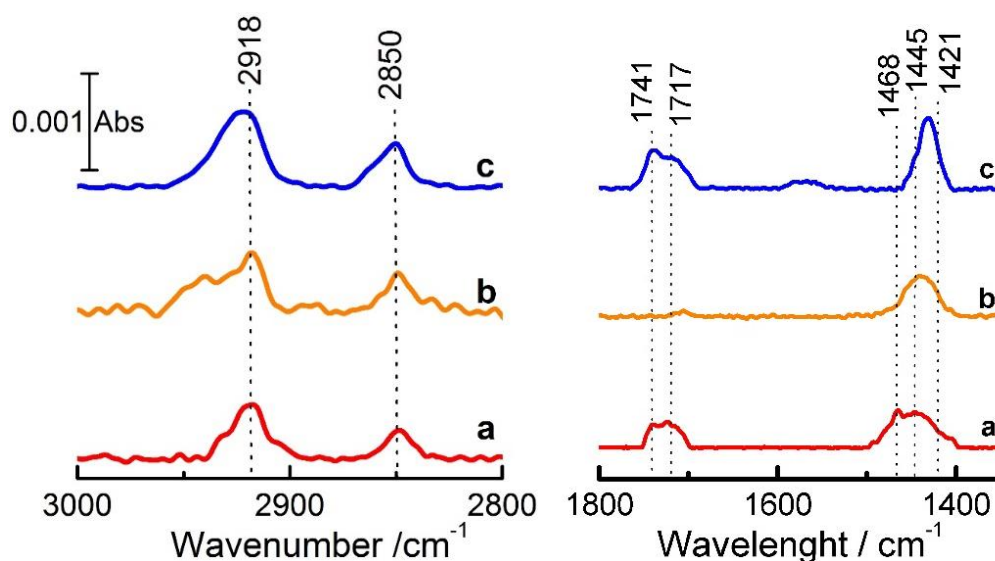
Figure 5. IRRAS spectra at the high and low wavenumber regions of MUA-SAMs formed from a) lyotropic micellar medium, t_{mod} = 15min; b) potentiodynamic method, t_{mod} = 10min at E_{for} = -0.4V, and c) ethanol solution, t_{mod} = 24h.

It is interesting to highlight that the bands associated with the –COOH group do not appear in the low frequency spectra for the SAM deposited under potential control, owing to the basic conditions used in this experiment (KOH 0.1 M aqueous solutions). The well-organized negatively charged carboxylates groups of these assemblies may be associated to: i) the Van der Waals forces between the neighbouring alkyl chain and ii) the possible extra-stabilisation contribution of a two-dimensional ionic crystal layer compose by carboxylates groups and the counterions of the alkaline solution.[34] On the other hand, the MUA-SAMs spontaneously formed from ethanol or micellar media, show a high proportion of -COOH groups associated by H-bonding interactions.

A set of IRRAS measurements are performed to elucidate the relationship between the structure of these surface-confined molecules and their deprotonation/protonation interfacial behaviour. These measurements have been carried out by contacting freshly prepared MUA-SAMs with aqueous buffer solutions of different pH during enough time to equilibrate the carboxy-terminal groups of the SAM. Then, substrates were removed from the solutions and dried with a N_2 flow. Figure 6 shows a series of IR spectra at the low wavenumber region in the pH interval from 2 to 11. A striking dependence of the stretching modes belonging to -COOH and $-COO^-$ groups with the increase of the pH electrolyte solution is observed. There is a continuous decrease of the C=O absorption at 1741 and 1710 cm^{-1} (disappearance of COOH groups), that can be correlated with the concomitant increase of one of the absorption bands assigned to the carboxylate groups. This behaviour perfectly agrees with changes in deprotonation/protonation at the monolayer/electrolyte interface.

A first comparison of the spectra allows stablishing an important difference to be commented. At the highest pH assayed (pH = 11), the SAM formed from ethanolic solutions shows the IR bands that would correspond to free and H-bonded carboxylic acids. Taking into account that the pK_a of carboxylic groups in homogeneous solution is of around 4, the existence of these signals in the spectra are inconsistent with an expected fully deprotonated state of the SAM endgroups.

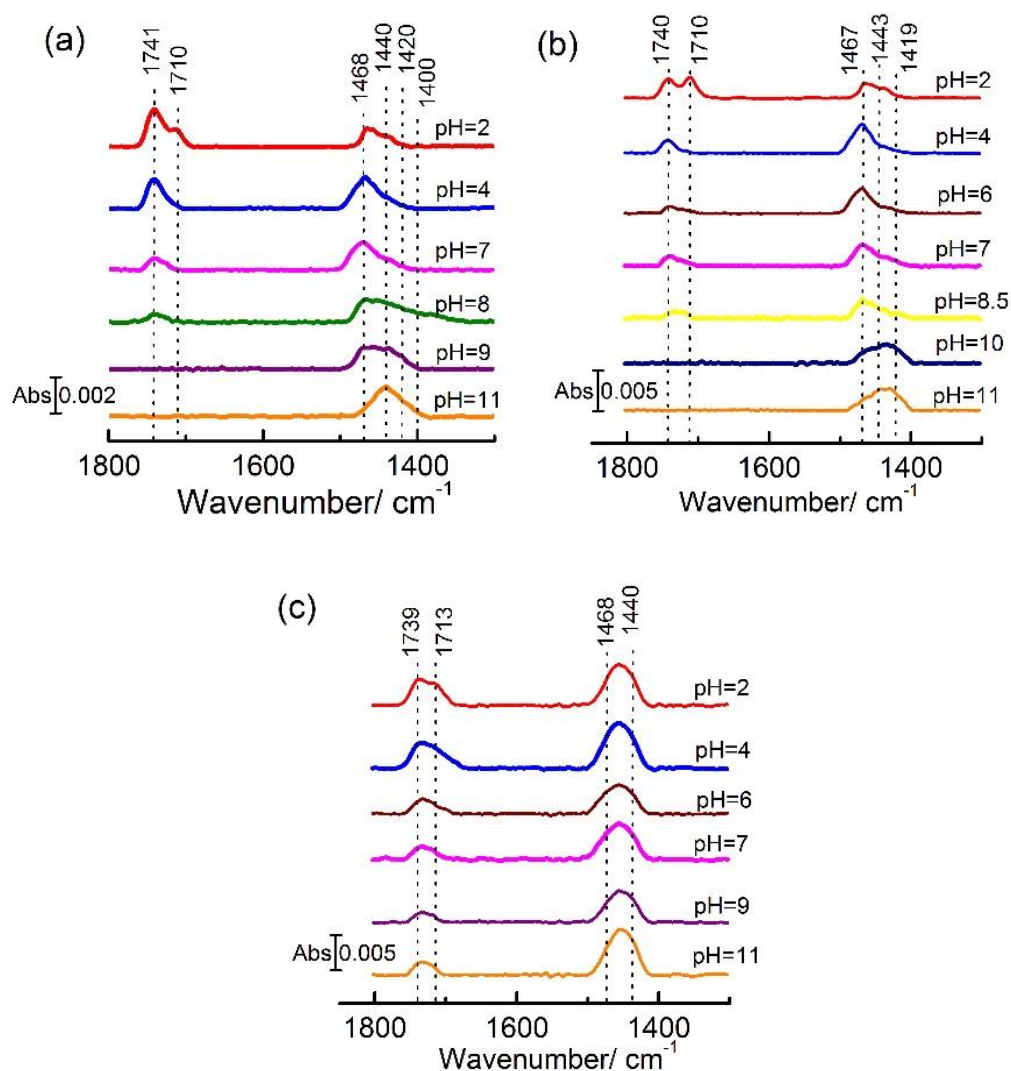**Figure 6.** IRRAS spectra of MUA-SAMs recorded after equilibration of the layers with a buffer solution at different pHs. The spectra series correspond to SAMs formed a) lyotropic micellar medium, t_{mod} = 15min; b) potentiodynamic method, E = -0.4V; c) ethanol solution, t_{mod} = 24h.

However, literature reports on the structure of carboxylic-terminated alkanethiol SAMs formed from ethanol have shown contradictory results. One

of the pioneering works dealing with these SAMs showed that a terminal carboxylic acid had not a big impact on the structural ordering of the alkyl chains,[33] but others stated that the SAMs formed from ethanolic solutions were unstructured.[32, 35]

The addition of acid to the modification solution has been proposed as a strategy to reduce electrostatic interactions between carboxylate groups that might be formed for the presence of trace amounts of cations in solution. In this way, the acid will restore the carboxyl group into the acidic form, which will facilitate the formation of densely packed and ordered assemblies, [32] and reduces the risk of bilayer formation through the association of -COOH dimers.[36, 37] However, under conditions of acid additions, IR absorption peaks corresponding to ester derivatives have been found.[32] It has been since proposed that the carboxylic acid reacts with ethanol in the presence of acid to form an ethyl ester. More recently, it has also been found that even in the absence of acid in the ethanolic solution, the -COOH group can be converted into the ethyl ester group.[38] The fact is that the peak for C=O stretching for a non-hydrogen-bonded -COOH group and that for the $-COOCH_3$ coincides in frequency (1741 cm^{-1}). For this reason, is very difficult to assess the origin of the peaks in the spectra of the MUA-SAM, formed from an ethanolic solution, at pH = 11. It is more plausible that the peak corresponds to the ethyl ester than to carboxylic acid species originated at this very high pH.

To analyse the IRRAS results in terms of changes in the protonation state of the carboxylic groups, we have used a deconvolution procedure of the bands associated to the $-COOH$ and $-COO^-$ groups, to determine the amount of such species at a given pH. The results obtained have been transformed

into the ratio of carboxylate species, θ. In Figure 7, the θ values are plotted versus pH for the SAMs deposited by the three different procedures, and the apparent $pK_{1/2}$ determined as the midpoints of the sigmoidal curves are gathered in Table 1. As can be seen, the titration curve corresponding to the MUA-SAM formed from ethanol shows a gradual decrease from alkaline to acid medium without a clear transition that is considered to occurs at an apparent $pK_{1/2}$ of approximately 5.7 (i.e. close to the solution pK_a value for alkanoic acids).
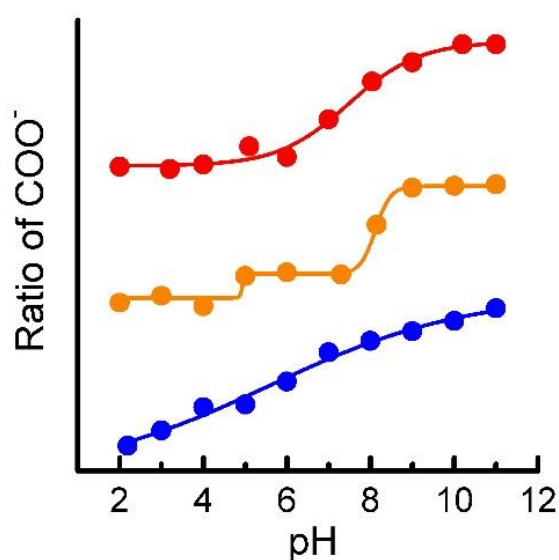

Figure 7. IRRAS titration curves of MUA-SAMs formed from: (● −) lyotropic micellar medium, t_{mod} = 15min; (● −) potentiodynamic method, E = -0.4 V; (● −) ethanol solution, t_{mod} = 24h.

Table 1. $pK_{1/2}^{app}$ values of MUA-SAMs determined from the IR titration curves.

Preparation method	$pK_{1/2}^{app}$	
Lyotropic medium; t_{mod} = 15min	-	7.7
Ethanolic solution; t_{mod} = 24h	-	5.7
Electrochemical control: E = -0.4V	4.9	8.1

In the case of the MUA-SAM formed from a lyotropic medium, the inflection point observed appears at pH 7.7. This value agrees with many studies in literature that explain the increase of the apparent surface pK_a of ω-carboxy-terminated SAMs with respect to the solution pK as being due to the stabilization of the protonated state by hydrogen bond formation in the adsorbed state and the increase of the SAM structural order by van der Waals intermolecular interactions between alkyl chains.[21, 39-50] However, the extended literature in this topic concludes that the apparent pK values obtained are highly dependent on the technique used for its determination as well as experimental conditions (*e.g. solution ionic strength*). Another important factor to consider is the SAM fabrication method, being most of the results reported on the spontaneously formed monolayers from ethanolic solutions.

On the other hand, MUA-SAMs formed under electrochemical control, have shown a more complex behavior as two inflection points are distinguished at pH 4.9 and 8.1, respectively. In this case, it is important to highlight two main different aspects: (i) the SAM is formed under electrochemical control and, therefore, is forced to reach a specific potential-dependent final estate, and (ii) the SAM is prepared from aqueous alkaline

138

solution where –COO⁻ groups should accommodate in the surface of the *as prepared* layer. In this sense, it is not expected that hydrogen bonding should proceed in the same way as it does for that layers built from preformed -COOH groups that can interact trough hydrogen bonds in the first moments of assembly contributing to stabilize the complete layer structure. Moreover, it has been suggested that a balance among differently associated –COO⁻ groups with the K⁺ counterion layer at the SAM/electrolyte interface, probably facilitates the titration of two different domains of molecules with different acid-basic chemical properties. Gershevitz et al.[20] have reported the direct observation of two different pK_a values by FTIR-ATR measurements on siloxane-COOH self-assembled monolayers. They proposed that the monomeric carboxylic groups domains are the least stable domains as the pD increases contributing to the first pK_a values around 4.9, while the titration of bridges species (dimeric and oligomeric carboxylic groups) determine the higher pK value of 9.3.

3.4.   Conclusions

- The assembly and characterization of MUA-SAMs on Au (111) surfaces has been accomplished by three different deposition methods.

- The structure of the SAMs formed are compatible with a (√3x√3) R30° overlayer structure of molecules organized in an up-right configuration.

139

- FT-IRRAS characterization reveals that the assemblies built from a micellar environment or under potential control arrange into "crystalline-like" structures of alkyl chains packed in 2D-arrays, where as those deposited ethanol display a lower degree of ordering.

- The changes in the acid-basic interfacial properties of the studied MUA SAMs are mainly attributed to differences in the organization of the alkyl chains structure and differently coupled domains of carboxylates groups with the counterions layer at the SAM/electrolyte interface. In the particular case of the monolayers formed from ethanol, it cannot be discarded the formation of ethyl ester terminal groups which may partially affects the acid/base interfacial properties of the SAM.

3.5.   References

1.   Love, J. C.; Estroff, L. A.; Kriebel, J. K.; Nuzzo, R. G.; Whitesides, G. M., Self-Assembled Monolayers of Thiolates on Metals as a Form of Nanotechnology. *Chem. Rev.* **2005,** *105* (4), 1103-1169.

2.   Shon, Y. S.; Lee, S.; Colorado, R.; Perry, S. S.; Lee, T. R., Spiroalkanedithiol-based SAMs Reveal Unique Insight into the Wettabilities and Frictional Properties of Organic Thin Films. *J. Am. Chem. Soc.* **2000,** *122* (31), 7556-7563.

3.   Lee, D. H.; Kim, D.; Oh, T.; Cho, M., Phase State Effect on Adhesion Behavior of Self-Assembled Monolayers. *Langmuir* **2004,** *20* (19), 8124-8130.

4.   Dechtrirat, D.; Gajovic-Eichelmann, N.; Bier, F. F.; Scheller, F. W., Hybrid Material for Protein Sensing Based on Electrosynthesized MIP on a Mannose Terminated SelfAssembled Monolayer. *Adv. Funct. Mater.* **2014,** *24* (15), 2233-2239.

5.   Crudden, C. M.; Horton, J. H.; Narouz, M. R.; Li, Z. J.; Smith, C. A.; Munro, K.; Baddeley, C. J.; Larrea, C. R.; Drevniok, B.; Thanabalasingam, B.; McLean, A. B.; Zenkina, O. V.; Ebralidze, II; She, Z.; Kraatz, H. B.; Mosey, N. J.; Saunders, L. N.; Yagi, A., Simple Direct Formation of Self-Assembled N-Heterocyclic Carbene Monolayers on Gold and their Application in Biosensing. *Nature Commun.* **2016,** *7*.

6.   Yang, W. J.; Li, T. Q.; Zhou, H. H.; Huang, Z.; Fu, C. P.; Chen, L.; Li, M. B.; Kuang, Y. F., Electrochemical and Anti-Corrosion Properties of Octadecanethiol and Benzotriazole Binary Self-Assembled Monolayers on Copper. *Electrochim. Acta* **2016,** *220*, 245-251.

7.   Samanta, D.; Sarkar, A., Immobilization of Bio-Macromolecules on Self-Assembled Monolayers: Methods and Sensor Applications. *Chem. Soc. Rev.* **2011,** *40* (5), 2567-2592.

8.   Gooding, J. J.; Ciampi, S., The Molecular Level Modification of Surfaces: from Self-Assembled Monolayers to Complex Molecular Assemblies. *Chem. Soc. Rev.* **2011,** *40* (5), 2704-2718.

9.   Kafer, D.; Witte, G.; Cyganik, P.; Terfort, A.; Woll, C., A Comprehensive Study of Self-Assembled Monolayers of Anthracenethiol on Gold: Solvent Effects, Structure, and Stability. *J. Am. Chem. Soc.* **2006,** *128* (5), 1723-1732.

10.   Shen, C. H.; Lin, J. C., Solvent and Concentration Effects on the Surface Characteristics and Platelet Compatibility of Zwitterionic Sulfobetaine-Terminated Self-Assembled Monolayers. *Colloid Surface B* **2013,** *101*, 376-383.

11.   Bain, C. D.; Troughton, E. B.; Tao, Y. T.; Evall, J.; Whitesides, G. M.; Nuzzo, R. G., Formation of Monolayer Films by the Spontaneous Assembly of Organic Thiols from Solution onto Gold. *J. Am. Chem. Soc.* **1989,** *111* (1), 321-335.

12.   Garcia Raya, D.; Silien, C.; Blazquez, M.; Pineda, T.; Madueno, R., Electrochemical and AFM Study of the 2D-Assembly of Colloidal Gold Nanoparticles on Dithiol SAMs Tuned by Ionic Strength. *Journal of Physical Chemistry C* **2014,** *118* (26), 14617-14628.

13.   Sur, U. K.; Lakshminarayanan, V., A Study of the Hydrophobic Properties of Alkanethiol Self-Assembled Monolayers Prepared in Different Solvents. *J. Electroanal. Chem.* **2004,** *565* (2), 343-350.

14.   Fragoso, A.; Laboria, N.; Latta, D.; O'Sullivan, C. K., Electron Permeable Self-Assembled Monolayers of Dithiolated Aromatic Scaffolds on Gold for Biosensor Applications. *Analytical Chemistry* **2008,** *80* (7), 2556-2563.

15.   Gonzalez-Granados, Z.; Sanchez-Obrero, G.; Madueno, R.; Sevilla, J. M.; Blazquez, M.; Pineda, T., Formation of Mixed Mono layers from 11-Mercaptoundecanoic Acid and Octanethiol on Au(111) Single Crystal Electrode under Electrochemical Control. *J. Phys. Chem. C* **2013,** *117* (46), 24307-24316.

16.   Arnold, R.; Azzam, W.; Terfort, A.; Woell, C., Preparation, Modification, and Crystallinity of Aliphatic and Aromatic Carboxylic Acid Terminated Self-Assembled Monolayers. *Langmuir* **2002,** *18* (10), 3980-3992.

17.   Collman, J. P.; Devaraj, N. K.; Eberspacher, T. P. A.; Chidsey, C. E. D., Mixed Azide-Terminated Monolayers: A Platform for Modifying Electrode Surfaces. *Langmuir* **2006,** *22* (6), 2457-2464.

18.   Adaligil, E.; Slowinski, K., Electron Tunneling through Monolayers of Alkanethiols Self-Assembled on a Hanging Mercury Drop Electrode in the Presence of Aliphatic Alcohols. *J. Electroanal. Chem.* **2010,** *649* (1-2), 142-148.

19.   Cheng, Q.; BrajterToth, A., Permselectivity Sensitivity, and Amperometric pH Sensing at Thioctic Acid Monolayer Microelectrodes. *Anal. Chem.* **1996,** *68* (23), 4180-4185.

20.   Gershevitz, O.; Sukenik, C. N., In situ FTIR-ATR Analysis and Titration of Carboxylic Acid-Terminated SAMs. *J. Am. Chem. Soc.* **2004,** *126* (2), 482-483.

21.   Kakiuchi, T.; Iida, M.; Imabayashi, S.; Niki, K., Double-Layer-Capacitance Titration of Self-Assembled Monolayers of Omega-Functionalized Alkanethiols on Au(111) Surface. *Langmuir* **2000,** *16* (12), 5397-5401.

22.   Schweiss, R.; Werner, C.; Knoll, W., Impedance Spectroscopy Studies of Interfacial Acid-Base Reactions of Self-Assembled Monolayers. *J. Electroanal. Chem.* **2003,** *540*, 145-151.

23.   Wallwork, M. L.; Smith, D. A.; Zhang, J.; Kirkham, J.; Robinson, C., Complex Chemical Force Titration Behavior of Amine-Terminated Self-Assembled Monolayers. *Langmuir* **2001,** *17* (4), 1126-1131.

24.   He, H. X.; Huang, W.; Zhang, H.; Li, Q. G.; Li, S. F. Y.; Liu, Z. F., Demonstration of High-Resolution Capability of Chemical Force Titration via Study of Acid/Base Properties of a Patterned Self-Assembled Monolayer. *Langmuir* **2000,** *16* (2), 517-521.

25.   Zhang, H.; He, H. X.; Mu, T.; Liu, Z. F., Force Titration of Amino Group-Terminated Self-Assembled Monolayers of 4-Aminothiophenol on Gold Using Chemical Force Microscopy. *Thin Solid Films* **1998,** *327*, 778-780.

26.   Creager, S. E.; Clarke, J., Contact-Angle Titrations of Mixed ω-Mercaptoalkanoic Acid/Alkanethiol Monolayers on Gold. Reactive vs Nonreactive Spreading, and Chain Length Effects on Surface pKa Values. *Langmuir* **1994,** *10* (10), 3675-83.

27.   Vericat, C.; Vela, M. E.; Benitez, G.; Carro, P.; Salvarezza, R. C., Self-Assembled Monolayers of Thiols and Dithiols on Gold: New Challenges for a Well-Known System. *Chem. Soc. Rev.* **2010,** *39* (5), 1805-1834.

28.   Loglio, F.; Schweizer, M.; Kolb, D. M., In situ Characterization of Self-Assembled Butanethiol Monolayers on Au(100) Electrodes. *Langmuir* **2003,** *19* (3), 830-834.

29.   Cohen, R.; Mazuz, Y.; Tikhonov, M.; Sukenik, C. N., Carboxylic Acid Decorated Self-Assembled Mono layer Films: New Acid Synthesis Chemistry and Reaction Chemistry Including Bridged Diacyl Peroxide Preparation. *Langmuir* **2015,** *31* (10), 3049-3058.

30.   Ruck-Braun, K.; Petersen, M. A.; Michalik, F.; Hebert, A.; Przyrembel, D.; Weber, C.; Ahmed, S. A.; Kowarik, S.; Weinelt, M., Formation of Carboxy- and Amide-Terminated Alkyl Monolayers on Silicon(111) Investigated by ATR-FTIR, XPS, and X-ray Scattering: Construction of Photoswitchable Surfaces. *Langmuir* **2013,** *29* (37), 11758-11769.

31.   Saavedra, H. M.; Thompson, C. M.; Hohman, J. N.; Crespi, V. H.; Weiss, P. S., Reversible Lability by in Situ Reaction of Self-Assembled Monolayers. *J. Am. Chem. Soc.* **2009,** *131* (6), 2252-2259.
32.   Arnold, R.; Azzam, W.; Terfort, A.; Woll, C., Preparation, Modification, and Crystallinity of Aliphatic and Aromatic Carboxylic Acid Terminated Self-Assembled Monolayers. *Langmuir* **2002,** *18* (10), 3980-3992.

33.   Nuzzo, R. G.; Dubois, L. H.; Allara, D. L., Fundamental Studies of Microscopic Wetting on Organic Surfaces. 1. Formation and Structural Characterization of a Self-Consistent Series of Polyfunctional Organic Monolayers. *J. Am. Chem. Soc.* **1990,** *112* (2), 558-69.

34.   Kitagawa, Y.; Hobara, D.; Yamamoto, M.; Kakiuchi, T., Counterion Binding Induces Attractive Interactions between Negatively-Charged Self-Assembled Monolayer of 3-Mercaptopropionic Acid on Au(111) in Reductive Desorption. *J. Solid State Electrochem.* **2008,** *12* (4), 461-469.

35.   Dannenberger, O.; Weiss, K.; Himmel, H. J.; Jager, B.; Buck, M.; Woll, C., An Orientation Analysis of Differently Endgroup-Functionalised Alkanethiols Adsorbed on Au Substrates. *Thin Solid Films* **1997,** *307* (1-2), 183-191.

36.   Wang, H.; Chen, S. F.; Li, L. Y.; Jiang, S. Y., Improved Method for the Preparation of Carboxylic Acid and Amine Terminated Self-Assembled Monolayers of Alkanethiolates. *Langmuir* **2005,** *21* (7), 2633-2636.

37.   Willey, T. M.; Vance, A. L.; van Buuren, T.; Bostedt, C.; Nelson, A. J.; Terminello, L. J.; Fadley, C. S., Chemically Transformable Configurations of Mercaptohexadecanoic Acid Self-Assembled Monolayers Adsorbed on Au(111). *Langmuir* **2004,** *20* (7), 2746-2752.

38.   Myrskog, A.; Anderson, H.; Aastrup, T.; Ingemarsson, B.; Liedberg, B., Esterification of Self-Assembled Carboxylic-Acid-Terminated Thiol Monolayers in Acid Environment: A Time-Dependent Study. *Langmuir* **2010,** *26* (2), 821-829.

39.   Ramirez, P.; Andreu, R.; Cuesta, A.; Calzado, C. J.; Calvente, J. J., Determination of the Potential of Zero Charge of Au(111) Modified with Thiol Monolayers. *Anal. Chem.* **2007,** *79* (17), 6473-6479.

40.   Burgess, I.; Seivewright, B.; Lennox, R. B., Electric Field Driven Protonation/Deprotonation of Self-Assembled Monolayers of Acid-Terminated Thiols. *Langmuir* **2006,** *22* (9), 4420-4428.

41.   Wang, J.; Frostman, L. M.; Ward, M. D., Self-Assembled Thiol Monolayers with Carboxylic Acid Functionality: Measuring pH-Dependent Phase Transitions with the Quartz Crystal Microbalance. *J. Phys. Chem.* **1992,** *96* (13), 5224-8.

42.   Anjum, S.; Qi, W.; Gao, W.; Zhao, J.; Hanif, S.; Aziz Ur, R.; Xu, G., Fabrication of Biomembrane-Like Films on Carbon Electrodes using Alkanethiol and Diazonium Salt and Their Application for Direct Electrochemistry of Myoglobin. *Biosensors & Bioelectronics* **2015,** *65*, 159-165.

43.   Xing, Y. F.; Li, S. F. Y.; Lau, A. K. H.; O'Shea, S. J., Electrochemical Impedance Spectroscopy Study of Mixed Thiol Monolayers on Gold. *J. Electroanal. Chem.* **2005,** *583* (1), 124-132.

44.   Zhao, J. W.; Luo, L. Q.; Yang, X. R.; Wang, E. K.; Dong, S. J., Determination of Surface pK(a) of SAM using an Electrochemical Titration Method. *Electroanalysis* **1999,** *11* (15), 1108-1111.

45.   Smith, D. A.; Wallwork, M. L.; Zhang, J.; Kirkham, J.; Robinson, C.; Marsh, A.; Wong, M., The Effect of Electrolyte Concentration on the Chemical Force Titration Behavior of Omega-Functionalized SAMs: Evidence for the Formation of Strong Ionic Hydrogen Bonds. *J. Phys. Chem. B* **2000,** *104* (37), 8862-8870.

46.   Hamoudi, H.; Esaulov, V. A., Self-Assembly of α,ω-Dithiols on Surfaces and Metal Dithiol Heterostructures. *Ann. Phys. (Berlin, Ger.)* **2016,** *528* (3-4), 242-263.

47.   Smalley, J. F.; Chalfant, K.; Feldberg, S. W.; Nahir, T. M.; Bowden, E. F., An Indirect Laser-Induced Temperature Jump Determination of the Surface pK(a) of 11-Mercaptoundecanoic Acid Monolayers Self-Assembled on Gold. *J Phys. Chem. B* **1999,** *103* (10), 1676-1685.

48.   Smalley, J. F., Indirect Laser-Induced Temperature Jump Study of the Chain-Length Dependence of the pK(a)'s of Omega-Mercaptoalkanoic Acid Monolayers Self-Assembled on Gold. *Langmuir* **2003,** *19* (22), 9284-9289.

49.   Ramirez, P.; Granero, A.; Andreu, R.; Cuesta, A.; Mulder, W. H.; Jose Calvente, J., Potential Of Zero Charge as a Sensitive Probe for the Titration of Ionizable Self-Assembled Monolayers. *Electrochem. Commun.* **2008,** *10* (10), 1548-1550.

50.   Luque, A. M.; Mulder, W. H.; Jose Calvente, J.; Cuesta, A.; Andreu, R., Proton Transfer Voltammetry at Electrodes Modified with Acid Thiol Monolayers. *Anal. Chem.* **2012,** *84* (13), 5778-5786.

CHAPTER 4

Mixed SAMs of MUA/DT Formed in Lyotropic Medium

4. Mixed SAMs of MUA/DT formed in lyotropic medium

4.1. Introduction

The control of the spatial confinement of individual functional molecules and nano-objects on surfaces is a highlight topic in studying single-molecule properties, such as reactivity and kinetics, and provides new insights into the design of molecular switches and motors, opening new applications in the field of biochemical sensors, molecular electronics, catalysis and surface material chemistry.[1-7]

Of particular importance is the building up of multifunctional architectures on solid substrates to make their active functional groups

accessible and to create molecular recognition sites that can act either as receptors or favoring the specific adsorption of different kind of biomolecules, such as proteins. Among the different methodologies proposed to achieve the assembly of functional molecules on solid substrates, the chemisorption of self-assembled monolayer (SAMs) on gold has been widely studied.[8] Particularly, the strategy of building up mixed monolayers by the dilution of ω-functionalized alkanethiols in a homogeneous two-dimensional array is a way for tailoring the surface properties of these SAMs (*Chapter 1 - Section 1.2.4*). However, in many cases a true mixing of the components is not reached at the molecular level and, phase segregation in single-component domains is observed.[9-11] To achieve this goal, the control of determined factors affecting the balance of the intermolecular interactions during the self-assembly process, such as different molecular chain length, nature of the functional groups and solvent, is crucial for obtaining binary SAMs with the expected mixing properties.

Developing of these strategies requires understanding of the intrinsic phase behavior of the mixed thiol monolayers. In this sense, Folkers et al., by using the Bragg-Williams model, described the behavior of binary alkanethiolate SAMs at gold surfaces.[12] They concluded that only one phase consisting of a homogeneous mixture of both alkanethiolates would exist under equilibrium conditions, being the strength of the interactions between neighboring molecules the factor that determines the actual composition of the phase. Consequently, it can be inferred that it would be possible to obtain fully miscible and crystalline intermixed domains of two-component SAMs favoring hetero-molecular interactions.

Electrochemical and infrared spectroscopy techniques have emerged as useful tools to elucidate the phase behavior in multicomponent SAMs systems from a macroscopic point of view.[11,13,14] Although macroscopic in nature, these techniques afford to get also valuable information related with the feasible nanoscopic scheme of the monolayer organization. In this sense, it has been reported that a mixed monolayer with domains containing 50 molecules exhibits two-dimensional bulk properties[15] which has been used to infer a complete mixing in these quasi-two dimensional systems.[11,14]

Most of the studies carried out to explore phase segregation of binary SAMs formed from molecules of similar chain length and intermolecular interactions have been based on SAMs built up from ethanolic solutions.[14,16] More recently, the preparation of alkanethiolate SAMs on gold from micellar solutions has been reported as an environmentally friendly process that yields almost defect-free structures with greater packing density than those for the SAMs formed from organic solvents.[17,18] Indeed, in the previous Chapter 3 was found that MUA SAMs formed from micellar medium and in KOH solution (*under potential control*) showed an excellent insulating behavior and crystalline-like organization even for modification times as short as 10-15 min. It is well known that monolayers of molecules presenting defects are more prone to conformational fluctuations and, this lack of order would disfavor the possibility of attain intermixed crystalline domains at the molecular level.

Therefore, a lyotropic medium consisting of Triton X-100 and water can be used as a system that produces well ordered alkanethiolate monolayers [19,20], and in this chapter will be demonstrated that this approach is also suitable for the formation of molecularly mixed thiol monolayers at Au

(111) surfaces. The higher viscosity and size of the micelles respect to the thiol molecules is thought to be the reason for the absence of the solvent inclusion into the monolayer lattice and accordingly the improvement of the quality of the assemblies' organization (*Chapter 1 – Section 1.2.3.3*).

On the other hand, the formation of a mixed monolayer of 11-mercaptoundecanoic acid (MUA) and octanethiol (OT) under electrochemical control has been put forward the existence of macroscopically homogeneous and completely homogeneous mixed layers at higher and lower MUA:OT molar ratios, respectively. The macroscopically mixed layer should be formed by small domains that keep the same energetic behavior as the single-component SAM of the thiol constituents, and the completely homogeneous mixed one should be formed by few MUA molecules diluted in an OT layer.[21] Then, the purpose would be to take advantage of the different solubility of molecules on the hexagonal micelles in the lyotropic medium to obtain mixed monolayers of MUA and 1-decanethiol (DT) on Au (111) electrodes of definite composition.

In this sense, this work presents the first reported example of mixed SAMs formed from micellar solvents succeeding to achieve fully homogeneous mixed components in a wide range of molar concentration ratios. The characterization of the binary SAMs is carried out by electrochemical techniques, such as cyclic voltammetry (CV) and electrochemical impedance spectroscopy (EIS) and, by infrared reflection-absorption spectroscopy (IRRAS). In order to estimate the changes in the spatial distribution of the components of the binary SAMs formed under near

thermodynamic equilibrium and non-equilibrium conditions, a theoretical analysis has been applied based on the Bragg-Williams model (*Appendix*).

4.2. Materials and Methods

Chemical reagents. 11-mercaptoundecanoic acid (MUA), 1-decanethiol (DT), Triton X-100, potassium ferrocyanide ($K_4Fe(CN)_6$), potassium ferricyanide ($K_3Fe(CN)_6$) and semiconductor grade purity KOH was purchased from Aldrich-Sigma (purity ≥ 99%). The rest of the reagents were from Merck analytical grade. All solutions were prepared with deionized ultrapure water produced by Millipore system.

Methods. A conventional three electrode cell comprising a platinum coil as the counter electrode, a 50 mM KCl calomel electrode as the reference electrode and an Au(111) single crystal as the working electrode were used. The Au(111) surfaces were cleaned and modified with MUA and/or DT as indicated in the protocols described in the Chapter 2 (*Sections 2.3.1. and 2.3.2.*). In this particular case, the adsorption times assayed in lyotropic liquid mixtures were 15 min and 18 hours. Electrochemical characterization was carried out by CV and EIS techniques accordingly to the specifications and working conditions included, unless otherwise stated, in the Chapter 2 (*Section 2.4.1.*).

Au (111) textured surfaces were modified in the same experimental conditions indicated for Au(111) single crystal (*Chapter 2 – Sections 2.3.1., 2.3.2.*) and characterized by FT-IRRAS technique (*Chapter 2 – Section 2.4.2.1.*). Electrochemical and spectroscopic data were further analyzed and processed as indicated in Chapter 2 (*Sections 2.4.1.2 and 2.5.*).

4.3   Results and discussion

4.3.1. Cyclic voltammetry of the reductive desorption process of mixed MUA/DT SAMs

Cyclic voltammetry of the reductive desorption (RD) process is a useful technique to explore the structure and stability of the mixed SAMs. Figure 1 shows a series of cyclic voltammograms (CVs) for the RD processes in KOH 0.1M of the SAMs obtained at different MUA/DT molar ratios in the lyotropic medium after 15 min and 18 h of modification time (t_{mod}). The desorption processes of the single-component layers take place at -1.07 V and -1.10 V for MUA and -1.14 V and -1.18 V for DT at low and high modification times, respectively and, the mixed monolayers obtained at different component ratios show peak potentials comprised within these values. It is interesting to note that, under all the experimental conditions tested, the mixed-monolayer reductive desorption processes produce single desorption peaks indicating that the SAMs do not contain macroscopically phase separated domains (*Chapter 1-Section 1.2.4.*). However, this effect is expected if we take into account that phase-separated domains are only macroscopically observed by

154

two well-separated peaks when the potential difference for the single component SAMs are greater than 0.2 V.[22] Otherwise, the system is considered to be homogeneously mixed either as segregated domains of the components at the nanoscale or ideally to the molecular level.

As it is shown in Figure 2, the variation of the peak potentials with the solution molar ratio of the components do not follow the linear trend expected for an ideal behavior.[22] At low modification time, the peak potentials hardly vary from that of the MUA single component SAM at X_{MUA}^{sol} > 0.5. However, at lower MUA molar fractions, these values tend to these expected for an ideal behavior. On the contrary, the observed trend for the SAMs obtained at high modification time is near ideality at higher X_{MUA}^{sol} and show a higher deviation at X_{MUA}^{sol} < 0.5. Therefore, an enrichment of MUA molecules in the layers in respect to the modification solution composition is obtained under all the conditions, although the extent of this effect is dependent on t_{mod}.
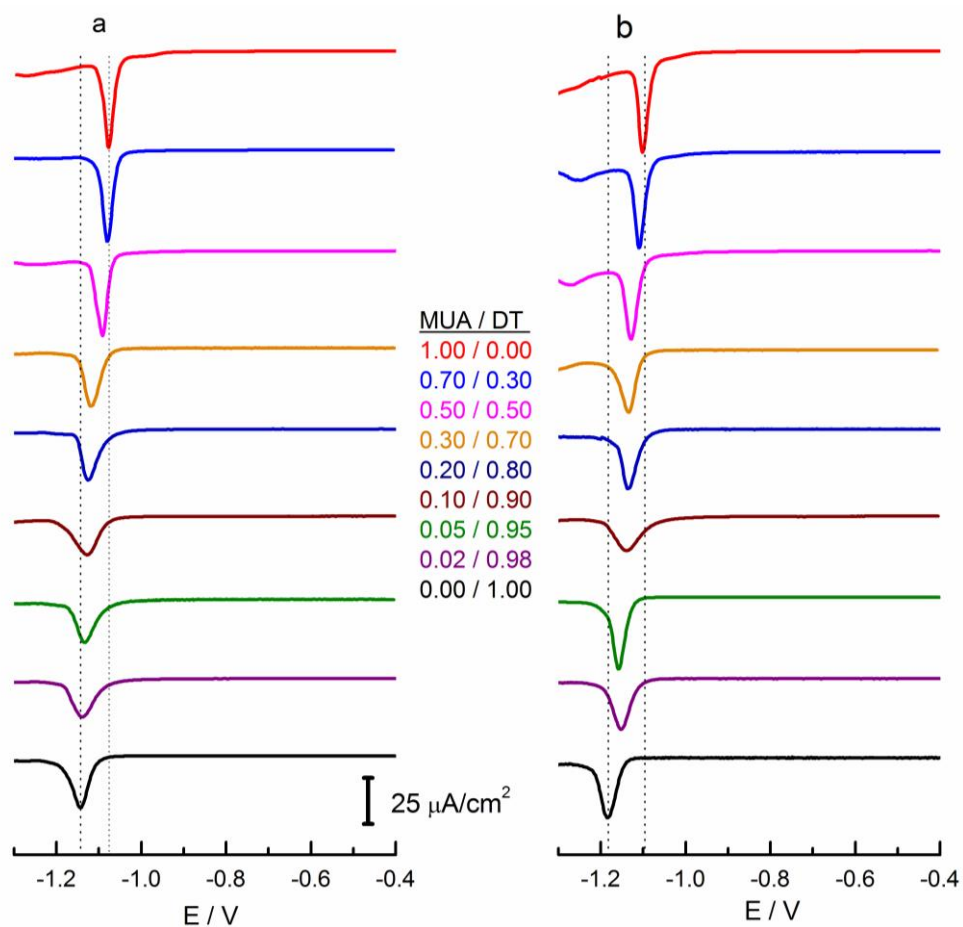
Figure 1. Cyclic voltammograms for the reductive desorption process in KOH 0.1 M of MUA/DT mixed monolayers formed at different MUA/DT molar ratios in a lyotropic medium on Au(111) single crystal electrodes at 15 min (a) and 18 h (b) modification time. Total thiol concentration is 1 mM. Scan rate: 20 mV/s.
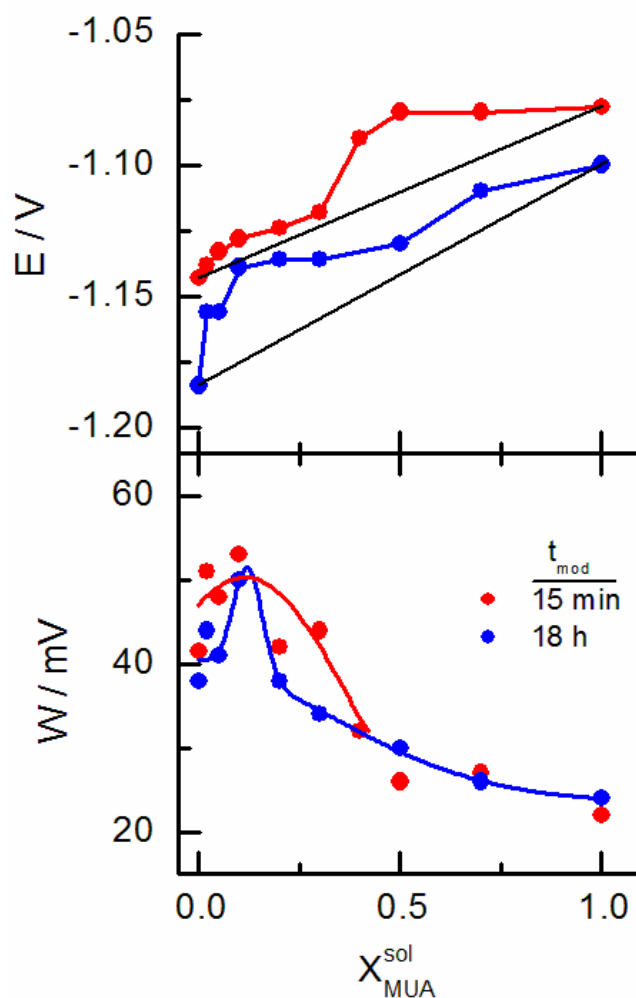
Figure 2. Changes in the peak potential (E) and half-width (W) of the reductive desorption peaks for MUA/DT SAMs formed at different molar concentration ratios at 15 min and 18 h modification time. Red and blue lines are presented as a guide for the eyes.

The half width of the reduction peaks (W) behaves in a similar way at higher MUA solution ratios. In fact, the values approach to that of the MUA single-component SAM. At low MUA solution ratio, the peaks broaden up to

values that are even higher than the half-width of the DT single-component SAM. This broadening of desorption peaks can be explained either by an overlapping of the peaks corresponding to the individual molecules that could form phase segregated domains at the nanoscale [22,23] or by the weakening of the attractive interactions between molecules in 2D arrays.[24,25] The first hypothesis has been tested by carrying out the deconvolution of the broaden desorption peaks using the peak parameters obtained for the single component SAMs reduction peaks.[21] In any of the cases, the CV curves cannot be properly fitted. Thus, the possibility of formation of segregated domains composed of MUA or DT molecules maintaining the same properties as the single component SAMs can be discarded and the occurrence of some disorder introduced by the mixing of these two molecules in the monolayer under these conditions should be taken into account.

Considering that in the present case, the length of the alkane chains of both components in the mixed SAM is similar, we can assume that Van der Waals interactions between molecules are favored. However, the presence of the bulkier terminal carboxylate group in the MUA molecules can act as monolayer destabilizing group. It has been reported [26] that the reductive desorption peaks for a 3-mercaptopropionic acid (MPA) monolayer are very narrow, showing a W value of 20 mV irrespective to the type of cation contained in the alkaline electrolyte solution. This fact is in agreement with the low W values observed for the pure MUA SAM and the mixed layers with higher molar ratios of MUA. Then, it can be thought that the negatively charged carboxylate groups can bind counterions in alkaline solutions in a way that they can induce an additional interaction by forming a two-dimensional

ionic crystal and, when the surface concentration of DT increases at low MUA mole fractions, the counterion layer can break and a partial loss of stability of the SAM takes place.

Although the trend of the peak half widths is similar for the SAMs formed at different t_{mod}, the values for the SAMs formed at 18 h present a narrower range of concentration ratios where the strong peak broadening is observed. This fact can be in agreement with the larger deviation of the peak potential to values that account for a higher MUA content in the SAM.

On the other hand, the charge involved in the reduction processes is nearly constant for the SAMs studied. The average value upon capacitive contribution subtraction is 66 ± 7% $\mu C/cm^2$ and 69 ± 5% $\mu C/cm^2$ for the mixed SAMs formed at the shorter and longer modification time, respectively. Then, the thiol surface concentrations for the SAMs are $6.9 \cdot 10^{-10}$ mol/cm^2 (±7 %) and $7.2 \cdot 10^{-10}$ mol/cm^2 (±5%), respectively, which are close to the expected coverage value of $7.6 \cdot 10^{-10}$ mol/cm^2 for an ($\sqrt{3} X \sqrt{3}$) R30º overlayer structure of molecules organized in an up-right configuration on Au (111).

Binary SAMs formed by alkanethiols with similar features have been studied in order to explore the possibilities of phase segregation at the nanometer scale.[16,22] Kakiuchi et. al. have reported similar one peak-voltammograms for mixed monolayers of MUA and 1-undecathiol (UDT) on gold surfaces and have shown that both thiolates molecules phase separate under ambient conditions into nanometer scale domains. These kinds of mixed SAMs are considered *macroscopically homogeneous* when the domains size does not exceed 15 nm^2 and produce only *one reductive desorption peak*.[22,23] Thus, this *"macroscopically homogeneous state"* has been defined

to be somewhere between the truly homogeneous state at the molecular level and a phase-segregated one that is enough to give two macroscopically discernable reductive desorption peaks in techniques such as voltammetry.

To determine mixed SAMs surface composition [22,27-29], it is assumed the approach that the reduction peak potential (E_{peak}) of each mixed monolayer is a simple weighted average of those of the single component SAMs:

$$E_{peak} = E_{MUA} \chi^{surf}_{MUA} + E_{DT} \chi^{surf}_{DT} \qquad (1)$$

$$\chi^{surf}_{MUA} + \chi^{surf}_{DT} = 1 \qquad (2)$$

where E_{MUA} and E_{DT} are the peak potentials for the pure MUA and DT SAMs, respectively, and X_{MUA}^{surf} and X_{DT}^{surf} are the surface mole fraction for each component in the mixed SAMs. From equations (1) and (2) and assuming that the packing density of the alkanethiolates is approximately constant with the surface composition, as stated above, the surface composition of MUA can be given by:

$$\chi^{surf}_{MUA} = \frac{E_{peak} - E_{DT}}{E_{MUA} - E_{DT}} \qquad (3)$$

Figure 3 shows the variation of the X_{MUA}^{surf} determined by using eqn. 3 with the concentration ratio of MUA in solution, X_{MUA}^{sol}, for the mixed SAMs studied. A linear behavior is not obtained for any of the conditions tested. Interestingly, the surface enrichment of MUA molecules over DT as a function

160

of X_{MUA}^{sol} is observed at lower modification times and, this trend is more pronounced at SAMs built at higher modification times, where the system can be thought near the thermodynamics equilibrium conditions. The nature of the adsorbate-adsorbate and adsorbate-solvent interactions may influence the composition and the structure of mixed SAMs in many ways. Different solvents will change the adsorbate activities in the solution and then, affect the monolayer composition at or near thermodynamics equilibrium.

Kakiuchi et. al.[22] using ethanol as solvent investigated the composition of binary SAMs composed by MUA and UDT, concluding that the adsorption of the methyl-terminated thiol is preferred at any UDT concentrations. This finding is opposite to the present results, indicating that the different adsorbate-solvent interactions of the two molecules in solution influence the SAM surface composition. In this sense, using an non-polar solvent as isooctane, Bain et al.[28] have reported a remarkable strong preference for the 11-mercapto-1-undecanol (MU) from mixtures of UDT/MU.

The prevalence of specific interactions between terminal groups such as hydrogen bonding can ultimately control the phase properties of these layers. Carot et al.[29] have formed a homogeneous mixed monolayer of MUA and MPA demonstrating that the changes from two distinct to a unique homogeneous phase is driven by strong hydrogen bonding between the unlike molecules.
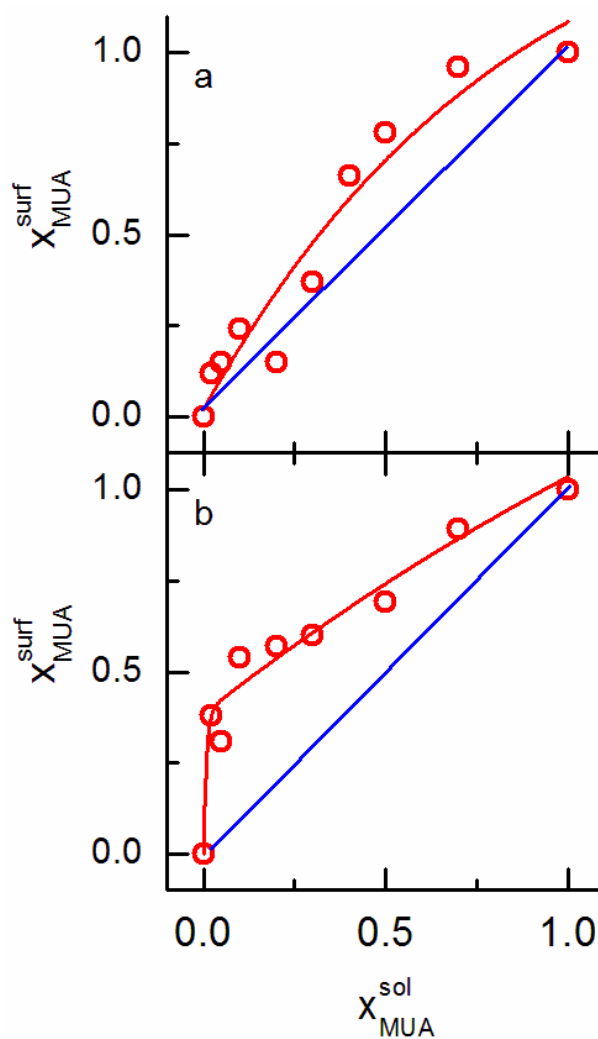
Figure 3. MUA surface composition (determined by Eqn. 3) as a function of the MUA solution mole fraction at 15 min (a) and 18 h (b) modification times. Red lines are presented as a guide for the eyes.

In the present work, an aqueous micellar solution consisting in a lyotropic hexagonal crystalline liquid as solvent for the assembly process has been used. The interactions of the micelles with the alkanethiols should determine the adsorption mechanism (*Chapter 1 - Section 1.2.3.3.*). It is believed that the

micelles act as vehicles to transport and deliver the thiols to the metal surface. The mechanism proposed to explain the micelle-assisted SAM-formation consists of three steps: (1) the diffusion of the micelles containing the alkanethiols to the proximity of the Au surfaces, (2) the release of the alkanethiols from the micelles adsorbed at the metal surface (admicelles) and, (3) the chemisorption of the alkanethiols on the surfaces after admicelles removal.[30,31] Yang al.[30] have proposed that the transfer of the thiols from micelles in solution to admicelles in metal surfaces likely occurs through a collision induced activated diffusion process that explains the exponential decrease of the SAM formation rate constant with the alkanethiol chain length.

Assuming that both molecules are solubilized in the hexagonal micelles formed in the lyotropic medium, the different solubility of MUA and DT on the micelles can be taken as responsible for the more favorable delivery of MUA over DT at the surface. In this sense, DT is probably better inserted in the hydrophobic part of the micelles than MUA does, which eventually affects the adsorbate activities in the micellar solution and thermodynamics of the assembly process.

4.3.2. *Thermodynamics analysis of phase behavior in mixed SAMs*

As it has just been stated, the nature of the solvent has a significant influence in the composition of the binary SAMs. However, the intermolecular interactions between the like and unlike components should also play a major

role in the final SAM structure and composition. Knowledge of these interactions would shed light about important questions on the molecule spatial distribution and, therefore, on the mixing behavior of the components in the binary SAMs. The strength of the interactions between these molecules will be the factor in determining these properties.

In earlier studies, Folkers et al.[12] formulated a thermodynamic model that explains the relationship between the mole fraction of one thiolate in the mixed SAM and the ratio of both thiols in solution based on the Bragg-William solution theory.[32] In this model they only consider the interactions between the nearest neighbor's molecules, assuming that thiols don't interact in solution and maintain the same configuration in solution and within the SAM.

They have elegantly deduced an equation relating the mole fraction of the thiolate of longer chain length (X_{Lg}) in the two-components SAM and the ratio of thiols in solution ($R_{sol} = X_{Lg} / X_{Sh}$; where X_{Lg} and X_{Sh} are the mole fraction of the longer and short chain length thiols in solution, respectively) taking into account the mixing of the components as:

$$\ln R_{so\ln} = \ln(X_{Lg}/(1-X_{Lg})) + (\omega/kT)(1-2X_{Lg}) + \Delta(\Delta\mu)/kT \qquad (4)$$

where ω is the interaction parameter which describes intermolecular interactions within the SAM and, $\Delta(\Delta\mu)$ is the chemical potential variation between the thiols in solution and the thiolates at the SAM.[12]

Figure 4 shows the relationship between X_{MUA}^{surf} and the ratio of the two different thiols in the solution (as explained in the Figure legend). The

experimental data have been obtained from the peak potentials of the RD processes studied at different solution ratios (Eqn. 3). Additionally, IRRAS measurements were carried out to quantitatively determine surface compositions. For this purpose, IR spectra of the mixed SAMs were analyzed in the C-H stretching wavenumbers region (gathered in Figures 7 and 9) and, the X_{MUA}^{surf} values calculated by both electrochemical and spectroscopic methods (Figure 4). These results are also compared with the theoretical curves calculated for different values of ω, the interaction parameter, which determines the phase behavior of the SAMs. [12]

The physical interpretation of ω gives three different regimes that can be related to the mixing behavior of the two thiolates in the SAM under thermodynamic conditions:

(1) When $\omega < 0$, the interactions between the unlike molecules (*hetero-molecular*) predominate over the interaction between the like ones (*homo-molecular*). At $\omega = 0$, an ideal bi-dimensional mixture where the components are energetically equivalent are formed.

(2) When $0 < \omega < 2kT$, the interactions between the thiolates of the same nature are more favorable than those of different nature, thus showing complete molecular mixing. At $\omega = 2kT$, a critical point in the mixing behavior is obtained.

(3) At $\omega > 2kT$ the mixing of the components is not favored.
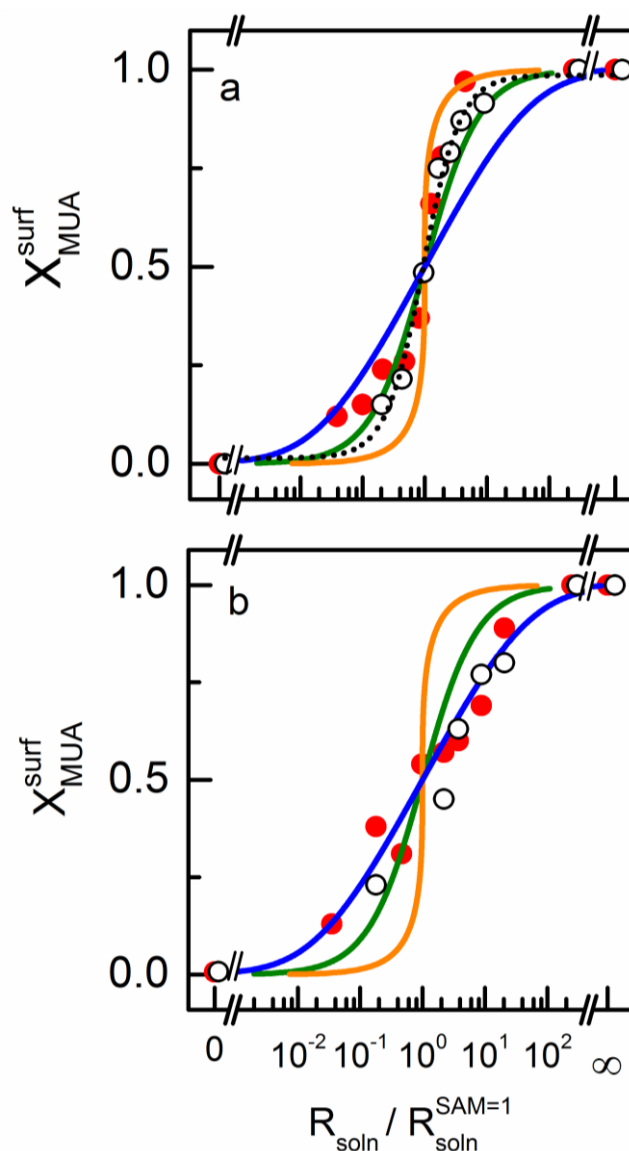
Figure 4. Plots of the MUA surface concentration versus the ratio of thiols in solution (R_{soln}= [MUA]$_{sol}$ / [DT]$_{sol}$ where $R_{soln}^{SAM=1}$ represents the value of R_{soln} that yields equimolar quantities of thiolates in the SAM) for mixed SAMs built at 15 min (a) and 18 h (b). Experimental data are determined from: (●) CV (peak potentials) and (○) IRRAS measurements (–CH$_3$ asymmetric stretching peak); Lines are the theoretical representation of eqn. 4 determined for interaction parameters corresponding to: (——) ω = -2 kT; (——) ω = 0 and (——) ω = 2 kT. Black dotted line is a guide for the eyes.

166

The experimental data for X_{MUA}^{surf} versus $R_{soln}/R_{soln}^{SAM=1}$ for the monolayers formed at longer modification time (Figure 4b) are well fitted to the theoretical curve with $\omega = -2kT$, indicating the prevalence of the interactions MUA-DT over MUA-MUA and DT-DT in the SAM structure. From these results it can be hypothesized that the DT molecules must be completely diluted in the MUA domains, or viceversa, forming a homogeneously mixed layer at the molecular level comprising a single phase probably close to the thermodynamic equilibrium. A similar mixing behavior has been observed at low X_{OT}^{surf} in mixed SAMs of MUA/OT formed under electrochemical control from alkaline solutions.[21] By using STM techniques, Pace et al.[33] have achieved a subnanometer-resolved patterning of bi-component domains formed by an alkyl amide derivative and DT and, Chen et al.[34] have built true molecular-scale uniform SAMs of C14/C8 and C12/C8 molecules on Au (111) surfaces, as a few examples of homogeneously mixed layers at the molecular level.

However, other type of interactions seems to prevail in the SAMs formed at shorter modification time (Figure 4a). In this case, the experimental points are mainly localized between the theoretical curves of $\omega = 0$ and $\omega = 2kT$. This behavior can be interpreted as a different surface distribution where the molecules prefer to form nanoscale domains of their own kind, where the interaction energy is not sufficient to overcome the entropy of mixing. If the short modification time used to build these monolayers is taken into account, it can be thought that equilibrium conditions are not still achieved for an ideal mixing and most likely, the compositions correspond to kinetically trapped, metastable states of small domains of the same kind of molecules.

In this sense, Figure 4a shows higher and lower surface MUA content deviation for $R_{soln}/R_{soln}^{SAM=1} > 1$ and $R_{soln}/R_{soln}^{SAM=1} < 1$, respectively, in comparison to the SAMs formed at higher immersion time and the theoretical representation of eqn.4 with an interaction parameter value of $\omega = -2kT$ (Figure 4b). Such behavior is related to that previously commented for the variation of the peak potentials with X_{MUA}^{sol} in this system (Figure 2). This fact can be tentatively interpreted by the balance of the MUA-MUA and DT-DT molecular interactions that still runs the system into MUA-enriched or DT-enriched segregated domains of like-molecules at high or low X_{MUA}^{sol}, respectively. Otherwise, the closer the system is to the ideal thermodynamic equilibrium conditions, the heteromolecular interactions are favored, as expected, and the assemblies might evolve to a molecularly homogeneous mixing of the components by balancing of the MUA and DT surface content in the DT-enriched and MUA-enriched domains, respectively. Both scenarios could be validated by the similar evolution of the X_{MUA}^{surf} values shown in Figure 4, as determined by two different experimental methods.

4.3.3. Blocking properties studied by CV and EIS

The monolayer barrier properties of the mixed SAMs have been checked by studying the electron-transfer reactions of the redox probe molecules $K_4Fe(CN)_6/K_3Fe(CN)_6$. The ability of SAMs to block the electron transfer between the metal surface and redox species in solution is very well-known and it is used as a way to evaluate the molecular organization and the monolayer quality (*Chapter 1 – Section 1.2.9.*).[19,35] Figure 5 shows the

voltammetric response of $K_4Fe(CN)_6/K_3Fe(CN)_6$ for pure and mixed MUA and DT monolayers formed at two different modification times.

Cyclic voltammograms (CVs) recorded in the presence of the SAMs don't show the typical peaked shape for a diffusion-controlled reversible redox mechanism, indicating the blocking effect of the redox reaction in the modified surfaces. However, a stronger blocking effect is observed for the mixed monolayers built at longer times (Figure 5b) accordingly to the much lower current density values obtained in this case.

Electrochemical impedance spectroscopy (EIS) of redox probes is a powerful tool to study the interface properties of the electrode modified surfaces and it can give complementary information to that supported by the cyclic voltammetry experiments. EIS measurements provide an easy way for the determination of the kinetic parameters of the electron transfer process as well as the detection of the presence of pores and pinholes in the monolayer structure. A parallel study of this presented by cyclic voltammetry (Figure 5) has been carried out by EIS and the results are plotted in Figure 6.
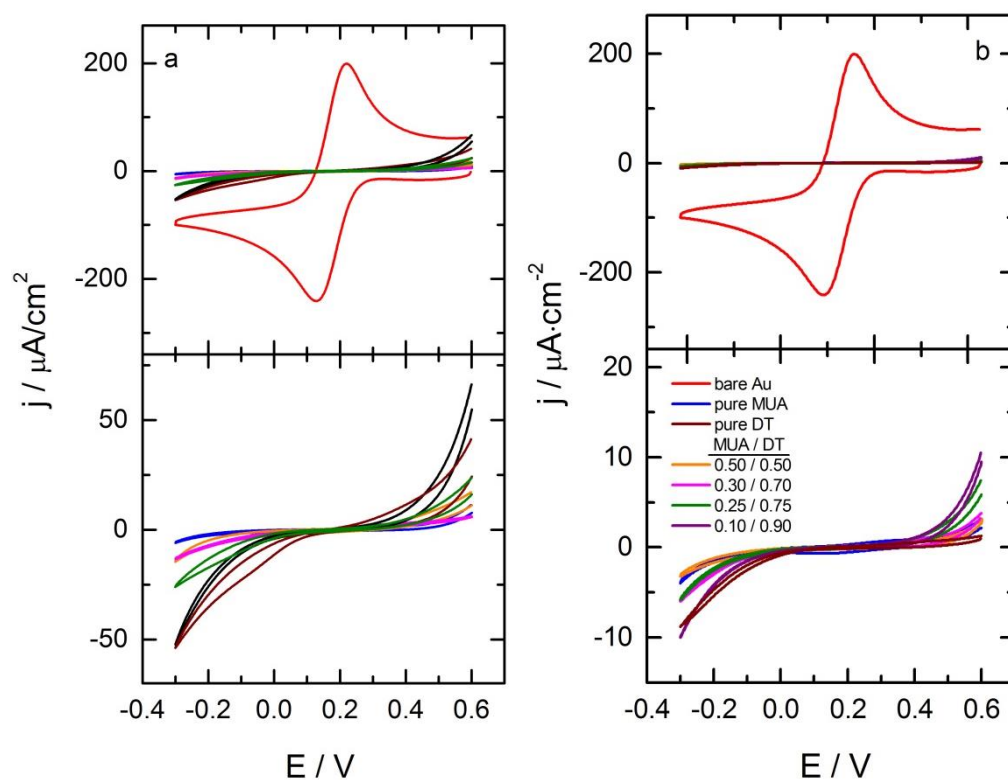
Figure 5. Cyclic voltammograms of 1mM of $K_4Fe(CN)_6$/$K_3Fe(CN)_6$ in 0.1M KNO_3. Scan rate: 0.1 V/s. The curves have been recorded for bare and modified electrodes under the conditions gathered at different modification times: (a) 15 min, (b) 18 h.

The analysis of the impedance spectra has been performed by data fitting to a Randles equivalent circuit consisting of a parallel combination of capacitor represented by C and Faradaic impedance Z_f in series with the uncompensated solution resistance R_u (*Chapter 1 – Section 1.2.9. and Chapter 2 -2.4.1.*). The magnitude Z_f is a combination of charge transfer resistance R_{CT} and the Warburg impedance W. For the SAM modified electrodes the impedance spectra show only the contribution of the charge transfer resistance. By using the relationship between the charge transfer resistance,

R_{CT} and the apparent electron transfer rate constants, k_{ET}^{app} (Eqn. 5), this parameter can be determined for the different SAM compositions.[36]

$$R_{CT} = \frac{RT}{n^2 F^2 A k_{ET}^{app} c}$$ (5)
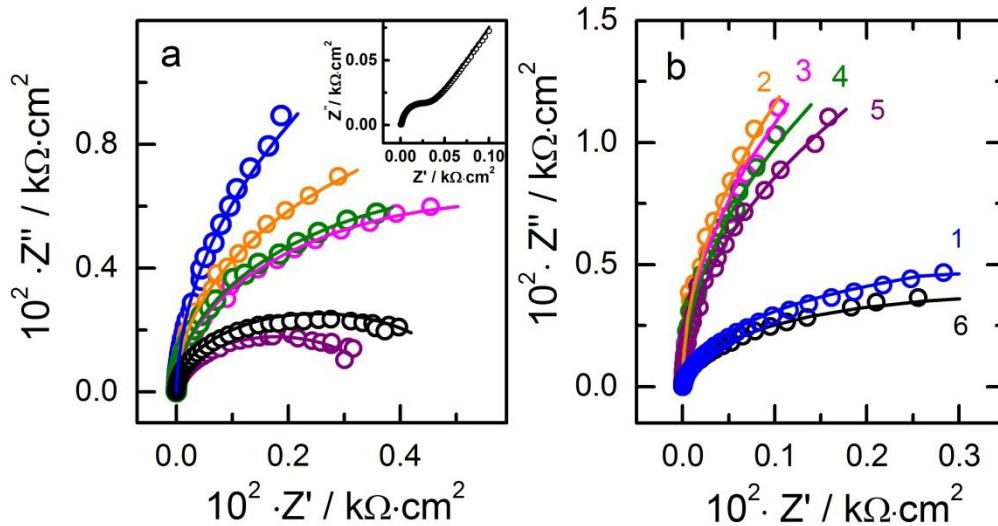
Figure 6. Nyquist plot of 1mM of $K_4Fe(CN)_6/K_3Fe(CN)_6$ in 0.1M KNO_3. The curves have been recorded for bare (Inset) and modified electrodes with pure and mixed SAMs of MUA and DT at different modification times: (a) 15 min, (b) 18 h. (1) MUA-SAM, MUA/DT molar ratio: (2) 0.5/0.5, (3) 0.3/0.7, (4) 0.2/0.8, (5) 0.05/0.95 and (6) DT-SAM. The solid lines are the fits to the simplified Randles equivalent circuit ($R_u[CR_{ct}]$) without the Warburg impedance contribution (mass transfer).

In equation (5), R is the gas constant, T the temperature, F the Faraday constant, n the number of electrons, A the area of the electrode, and c the concentration of the redox couple. The apparent electron transfer rate constants obtained are gathered in Table 1.

171

Table 1. Apparent electron transfer rate constant (k_{ET}^{app}) and capacitance (C) values determined for pure and mixed MUA and DT SAMs.

MUA/DT[a]	$X_{MUA}^{(1)}$	$C^{(1)}$ $\mu F \cdot cm^{-2}$	$k_{ET}^{app\,(1)}$ cm/s	$X_{MUA}^{(2)}$	$C^{(2)}$ $\mu F \cdot cm^{-2}$	$k_{ET}^{app\,(2)}$ cm/s
1.00/0.00	1.00	3.05	$7.15 \cdot 10^{-7}$	1.00	3.02	$2.26 \cdot 10^{-6}$
0.50/0.50	0.76	2.89	$1.16 \cdot 10^{-6}$	0.73	2.74	$2.14 \cdot 10^{-7}$
0.30/0.70	0.41	2.81	$2.07 \cdot 10^{-6}$	0.60	2.59	$2.25 \cdot 10^{-7}$
0.20/0.80	0.33	2.74	$2.79 \cdot 10^{-6}$	0.56	2.59	$2.74 \cdot 10^{-7}$
0.05/0.95	0.15	1.51	$3.70 \cdot 10^{-6}$	0.31	2.59	$3.57 \cdot 10^{-7}$
0.00/1.00	0.00	1.86	$3.47 \cdot 10^{-6}$	0.00	1.80	$3.36 \cdot 10^{-6}$

[a] Solution ratio of MUA/DT. [1] Parameters referred to SAMs formed at 15 min. [2] Parameters referred to SAMs formed at 18 h. X_{MUA} is the surface mole fraction of MUA in the mixed monolayer as determined from Eqn. 3. The standard deviations for C and k_{ET}^{app} values are lower than 8 % in all cases.

In the case of well-ordered structures with low defect densities, an exponential decrease of the electron transfer rate constant is usually observed [37-39] and, the electron tunneling through the electronic states of the SAM control the electron transfer process (*Chapter 1 – Section 1.2.9.*). The tunneling process can be represented as,

$$k_{et} = k^o e^{-\beta_n n} \tag{6}$$

where β_n is the tunneling constant per carbon, n is number of carbon atoms and k^o is the apparent rate constant of the clean Au electrode. The coupling coefficient β for saturated alkane monolayers has been estimated to be in the range of 0.8-1.2 Å^{-1}.[40-43] The apparent electron transfer rate constant for the redox probe ferro/ferricyanide in the bare Au(111) surfaces is 0.026 cm/s, as

determined from the analysis (Eqn. 5) of the impedance spectrum (Figure 6a Inset), which is within the range of reported values.[44-47] Using the Eqn. 6 and $\beta_n=1$, k_{et} values for ideally free-defect monolayers of DT and UDT monolayers under ET tunneling conditions can been calculated as $1.2 \cdot 10^{-6}$ and $4.3 \cdot 10^{-7}$ cm/s, respectively. From these values and the k_{ET}^{app} constants determined for the mixed monolayers (Table 1), we can conclude that only the mixed SAMs obtained at higher modification times act as a highly ordered 2-D organic layer that prevents the approach of the redox probe to the metal surface, and consequently the electron transfer should take place by a tunneling mechanism.

As it can be expected, the Nyquist plots for the mixed monolayers obtained at lower modification time (Figure 6a) show an increase R_{CT} and C values with the increase in MUA surface concentration (Table 1). These results reflect that from a microscopic perspective, each component of the binary mixed SAM contributes almost proportionally to the overall R_{CT} and C values in respect to its surface composition,[48] which should correspond with SAMs composed by domains of the same kind of molecules at the nanometer scale. Interestingly, a different behavior is apparently observed for the mixed SAMs obtained a longer modification times (Figure 6b), where the impedance curves show higher R_{CT} values and, C values don´t significantly change with the surface fraction of the components of the binary SAMs. It should be pointed out that this fact would be indicative of a different spatial distribution of the components into the SAMs lattice and is in agreement with a model consisting in a homogeneous distribution of the two different thiol moieties at the molecular level. Consequently, a homogeneous arrangement of the carboxyl

173

groups and, therefore, of the negative charge density at the top of these mixed layers, would make possible the negligible variations in the capacitance and the high R_{CT} values obtained when the MUA surface concentration changes (Table 1).
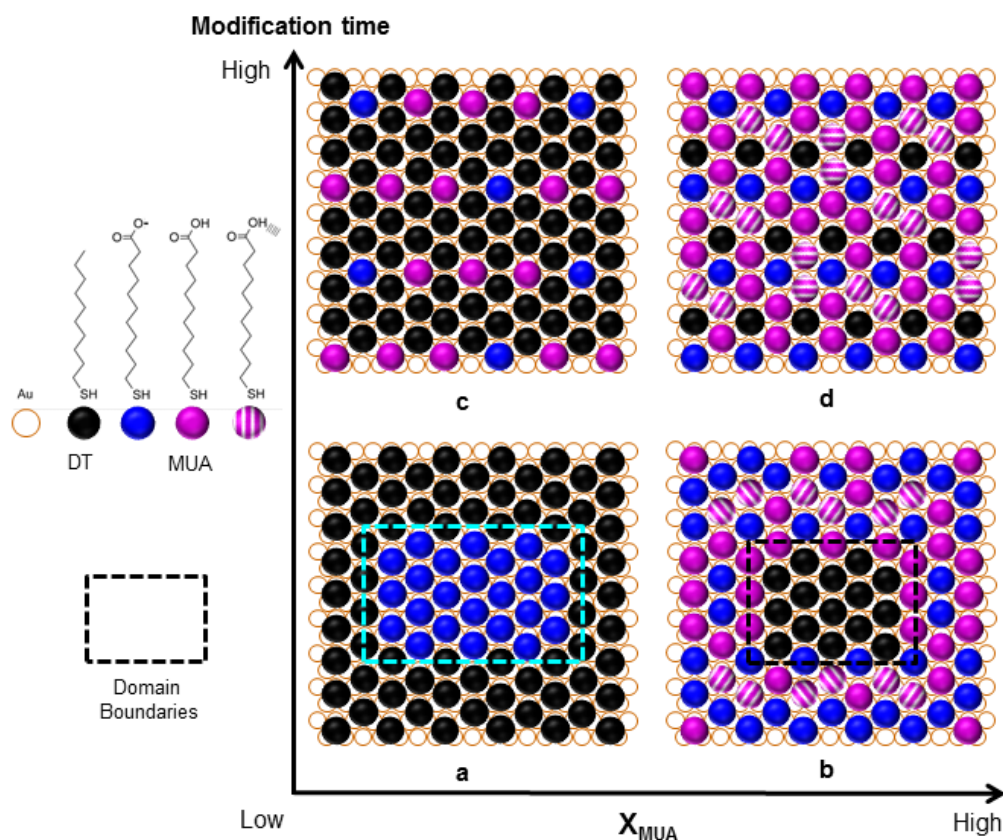
Scheme 1. Homogeneously MUA/DT mixed SAMs composed by segregated nanodomains (lower depicted figures) and molecularly distributed (upper depicted figures) arrangements at different MUA surface compositions, X_{MUA}: (a) 0.25, (b) 0.84, (c) 0.23 and (d) 0.8

Thus, these features could be explained by considering the spatial distribution of MUA and DT molecules in the different mixed thiol SAMs studied, together with the probable existence of a population of MUA molecules in carboxylate form on the SAM exposed surface. In this sense, the nanodomains segregated pattern, previously described for SAMs formed at lower modification times, could increase the repulsive interactions between neighbors' carboxylates and induce some kind of defects and disordering in the domains, either inside them and/or at their edges/boundaries, eventually favoring the increase of the electron transfer rate process (Scheme 1a-b). In an opposite way, the intermixed domains of SAMs formed at higher modification times should distribute the negative surface charge density of carboxylate groups in a 2-D homogeneous arrangement, leading to a long-range ordered assembly that completely hinders the electron transfer reaction (Scheme 1c-d). Then, electron transfer should occur through a tunneling mechanism probably due to the much lower number of SAM defects and pinholes [49-52] and, to the decay of the interfacial concentration of anionic redox species driven by the repulsive interaction with the negatively charged terminal carboxylate group on top of the surfaces.

4.3.4. FT-IRRAS characterization of MUA/DT mixed SAMs

Pure and mixed MUA / DT SAMs formed by modification times of 15 min and 18 h were characterized by infrared spectroscopy (Figures 7-10). IRRA spectra of the C-H stretching wavenumbers region were obtained in the range of 2800-3000 cm^{-1}. Modes assignments are given in table 2.[53-55]

IRRAS, XPS and STM techniques can be used as reliable methods to calculate the relative surface coverage values of mixed SAMs constituents, yielding quantitative results that are in good agreement.[16] The presence of DT molecules in the mixed SAMs is shown in the IRRAS spectra by the appearance of the peaks corresponding to the symmetric (r^+, 2878 cm^{-1}) and asymmetric (r_a^-, 2964 cm^{-1}) C-H stretching vibrational modes assigned to the terminal $-CH_3$ groups. Since, the intensity ratio of both peaks does not significantly vary across the composition series in the mixed SAMs formed at the same immersion time, the methyl group orientation can be assumed to remain almost unaltered in such assemblies. Moreover, it is observed that the peak wavenumber values are composition independent. Therefore, the absorption coefficients can be considered constant and the integrated absorption of the peaks used to determine the relative surface coverage of DT and MUA in the SAMs. The results obtained for X_{MUA}^{surf} (IR spectra in Figures 7 and 9) are generally in good agreement with those derived from the VC peak potentials values by using eqn. 3 (Figure 3 and Table 1). This fact is also supported by the similar trends observed in the evolution of X_{MUA}^{surf} vs $R_{soln}/R_{soln}^{SAM=1}$ that fit for both methods (Figure 4).

Figure 7 shows that the position and width of peaks assigned to the methylene groups in the C-H stretching region change with the surface composition in the mixed SAMs formed at low immersion time. At MUA surface coverages larger than 0.67, the peaks associated with the symmetric and antisymmetric (d^+ and d^- modes, respectively) of the CH_2 groups' exhibit composition independent values of 2849-2850 and 2918-2919 cm^{-1}, respectively. It can be noted, based on the position of these peaks, that these

spectra correspond to SAMs with densely packed assemblies of alkyl chains, mainly in all-trans conformations.[56,57]

However, in the mixed films with lower MUA surface coverage (54% and 25% of MUA molecules), the CH_2 symmetric and antisymmetric peaks shifts to higher frequencies and the shape of the antisymmetric bands varies markedly, indicating the existence of domains where the alkyl chains are somewhat disordered showing a more liquid-like conformational order.[56-60]

Moreover, it should be highlighted that the changes in the intensity of these peaks have been also attributed to the diminished conformational order of the alkyl chains.[61] The intensity of these bands depends on the transition dipole moments projections of the C-H stretching vibrations along the surface normal direction (Table 2) and, consequently, the increase in the intensity and broadening of the d^+ and d^- bands could be explained in terms of different orientations of the latter SAMs. Therefore, the alkyl chains on the disordered domains should have different configurations that are distinctly different from the canted orientations existing when the monolayer possesses a crystalline conformational order. This lack of organization may be associated to the distribution and charge state of the carboxyl terminal groups. In fact, these groups are completely deprotonated in carboxylate form as it is indicated by the absence of any band at around 1700 – 1750 cm^{-1} (-COOH stretching vibrations) and the presence of the symmetric stretching modes of carboxylate groups at 1420 cm^{-1} [62] (Figure 8). Then, the electrostatic repulsion forces between nearest carboxylates molecules in the nanodomains should lead to the alkyl chain disordering in these SAMs (Scheme 1a).
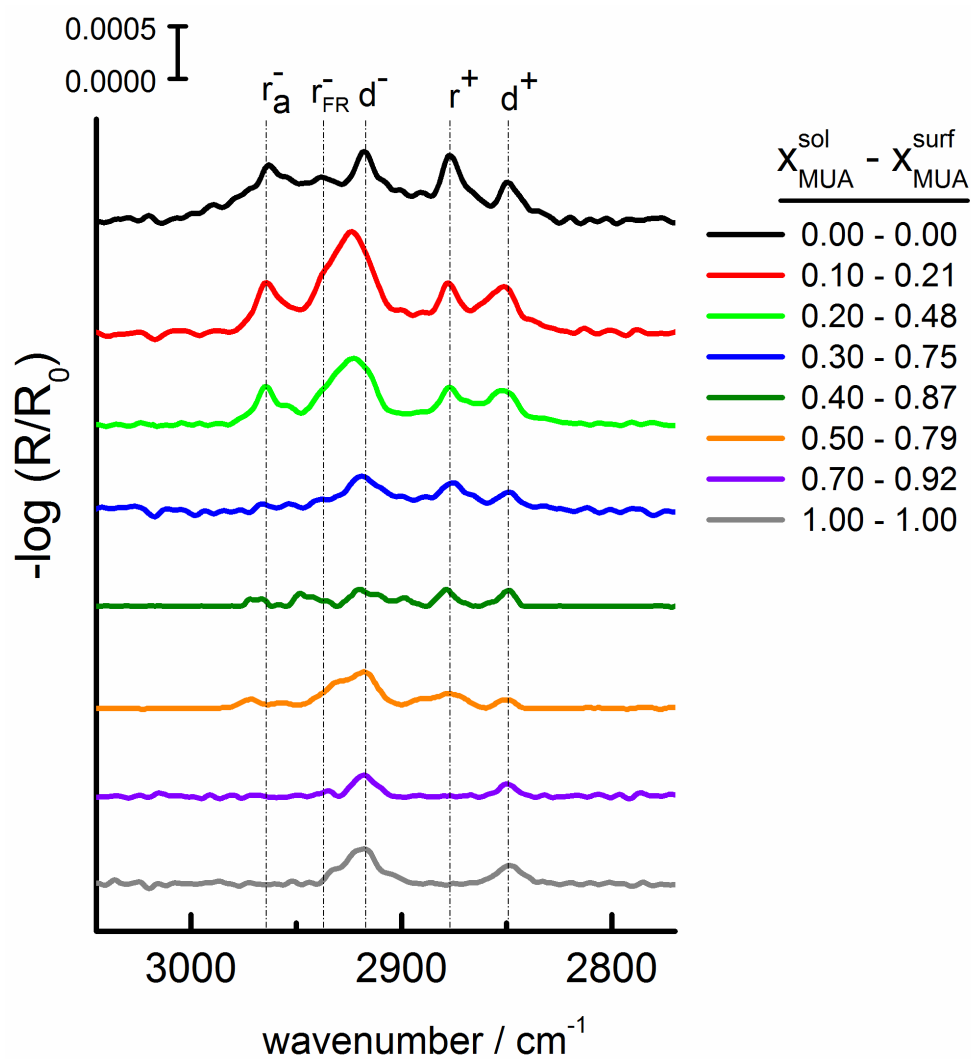
Figure 7. Infrared spectra of pure and mixed monolayers formed at a modification time of 15min from a lyotropic medium containing different mixtures of MUA and DT on Au (111) surfaces. The integrated intensity of the methyl stretching mode adsorption at 2964 cm^{-1} (r_a^-), only present for the methyl-terminated thiol, was used to estimate the fraction of MUA surface coverage. Dashed lines represent the wavenumber values for a crystalline-like assembly of an alkanethiolate overlayer.

Table 2. Spectral assignments and transition dipole moment directions for C-H vibrational modes of alkanethiol SAMs on Au.

Mode description	Abbrevn[a]	C-H / cm^{-1}	Direction of Transition Dipole Moment
-CH$_3$ asym (ip)	r_a^-	2964	ip of CCC, perpendicular to C-CH$_3$ bond
-CH$_3$ asym (op)	r_b^-	2954	perpendicular to CCC backbone plane
-CH$_3$ sym	r^+ (FR)	2937	parallel to C-CH$_3$ bond
-CH$_3$ sym	r^+	2878	parallel to C-CH$_3$ bond
-CH$_2$- asym	d^-	2918	perpendicular to CCC backbone plane
-CH$_2$- sym	d^+	2850	ip CCC backbone plane,

[a] Abbreviations: asym : asymmetric; sym : symmetric; ip : in plane; op : out of plane; FR : Fermi Resonance.

On the other hand, in those SAMs showing a crystalline-like arrangement, accordingly to the peaks position of the CH$_2$ stretching modes (for instance a SAM with 84% of surface MUA molecules, as included in Figures 7 and 8), a vibration band appears at the 1740 cm^{-1} region that can be well fitted with two individual components centered at 1740 and 1713 cm^{-1}. Both bands represent C=O stretching modes corresponding to non-hydrogen (70 %) and hydrogen bonding (30 %) interactions of the -COOH terminal groups, respectively,[56] and account approximately for the 53 % of the total area that could be ascribed to the different vibrational modes of the surface carboxyl groups. In fact, the additional band observed at around 1460 cm^{-1}

179

can be also decomposed in two main peaks at 1470 cm^{-1} (CH$_2$ scissoring) and 1442 cm^{-1} (C-O stretching). We believe that the existence of the protonated carboxylic groups prevents the approach of carboxylate molecules diminishing the repulsive electrostatic interactions in the domains and, as a consequence, the alkyl chains are able to organize themselves in a crystalline-like packing (Scheme 1b).[63]

Figure 8. Infrared spectra at the low wavenumbers region of three representative mixed monolayers (15min) with different surface ratios of HS(CH$_2$)$_{10}$COOH and HS(CH$_2$)$_9$CH$_3$ on Au (111).

180

IR spectra in the CH stretching region for pure and mixed monolayer of MUA and DT at 18 h of modification time are shown in Figure 9. The peak positions for the methylene stretching bands at 2918 cm^{-1} and 2850 cm^{-1} reveals a crystalline conformational order of the alkyl chains that is independent of the surface composition. These results suggest the existence of fully miscible and crystalline multicomponent arrangements with favorable heteromolecular interactions, reached under cuasi-thermodynamic equilibrium conditions, and supported by the conclusions explained in the former section derived by applying of the Bragg-William approach as well as by the trend observed in the EIS results (Scheme 1c-d).
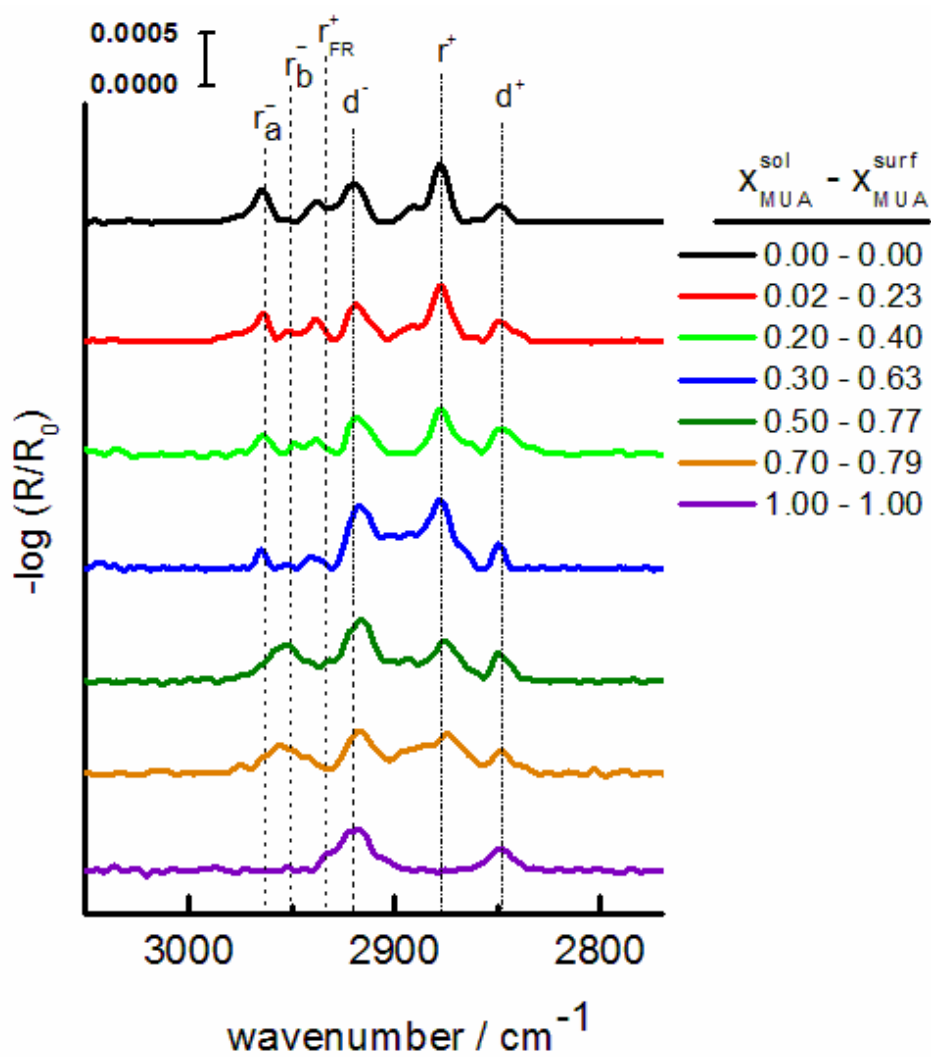
Figure 9. IR spectra of pure and mixed monolayers formed at modification times of 18 h from a lyotropic medium containing mixtures MUA and DT at Au (111) surfaces. The integrated intensity of the asymmetric methyl stretching mode adsorption at 2964 cm^{-1} (r_a^-) was used to determine the fraction of MUA surface coverage. Dashed lines represent the wavenumber values for a crystalline-like assembly of an alkanethiolate overlayer.
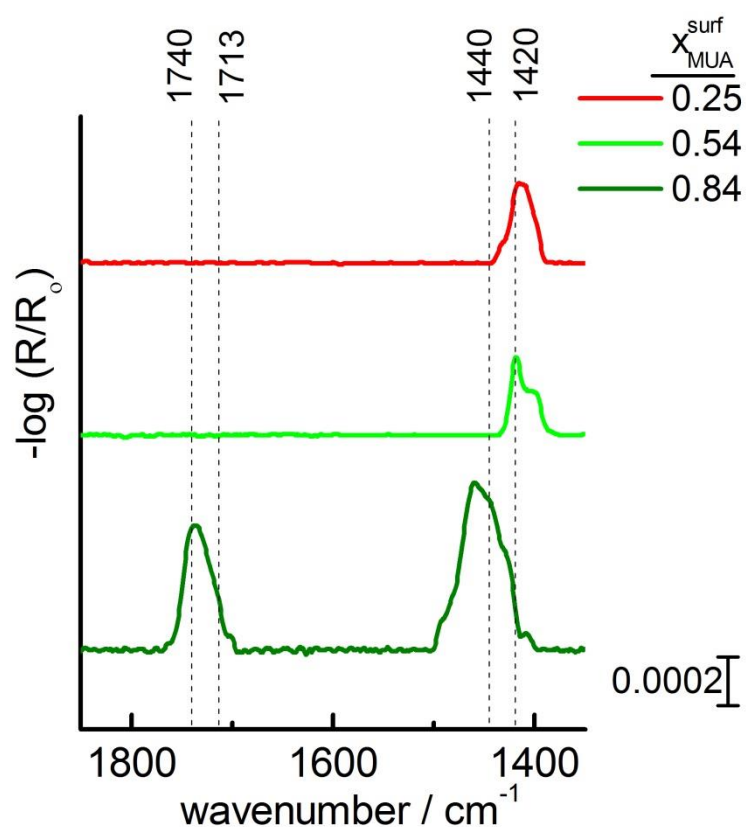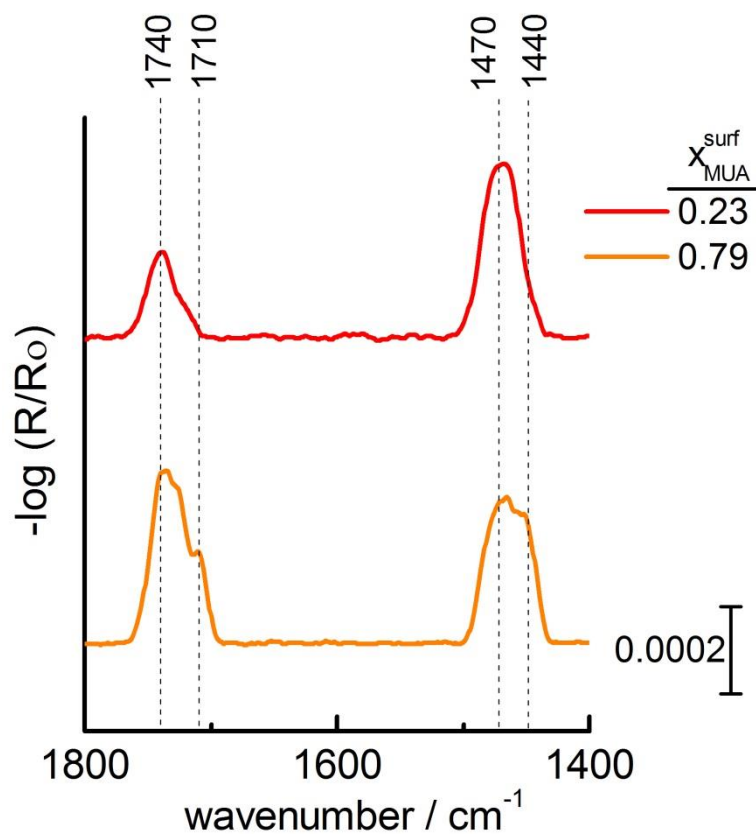
Figure 10. Infrared spectra at the low wavenumbers region of two representative mixed monolayers (18 h) with different surface ratios of $HS(CH_2)_{10}COOH$ and $HS(CH_2)_9CH_3$ on Au (111).

The low wavenumber region of these spectra (Figure 10) provides more insights into the intermolecular environment of the alkyl chains in these 2-D films. The stretching C=O band at 1740 cm^{-1} is observed at low as well as at high surface MUA concentration. The band at 1460 cm^{-1} can be fitted, as in the case of the layers formed at low modification time, by two bands at 1440 (C-O stretching) and 1470 cm^{-1} (CH$_2$ scissoring), being the contribution of the

former in the spectrum of low MUA concentration, only 20 % of the total peak area and 28 % of the total MUA in the monolayer. Thus, under conditions where only a MUA surface mole fraction of 0.23 is present, hydrogen bonds are not preferentially formed and the carboxylic groups coexist with carboxylate ones but, as the alkane chains show characteristics signals of a highly organized layer, carboxylates must be very well separated and do not effectively interact each other (Scheme 1c). Similarly, in the case of the layer containing a MUA surface mole fraction of 0.79, again the C-O stretching band ascribed to the carboxylate groups accounts for a 28 % of the total MUA in the SAM. This fact seems not to be casual accordingly to a MUA/DT crystalline-like arrangement where hetero-molecular interactions of both components are balanced to a molecular level, independently of their surface mole composition. However, at high MUA surface coverage, the stretching C=O band shows two contributions at 1740 and 1710 cm^{-1}, corresponding to carboxylic acid terminal groups interacting by non-hydrogen (70%) and hydrogen bonding (30%), respectively. In such a case, a small amount of hydrogen bonds can be detected between MUA molecules (around 20 %), as it was also previously described for the crystalline-like SAM formed at low modification time (Scheme 1d).

Therefore, it can be concluded that a homogenous distribution of the carboxylic/carboxylate groups must play a major role in the crystallinity observed for the alkane chains in the SAMs organized at large modification time. Earlier results reported by Chambers [11] et. al. on ferrocene terminated and amide-containing alkanethiol mixed monolayers, lead to an homogeneous distribution of the thiolates driven by buried interchain hydrogen-bonding

interactions. More recently, Pace et. al. reported the first example of the formation of SAMs composed by completely miscible bicomponent domains of UDT and ω-substituted alkanethiol derivatives chemisorbed on a metallic surface.[33] The authors argued that the assembly was affected by the relative concentration of both compounds in solution and by their molecular structure. The kinetic control during the formation of mixed crystalline domains at the subnanometer scale was demonstrated for a specific solution molar ratio 1:9 of a pyridine-amide ω-substituted alkanethiol and UDT, respectively. They concluded that the mixed SAM was trapped into a local thermodynamic minimum when the solution concentration of both molecules and the incubation times were varied. Finally, the authors also remarked the still pending goal to achieve the formation of crystalline mixed SAMs under thermodynamic control by stabilization of their hetero-molecular interactions. From since to now, to the best of our knowledge, this goal had not been achieved for mixed SAMs in a wide range of surface ratio compositions under quasi-equilibrium thermodynamic assembly conditions.

4.4. *Conclusions*

- The structure of mixed SAMs of MUA/DT formed at low and high modification times from a lyotropic medium have been characterized by CV, EIS and FT-IRRAS.
- The mixed layers exhibit well-ordered structures, composed by molecules in an up-right configuration with favored adsorption of the polar component (-COOH) from the micelles onto Au (111) surfaces.

185

- The reductive desorption of SAMs shows one CV single peak, which is typical of macroscopically homogeneous films.

- CV, EIS and IRRAS have demonstrated a clear improvement in the mixing properties of these assemblies to the molecular level with the increase of time, which is attributed to an increment in the MUA/DT hetero-intermolecular interactions that probably occurs at quasi-equilibrium thermodynamic conditions.

- The degree of the miscibility of both components has been addressed varying the modification time where their spatial distribution can be controlled by creating two surface patterns:

(1) The first one consists in small nanodomains of like molecules formed probably by kinetically trapped metastable compositions.
(2) The second one is a molecularly mixed monolayer favored by interactions between unlike molecules.

- Depending on the applications, both type of SAM-based patterns are attractive for electron/charge transport across molecular and nanoscale junctions (*e.g. molecular electronics*), as biomimetic surfaces for effective electrostatic immobilization of charged biomolecules, and to create specific molecular recognition or receptor sites (*e.g. design of biomaterials and biocompatible nanomaterials, biosensing, etc.*).

186

4.5. Appendix

A. Bragg-Williams thermodynamic approach for binary SAMs

Bragg-William theory describes phase diagrams thermodynamics on binary alloys where their composition is explained by the nature of their binding forces. Such idea can be extrapolated to binary SAMs formed from solutions of alkanethiols with different alkyl chain length (*Lg = longer and Sh = shorter chain*) (1). [12] In our case, Lg and Sh refers to MUA and DT molecules forming SAMs with different terminal groups and thus, interaction energies. The following approximations are assumed:

(I)   Thiols in solution are dilute and not interacting

(II)   Nearest neighbours interactions are only considered

(III)   Internal structure of adsorbates is the same in solution as in the monolayer.

$$MUA_{soln} + DT_{soln} \longleftrightarrow MUA_{SAM} + DT_{SAM} \qquad (A1)$$

The chemical potential of a thiol in solution and within the monolayer can be expressed by equations (A2) and (A3):

$$\mu_i^{soln} = \mu_i^\dagger + kT\, lnY_i \qquad (A2)$$

$$\mu_i^{SAM} = \mu^* + kT\, lnX_i + \varpi(1-X_i)^2 \qquad (A3)$$

where Y_i is the mole fraction of the thiol in solution and $\mu_i^\dagger$ is the chemical potential of the thiol at infinite dilution, μ^* is the chemical potential of the

187

thiolate in the single component monolayer, X_i is the mole fraction of the thiol in the binary arrays ($X_i + X_j = 1$, $i = MUA$ and $j = DT$), and ϖ is the interaction parameter describing intermolecular interactions within the 2-D assembly.

Then, the interaction parameter is obtained from the difference in the internal energy between the two-component mixed (Eqn. A4) and the two-separate pure alkanethiolate SAMs (Eqn. A5 - *reference state*), and is defined by the equation A6:

$$E_{mixed}^{SAM} = [\omega_{MUA\text{-}MUA} N_{MUA\text{-}MUA}^{SAM} + \omega_{DT\text{-}DT} N_{DT\text{-}DT}^{SAM} + \omega_{MUA\text{-}DT} N_{MUA\text{-}DT}^{SAM}] \quad (A4)$$

$$E_{ref}^{SAM} = \frac{Z}{2} [\omega_{MUA\text{-}MUA} N_{MUA}^{SAM} + \omega_{DT\text{-}DT} N_{DT}^{SAM}] \quad (A5)$$

$$\varpi = \frac{Z}{2} [2\omega_{MUA\text{-}DT} - \omega_{MUA\text{-}MUA} - \omega_{DT\text{-}DT}] \quad (A6)$$

ω_{ij} is the interaction energy between the molecules i and j, N_{ij}^{SAM} is the number of nearest-neighbour interactions of a specific type within the SAM, N_i^{SAM} is the number of molecules of the kind i in the monolayer and Z is the number of nearest neighbours.

The aim of this model is obtaining a thermodynamic relationship between the surface mole fraction of a component i, X_{MUA}, and the mole fraction ratio in solution of both components, $R_{soln} = \frac{Y_{MUA}}{Y_{DT}}$. To attain this objective, the change in the Gibbs free energy for the formation of a binary SAM is determined ($\Delta f = \chi_{MUA}(\mu_{MUA}^{SAM} - \mu_{MUA}^{soln}) + \chi_{DT}(\mu_{DT}^{SAM} - \mu_{DT}^{soln})$, and the definitions of the chemical potentials for thiols in solution and thiolates in the

SAM (Eqns. A2 and A3) inserted in this expression. Then, it can be deduced the free energy of mixing of both components in the monolayer:

$$\Delta f = X_{DT}\left(\mu_{DT}^{*}-\mu_{DT}^{\dagger}\right) - X_{DT}\, kT\, lnY_{DT} - \Delta f_{mixing}^{SAM} \qquad (A7)$$

where the free energy of mixing of the individual molecules in the SAM is:

$$\Delta f_{mixing}^{SAM} = kT(X_{MUA}lnX_{MUA}+ X_{DT}lnX_{DT}) + \varpi\, X_{MUA}X_{DT} \quad (A8)$$

The first term in equation A8 represents the entropy of mixing and the second term is the internal energy of mixing (~enthalpy of mixing).

In the case of mixing of both components in the SAM, Eqn. A7 can be minimize respect to X_{MUA}, ($\frac{d(\Delta f)}{dX_{MUA}} = 0$), and after rearrangement the following equation (A9) remains relating the mole fraction of X_{MUA} in the mixed SAMs and the ratio of thiols in solution $R_{soln} = \frac{Y_{MUA}}{Y_{DT}}$:

$$lnR_{soln}= ln\left(\frac{X_{MUA}}{1-X_{MUA}}\right) + \frac{\varpi}{kT}(1-2X_{MUA}) + \frac{\Delta(\Delta\mu)}{kT} \qquad (A9)$$

The two unknown parameters in Eqn. A9 are $\Delta(\Delta\mu)$ and ϖ, as R_{soln} can be controlled experimentally and X_{MUA} can be determined experimentally.

The term $\Delta(\Delta\mu)/kT$ (i.e. shift of X_{MUA} from 0.5 when $R_{soln}= 1$) is related to the preference of one component over the other in the SAM relative to the solution. It can be observed from Eqn. A9 that when $\Delta(\Delta u)> 0$ and $X_{MUA}= 0.5$

the values of R_{soln} will be larger than 1 implying that the driving force for having DT molecule on the surface relative to having it in solution is greater than that for MUA. When $\Delta(\Delta u) < 0$, there is a shift of R_{soln} values to lower values than 1 and MUA is enriched on the surface.

4.6. References

1.   Huskens, J.; Deij, M. A.; Reinhoudt, D. N. Attachment of Molecules at a Molecular Printboard by Multiple Host-Guest Interactions. *Angew. Chem., Int. Ed.* **2002**, *41*, 4467-4471.

2.   Coleman, A. C.; Areephong, J.; Vicario, J.; Meetsma, A.; Browne, W. R.; Feringa, B. L. In Situ Generation of Wavelength-Shifting Donor-Acceptor Mixed-Monolayer-Modified Surfaces. *Angew. Chem., Int. Ed.* **2010**, *49*, 6580-6584.

3.   Shamai, T.; Ophir, A.; Selzer, Y. Fabrication and Characterization of "On-Edge" Molecular Junctions for Molecular Electronics. *Appl. Phys. Lett.* **2007**, *91*, 102108/102101-102108/102103.

4.   Kay, E. R.; Leigh, D. A.; Zerbetto, F. Synthetic Molecular Motors and Mechanical Machines. *Angew. Chem., Int. Ed.* **2007**, *46*, 72-191.

5.   Balzani, V.; Credi, A.; Raymo, F. M.; Stoddart, J. F. Artificial Molecular Machines. *Angew. Chem., Int. Ed.* **2000**, *39*, 3348-3391.

6.   Browne, W. R.; Feringa, B. L. Making Molecular Machines Work. *Nat. Nanotechnol.* **2006**, *1*, 25-35.

7.   Chen, Y.-S.; Hong, M.-Y.; Huang, G. S. A Protein Transistor Made of an Antibody Molecule and Two Gold Nanoparticles. *Nature Nanotechnol.* **2012**, *7*, 197-203.

8.   Love, J. C.; Estroff, L. A.; Kriebel, J. K.; Nuzzo, R. G.; Whitesides, G. M. Self-Assembled Monolayers of Thiolates on Metals as a Form of Nanotechnology. *Chem. Rev.* **2005**, *105*, 1103-1169.

9.   Hobara, D.; Kakiuchi, T. Domain Structure of Binary Self-Assembled Monolayers Composed of 3-Mercapto-1-Propanol and 1-Tetradecanethiol on Au(111) Prepared by Coadsorption. *Electrochem. Commun.* **2001**, *3*, 154-157.

10.   Hobara, D.; Sasaki, T.; Imabayashi, S.-i.; Kakiuchi, T. Surface Structure of Binary Self-Assembled Monolayers Formed by Electrochemical Selective Replacement of Adsorbed Thiols. *Langmuir* **1999**, *15*, 5073-5078.

11.   Chambers, R. C.; Inman, C. E.; Hutchison, J. E. Electrochemical Detection of Nanoscale Phase Separation in Binary Self-Assembled Monolayers. *Langmuir* **2005**, *21*, 4615-4621.

12.   Folkers, J. P.; Laibinis, P. E.; Whitesides, G. M.; Deutch, J. Phase-Behavior of 2-Component Self-Assembled Monolayers of Alkanethiolates on Gold. *J. Phys. Chem.* **1994**, *98*, 563-571.

13.   Hobara, D.; Ota, M.; Imabayashi, S.; Niki, K.; Kakiuchi, T. Phase Separation of Binary Self-Assembled Thiol Monolayers Composed of 1-Hexadecanethiol and 3-Mercaptopropionic Acid on Au(111) Studied by Scanning Tunneling Microscopy and Cyclic Voltammetry. *J. Electroanal. Chem.* **1998**, *444*, 113-119.

14.   Bertilsson, L.; Liedberg, B. Infrared Study of Thiol Monolayer Assemblies on Gold: Preparation, Characterization, and Functionalization of Mixed Monolayers. *Langmuir* **1993**, *9*, 141-149.

15.   Imabayashi, S.; Gon, N.; Sasaki, T.; Hobara, D.; Kakiuchi, T. Effect of Nanometer-Scale Phase Separation on Wetting of Binary Self-Assembled Thiol Monolayers on Au(111). *Langmuir* **1998**, *14*, 2348-2351.

16.   Stranick, S. J.; Parikh, A. N.; Tao, Y. T.; Allara, D. L.; Weiss, P. S. Phase Separation of Mixed-Composition Self-Assembled Monolayers into Nanometer Scale Molecular Domains. *J. Phys. Chem.* **1994**, *98*, 7636-7646.

17.   Yan, D.; Jordan, J. L.; Burapatana, V.; Jennings, G. K. Formation of n-Alkanethiolate Self-Assembled Monolayers onto Gold in Aqueous Micellar Solutions of n-Alkyltrimethylammonium Bromides. *Langmuir* **2003**, *19*, 3357-3364.

18.   Yan, D.; Saunders, J. A.; Jennings, G. K. Enhanced Chain Densities of n-Alkanethiolate Self-Assembled Monolayers on Gold from Aqueous Micellar Solutions. *Langmuir* **2000**, *16*, 7562-7565.

19.   García Raya, D.; Madueno, R.; Blazquez, M.; Pineda, T. Formation of a 1,8-Octanedithiol Self-Assembled Monolayer on Au(111) Prepared in a Lyotropic Liquid-Crystalline Medium. *Langmuir* **2010**, *26*, 11790-11796.

20.   Garcia Raya, D.; Silien, C.; Blazquez, M.; Pineda, T.; Madueno, R. Electrochemical and AFM Study of the 2D-Assembly of Colloidal Gold Nanoparticles on Dithiol SAMs Tuned by Ionic Strength. *J. Phys. Chem. C* **2014**, *118*, 14617-14628.

21.   Gonzalez-Granados, Z.; Sanchez-Obrero, G.; Madueno, R.; Sevilla, J. M.; Blazquez, M.; Pineda, T. Formation of Mixed Mono layers from 11-Mercaptoundecanoic Acid and Octanethiol on Au(111) Single Crystal Electrode under Electrochemical Control. *J. Phys. Chem. C* **2013**, *117*, 24307-24316.

22.   Kakiuchi, T.; Iida, M.; Gon, N.; Hobara, D.; Imabayashi, S.; Niki, K. Miscibility of Adsorbed 1-Undecanethiol and 11-Mercaptoundecanoic Acid Species in Binary Self-Assembled Monolayers on Au(111). *Langmuir* **2001**, *17*, 1599-1603.

23.   Azehara, H.; Yoshimoto, S.; Hokari, H.; Akiba, U.; Taniguchi, I.; Fujihira, M. Investigation of the Structure of Self-Assembled Monolayers of Asymmetrical Disulfides on Au(111) Electrodes by Electrochemical Desorption. *J. Electroanal. Chem.* **1999**, *473*, 68-74.

24.   Ooi, Y.; Hobara, D.; Yamamoto, M.; Kakiuchi, T. Ideal Nonideality in Adsorption of 2-Aminoethanethiol and 2-Mercaptoethane Sulfonic Acid To Form Electrostatically Stabilized Binary Self-Assembled Monolayers on Au(111). *Langmuir* **2005**, *21*, 11185-11189.

25.   Kakiuchi, T.; Usui, H.; Hobara, D.; Yamamoto, M. Voltammetric Properties of the Reductive Desorption of Alkanethiol Self-Assembled Monolayers from a Metal Surface. *Langmuir* **2002**, *18*, 5231-5238.

26.   Kitagawa, Y.; Hobara, D.; Yamamoto, M.; Kakiuchi, T. Counterion Binding Induces Attractive Interactions between Negatively-Charged Self-Assembled Monolayer of 3-Mercaptopropionic Acid on Au(111) in Reductive Desorption. *J. Solid State Electrochem.* **2008**, *12*, 461-469.

27.   Laibinis, P. E.; Fox, M. A.; Folkers, J. P.; Whitesides, G. M. Comparisons of Self-Assembled Monolayers on Silver and Gold: Mixed Monolayers Derived from $HS(CH_2)_{21}X$ and $HS(CH_2)_{10}Y$ (X, Y = CH_3, CH_2OH) Have Similar Properties. *Langmuir* **1991**, *7*, 3167-3173.

28.   Bain, C. D.; Evall, J.; Whitesides, G. M. Formation of Monolayers by the Coadsorption of Thiols on Gold - Variation in the Head group, Tail Group, and Solvent. *J. Am. Chem. Soc.* **1989**, *111*, 7155-7164.

29.   Carot, M. L.; Macagno, V. A.; Paredes-Olivera, P.; Patrito, E. M. Structure of Mixed Carboxylic Acid Terminated Self-Assembled Monolayers: Experimental and Theoretical Investigation. *J. Phys. Chem. C* **2007**, *111*, 4294-4304.

30.   Yan, D.; Saunders, J. A.; Jennings, G. K. Kinetics of Formation for n-Alkanethiolate Self-Assembled Monolayers onto Gold in Aqueous Micellar Solutions of $C_{12}E_6$ and $C_{12}E_7$. *Langmuir* **2002**, *18*, 10202-10212.

31.   Ganesh, V.; Lakshminarayanan, V. Self-Assembled Monolayers of Alkanethiols on Gold Prepared in a Hexagonal Lyotropic Liquid Crystalline Phase of Triton X-100/Water System. *Langmuir* **2006**, *22*, 1561-1570.

32.   Bragg, W. L.; Williams, E. J. Effect of Thermal Agitation on Atomic Arrangement in Alloys. *Proc. R. Soc. London, Ser. A* **1934**, *145*, 699-730.

33.   Pace, G.; Petitjean, A.; Lalloz-Vogel, M.-N.; Harrowfield, J.; Lehn, J.-M.; Samori, P. Subnanometer-Resolved Patterning of Bicomponent Self-Assembled Monolayers on Au(111). *Angew. Chem., Int. Ed.* **2008**, *47*, 2484-2488.

34.   Chen, S.; Li, L.; Boozer, C. L.; Jiang, S. Controlled Chemical and Structural Properties of Mixed Self-Assembled Monolayers of Alkanethiols on Au(111). *Langmuir* **2000**, *16*, 9287-9293.

35.   Garcia-Raya, D.; Madueno, R.; Sevilla, J. M.; Blazquez, M.; Pineda, T. Electrochemical Characterization of a 1,8-Octanedithiol Self-Assembled Monolayer (ODT-SAM) on a Au(111) Single Crystal Electrode. *Electrochim. Acta* **2008**, *53*, 8026-8033.

36.   Sabatani, E.; Rubinstein, I.; Maoz, R.; Sagiv, J. Organized Self-Assembling Monolayers on Electrodes : Part I. Octadecyl Derivatives on Gold. *J. Electroanal. Chem.* **1987**, *219*, 365-371.

37.   Finklea, H. O.; Hanshew, D. D. Electron-Transfer Kinetics in Organized Thiol Monolayers with Attached Pentaammine(Pyridine)Ruthenium Redox Centers. *J. Am. Chem. Soc.* **1992**, *114*, 3173-3181.

38.   Adams, D. M.; Brus, L.; Chidsey, C. E. D.; Creager, S.; Creutz, C.; Kagan, C. R.; Kamat, P. V.; Lieberman, M.; Lindsay, S.; Marcus, R. A.; "et.al.". Charge Transfer on the Nanoscale: Current Status. *J. Phys. Chem. B* **2003**, *107*, 6668-6697.

39.   Hsu, C.-P. Application of the Sequential Formula: The Electronic Coupling and the Distance Dependence in the Electron Transfer of Ferrocene-Terminated Alkanethiol Monolayers. *J. Electroanal. Chem.* **1997**, *438*, 27-35.

40.   Smalley, J. F.; Feldberg, S. W.; Chidsey, C. E. D.; Linford, M. R.; Newton, M. D.; Liu, Y.-P. The Kinetics of Electron Transfer Through Ferrocene-Terminated Alkanethiol Monolayers on Gold. *J. Phys. Chem.* **1995**, *99*, 13141-13149.

41.   Slowinski, K.; Fong, H. K. Y.; Majda, M. Mercury-Mercury Tunneling Junctions. 1. Electron Tunneling across Symmetric and Asymmetric Alkanethiolate Bilayers. *J. Am. Chem. Soc.* **1999**, *121*, 7257-7261.

42.   Holmlin, R. E.; Ismagilov, R. F.; Haag, R.; Mujica, V.; Ratner, M. A.; Rampi, M. A.; Whitesides, G. M. Correlating Electron Transport and Molecular Structure in Organic Thin Films. *Angew. Chem., Int. Ed.* **2001**, *40*, 2316-2320.

43.   Engelkes Vincent, B.; Beebe Jeremy, M.; Frisbie, C. D. Length-Dependent Transport in Molecular Junctions Based on SAMs of Alkanethiols and Alkanedithiols: Effect of Metal Work Function and Applied Bias on Tunneling Efficiency and Contact Resistance. *J. Am. Chem. Soc.* **2004**, *126*, 14287-14296.

44.   Krysinski, P.; Brzostowska-Smolska, M. Three-Probe Voltammetric Characterization of Octadecanethiol Self-Assembled Monolayer Integrity on Gold Electrodes. *J. Electroanal. Chem.* **1997**, *424*, 61-67.

45.   Janek, R. P.; Fawcett, W. R.; Ulman, A. Impedance Spectroscopy of Self-Assembled Monolayers on Au(111): Sodium Ferrocyanide Charge Transfer at Modified Electrodes. *Langmuir* **1998**, *14*, 3011-3018.
46.   Geblewicz, G.; Schiffrin, D. J. Electron Transfer between Immiscible Solutions. The Hexacyanoferrate-Lutetium Biphthalocyanine System. *J. Electroanal. Chem.* **1988**, *244*, 27-37.

47.   Peter, L. M.; Duerr, W.; Bindra, P.; Gerischer, H. Effect of Alkali Metal Cations on the Rate of the Hexacyanoferrate(4-)/Hexacyanoferrate(3-) Electrode Process. *J. Electroanal. Chem.* **1976**, *71*, 31-50.

48.   Xing, Y. F.; Li, S. F. Y.; Lau, A. K. H.; O'Shea, S. J. Electrochemical Impedance Spectroscopy Study of Mixed Thiol Monolayers on Gold. *J. Electroanal. Chem.* **2005**, *583*, 124-132.

49.   Becka, A. M.; Miller, C. J. Electrochemistry at ω-Hydroxy Thiol Coated Electrodes. 3. Voltage Independence of the Electron Tunneling Barrier and Measurements of Redox Kinetics at Large Overpotentials. *J. Phys. Chem.* **1992**, *96*, 2657-2668.

50.   Terrettaz, S.; Becka, A. M.; Traub, M. J.; Fettinger, J. C.; Miller, C. J. ω-Hydroxythiol Monolayers at Au Electrodes. 5. Insulated Electrode Voltammetric Studies of Cyano/Bipyridyl Iron Complexes. *J. Phys. Chem.* **1995**, *99*, 11216-11224.

51.   Miller, C.; Cuendet, P.; Graetzel, M. Adsorbed ω-Hydroxy Thiol Monolayers on Gold Electrodes: Evidence for Electron Tunneling to Redox Species in Solution. *J. Phys. Chem.* **1991**, *95*, 877-886.

52.   Becka, A. M.; Miller, C. J. Electrochemistry at Omega-Hydroxy Thiol Coated Electrodes .4. Comparison of the Double-Layer at Omega-Hydroxy Thiol and Alkanethiol Monolayer Coated Au Electrodes. *J. Phys. Chem.* **1993**, *97*, 6233-6239.

53.   Allara, D. L.; Nuzzo, R. G. Spontaneously Organized Molecular Assemblies. 2. Quantitative Infrared Spectroscopic Determination of Equilibrium Structures of Solution-Adsorbed n-Alkanoic Acids on an Oxidized Aluminum Surface. *Langmuir* **1985**, *1*, 52-66.

54.   Laibinis, P. E.; Whitesides, G. M.; Allara, D. L.; Tao, Y. T.; Parikh, A. N.; Nuzzo, R. G. Comparison of the Structures and Wetting Properties of Self-Assembled Monolayers of n-Alkanethiols on the Coinage Metal Surfaces, Copper, Silver, and Gold. *J. Am. Chem. Soc.* **1991**, *113*, 7152-7167.

55.   Nuzzo, R. G.; Fusco, F. A.; Allara, D. L. Spontaneously Organized Molecular Assemblies .3. Preparation and Properties of Solution Adsorbed Monolayers of Organic Disulfides on Gold Surfaces. *J. Am. Chem. Soc.* **1987**, *109*, 2358-2368.

56.   Nuzzo, R. G.; Dubois, L. H.; Allara, D. L. Fundamental Studies of Microscopic Wetting on Organic Surfaces. 1. Formation and Structural Characterization of a Self-Consistent Series of Polyfunctional Organic Monolayers. *J. Am. Chem. Soc.* **1990**, *112*, 558-569.

57.   Porter, M. D.; Bright, T. B.; Allara, D. L.; Chidsey, C. E. D. Spontaneously Organized Molecular Assemblies. 4. Structural Characterization of Normal-Alkyl Thiol Monolayers on Gold by Optical Ellipsometry, Infrared-Spectroscopy, and Electrochemistry. *J. Am. Chem. Soc.* **1987**, *109*, 3559-3568.

58.   Snyder, R. G.; Hsu, S. L.; Krimm, S. Vibrational Spectra in the Carbon-Hydrogen Stretching Region and the Structure of the Polymethylene Chain. *Spectrochim. Acta, Part A* **1978**, *34A*, 395-406.

59.   Snyder, R. G.; Strauss, H. L.; Elliger, C. A. Carbon-Hydrogen Stretching Modes and the Structure of n-Alkyl Chains. 1. Long, Disordered Chains. *J. Phys. Chem.* **1982**, *86*, 5145-5150.

60.   MacPhail, R. A.; Strauss, H. L.; Snyder, R. G.; Elliger, C. A. Carbon-Hydrogen Stretching Modes and the Structure of n-Alkyl Chains. 2. Long, All-Trans Chains. *J. Phys. Chem.* **1984**, *88*, 334-341.

61.   Bethencourt, M. I.; Srisombat, L.-o.; Chinwangso, P.; Lee, T. R. SAMs on Gold Derived from the Direct Adsorption of Alkanethioacetates Are Inferior to Those Derived from the Direct Adsorption of Alkanethiols. *Langmuir* **2009**, *25*, 1265-1271.

62.   Sugihara, K.; Shimazu, K.; Uosaki, K. Electrode Potential Effect on the Surface pKa of a Self-Assembled 15-Mercaptohexadecanoic Acid Monolayer on a Gold/Quartz Crystal Microbalance Electrode. *Langmuir* **2000**, *16*, 7101-7105.

63.   Jiang, X.; Ataka, K.; Heberle, J. Influence of the Molecular Structure of Carboxyl-Terminated Self-Assembled Monolayer on the Electron Transfer of Cytochrome c Adsorbed on an Electrode: In Situ Observation by Surface-Enhanced Infrared Absorption Spectroscopy. *J. Phys. Chem. C* **2008**, *112*, 813-819.

CHAPTER 5

Patterning Influence in Surface pKa of MUA/DT Mixed SAMs

5. Patterning Influence in Surface pKa of MUA/DT Mixed SAMs

5.1. Introduction

In the previous chapter, it has been demonstrated that the surface coverage of MUA and DT can be controlled in binary SAMs formed on Au(111) surfaces from a micellar medium by changing the molar ratio of both molecules.[1] Even though homogenous mixing of the components is achieved, different mixing patterns were proposed to form upon variation of the modification time. Thus, the formation of small nanodomains of like-molecules (MUA-MUA and DT-DT) seems to be favoured at lower times (*i.e. non-thermodynamic conditions*) as compared to monolayers composed of unlike-components (MUA-DT) molecularly mixed that seems to prevail at higher ones (*i.e. near to thermodynamic conditions*).

199

Control in the spatial confinement of individual functional molecules and nano-objets on surfaces (*i.e. surface nanopatterning*) is important for a wide variety of applications.[2] In particular, the design of devices based on molecular electronics and junctions is actually of special relevance, where surface chemistry tailored with SAMs and the presence of structural defects in the molecular constituents matter their electrical and thermal performance.[3-5] Thus, the formation of molecularly mixed patterns of components with a high structural order in a wide range of surface compositions, as argued to be the case for MUA-DT SAMs formed from micellar media under equilibrium conditions, might meet these challenging requirements. Additionally, this provides the possibility to explore the performance of organic electronic devices according to well-defined and tuneable gradients of rectification, where local molecular environment affects the interfacial transport physics.[4, 5]

These multicomponent SAM surfaces may also be biocompatible and stimuli responsive (*e.g. electrical, chemical/biochemical, optical, temperature, etc.*),[6, 7] where their composition, organization, thickness, conformation and mixing of the components play a crucial role in tailoring such surface properties.[8] Then, surface gradients of these SAMs can be tuned between "on-off" states that modulate, for example, the activity and function of biomolecules, protein immobilization and cell adhesion (*e.g. pH responsive biomimetic SAMs containing acid-base ionisable groups diluted into a hydrophobic environment*).[6, 7] This is of particular importance to create molecular recognition or receptor sites for controlling the specific adsorption of different kind of macromolecules, such as proteins, in prospect of getting

insight into the design of biocompatible surfaces and nanomaterials to develop new biosensing and biomedical applications.[9-18]

At present, mixed SAMs offers the best option for controlling the density and spatial distribution of biomolecules on surfaces while preserving their biological activity in many cases. In the particular case of redox proteins either covalently or non-covalently bound to these SAMs, fundamental understanding of electron transfer (ET) processes and control of electrochemical reactions at surfaces can be gained by mimicking the biological milieu on an electrode.[10, 19-21] Proteins can be non-covalently immobilized on surfaces by the balance of electrostatic and hydrophobic interactions between its constituent amino-acid residues and the components of the mixed SAMs. Specifically, ω-alkanethiol compounds containing ionizable carboxyl and/or amino end groups have been employed to anchor charged proteins on SAMs as a manner to study the influence of the SAM/electrolyte interface on the redox protein behavior. [22-25]

Several factors can affect the interfacial properties of SAMs, and thus, the interaction with biomolecules such as, the polarity of the surface, hydrogen bonding effects, interfacial electrostatic fields, and the local structure of the solvent among others.[26] In this sense, the knowledge of the acid/base properties of these functionalized surface-confined molecules becomes an important parameter to develop complex molecular assemblies.

Contact angle titration,[27,28] quartz crystal microbalance,[28,29] amperometry,[30] voltammetry,[31] laser-induced temperature,[32] electrochemical titration,[33-42] double-layer capacitance,[43] and chemical force microscopy measurements [44-46] have been used to determine the surface pK$_a$

of carboxyl- and amine-terminated self-assembled monolayers. Despite the overall changes in the ionization of surface-confined carboxyl groups are broader than what is seen in aqueous environments, the pK$_a$ values measured through different techniques give a wide range of values that fluctuates between 5.2-10. For example, the surface pK$_a$ of MUA was found to be 5.7±0.2 by Indirect Laser-Induced Temperature Jump (ILIT) [32] and 10.3 by double layer-capacitance measurements.[43] In some cases, such a different behavior of the acid/base properties of the SAM might be related to different experimental details used to carry out the experiments.

Electrochemical impedance spectroscopy (EIS) [23, 34, 37, 40, 47] and FTIR [41,42, 48,49] spectroscopies have been also applied to study the acid/base chemistry of ω-carboxyl monolayers. The pK$_a$ values for MUA SAMs determined by EIS and FT-IRRAS measurements are usually ranging between 5.3-8. The reported apparent pK$_a$ (pK$_{1/2}^{app}$) values are 1-4 pH units more alkaline than those for the bulk alkanoic acid pK$_a$ value in 0.1 M NaClO$_4$ aqueous solution.[32] Several factors can cause an apparent increase on the pK$_a$:

(I)   Repulsive interactions between neighboring ionized groups. Their effect on the interfacial protonation-deprotonation process can be predicted by the double layer continuous-charge 1-pK$_a$ model (*Appendix A*).[50]

(II)   Hydrogen bonding between terminal groups

(III) Lowering of the dielectric constant, ε$_S$, in the inner part of the double layer (*Scheme 1-Appendix A*), which affects ion solvation.

(IV) Applying a surface potential, E, more positive than the potential of zero charge, E$_{pzc}$, of the layer.

Therefore, the ionization onset for –COOH moieties on the surface is usually higher and their titration curve extends over several pH units. Such spreading of the titration curves has been invoked to be due to electrostatic interactions between neighboring ionized groups. In a typical 0.1 M monovalent electrolyte solution the distance between ions of the same charge is around 2-3 nm, whereas in a SAM on Au(111) is about 0.5 nm. Moreover, electrostatic interactions are more efficiently reduced by Coulomb screening in solution where Debye screening lengths are around 1 nm for a 1:1 salt at 0.1 M concentration. For that reason, interactions tend to make the ionization of the surface –COOH groups more difficult. This effect increases with the fraction of ionized –COO$^-$, θ. Therefore, the proton concentration near the surface (*Helmholtz plane acid dissociation-PAD. Appendix A*) is larger than in the bulk solution according to Boltzmann statistics distribution. As a result, because of the –COOH moieties suffer restricted access to the outer space and their ionization is hindered then, the reduced solvation of ionized –COO$^-$ surface groups is responsible for the displacement of the intrinsic $pK_{1/2}^{app}$ value to positive values of pH, and its spreading before complete ionization. Then $pK_{1/2}^{app}$ shifts and titration curves broadening could be explained by the 1-pK$_a$ model assuming an increment of the molecular interaction parameter, $\beta\bar{E}$ (*Appendix A*).

However, a shift of several pH units of the $pK_{1/2}^{app}$ compared to the solution pK$_a$ cannot be easily accounted only by repulsive interactions, and there must be considered aside other factors responsible for explaining such stabilizing behavior of the uncharged state (e.g. hydrogen bonding, [43, 51, 52] ion

solvation/polarity [31, 42, 43, 49, 52-54] or potential effects [34, 42]). In the case of electrochemical techniques where the SAM titration curves are obtained by applying potential to the surface (*e.g. EIS measurements at the half wave potential, E$_{1/2}$, of the Fe(CN)$_6{}^{3-/4-}$ redox reaction*), this can have an influence on the interfacial surface charge and, consequently, in the pK$_{1/2}^{app}$ determined. [34, 42] In this sense, Sanders et al. showed that pK$_{1/2}^{app}$ values of MUA-SAMs determined by EIS using an anionic (Fe(CN$_6$)$^{3-/4-}$) or cationic (Ru(NH$_3$)$_6{}^{3+/2+}$) redox probe were 5.5 and 7.5, respectively.[34] This result was taking as characteristic of the influence that the applied potential has on interfacial pH and its impact on the ionization of the monolayer. The Fe(CN$_6$)$^{3-/4-}$ and Ru(NH$_3$)$_6{}^{3+/2+}$ standard potentials, E$_{1/2}$, applied to the substrate to carry out the EIS experiments are positive and negative, respectively, in respect to the E$_{pzc}$ value of MUA-SAMs (around -0.13 V vs Ag/AgCl reference). In the case of the anionic redox probe, as E$_{applied}$ = +0.2 V > E$_{pzc}$, anionic species of the electrolyte should be in greater concentration in the interface, and then, the interfacial pH should be more basic than the solution value. As a consequence, ionization of –COOH is favored (*i.e. intrinsic pK$_a$ is lowered*) and the subsequent electrostatic repulsion between –COO$^-$ groups and the anionic probe increases the charge resistance values, R$_{CT}$. Therefore, the actual pK$_a$ of the MUA-SAM would lie somewhere between the pK$_{1/2}^{app}$ values determined from both redox probes ($\sim$ 6).

The effect of surface coverage in the pK$_{1/2}^{app}$ values and broadening of the transition region of the titration curves of –COOH/-CH$_3$ terminated binary SAMs has been analyzed by several research groups. Although there are still

some discrepancies in the results reported in literature, the following behaviors have been described:

(I)   Mixed SAMs of short ω-terminated alkanethiols (*e.g. SH-(CH$_2$)$_6$-COOH and SH-(CH$_2$)$_n$-CH$_3$ with n=4-6*) are speculated to have high pK$_{1/2}^{app}$ values because of the greater degree of disorder in these SAMs compared to longer ones (n>10).[27] The argued reason is that –COOH groups would be buried in the monolayers while –CH$_3$ groups were more exposed, which was interpreted as a predominant contribution of microenvironment effects (ion solvation/dielectric constant factors) compared to electrostatic ones in the surface pK$_a$ shift. In the case of mixed SAMs of longer alkyl chain (*e.g. MUA, n=10*), it was observed that increasing the chain length of diluent –CH$_3$ alkanethiols (*e.g. n = 9-12*) raised the surface pK$_a$, reflecting a progressively less polar environment surrounding the –COOH sites. This would also be in agreement with a lower dielectric constant that would disfavor the formation and solvation of –COO$^-$.[27]

(II)   Kakiuchi et al.[43] have argued that SH-(CH$_2$)$_6$-COOH (MHA) SAM leads to a greater magnitude of the pK$_a$ (~8.5) shift than that predicted by the electrostatic mean-field model, and a considerable contribution of hydrogen bonding and hydrophobic effects might be present in the SAM vicinity. However, the dilution of the –COOH groups by SH-(CH$_2$)$_2$-CH$_3$ (PT) molecules decreases the pK$_a$ value in ~0.5 pH units. In a homogenously mixed SAM, this fact would be consistent with the predominant effect of the lowering of the electrostatic interactions compared to the lowering of ε$_S$ by the insertion of –CH$_3$ while decreasing the number of -COOH groups. However, this seems not to reconcile with the results obtained by Kim et

al. for SH-$(CH_2)_2$-COOH (MPA) and ethanethiol (ET) mixed SAMs where surface pK$_a$ of sparsely adsorbed MPA molecules is more sensitive to the increase of hydrophobicity than the reduction of intermolecular interactions, such as hydrogen bonding or repulsive interactions.

As it will be commented in the results and discussion section of this chapter, SAM ordering and backbone length of the –COOH and –CH$_3$ diluent molecules may play a role to reconcile both results. In this sense, it is probable that –COOH/-CH$_3$ mixed SAMs of similar chain lengths and/or some degree of disorder in their structure would reflect a predominant effect of the hydrophobic environment in its interface vicinity while diluting COOH sites. On the other hand, well-ordered and homogenously mixed SAMs composed of longer –COOH and shorter –CH$_3$ alkanethiol molecules *(i.e. –CH$_3$ groups embedded underneath the –COOH moieties)* may reflect a predominant effect of the lowering of in-plane repulsive interactions between –COOH groups as compared to hydrogen bonding or hydrophobicity effects. In fact, it has been inferred that ionization of –COOH groups appears to be independent of the surrounding –CH$_3$ groups even when the alkyl chain length is the same or shorter only by 2 and 4 methylene units than that of the acidic groups. This would be contradictory for a homogeneous distribution of –COOH and –CH$_3$ groups with all of them being accessible by water molecules *(hard sphere diameter of water is 2.5 Å)*, and where –COO$^-$ solvation should be still affected by the hydrophobic environment created by –CH$_3$ groups closely placed underneath. However, -COOH groups could be homogeneously rearranged with its upper part lying on the surrounding –

CH$_3$ terminations, hence minimizing hydrophobic and promoting electrostatic interactions. [49, 55]

(III) Surface patterning of mixed SAMs has been also demonstrated to play a role in the surface pK$_{1/2}$ values determined as a function of –COOH surface coverage. For example, using patterned MUA and dodecanethiol (DDT) SAMs by contact printing, with at least ~1μm of spatial resolution between MUA and DDT patches, it was found that the pK$_{1/2}$ obtained from chemical AFM titration curves was virtually identical for a pure unpatterned -COOH surface and patterned –COOH regions.[54] The same experiment was carried out by contact angle technique. In this case, the titration curves of the patterned surface revealed the pK$_{1/2}$ value to be 5 pH units higher than that of the force titration result, and strongly correlated to the COOH surface coverage percentage. [54] This was assumed to reflect the average property of a chemically inhomogeneous surface.

Aureau et al.[49] carried out titration curves of well-defined mixed carboxyl/methyl-terminated SAMs, with the same number of methylene units (C$_{10}$), grafted on Si(111) by quantitative analysis of calibrated FT-IRRAS spectra. They also observed that the comparison of calculated with experimental titration curves suggests "microscopic" segregation of –COOH and –CH$_3$ domains by considering an acid-base equilibrium mainly determined by electrostatic interactions. In this case, the –COOH groups in the mixed SAMs behave like in a pure acid layer. Thus, the local environment was found to be independent of –COOH surface coverage (*from 31-100 %*) as all the titration curves showed the same pK$_{1/2}$ and

spreading behavior. Contrarily, if a homogeneous behavior had been found accordingly to electrostatic interactions effects, then, a decrease of the pK$_{1/2}$ value and of the spreading of the titration curves (*i.e. lower molecular interactions and* $\beta\bar{E}$ *parameter*) should have been progressively manifested while diminishing –COOH surface coverage.

In this sense, this chapter aims to the systematic study of the acid/base surface properties of MUA and DT mixed SAMs formed from lyotropic medium under different experimental conditions (*See Chapter 4*). Titration curves will be obtained by EIS and FT-IRRAS measurements, and the results analyzed and commented in the framework exposed above. This will allow to get insight into the possible explanation of different acid/base surface behaviors for these 2D-arrays that might be related to the structural organization, surface coverage or spatial distribution (*e.g. different nanopatterns*) of the –COOH surface groups.

5.2. *Materials and Methods*

Chemical reagents. MUA, DT, Triton X-100, K$_4$Fe(CN)$_6$, K$_3$Fe(CN)$_6$ and semiconductor grade purity KOH was purchased from Aldrich-Sigma (purity ≥ 99%). HCl, KNO$_3$, KCl and H$_3$PO$_4$ reagents were from Merck analytical grade. All solutions were prepared with deionized ultrapure water.

Methods. A conventional three electrode cell comprising a platinum coil as the counter electrode, a 50 mM KCl calomel electrode as the reference

electrode and an Au(111) single crystal as the working electrode were used. The polyfaceted and Au(111) surfaces were cleaned and modified with MUA and/or DT as indicated in the protocols described in the Chapter 2 (*Sections 2.3.1. and 2.3.2.*). The adsorption times assayed in lyotropic liquid mixtures were 15 min and 18 hours. Surface compositions of the mixed SAMs were determined as described in the Chapter 4 (*Section 4.3*).[1]

In the pH titration experiments, samples were immersed either in 5 mM HCl or KOH aqueous solutions at the adjusted pH, and allowed to equilibrate during 20 minutes. Then, if necessary, the modified substrates were dried with nitrogen for further characterization by FT-IRRAS (*i.e. non-reactive spreading protocol*).[27] Similarly, samples were transferred to the electrochemical cell containing 1 mM $K_4Fe(CN)_6$ and $K_3Fe(CN)_6$ in 0.1 M phosphate buffered solutions at the corresponding pH, and equilibrated during 20 min. before the EIS measurements were recorded. Titrations were performed from alkaline to acidic direction, and vice versa, by changing the solution pH upon addition of KOH or HCl. Two or three freshly prepared samples for each SAM surface composition were titrated either by EIS or FT-IRRAS methodologies.

Electrochemical characterization was carried out accordingly to the specifications and working conditions included, unless otherwise stated, in the Chapter 2 (*Section 2.4.1.*). Characterization of the samples was also performed by FT-IRRAS as previously indicated (*Chapter 2 – Section 2.4.2.1.*).

Electrochemical and spectroscopic data were further analyzed and processed (*Chapter 2 - Sections 2.4.1.2 and 2.5.*). In the particular case of FT-IRRAS analysis, the relative surface coverage of –COOH (1-θ) and –COO$^-$ (θ) was

determined from the integrated area of the vC=O vibrational bands corresponding to the stretching modes characteristic of carboxylic (1700-1750 cm^{-1}) and carboxylate (1400-1445 cm^{-1}) groups. Similarly, R$_{CT}$ values at acidic and alkaline pH were considered as representative of –COOH and –COO$^-$ covered surfaces, and their changes related to their surface coverage and acid-base interfacial properties (*Appendix A*).

5.3. Results and Discussion

5.3.1. *EIS titration of pure and mixed SAMs of MUA and DT*

As already described, the ability of SAMs to block the electron transfer (ET) of charged redox species in solution is a convenient way to evaluate the quality of a monolayer and its interfacial properties (*Chapter 1 – Section 1.2.9. Chapter 4 – Section 4.3.3*). Figure 1 shows the EIS response (*Nyquist plots*) of the ET of Fe(CN)$_6^{3-/4-}$ on Au surfaces modified with pure and mixed MUA/DT SAMs, at different modification times (15 minutes and 18 h) and surface compositions, as a function of the solution pH.
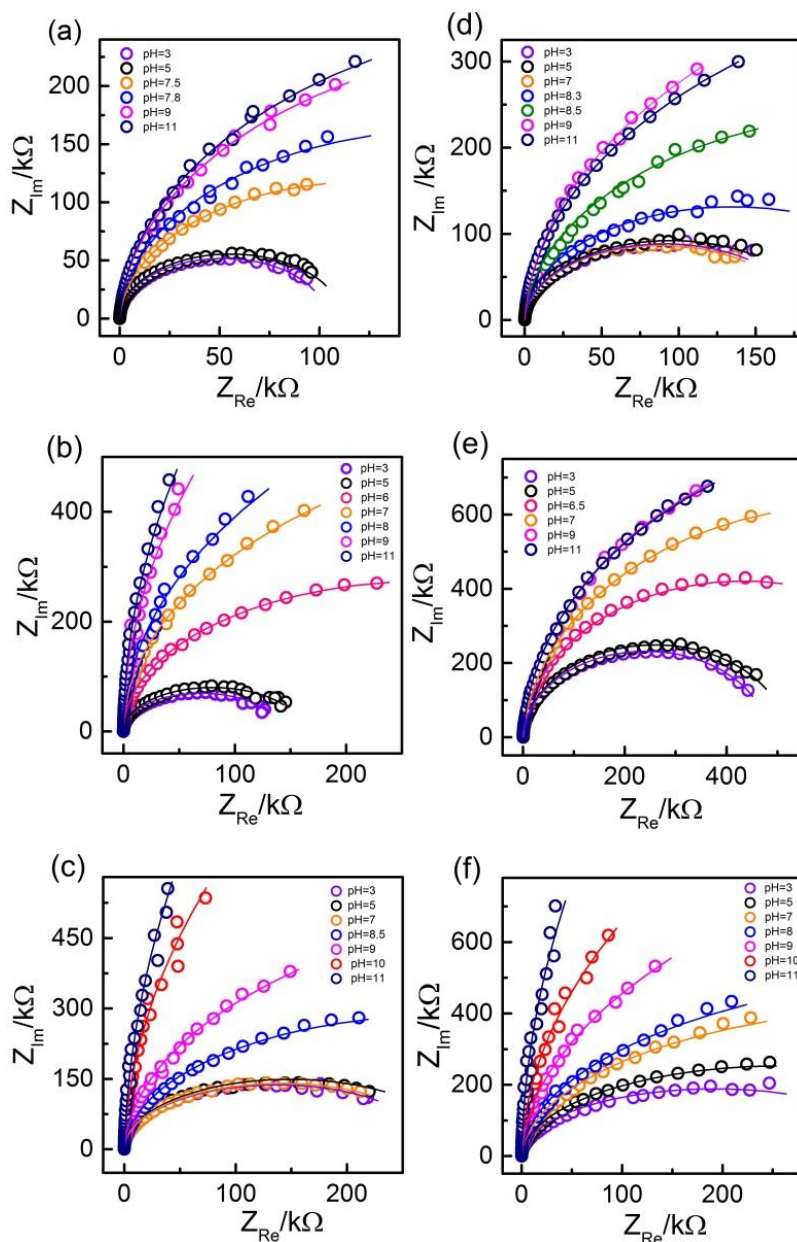
Figure 1. Nyquist plots as a function of pH of SAMs formed by different MUA:DT surface molar ratios at 15 min: a) 1.00/0.00 b) 0.41/0.59 c) 0.15/0.85, and 18h: d) 1.00/0.00 e) 0.60/0.40 f) 0.30/0.70 from a lyotropic medium. E$_{1/2}$ = 0.17 V vs SCE. K$_4$Fe(CN)$_6$/K$_3$Fe(CN)$_6$ in 0.1 M KNO$_3$. The solid lines are the fits to the simplified Randles equivalent circuit (R$_u$[CR$_{ct}$]) without considering mass transfer contribution.

It is observed from the Nyquist plots ($-Z_{im}$ vs Z_{re} representation) that the diameter of the semicircle gets larger while increasing the solution pH, independently of the modification time and surface composition of the SAMs. This is directly related to an increase of the charge transfer resistance values, R_{CT}, due to the influence that SAMs have over the kinetics of the redox reaction. This clearly indicates that the apparent heterogeneous rate constant, k_{ET}^{app}, of the ET interfacial reaction of the $Fe(CN)_6^{3-/4-}$ must be altered by the solution pH in response to the acid-base reaction of the ionisable −COOH groups at the SAMs/electrolyte interface.[34, 37, 40, 56] Hence, the higher the content of deprotonated −COO$^-$ groups is at the surface upon increasing pH the lower is the ET rate of the process. The main reason is that the negatively charged interface prevents the electroactive anions of the redox probe from effectively approaching the surface due to electrostatic repulsion, which in turns causes the depletion of the $Fe(CN)_6^{3-/4-}$ surface concentration. As a result, at high pHs the ET response is further hindered which is manifested as an improvement of the blocking behaviour of the SAM interface. In brief, the charge density of the monolayer interface directly impinges on the experimentally observed R_{CT} values (*Appendix A - Eqns. A7/A8*).[47]

Similarly, the interfacial capacitance (C_{dl}) must be influenced by the dielectric properties of the SAM and its ability to limit the distance of closest approach of the redox probe as a function of the solution pH. Therefore, it is reasonable to assume that observed changes in C_{dl} ($C_{dl} \sim C_m^{SAM}$) would reflect

changes in surface composition of the mixed SAMs and also in the degree of dissociation of the ω–carboxylic groups.[31, 43, 57, 58]

In addition, it is also worth noting that R$_{CT}$ values increased by a factor of ≈ 2 for the pure and mixed SAMs built at the larger modification time (Figure 1d-f) compared to the lower one (Figure 1a-c). As commented in the previous chapter, this is interpreted as a consequence of the improvement in the ET blocking properties of almost defect-free SAM structures formed near-to-equilibrium conditions. Moreover, the almost molecular homogeneous intermixing of MUA and DT domains might give rise to a more effective repulsive electrostatic interaction between the negatively charged carboxylate groups and the Fe(CN)$_6^{-3/-4}$ anions, than the segregated nanodomains of MUA and DT molecules. Consequently, a more homogeneous arrangement of the negatively charged carboxyl groups and, therefore, of the distribution of the interfacial electrical fields at the top of the mixed SAMs would be responsible for such behavior.

The analysis of the impedance spectra has been performed by data fitting to a simplified Randles equivalent circuit consisting of a parallel combination of a capacitor, represented by C, and Faradaic impedance, R$_{CT}$, in series with the uncompensated solution resistance R$_u$ (*Chapter 1 – Section 1.2.9. and Chapter 2 – Section 2.4.1.*). The C and R$_{CT}$ values determined for the mixed SAMs are shown as a function of the solution pH in the Figures 2 and 3.

Figure 2 shows that interfacial capacitance, C, mainly varies with the surface composition of MUA and DT, while changes in C with pH are barely observable for pure MUA and MUA/DT mixed SAMs. The latter effect has

been already reported by Kakiuchi et al.[43], where capacitance titration curves of ionisable SAMs were only applicable to monolayers with shorter chain lengths (n < 10).
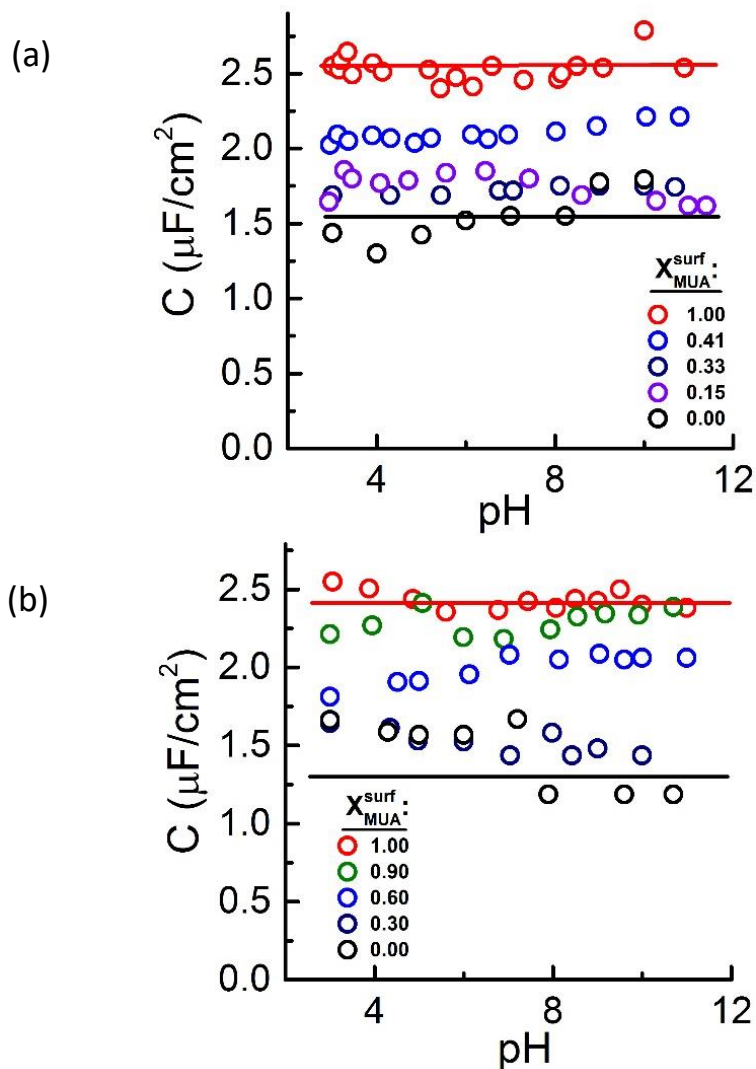

Figure 2. Representation of Capacitance values vs pH for pure and mixed monolayers of MUA and DT formed from a lyotropic environment at a) 15min and b) 18h. χ_{MUA}^{surf} *determined from the RD peak potentials (Eqn. (3) in Chapter 4 – Section 4.3.1) are roughly similar to those obtained from Eqn. 2.*

Then, assuming that there are not significant contributions from ionized groups at the outer layer of the SAMs to the measured capacitance with pH, C could be averaged (*Figure 2 – red and black lines*) with their value only related to the surface composition changes of both components. C would be composed of two capacitances in series: C_m^{SAM} (monolayer) and C_{dl} (double layer). C_m^{SAM} of long chain alkanethiol SAMs is in general more than an order of magnitude smaller than C_{dl} in electrolytes of $\sim$0.1 M concentration.[59] Therefore, the interfacial capacitance ($C^{-1} = C_m^{-1} + C_{dl}^{-1}$), can be assumed to be essentially that of the monolayer ($C \cong C_m^{SAM}$). From a macroscopic perspective, the total capacitance, C, of the binary mixed SAMs will consist of the sum of capacitances C_m^{MUA} and C_m^{DT}, representing the values for a pure SAM of each component, weighted by their mole surface fractions:[57]

$$C = C_m^{MUA} \cdot \chi_{MUA}^{surf} + C_m^{DT} \cdot \chi_{DT}^{surf} = C_m^{MUA} \cdot \chi_{MUA}^{surf} + C_m^{DT} \cdot (1 - \chi_{MUA}^{surf}) \qquad (1)$$

$$\chi_{MUA}^{surf} = \frac{C - C_m^{DT}}{C_m^{MUA} - C_m^{DT}} \qquad (2)$$

The surface composition of mixed SAMs can be calculated by using eqn. (2). The values obtained (χ_{MUA}^{surf}) are in reasonable agreement with those obtained from the CV method, which is based on the peak potential value of the SAM reductive desorption (*Chapter 4 – Section 4.3.1.*), and that are included in the Figures 2 and 3. The underlying limitations of this indirect method are similar to others and, in this particular case, to the assumption that the "effective thickness" is equivalent to the dielectric thickness and remains constant with

215

changes in the mixed SAM composition. Additionally, the low capacitance values would indicate the presence of well-organized and compact SAMs. These kinds of SAMs behave as an ideal dielectric layer that can be analyzed by a simple double layer capacitor model:

$$C = \frac{A}{d}\varepsilon_o \cdot \varepsilon_m \qquad\qquad (3)$$

where C is the SAM capacitance, d the layer thickness, ε_o the permittivity of free space, and ε_m the relative permittivity of the layer.

Then, the relative permittivity determined for the pure SAM should be taken as an average of the film quality. Assuming, that the SAMs are formed by well-packed molecules (either MUA or DT) in an all-trans configuration for the hydrocarbon chains with a tilt angle of 30°, the thickness can be determined by using the equation d = 1.3·10^{-10}·n·cosθ, where n is the number of carbons in the chain and θ the tilt angle of 30° (d=12.5 and 11.2 Å for MUA and DT, respectively).[60] Then, by using eqn. (3), the ε_m values calculated are 1.8-2.0 and 3.4-3.6 for pure MUA and DT SAMs formed at 15 min. and 18 h of modification time, respectively. The value of ε_m for DT agrees with those reported for the dielectric constant of polyethylene and well-ordered alkanethiol SAMs (*e.g. ε_m=2-2.3*).[61-63] Similarly, the values of ε_m for MUA are consistent with the higher polar character of well-packed ω-terminated SAMs (*e.g. ε_m = 3, 4 and 3.5-6.6 for –OH, –SH and –COOH as terminal groups, respectively*).[43, 63-65] These results confirm that these SAMs behave as a dielectric medium of approximately the expected thickness, and in turn they

can be used as a valid method to determine the surface molar composition of their components.

Figure 3 shows that R$_{CT}$ changes with pH are clearly discernable for each SAM in comparison to what happens to interfacial capacitance. Therefore, R$_{CT}$ titration curves reflects the change in the degree of the dissociation of the – COOH groups in the pure MUA and mixed SAMs. Under acidic conditions, the R$_{CT}$ remains constant, which is characteristic of SAMs with interfacial charge densities that keep pH-independent because the –COOH terminal groups are fully protonated and uncharged. Under very basic conditions, the R$_{CT}$ increases to almost attain a limiting value that is greater than that found at acidic pHs. These larger values for R$_{CT}$ are taking as representative of SAMs almost fully deprotonated with high charge densities due to the dissociation of –COOH into –COO$^-$ groups. At intermediate pH values, there is a transition between low to high R$_{CT}$ values, which extends over several pH units while increasing the degree of dissociation of the ionizable groups, θ. Such spreading of the titration curve is due to electrostatic interactions between neighboring charged groups (*i.e. higher spreading relates to a larger* β$\bar{E}$ *interaction parameter – Appendix A*). The pH at the steepest slope of the curves may be taken as the apparent surface pK$_a$ value of the SAM (pK$_{1/2}$). All EIS titration curves showed a single transition, pK$_{1/2}$, for the acid-base equilibrium reaction at the SAM interface.

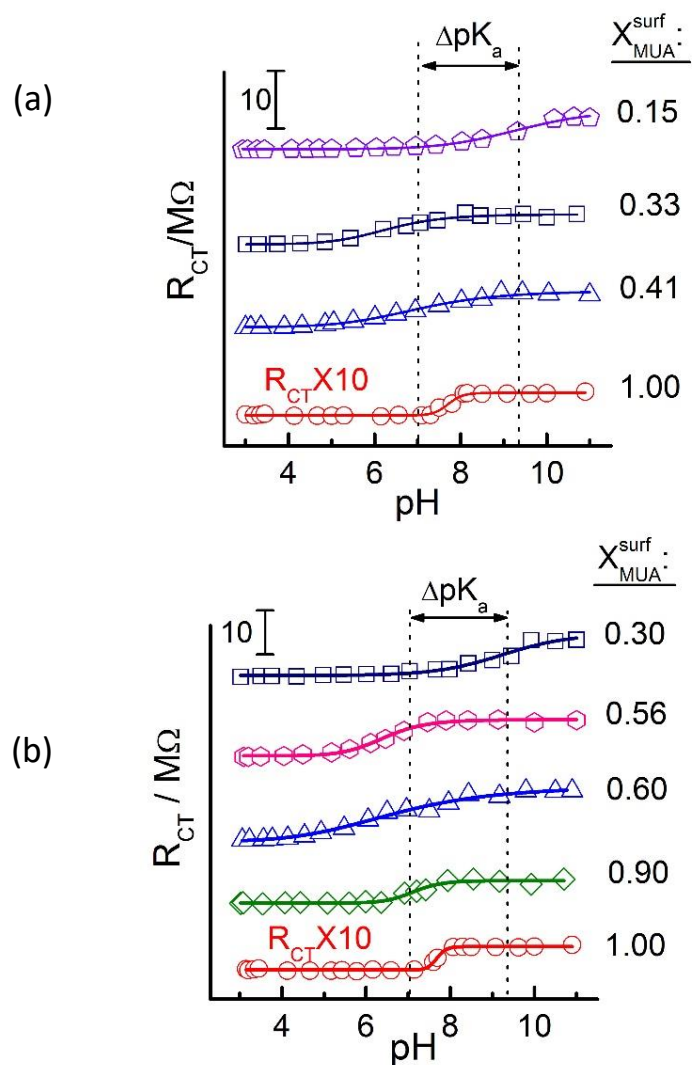**Figure 3.** Titration curves obtained by plotting the R$_{CT}$ values obtained from EIS data fitted by a simplified Randles equivalent circuit as a function of the solution pH. Fe(CN)$_6^{-3/-4}$ was used as redox probe and mixed monolayers of MUA and DT formed at a) 15min and b) 18h from a lyotropic medium with different surface compositions (*Determined from their RD peak potentials: Eqn. (3) in Chapter 4 – Section 4.3.1.*).

Under these experimental conditions, the apparent pK$_{1/2}$ values are 7.7 and 8.3 for the MUA layers formed at low and high modification times, respectively. This is about 3.5 units higher than the pK values of alkanoic acids in solution. As previously commented, such increase in the apparent pK$_{1/2}$ of the MUA SAMs is greater than that predicted by the electrostatic mean-field model, and an additional contribution of hydrogen bonding, ion solvation and hydrophobic effects must be present in the vicinity of the SAM PAD layer (*Introduction and Appendix A*).

Both pK$_{1/2}$ values are very similar to one of the two pK$_a$ values determined for MUA SAMs deposited electrochemically from an alkaline medium (pK$_{1/2}$^{a} = 4.9 and pK$_{1/2}$^{b} = 8.1), as well as the spreading of the titration curves is also quite similar between them (*Chapter 3*). However, the pK$_{1/2}$ values are greater and the spreading of the titration curves narrower compared to that of the MUA SAMs formed from ethanol (pK$_{1/2}$ = 5.7 − *Chapter 3*). pK$_a$ values reported in the literature for -COOH terminated SAMs formed from ethanol, and determined from CV and EIS titration curves using Fe(CN)$_6$$^{3-/4-}$ as redox probe, ranged between 5.3-6.[23, 33, 34, 37, 40, 47] This is in good agreement with the results reported here.

FTIRRAS results confirmed that MUA SAMs formed either from a micellar medium or under potential control were better organized into a crystalline-like structure than those deposited from ethanol (*Chapter 3*), as it has been also reported for other kind of alkanethiol SAMs.[66-69] Then, MUA SAMs with a lower number of structural defects and compactness must be more efficiently stabilized by intermolecular interactions than SAMs with some degree of structural disorder. Consequently, the increment observed in

the pK$_{1/2}$ values of well-organized MUA SAMs can be partially related to the favored electrostatic repulsion between neighboring –COO$^-$ groups. However, the behavior observed for the spreading of the titration curves of the disordered SAMs seems counterintuitive. For that reason, an explanation based on the influencing factors described above could not be addressed. Otherwise, it can be speculated that highly disordered MUA SAMs may behave partially as a "reactive spreading" system even though, they are supposed to be pre-equilibrated at each pH to become into a "non-reactive spreading" system.[53]

Noteworthy, the EIS titration curves of both kinds of MUA/DT mixed SAMs display a similar behavior when the surface composition of MUA, χ_{MUA}^{surf}, is decreased by the insertion of DT molecules (Figure 3a and b). It is observed that dilution of the –COOH groups by DT molecules progressively decreases the pK$_{1/2}$ values up to ~1.5 pH units (Table 1). This trend is also reflected by the intrinsic pK$_a$ (*i.e. in absence of intermolecular interactions*) and $\beta\bar{E}/2.303$ values obtained from the best fits of the 1-pK model [50] (*Appendix A*) to the experimental data (Table 2).[33, 43] In this sense, either the intrinsic pK$_a$ (for similar interaction parameters) or $\beta\bar{E}$ (for a fixed intrinsic pK$_a$) diminish when surface coverage of the acid groups decreases. This is consistent with the predominant effect of the lowering of in-plane repulsive interactions between –COOH groups as compared to hydrophobic effects due to the lowering of the local dielectric constant, ε_S, by the insertion of –CH$_3$ terminal groups.[27, 43] Such behavior is resembled by well-ordered and homogeneously patterned SAMs (*i.e. non-segregated*) with –COOH groups molecularly and/or nanoscopically distributed into 2D arrays, as it would be the case here. [49, 54, 55] Hence,

220

minimizing hydrophobic and promoting electrostatic interactions would be possible by the rearrangement of the –COOH groups to lying on the surrounding –CH$_3$ terminated molecules. [49, 54, 55]

Table 1. Apparent pK values of MUA:DT mixed SAM obtained from titration curves.

χ^{surf} MUA/DT[a]	$pK_{1/2}^{app}$ EIS titration		$pK_{1/2}^{app}$ IR titration	
	15 min	**18 h**	**15 min**	**18 h**
1.00/0.00	7.7	8.3	7.5	7.7
0.90/0.10	-	7.1	6.9	7.2
0.60/0.40	-	6.7	-	9.1
0.41/0.59	7.0	-	4.0/7.3	-
0.30/0.70	6.3	9.2	-	9.4
0.15/0.85	9.4	-	4.5/9.7	-

[a] X_{MUA} and X_{DT} are the surface mole fraction of MUA and DT in the mixed monolayers as determined from Eqn. 3 (Chapter 4) by the CV reductive desorption method. The standard deviations for $pK_{1/2}^{app}$ values are lower than 12 % in all cases.

Nevertheless, when the surface molar ratio of DT is further increased, the pK$_{1/2}$ values display the opposite trend, and a large shift of ~3 pH units (pK$_{1/2}$ ~ 9-9.7) is observed towards the alkaline direction. It seems reasonable to assume that the gradual lessening of the interfacial polarity, which is related to a low dielectric "micro/nano-environment" of the –COOH moieties, contributes to a reduction of the group´s acidity.[27, 31, 37, 42, 52-54] This also relates to the strength of the electrostatic solvation and the stabilization of –COO$^-$ by counterions which depend on the degree of polarity at the SAM/electrolyte interface.

Table 2. Intrinsic pK and interaction parameter, $\beta\overline{E}$ values determined from the fitting of the experimental titration curves of pure and MUA:DT mixed SAMs.

χ^{surf} MUA/DT	EIS titration				IR titration			
	15 min		18 h		15 min		18 h	
	pK$_a$	$\dfrac{\beta\overline{E}}{2.303}$	pK$_a$	$\dfrac{\beta\overline{E}}{2.303}$	pK$_a$	$\dfrac{\beta\overline{E}}{2.303}$	pK$_a$	$\dfrac{\beta\overline{E}}{2.303}$
1.00/0.00	7.2	1	7.9	1	6.2 (6.2)	3 (3)	6.2	3
0.90/0.10	-	-	6.4	1-2	5.9 (6.2)	3 (2.4)	6.4	3
0.60/0.40	-	-	4.7*	5*	-	-	7.2	3
0.56/0.44	-	-	5.5	2	-	-	-	-
0.41/0.59	5.9	2	-	-	5.7 (6.2)	3 (2)	-	-
0.30/0.70	5.6	2	7.6	3	-	-	7.2	3
0.15/0.85	8.1	2	-	-	7.7 (6.2)	3 (6)	-	-

(a) Best fitting $\beta\overline{E}$ values by fixing the intrinsic pK$_a$ are included in parenthesis. When two pK$_a$ are found (IR titrations), the interaction parameter is only determined for the higher value.

Interestingly, this change in behavior occurs at a higher surface coverage of –COOH groups for those SAMs formed at the higher modification time ($\chi_{MUA}^{surf} < 0.3$) than that at the shorter time ($\chi_{MUA}^{surf} < 0.15$). This could be interpreted in the terms of a different spatial distribution of homogeneously mixed binary SAMs, as commented in the previous chapter. When the mixing of –COOH and –CH$_3$ groups is close to the molecular level (*i.e. ideal homogeneously mixed SAMs*), a feasible scenario would be that for a 1:1 surface composition of both components, the electrostatic interactions should decrease to a minimum compared to the pure MUA SAM. Further dilution of –COOH groups beyond $\chi_{MUA}^{surf} < 0.5$ would provoke a gradual increase of hydrophobicity in their local environment, which is due to the excess of –CH$_3$ surface groups that cannot be shielded all by neighboring –

222

COOH moieties. This is more closely resembled by the –COOH/-CH$_3$ mixed SAMs built at higher modifications times which are assumed to better meet the requirement of molecular mixing. Then, the effect of lowering of the local dielectric constant becomes predominant compare to the decrease of electrostatic interactions between neighboring acid groups. In the case of SAMs built at lower times, such effect does not become evident until an excess high enough of –CH$_3$ groups surrounds the MUA-enriched nanodomains (X$_{MUA}^{surf}$ < 0.15). In such situation, both molecularly mixed and a small number of MUA nanodomains (*i.e. highly diluted*) would converge into a less discernable scenario of quite similar local hydrophobic environments.

This conclusion is assumed to be valid in the basis of building well-ordered homogeneously mixed SAMs. However, a similar conclusion could be drawn when –COOH groups highly diluted (*i.e. high –CH$_3$ surface coverages*) become sparsely adsorbed and structurally disordered.[27, 37, 42] Then, the –COOH groups could be buried in the monolayers while –CH$_3$ groups were more exposed, which would also favor the contribution of microenvironment effects (ion solvation/dielectric constant factors) instead of electrostatic ones to the shift of the surface pK$_a$. In such as case, the mixed SAMs formed at lower modification time would be more prone to structural disordering (*X$_{MUA}^{surf}$ < 0.3 – Figures 2 and 7 of Chapter 4*), and the possible influence on the acid-base interfacial behavior should not be discarded. In any case, these results suggest that the distribution of alkanethiolates at the molecular scale can directly modulate the interfacial acid-base properties of binary SAMs, most likely by the changes of cooperative effects of the nearest carboxylic

moieties on their intermolecular interactions as a result of the sort of assembly patterns.

5.3.2. *IR titration of pure and mixed SAMs of MUA and DT*

Figure 4 shows the IRRA spectra of MUA monolayers deposited on Au(111) and subsequently exposed to acid or basic aqueous solutions. These MUA-SAMs show the vibrational absorption bands of the vC=O groups that are usually present at low wavenumbers of the IR region (1300-1800 cm^{-1}). Five bands are clearly identified.[70]

Bands centered at 1740 and 1715 cm^{-1} are assigned to the –C=O stretching modes associated with non-hydrogen and hydrogen bonding interactions of neighboring –COOH groups, respectively.[71, 72] The difference between these vibrational frequencies is due to the weakened C=O bonding strength upon formation of the interactions between the acid groups. The relative intensities of these peaks has been reported as a way to evaluate the quality of the SAMs due to its sensitiveness to the surface flatness and nanotopology of the Au(111) substrates.[73] In the case of single crystal Au(111) surfaces with a very low miscut angle (<0.1°), that are composed by large atomically flat smooth terraces (i.e. >100 nm in diameter), the uniformity of the SAMs is greatly improved by favoring intermolecular interactions. As a consequence, only one peak associated to hydrogen bonded –COOH groups appears (~1715 cm^{-1}).[73] However, in the case of Au(111)-textured surfaces gathering many grains (~20-50 nm in diameter and 1-3 nm in height), both peaks at ~1740 and ~1715 cm^{-1} are present due to the presence of extrinsic structural defects in the SAM (Figures 4-6) that are induced by the surface

topography (*e.g. Au step edges and grain boundaries. Chapter 1 - Section 1.2.8.*).[41, 73] This fact has been suggested to affect the acid-base behavior of carboxylic SAMs, in the way that electrostatic repulsion between terminal groups is lower than at atomically flat gold surfaces.[41, 73]
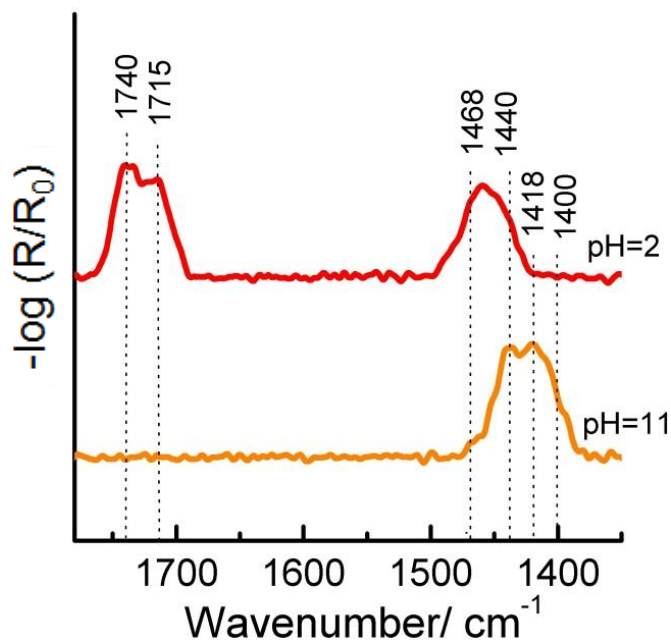

Figure 4. Typical IRRA spectra in the low frequency region of a pure MUA monolayer on Au(111) immersed in acid and alkaline media.

The vibrational band at 1468 cm^{-1} is attributed to the scissors deformation mode of the $-CH_2$ groups (δ_{sc}-CH$_2$) in the alkyl chain of the monolayers. The remaining bands are ascribed to asymmetric, v_{as} (1440 cm^{-1}) and symmetric, v_s (1410-1420 cm^{-1}) stretching modes of carboxylates groups (COO$^-$).[41, 70, 74]

Figures 5 and 6 show IRRA spectra of pure and mixed MUA:DT monolayers formed at 15 minutes and 18 h, respectively, which are titrated from basic to acid pHs (pH range = 2-11). As expected, all the SAMs tested

showed that the stretching modes belonging to carboxylic and carboxylate groups were pH-dependent. When the solution pH decreases, the characteristic vibrational signals corresponding to the −COO⁻ groups diminish while the vC=O stretching band at 1740 cm⁻¹ (*i.e. −COOH non-hydrogen bonded*) and the δ_{sc}-CH$_2$ mode concomitantly increase until the protonation of the MUA molecules is almost attained approximately at pH 4-5 (Figures 4-6). When pH is further decreased (pH=2), the general trend observed is that the δ_{sc}-CH$_2$ band now decreases while the vC=O stretching band at ∼1715 cm⁻¹ (*i.e. −COOH hydrogen bonded*) concomitantly appears and increases. In most of the cases, a small fraction of non-titrated −COO⁻ groups is still observed at the surface (v_{as} at 1440 cm⁻¹) even at this very low pHs. As it will be commented later, these changes must be related to additional structural rearrangements and different tilted orientations of the backbone and the −COOH terminal groups of the SAMs that take place during the titration experiments.

In the attempts to unravel this assumption, IRRA spectra of the SAMs have been analysed in the high wavenumbers region (2800-3000 cm⁻¹) that shows the characteristic absorption bands of the symmetric, d⁺, and asymmetric, d⁻, stretching modes of the -CH$_2$ groups of the hydrocarbon chain.

Figure 5. IR titration spectra of pure and mixed MUA/DT SAMs on Au(111) formed in lyotropic medium after 15 min. $\chi^{surf}_{MUA/DT}$: a) 1.00/0.00, b) 0.41/0.59 and 0.15/0.85.

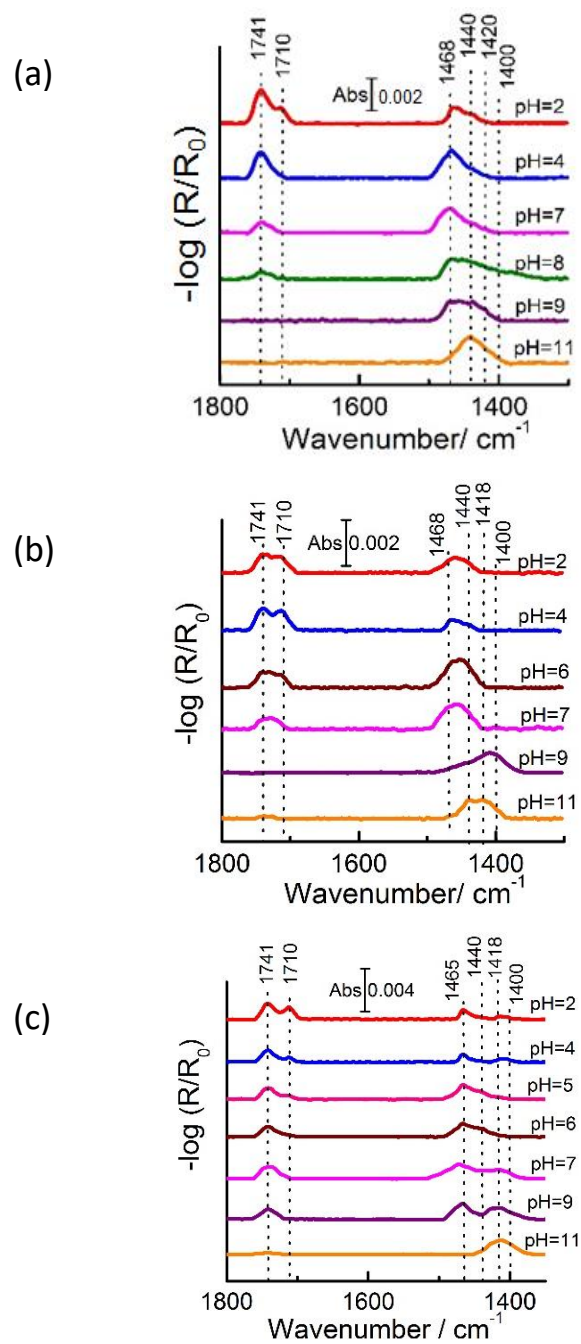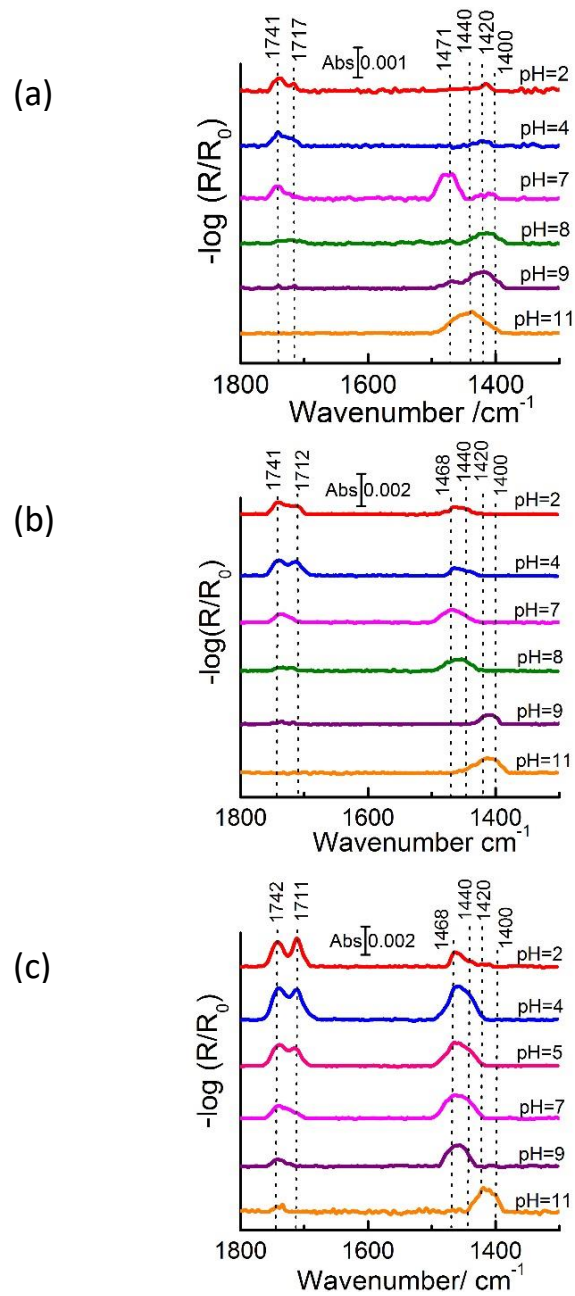**Figure 6.** IR titration spectra of pure and mixed MUA/DT SAMs on Au(111) formed in lyotropic medium after 18 h. $\chi_{MUA/DT}^{surf}$: a) 1.00/0.00, b) 0.60/0.40 and c) 0.30/0.70.

The peak position and width of the d$^+$ and d$^-$ vibrational modes are sensitive to the conformational order of the hydrocarbon chains in alkanethiol SAMs. Densely packed SAMs arranged into a crystalline ordering with the alkyl chains mainly in an all-trans conformation are usually associated with d$^+$ and d$^-$ bands positioned at 2849-2850 and 2818-2819 cm^{-1}, respectively.[61, 71, 75, 76] These bands are broadened and shifted to higher wavenumber when the conformational order of the alkyl chains progressively decreases and the structure becomes increasingly disordered. [61, 71, 75, 76]

Figure 7 shows that all the mixed SAMs formed and equilibrated at pH 11 exhibits a crystalline-like conformational order composition-independent behavior (d$^+$ and d$^-$ bands located at 2850 and 2919 cm^{-1}, respectively), except those formed at 15 minutes with lower MUA surface coverage ($\chi_{MUA/DT}^{surf}$ < 0.41) which exhibited a higher conformational disorder (d$^+$ and d$^-$ bands located at 2853 and 2924 cm^{-1}). This is in agreement with the results already reported in the previous chapter (*Sections 4.3.1 and 4.3.3*).[1] Taking into account that the titrations shown are performed from pH 11 to 2, d$^+$ and d$^-$ band broadens and displaces their position to higher wavenumber while their intensities increase when the pH is progressively diminished (Figure 7a). The changes in the position, intensity and half-width of these bands from that of the originally formed crystalline-like structure is attributed to the disordering of the alkyl chains during the protonation of the –COOH end groups.[76] This is related to the transition dipole moment projections of the C-H stretching vibrations along the surface normal direction and, consequently to configurations that are different from the canted orientations at SAMs with a crystalline-like structure.
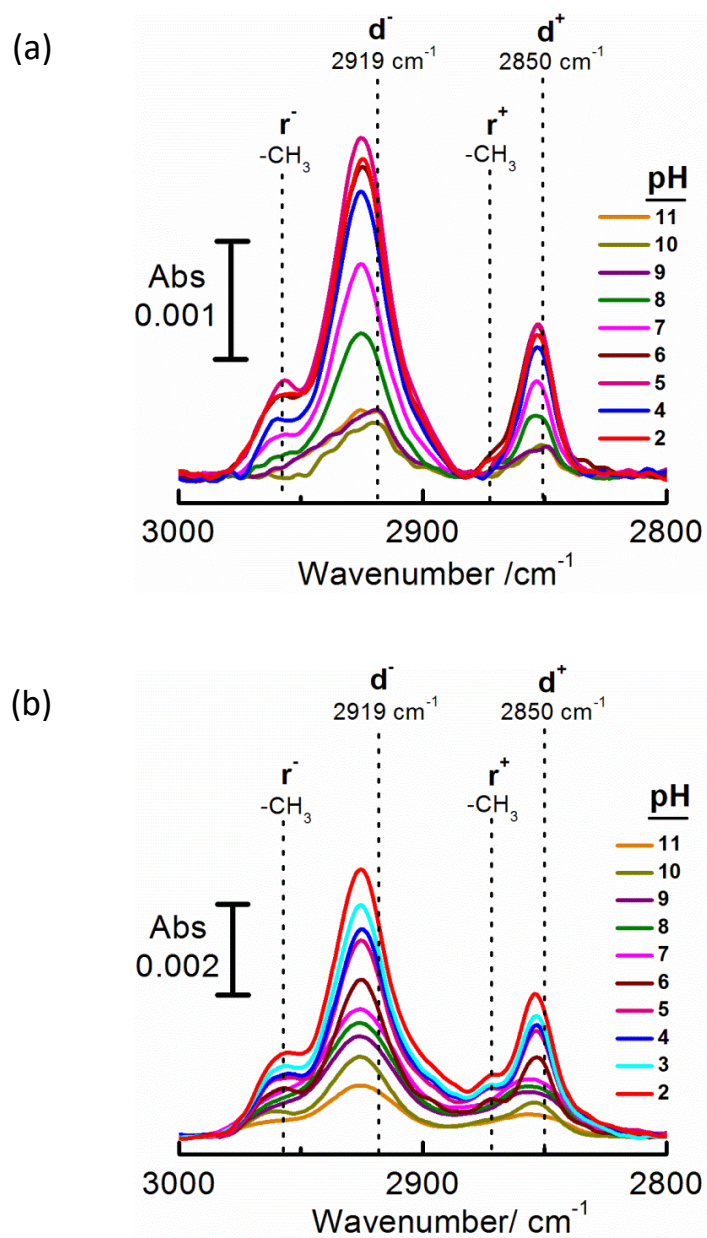
229

Figure 7. Representative behaviour of the evolution of the position and intensity of d^- and d^+ bands during the acidic titration of mixed MUA/DT SAMs formed at: a) 18 h at all $\chi_{MUA/DT}^{surf}$ compositions and 15 min at $\chi_{MUA}^{surf} > 0.41$, and b) 15 min for $\chi_{MUA/DT}^{surf} = 0.41/0.59$ and 0.15/0.85.

In the particular case of mixed SAMs formed at 15 minutes and $\chi^{surf}_{MUA} <$ 0.41, they remain disordered during the titration experiments (Figure 7b). This finding would agree with the fact that, in most of the cases, the δ_{sc}-CH$_2$ mode changes its intensity and a small fraction of –COO$^-$ surface groups cannot be titrated at very low pHs. The latter case may be associated to the burying of –COO$^-$ moieties because of the gradual disordering of the SAM structure induced by the protonation process. Assuming that extinction coefficients of v(COO-)/v(C=O) bands were approximately similar, the surface ratio of –COOH/-COO *titrated* in the SAMs can be determined from their integrated peak area. Then, this makes conceivable to study the deprotonation/protonation processes that take place at the SAM/solution interface by FT-IRRAS. Figure 8 illustrates the changes in the surface ratio of –COO$^-$, θ, with pH. These IR titration curves reflect the change in the degree of the dissociation of the –COOH groups for pure MUA and mixed MUA/DT SAMs with different surface compositions and modification times. The acid-base interfacial behaviour of the terminal groups titrated in these mixed assemblies is generally in good agreement with that of the electrochemical results previously commented (*Section 5.3.1.*). Then, dilution of the –COOH groups by DT molecules progressively decreases both apparent pK$_{1/2}$ and intrinsic pK$_a$ values (Tables 1 and 2), which is associated with the predominant effect of diminishing the in-plane repulsive interactions between charged moieties. This behaviour reflects a homogeneous mixing of the components, and it is observed in a wider range of surface compositions for the SAMs formed at 15 minutes. The opposite trend is observed in pK$_{1/2}$ and pK$_a$ values at higher

coverages of DT molecules mainly due to the increase of the local hydrophobic "microenvironment" surrounding the –COO⁻ groups.
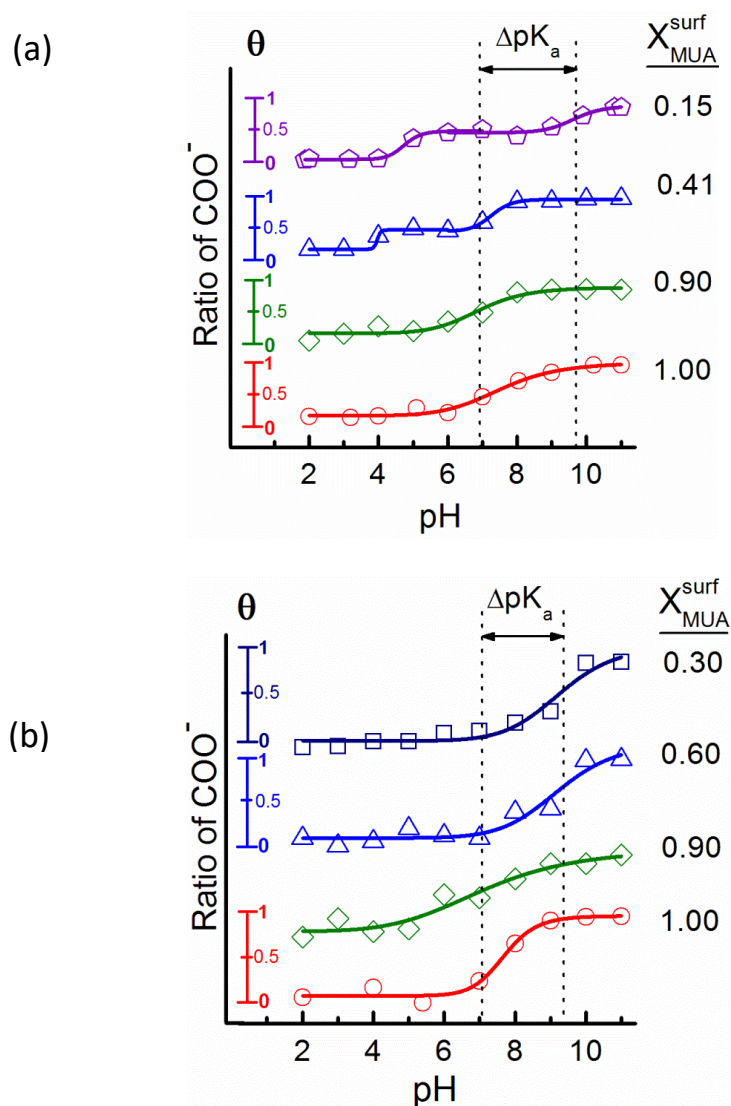
Figure 8. IR titration curves obtained by plotting the surface coverage, θ, of –COO⁻ titrated groups vs pH, for mixed monolayers of MUA/DT formed from lyotropic medium at: a) 15min and b) 18h, with different surface compositions ($\chi^{surf}_{MUA/DT}$). θ and 1-θ are determined from the integrated area of the ν(COO-)/ν(C=O) vibrational bands.

232
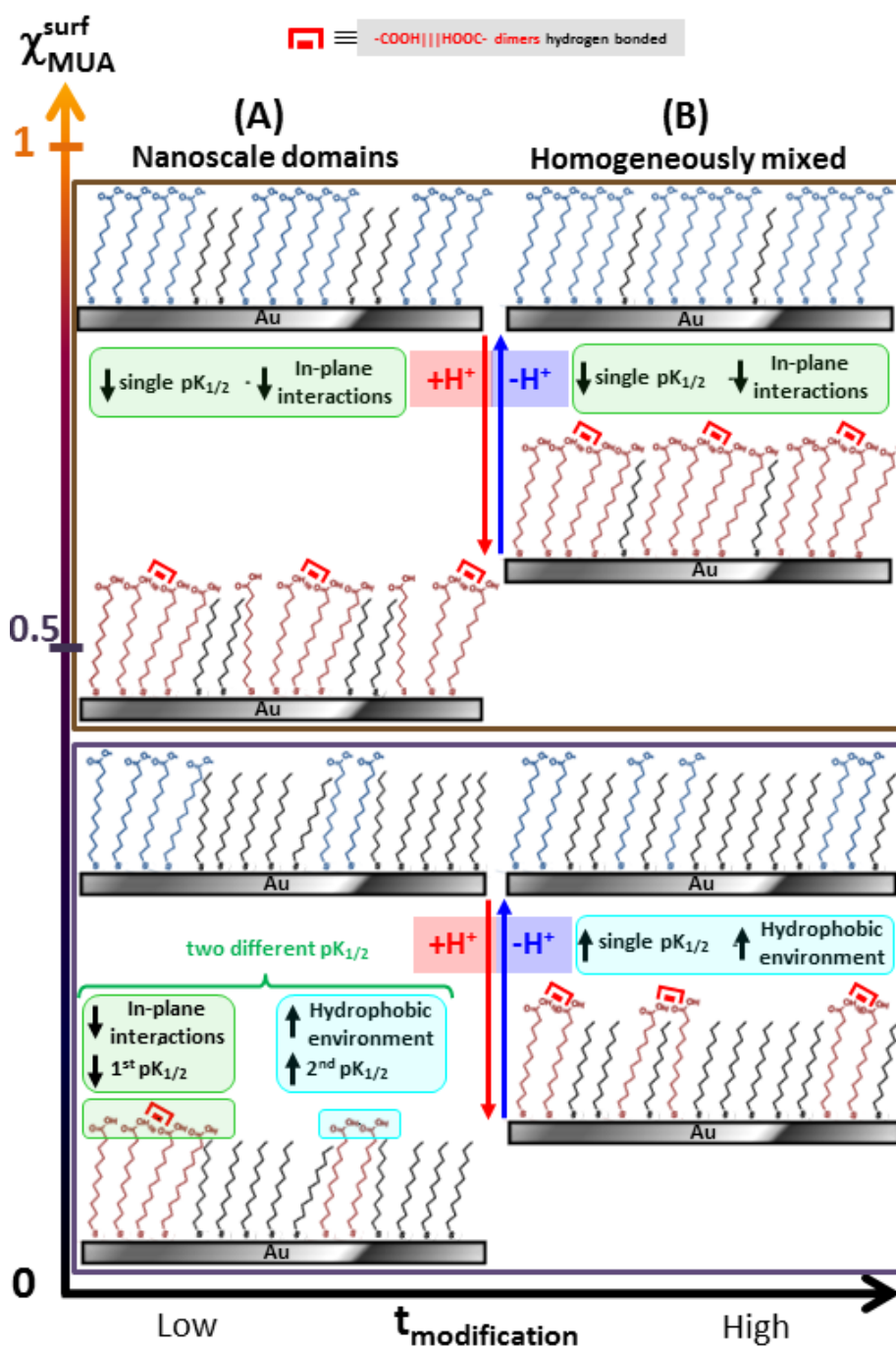
Scheme 1. Acid/base interfacial properties of homogeneously mixed MUA/DT SAMs vs composition: (A) nanodomains and (B) molecularly distributed components.

However, IR titration curves put forward some remarkable aspects in contrast to the electrochemical titration experiments. In this sense, two different scenarios can be described for the SAMs formed at low and high modification times (Scheme 1):

(I) Mixed SAMs formed at 15 minutes (Figure 8a) show a more complex acid/base interfacial behavior with two different surface $pK_{1/2}$ emerging at low surface coverages of MUA (χ_{MUA}^{surf}<0.41). This is an unusual case, and there are only a few examples reported in literature of SAMs, either with one or two surface-confined ionizable groups, where two discernible interfacial pK_a are directly observed.[48, 51, 77] Gershevitz et al.[48] firstly reported the appearance of two pK_a values by FTIR-ATR titration of carboxyl-terminated alkylsiloxane monolayers anchored on Si. The authors have shown the balance among differently associated interfacial –COOH groups on the surface (*e.g. –COOH monomers and water molecules, -COOH···HCOO- dimeric and -COOH···OCOH····HOOC- linear oligomeric structures linked by hydrogen bonding*), and argued that their association was related with changes in alkyl chain conformation and groups acidity. The first pK_a (~4.9) was associated to the deprotonation of –COOH monomers and the second one (~9.3) to that of dimeric and oligomeric species. Other authors have found that the formation of strong ionic hydrogen bonds (i.e. –COOH··· ⁻OOC-) leads to higher pK_a values (~8.4). [51, 78] This kind of hydrogen bonding interactions is favoured under low ionic strength conditions and a reduced local dielectric constant (ε~1), where the association of –COO⁻ with cations is

unfavourable and the water is expelled from the interaction volume (i.e. poor solvation).[51, 78, 79] Finally, Nuzzo et al.[71] addressed that mercaptohexadecanoic acid (MHDA) SAMs on gold exhibiting a high degree of molecular orientation were composed only by a small fraction of hydrogen bonded –COOH groups. They also proposed that such acidic groups were bounded by forming linear oligomers instead of head-to-head dimers. On the other hand, it has been also reported the existence of head-to-head dimers (vC=O at 1717 cm^{-1}) in MHDA and MUA monolayers whose structure is slightly distorted.

Then, the first scenario proposed to explain the present results is based on the surface distribution of MUA molecules and the different size of their nanodomains (Scheme 1).

- At $\chi_{MUA}^{surf} > 0.41$, the average size of the MUA domains may be still large enough for the –COO$^-$ groups to be mainly protonated in quite similar local environments, as it would happen to a 100% MUA SAM, but with their repulsive interactions reduced by the diluting effect of DT molecules. As commented above, some structural disorder is induced in the alkyl chains during this single protonation step (pK$_{1/2}$). However, when the pH << pK$_{1/2}$, an additional rearrangement of the alkyl chains and of the –COOH terminal groups takes place in the distorted structure of the SAMs, which probably provokes the formation of dimeric species associated by intermolecular hydrogen bonding (Figure 5b-c).

- At $\chi_{MUA}^{surf} < 0.41$, the size distribution of the MUA nanodomains probably becomes more heterogeneous while their average size decreases. It is feasible to assume that the MUA molecules might be mainly divided in

two different arrangements composed by: (a) smaller and (b) larger domains with a low and higher number of –COO⁻ groups, respectively. The smallest "domain" size would be ideally composed only by two –COO⁻ groups as a dimer. The MUA molecules associated in the smallest groups (*included isolated dimers*) and/or in larger ones, but located at the MUA/DT domain boundaries, will be firstly titrated at the higher pK$_a$ value due to their lowest local dielectric environment among the overall molecules of each domain. This effect can be favoured by the fact that this kind of mixed SAMs are already structurally disordered with a high number of gauche defects where some –COOH might be buried in the hydrocarbon scaffold. Then, the –COO⁻ moieties located mainly inside the larger MUA domains are subsequently protonated at the lower pK$_a$ value (~4 to 4.5), which is quite similar to that of free carboxylic acids in the bulk solution. Once this kind of –COO⁻ are protonated, the –COOH groups are able to rearrange and link together to probably form hydrogen bonded dimeric species as commented above.

Figure 8a clearly shows that titration curves with two pK$_a$ are directly observed when at least 50% of the size distribution of domains is composed of small enough arrangements of MUA molecules.

(II) Mixed SAMs formed at 18 hours (Figure 8b) show a different acid/base interfacial behavior based on the appearance of only one apparent surface pK$_a$. A second scenario is proposed to explain the results obtained (Scheme 1).

- At $\chi_{MUA}^{surf} > 0.60$ (at least $\chi_{MUA}^{surf} > 0.56$ for EIS titration - Table 2), although the average size distribution of the MUA domains may become smaller

than that of the mixed SAMs formed at lower time, the –COO$^-$ groups are also probably protonated in similar local environments where their repulsive interactions are diminished.

- At $\chi_{MUA}^{surf} < 0.60$ ($\chi_{MUA}^{surf} < 0.3$ for EIS titration - Table 2), a sufficient population of MUA domains below a critical size is readily achieved, which would lead ideally to a homogenous mixing of –COO$^-$/-CH$_3$ groups at the molecular level for surface compositions of $\chi_{MUA}^{surf} \leq 0.50$. Then, the effect of a low dielectric surrounding environment quickly prevails, even for slightly higher surface compositions of $\chi_{MUA}^{surf} > 0.50$ as expected for – CH$_3$ groups also distributed down to the molecular level. Under these circumstances, -COO$^-$ can be assumed to be distributed onto the surface in small groups of few MUA molecules, dimers and/or even totally isolated, and, thus, surrounded by quite similar local hydrophobic environments. Therefore, the protonation of –COO$^-$ is described by a single titration curve with an apparent surface pK$_a$ value of ~ 9.1-9.4 (Figure 8b). It is worth mentioning that again the –COOH groups titrated tend to form intermolecular hydrogen bonds upon structural rearrangement, most likely from pre-existing –COO$^-$ dimers than from isolated –COO$^-$ moieties closely placed in the surface (Figure 6b-c). In this sense, the existence of strong ionic hydrogen bonds might not be discarded as the present conditions would favour their formation.[51, 78]

5.4. Conclusions

- EIS experiments reveal that there is not a significant contribution from ionized groups at the outer layer of the SAMs to the measured capacitance, C, with pH. The averaged values of C allow determining the surface compositions of both components of well-packed SAMs, which are in good agreement with those obtained by the reductive desorption method (Chapter 4).

- Charge transfer resistance, R$_{CT}$, and IR titration curves clearly reflect the change in the degree of the dissociation of the –COOH groups in pure MUA and mixed MUA/DT SAMs on Au, which allows determining their apparent surface pK$_{1/2}$ values.

- The pK$_{1/2}$ value determined for MUA SAMs is greater than that predicted by the electrostatic mean-field model. It is assumed that additional contribution of hydrogen bonding, ion solvation and hydrophobic effects are present in the vicinity of the ionizable surface groups confined in these SAMs with a "crystalline-like" arrangement.

- The acid/base interfacial behavior of MUA/DT SAMs resembles that of homogeneously mixed systems. Such behavior mainly depends on the degree of homogeneous mixing and spatial distribution of both components arranging into different patterns at the surface.

- For mixed SAMs formed at low and high immersion times with surface compositions of $\chi_{MUA}^{surf} > 0.3$ and $\chi_{MUA}^{surf} > 0.60$, respectively, the dilution of MUA with DT progressively decreases the pK$_{1/2}$, pK$_a$, and the interaction parameter, $\beta\bar{E}$ (i.e. for a fixed intrinsic pK$_a$) values that are obtained from the best fits of the 1-pK model to the experimental data. This is consistent with the predominant effect of the lowering of in-plane repulsive interactions between –COOH groups. In both cases, a single pK$_{1/2}$ appears corresponding to the titration of MUA molecules associated in large domains that experiment similar local environments to that of the pure monolayer.

- In contrast, at $\chi_{MUA}^{surf} < 0.3$ (t=15 min) and $\chi_{MUA}^{surf} < 0.60$ (t=18 h), the pK$_{1/2}$ value increases several pH units when the MUA molecules are further diluted in the assemblies. Then, the effect of lowering of the local dielectric constant becomes predominant between neighboring ionizable groups.

- For SAMs formed at low time, the heterogeneity in the size distribution of the MUA nanodomains determines the appearance of two apparent surface pK$_{1/2}$ values. This is due to the coexistence of different environments created by –COOH groups associated in smaller and larger arrangements of MUA molecules. The –COOH associated in smaller arrangements and those located at the –CH$_3$ domain boundaries, contribute to the appearance of the higher pK$_a$ value as expected for the lowest local dielectric environment experienced among these groups in

the domains. The –COOH moieties located inside the larger MUA domains are subsequently protonated at the lower pK$_a$ value.

-   For the SAMs formed at higher time, -COOH moieties seems to be homogeneously distributed close to the molecular level. In this case, a single pK$_{1/2}$ is always observed that displaces to higher values. This can be explained by the similar local hydrophobic microenvironment experienced by all the –COOH surface groups which are assumed to be distributed in very small groups, as dimers or even isolated when a critical MUA/DT mixing ratio is achieved.

-   The formation of hydrogen bonding interactions between MUA molecules is observed upon rearrangement of the SAM structure. It is suggested that dimeric species (-COOH···HCOO-) are the most likely to form by the association of MUA molecules either inside of larger domains (e.g. SAMs formed at lower modification time) or as pre-existing dimers homogeneously mixed in the surface (e.g. SAMs formed at higher time).

-   Mixed SAMs formed at 15 minutes are more adequate to study their interaction with biomolecules at a physiological pH ~7, as a wider range of surface percentages of –COO$^-$ and –COOH groups (8-45%) are available to evaluate the effect of electrostatic (*i.e. influence of interfacial electrostatic fields*) and hydrogen bonding interactions, at the same time that the effect of hydrophobic interactions can be approached by the insertion of –CH$_3$ surface groups by tuning its percentage from 10-85%.

5.5. Appendix

A. Double layer continuous-charge surface pK$_a$ model

The dissociation of the terminal –COOH groups in a monolayer can be described by an equilibrium reaction between protonated and ionized moieties:

$$\text{-COOH}_{(surface)} \quad \leftrightarrows \quad \text{-COO}^-_{(surface)} + \text{H}^+_{(solution)} \qquad (A1)$$
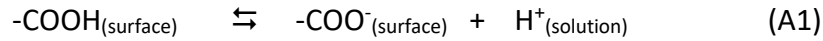
The equilibrium constant, K$_a$, of the surface reaction is given by:

$$K_a = \frac{\theta_{surf}^{COO^-}}{\theta_{surf}^{COOH}} [H^+]_{surf} \qquad (A2)$$

where $\theta_{surf}^{COO^-}$ is the fraction of surface acid dissociated and $[H^+]_{surf}$ is the proton concentration at the surface. $[H^+]_{surf}$ relates to the bulk proton concentration, $[H^+]_{sol}$ through a Boltzmann distribution:

$$[H^+]_{surf} = [H^+]_{sol} \cdot e^{-F\emptyset_2/RT} \qquad (A3)$$

where F is the Faraday constant and φ_2 the electrostatic potential at the surface which is related to the potential difference between the outer plane of closest approach of –COOH terminal groups in the SAM (Helmholtz plane of acid dissociation, PAD) , φ_{PAD}, and the bulk solution, φ_S (Scheme A1).[31] Combining expressions A2 and A3 it follows that:

241

$$\log \frac{\theta_{surf}^{COO^-}}{\theta_{surf}^{COOH}} = \log \frac{\theta}{1-\theta} = pH - pK_a + \frac{F\varnothing_2}{2.303RT} = pH - pK_{1/2}^{app} \quad (A4)$$

where θ is the fraction of surface carboxylates, K_a is the dissociation constant of the surface bound acid in the absence of any interfacial electric fields (*i.e.* $\varphi_{2} = \varphi_{PAD} - \varphi_S = 0$), pH relates to the proton activity in the bulk solution and $pK_{1/2}^{app}$ is the pH value at $\theta = 0.5$ that represents the shift of pK_a caused by electrostatic/intermolecular repulsions ($pH = pK_a - F\varphi_2/2.303RT$). Then, varying with the ionization of the SAM, φ_2 includes θ. According to the 1-pK model, and extended to ionizable solid-water interfaces by the statistical mechanical model developed by Borkovec et. al.,[50] titration curves takes the form:

$$\log \frac{\theta}{1-\theta} = pH - pK_a - \frac{\bar{E}\theta}{2.303RT} = pH - pK_a - \frac{\beta\bar{E}\theta}{2.303} \quad (A5)$$

where $\varphi_{2} = -\bar{E}\theta / F$, $\bar{E}$ (potential of mean force) is the energy of electrostatic interactions of charged molecules with its surroundings, and $\beta = 1/RT$. The increasing order of molecular interactions from $\beta\bar{E} = 0$ to 1, 2, 3, etc., broadens the titration curves and the inflection point ($\theta = 0.5$) shifts the $pK_{1/2}^{app}$ - $pK_a = \beta\bar{E}\theta/2.303$ with $\Delta pK_{1/2}^{app} = \beta\bar{E}/2.303$ to higher values.

Therefore, if the electrostatic contribution is not included in equations A4 and A5, they become the same equation as that for acid-base equilibrium of free carboxylic acids in bulk aqueous solution.
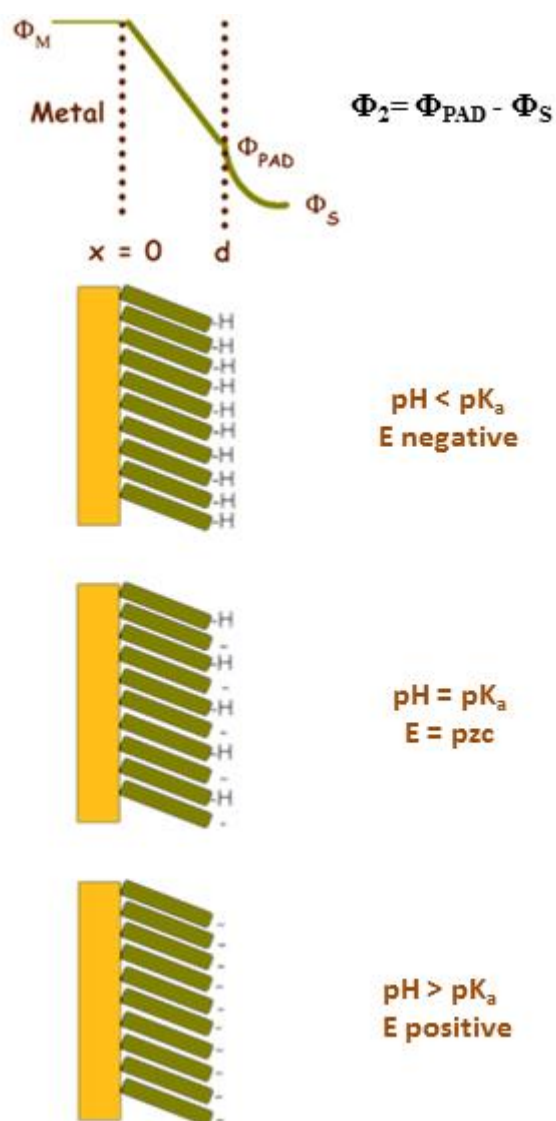
Scheme A1. Double layer model for ionizable –COOH SAMs.

The electrostatic potential associated with the SAM is given by the Gouy-Chapman theory of the electrical double layer, where the surface charge, σ, is related to φ$_2$ by the following equation:

$$\sigma = \varepsilon_o \varepsilon_S \kappa \frac{2RT}{F} \sinh\left(\frac{F\varphi_2}{2RT}\right) \qquad (A6)$$

where κ is the inverse Debye length of electrolyte solution with the dielectric constant ε$_S$, and assumed to be pH-independent and, ε$_o$ the free space permittivity. In a more realistic model, Fawcett et.al. have considered the discreteness-of-charge effects and the presence of a Stern layer adjacent to the molecular film comprising solvent molecules differently structured from the bulk liquid (*e.g. with local dielectric permittivity significantly lowered*).[80]

Nevertheless, this interaction model is usually well-reproduced by titration curves of different electrochemical and spectroscopic parameters such as capacitance (C), R$_{CT}$, k$_{ET}$ or carboxylate/carboxylic ratio of IR bands area ratio vs pH curves for pure and mixed –COOH SAMs.

Thus, the apparent heterogeneous rate constant, k$_{ET}^{app}$, of the surface reaction of a negatively charged redox probes (*e.g. Fe(CN)$_6^{3-/4-}$*) can be altered by the solution pH in response to the acid-base reaction of the ionizable –COOH groups at the SAM. At a constant electrode potential, the –COOH ionization shifts φ$_2$ at PAD to more negative values, which enhances the φ$_M$-φ$_2$ difference (*i.e. the driven force for electron tunneling across the SAM*), compared to the uncharged monolayer. The increase of ionized –COO$^-$ groups impedes the electroactive ions to approach the Au surface by electrostatic

repulsion. This fact causes the redox probe surface concentration to be depleted and electrons also impeded to exchange with the electrode. At high pHs as a result, electron transfer response is further inhibited and slow down. Then, a similar expression to A3 can be derived for the surface and solution concentrations of negatively charged ions.[47]

This is manifested by the increase of the charge transfer resistance, R$_{CT}$, values determined by EIS and the improved blocking behavior of the SAM shown by CV. Assuming that the potential drop at the diffuse double layer is pH-independent and constant at the electrolyte solution used, in the presence of the double layer effect, R$_{CT}$ can be expressed by the following equivalent equations: [47, 80, 81]

$$R_{CT} = R_{CT}^{o} \cdot e^{\left[(z-\beta n)\frac{F\varnothing_2}{RT}\right]} \tag{A7}$$

$$R_{CT} = e^{\left(A+B\frac{K_a^{-1}[H^+]}{1+K_a[H^+]}\right)} \tag{A8}$$

Similarly, when the potential across the interface (φ_M-φ_S) is changed, as occurs in CV experiments, the degree of acid dissociation is altered. For example, sweeping potential to negative values to that of the potential zero charge (pzc) will favor protonation of –COOH groups by reducing the electrostatic repulsion between negative charges located on the metal surface and those associated with the –COO$^-$ groups located at the PAD (Scheme A1). Conversely, positive electrode potentials compared to the E$_{pzc}$ will drive the deprotonation of the surface groups. In general, the acid-base equilibrium displaces in response to electrode potential to minimize the interfacial free

energy. Then, the results obtained for pK$_{1/2}^{app}$ from the titration curves carried out without an external potential applied (*i.e. under open circuit equilibrium conditions*) may differ to those obtained under different applied potentials.

5.6. References

1.   Puente Santiago, A. R.; Pineda, T.; Blazquez, M.; Madueno, R., Formation of 2-D Crystalline Intermixed Domains at the Molecular Level in Binary Self-Assembled Monolayers from a Lyotropic Mixture. *Journal of Physical Chemistry C* **2016,** *120* (16), 8595-8606.

2.   Smith, R. K.; Lewis, P. A.; Weiss, P. S., Patterning Self-Assembled Monolayers. *Prog. Surf. Sci.* **2004,** *75* (1-2), 1-68.

3.   Casalini, S.; Bortolotti, C. A.; Leonardi, F.; Biscarini, F., Self-Assembled Monolayers in Organic Electronics. *Chem. Soc. Rev.* **2017,** *46* (1), 40-71.

4.   Majumdar, S.; Malen, J. A.; McGaughey, A. J. H., Cooperative Molecular Behavior Enhances the Thermal Conductance of Binary Self-Assembled Monolayer Junctions. *Nano Lett.* **2017,** *17* (1), 220-227.

5.   Kong, G. D.; Kim, M.; Cho, S. J.; Yoon, H. J., Gradients of Rectification: Tuning Molecular Electronic Devices by the Controlled Use of Different-Sized Diluents in Heterogeneous Self-Assembled Monolayers. *Angew. Chem., Int. Ed.* **2016,** *55* (35), 10307-10311.

6.   Mendes, P. M., Stimuli-Responsive Surfaces for Bio-Applications. *Chem. Soc. Rev.* **2008,** *37* (11), 2512-2529.

7.   Yang, H.; Yuan, B.; Zhang, X.; Scherman, O. A., Supramolecular Chemistry at Interfaces: Host-Guest Interactions for Fabricating Multifunctional Biointerfaces. *Acc. Chem. Res.* **2014,** *47* (7), 2106-2115.

8.   Colangelo, E.; Comenge, J.; Paramelle, D.; Volk, M.; Chen, Q.; Levy, R., Characterizing Self-Assembled Monolayers on Gold Nanoparticles. *Bioconjugate Chem.* **2017,** *28* (1), 11-22.

9.   Prime, K. L.; Whitesides, G. M., Self-Assembled Organic Monolayers: Model Systems for Studying Adsorption of Proteins at Surfaces. *Science* **1991,** *252* (5009), 1164.

10.   Gooding, J. J.; Darwish, N., The Rise of Self-Assembled Monolayers for Fabricating Electrochemical Biosensors-An Interfacial Perspective. *Chem. Rec.* **2012,** *12* (1), 92-105.

11.   Frasconi, M.; Mazzei, F.; Ferri, T., Protein Immobilization at Gold-Thiol Surfaces and Potential for Biosensing. *Anal. Bioanal. Chem.* **2010,** *398* (4), 1545-1564.

12.   Arya, S. K.; Solanki, P. R.; Datta, M.; Malhotra, B. D., Recent Advances in Self-Assembled Monolayers Based Biomolecular Electronic Devices. *Biosens. Bioelectron.* **2009,** *24* (9), 2810-2817.

13.   Jonkheijm, P.; Weinrich, D.; Schroeder, H.; Niemeyer, C. M.; Waldmann, H., Chemical Strategies for Generating Protein Biochips. *Angew. Chem., Int. Ed.* **2008,** *47* (50), 9618-9647.

14.   Saha, K.; Agasti, S. S.; Kim, C.; Li, X.; Rotello, V. M., Gold Nanoparticles in Chemical and Biological Sensing. *Chem. Rev.* **2012,** *112* (5), 2739-2779.

15.   Dennis, A. M.; Delehanty, J. B.; Medintz, I. L., Emerging Physicochemical Phenomena along with New Opportunities at the Biomolecular-Nanoparticle Interface. *J. Phys. Chem. Lett.* **2016,** *7* (11), 2139-2150.

16.   Sapsford, K. E.; Algar, W. R.; Berti, L.; Gemmill, K. B.; Casey, B. J.; Oh, E.; Stewart, M. H.; Medintz, I. L., Functionalizing Nanoparticles with Biological Molecules: Developing Chemistries that Facilitate Nanotechnology. *Chem. Rev. (Washington, DC, U. S.)* **2013,** *113* (3), 1904-2074.

17.   Biju, V., Chemical Modifications and Bioconjugate Reactions of Nanomaterials for Sensing, Imaging, Drug Delivery and Therapy. *Chem. Soc. Rev.* **2014,** *43* (3), 744-764.

18.   Dreaden, E. C.; Alkilany, A. M.; Huang, X.; Murphy, C. J.; El-Sayed, M. A., The Golden Age: Gold Nanoparticles for Biomedicine. *Chem. Soc. Rev.* **2012,** *41* (7), 2740-2779.

19.   Fedurco, M., Redox Reactions of Heme-Containing Metalloproteins: Dynamic Effects of Self-Assembled Monolayers on Thermodynamics and Kinetics of Cytochrome C Electron-Transfer Reactions. *Coordination Chemistry Reviews* **2000,** *209* (1), 263-331.

20.   Samanta, D.; Sarkar, A., Immobilization of Bio-Macromolecules on Self-Assembled Monolayers: Methods and Sensor Applications. *Chem Soc Rev* **2011,** *40* (5), 2567-92.

21.   Murgida, D. H.; Hildebrandt, P.; Todorovic, S. In *Immobilized redox proteins: mimicking basic features of physiological membranes and interfaces*, InTech: **2010**; pp 21-47.

22.   Capdevila, D. A.; Marmisolle, W. A.; Williams, F. J.; Murgida, D. H., Phosphate Mediated Adsorption and Electron Transfer of Cytochrome C. A Time-Resolved SERR Spectroelectrochemical Study. *Phys. Chem. Chem. Phys.* **2013,** *15* (15), 5386-5394.

23.   Jin, B.; Wang, G.-X.; Millo, D.; Hildebrandt, P.; Xia, X.-H., Electric-Field Control of the pH-Dependent Redox Process of Cytochrome c Immobilized on a Gold Electrode. *J. Phys. Chem. C* **2012,** *116* (24), 13038-13044.

24.   Murgida, D. H.; Hildebrandt, P., Disentangling Interfacial Redox Processes of Proteins by SERR Spectroscopy. *Chem. Soc. Rev.* **2008,** *37* (5), 937-945.

25.   Chen, S.; Liu, L.; Zhou, J.; Jiang, S., Controlling Antibody Orientation on Charged Self-Assembled Monolayers. *Langmuir* **2003,** *19* (7), 2859-2864.

26.   Bain, C. D.; Whitesides, G. M., Modeling Organic Surfaces with Self-Assembled Monolayers. *Angew. Chem.* **1989,** *101* (4), 522-8.

27.   Creager, S. E.; Clarke, J., Contact-Angle Titrations of Mixed Omega-Mercaptoalkanoic Acid Alkanethiol Monolayers on Gold - Reactive vs Nonreactive Spreading, and Chain-Length Effects on Surface pK$_a$ Values. *Langmuir* **1994,** *10* (10), 3675-3683.

28.   Besharat, Z.; Wakeham, D.; Johnson, C. M.; Odnevall, W. I.; Luengo, G. S.; Greaves, A.; Gothelid, M.; Rutland, M. W., Mixed Monolayers of Alkane Thiols with Polar Terminal Group on Gold: Investigation of Structure Dependent Surface Properties. *J Colloid Interface Sci* **2016,** *484*, 279-290.

29.   Shimazu, K.; Teranishi, T.; Sugihara, K.; Uosaki, K., Surface Mass Titrations of Self-Assembled Monolayers of Omega-Mercaptoalkanoic Acids on Gold. *Chemistry Letters* **1998,** (7), 669-670.

30.   Cheng, Q.; Brajter-Toth, A., Selectivity and Sensitivity of Self-Assembled Thioctic Acid Electrodes. *Anal. Chem.* **1992,** *64* (17), 1998-2000.

31.   White, H. S.; Peterson, J. D.; Cui, Q.; Stevenson, K. J., Voltammetric Measurement of Interfacial Acid/Base Reactions. *J. Phys. Chem. B* **1998,** *102* (16), 2930-2934.

32.   Smalley, J. F.; Chalfant, K.; Feldberg, S. W.; Nahir, T. M.; Bowden, E. F., An Indirect Laser-Induced Temperature Jump Determination of the Surface pKa of 11-Mercaptoundecanoic Acid Monolayers Self-Assembled on Gold. *J. Phys. Chem. B* **1999,** *103* (10), 1676-1685.

33.   Clark, R. A.; Trout, C. J.; Ritchey, L. E.; Marciniak, A. N.; Weinzierl, M.; Schirra, C. N.; Christopher Kurtz, D., Electrochemical Titration of Carboxylic Acid Terminated SAMs on Evaporated Gold: Understanding the Ferricyanide Electrochemistry at the Electrode Surface. *J. Electroanal. Chem.* **2013,** *689*, 284-290.

34.   Sanders, W.; Vargas, R.; Anderson, M. R., Characterization of Carboxylic Acid-Terminated Self-Assembled Monolayers by Electrochemical Impedance Spectroscopy and Scanning Electrochemical Microscopy. *Langmuir* **2008,** *24* (12), 6133-6139.

35.   Marmisolle, W. A.; Capdevila, D. A.; de la Llave, E.; Williams, F. J.; Murgida, D. H., Self-Assembled Monolayers of NH$_2$-Terminated Thiolates: Order, pK$_a$, and Specific Adsorption. *Langmuir* **2013,** *29* (17), 5351-5359.

36.   Munakata, H.; Kuwabata, S., Detection of Difference in Acidity Between Arrayed Carboxy Groups and the Groups Dissolved in Solution by Reductive Desorption of a Self-Assembled Monolayer of Carboxy-Terminated Thiols. *Chem. Commun. (Cambridge, U. K.)* **2001,** (15), 1338-1339.

37.   Kim, K.; Kwak, J., Faradaic Impedance Titration of Pure 3-Mercaptopropionic Acid and Ethanethiol Mixed Monolayers on Gold. *J. Electroanal. Chem.* **2001,** *512* (1-2), 83-91.

38.   Dai, Z.; Ju, H., Effect of Chain Length on the Surface Properties of ω-Carboxy Alkanethiol Self-Assembled Monolayers. *Phys. Chem. Chem. Phys.* **2001,** *3* (17), 3769-3773.

39.   Zhao, J. W.; Luo, L. Q.; Yang, X. R.; Wang, E. K.; Dong, S. J., Determination of Surface pK$_a$ of SAM Using an Electrochemical Titration Method. *Electroanalysis* **1999,** *11* (15), 1108-1111.

40.   Pissinis, D. E.; Linarez Perez, O. E.; Cometto, F. P.; Lopez Teijelo, M., Preparation and Characterization of Self Assembled Monolayers of 2-Mercaptonicotinic Acid on Au(1 1 1). *J. Electroanal. Chem.* **2014,** *712*, 167-177.

41.   Tominaga, M.; Maetsu, S.; Kubo, A.; Taniguchi, I., Nano-Ordered Topographical Effects on Dissociation of Carboxylic Acid Terminated Self-Assembled Monolayers Adsorbed onto a Gold Surface. *J. Electroanal. Chem.* **2007,** *603* (2), 203-211.

42.   Luque, A. M.; Cuesta, A.; Calvente, J. J.; Andreu, R., Potentiostatic Infrared Titration of 11-Mercaptoundecanoic Acid Monolayers. *Electrochem. Commun.* **2014,** *45*, 13-16.

43.   Kakiuchi, T.; Iida, M.; Imabayashi, S.-i.; Niki, K., Double-Layer-Capacitance Titration of Self-Assembled Monolayers of ω-Functionalized Alkanethiols on Au(111) Surface. *Langmuir* **2000,** *16* (12), 5397-5401.

44.   Sheikh, K. H.; Evans, S. D.; Christenson, H. K., Titration of Ionizable Monolayers by Measurement of the Electric Double-Layer Force. *Langmuir* **2007,** *23* (13), 6893-6895.

45.   Wallwork, M. L.; Smith, D. A.; Zhang, J.; Kirkham, J.; Robinson, C., Complex Chemical Force Titration Behavior of Amine-Terminated Self-Assembled Monolayers. *Langmuir* **2001,** *17* (4), 1126-1131.

46.   He, H. X.; Li, C. Z.; Song, J. Q.; Mu, T.; Wang, L.; Zhang, H. L.; Liu, Z. F., Force Titration of a Carboxylic Acid Terminated Self-Assembled Monolayer Using Chemical Force Microscopy. *Mol. Cryst. Liq. Cryst. Sci. Technol., Sect. A* **1997,** *294*, 99-102.

47.   Komura, T.; Yamaguchi, T.; Shimatani, H.; Okushio, R., Interfacial Charge-Transfer Resistance at Ionizable Thiol Monolayer-Modified Gold Electrodes as Studied by Impedance Spectroscopy. *Electrochim. Acta* **2004,** *49* (4), 597-606.

48.   Gershevitz, O.; Sukenik, C. N., In Situ FTIR-ATR Analysis and Titration of Carboxylic Acid-Terminated SAMs. *J. Am. Chem. Soc.* **2004,** *126* (2), 482-483.

49.   Aureau, D.; Ozanam, F.; Allongue, P.; Chazalviel, J. N., The Titration of Carboxyl-Terminated Monolayers Revisited: In Situ Calibrated Fourier Transform Infrared Study of Well-Defined Monolayers on Silicon. *Langmuir* **2008,** *24* (17), 9440-9448.

50.   Borkovec, M., Origin of 1-pK and 2-pK Models for Ionizable Water-Solid Interfaces. *Langmuir* **1997,** *13* (10), 2608-2613.

51.   Smith, D. A.; Wallwork, M. L.; Zhang, J.; Kirkham, J.; Robinson, C.; Marsh, A.; Wong, M., The Effect of Electrolyte Concentration on the Chemical Force Titration Behavior of ω-Functionalized SAMs: Evidence for the Formation of Strong Ionic Hydrogen Bonds. *J. Phys. Chem. B* **2000,** *104* (37), 8862-8870.

52.   Bain, C. D.; Whitesides, G. M., A Study by Contact Angle of the Acid-Base Behavior of Monolayers Containing ω-Mercaptocarboxylic Acids Adsorbed on Gold: An Example of Reactive Spreading. *Langmuir* **1989,** *5* (6), 1370-8.

53.   Creager, S. E.; Clarke, J., Contact-Angle Titrations of Mixed ω-Mercaptoalkanoic Acid/Alkanethiol Monolayers on Gold. Reactive vs Nonreactive Spreading, and Chain Length Effects on Surface pKa Values. *Langmuir* **1994,** *10* (10), 3675-83.

54.   He, H.-X.; Huang, W.; Zhang, H.; Li, Q. G.; Li, S. F. Y.; Liu, Z. F., Demonstration of High-Resolution Capability of Chemical Force Titration via Study of Acid/Base Properties of a Patterned Self-Assembled Monolayer. *Langmuir* **2000,** *16* (2), 517-521.

55.   Troughton, E. B.; Bain, C. D.; Whitesides, G. M.; Nuzzo, R. G.; Allara, D. L.; Porter, M. D., Monolayer Films Prepared by the Spontaneous Self-Assembly of Symmetrical and Unsymmetrical Dialkyl Sulfides from Solution onto Gold Substrates: Structure, Properties, and Reactivity of Constituent Functional Groups. *Langmuir* **1988,** *4* (2), 365-85.

56.   Yan, Y.; Zheng, Q.; Yang, Y.; Liu, Y.; Shao, H., Regulating the Electrochemical Reversibility of Fe(CN)$_6^{3-/4-}$ by Altering the Surface Potential of the Compact Layer. *J. Electrochem. Soc.* **2016,** *163* (10), H982-H987.

57.   Xing, Y. F.; Li, S. F. Y.; Lau, A. K. H.; O'Shea, S. J., Electrochemical Impedance Spectroscopy Study of Mixed Thiol Monolayers on Gold. *J. Electroanal. Chem.* **2005,** *583* (1), 124-132.

58.   Molinero, V.; Calvo, E. J., Electrostatic Interactions at Self Assembled Molecular Films of Charged Thiols on Gold. *J. Electroanal. Chem.* **1998,** *445* (1-2), 17-25.

59.   Niu, L.; Kvarnstroem, C.; Ivaska, A., Evaluation of Coverage of Self-Assembled Polyaniline-Analogue Monolayer by Capacitance Measurements. *J. Electroanal. Chem.* **2007,** *600* (1), 95-102.

60.   Widrig, C. A.; Chung, C.; Porter, M. D., The Electrochemical Desorption of n-Alkanethiol Monolayers from Polycrystalline Au and Ag Electrodes. *Journal of Electroanalytical Chemistry and Interfacial Electrochemistry* **1991,** *310* (1), 335-359.

61.   Porter, M. D.; Bright, T. B.; Allara, D. L.; Chidsey, C. E. D., Spontaneously Organized Molecular Assemblies. 4. Structural Characterization of n-Alkyl Thiol Monolayers on Gold by Optical Ellipsometry, Infrared Spectroscopy, and Electrochemistry. *J. Am. Chem. Soc.* **1987,** *109* (12), 3559-3568.

62.   Slowinski, K.; Chamberlain, R. V., II; Bilewicz, R.; Majda, M., Evidence for Inefficient Chain-to-Chain Coupling in Electron Tunneling through Liquid Alkanethiol Monolayer Films on Mercury. *J. Am. Chem. Soc.* **1996,** *118* (19), 4709-10.

63.   Gonzalez-Granados, Z.; Sanchez-Obrero, G.; Madueno, R.; Sevilla, J. M.; Blazquez, M.; Pineda, T., Formation of Mixed Monolayers from 11-Mercaptoundecanoic Acid and Octanethiol on Au(111) Single Crystal Electrode under Electrochemical Control. *J. Phys. Chem. C* **2013,** *117* (46), 24307-24316.

64.   Garcia-Raya, D.; Madueno, R.; Blazquez, M.; Pineda, T., Formation of 1,8-Octanedithiol Mono- and Bilayers under Electrochemical Control. *J. Phys. Chem. C* **2010,** *114* (8), 3568-3574.

65.   Miller, C.; Cuendet, P.; Gratzel, M., Adsorbed omega-Hydroxy Thiol Monolayers on Gold Electrodes - Evidence for Electron-Tunneling to Redox Species in Solution. *J. Phys. Chem.* **1991,** *95* (2), 877-886.

66.   Yan, D.; Jordan, J. L.; Burapatana, V.; Jennings, G. K., Formation of n-Alkanethiolate Self-Assembled Monolayers onto Gold in Aqueous Micellar Solutions of n-Alkyltrimethylammonium Bromides. *Langmuir* **2003,** *19* (8), 3357-3364.

67.   Ganesh, V.; Lakshminarayanan, V., Self-Assembled Monolayers of Alkanethiols on Gold Prepared in a Hexagonal Lyotropic Liquid Crystalline Phase of Triton X-100/Water System. *Langmuir* **2006,** *22* (4), 1561-1570.

68.   Raya, D. G.; Madueno, R.; Blazquez, M.; Pineda, T., Formation of a 1,8-Octanedithiol Self-Assembled Monolayer on Au(111) Prepared in a Lyotropic Liquid-Crystalline Medium. *Langmuir* **2010,** *26* (14), 11790-11796.

69.   Gonzalez-Granados, Z.; Sanchez-Obrero, G.; Madueno, R.; Sevilla, J. M.; Blazquez, M.; Pineda, T., Formation of Mixed Mono layers from 11-Mercaptoundecanoic Acid and Octanethiol on Au(111) Single Crystal Electrode under Electrochemical Control. *Journal of Physical Chemistry C* **2013,** *117* (46), 24307-24316.

70.   Jiang, X.; Ataka, K.; Heberle, J., Influence of the Molecular Structure of Carboxyl-Terminated Self-Assembled Monolayer on the Electron Transfer of Cytochrome C Adsorbed on an Electrode: In Situ Observation by Surface-Enhanced Infrared Absorption Spectroscopy. *J. Phys. Chem. C* **2008,** *112* (3), 813-819.

71.   Nuzzo, R. G.; Dubois, L. H.; Allara, D. L., Fundamental Studies of Microscopic Wetting on Organic Surfaces. 1. Formation and Structural Characterization of a Self-Consistent Series of Polyfunctional Organic Monolayers. *J. Am. Chem. Soc.* **1990,** *112* (2), 558-69.

72.   Arnold, R.; Azzam, W.; Terfort, A.; Woell, C., Preparation, Modification, and Crystallinity of Aliphatic and Aromatic Carboxylic Acid Terminated Self-Assembled Monolayers. *Langmuir* **2002,** *18* (10), 3980-3992.

73.   Hirata, N.; Suga, S.; Noguchi, Y.; Shibuta, M.; Tsunoyama, H.; Eguchi, T.; Nakajima, A., Highly Ordered Self-Assembled Monolayers of Carboxy- and Ester-Terminated Alkanethiol on Au(111): Infrared Absorption and Hyperthermal-Deposition Experiments with Cr(benzene)2 Ions. *J. Phys. Chem. C* **2017**, Ahead of Print.

74.   Sugihara, K.; Shimazu, K.; Uosaki, K., Electrode Potential Effect on the Surface pK$_a$ of A Self-Assembled 15-Mercaptohexadecanoic Acid Monolayer on a Gold/Quartz Crystal Microbalance Electrode. *Langmuir* **2000,** *16* (18), 7101-7105.

253

75.   Snyder, R. G.; Strauss, H. L.; Elliger, C. A., Carbon-Hydrogen Stretching Modes and the Structure of n-Alkyl Chains. 1. Long, Disordered Chains. *J. Phys. Chem.* **1982,** *86* (26), 5145-50.

76.   Bethencourt, M. I.; Srisombat, L.-o.; Chinwangso, P.; Lee, T. R., SAMs on Gold Derived from the Direct Adsorption of Alkanethioacetates Are Inferior to Those Derived from the Direct Adsorption of Alkanethiols. *Langmuir* **2009,** *25* (3), 1265-1271.

77.   de F. Paulo, T.; Abruna, H. D.; Diogenes, I. C. N., Thermodynamic, Kinetic, Surface pKa, and Structural Aspects of Self-Assembled Monolayers of Thio Compounds on Gold. *Langmuir* **2012,** *28* (51), 17825-17831.

78.   Meot-Ner, M.; Elmore, D. E.; Scheiner, S., Ionic Hydrogen Bond Effects on the Acidities, Basicities, Solvation, Solvent Bridging, and Self-Assembly of Carboxylic Groups. *J. Am. Chem. Soc.* **1999,** *121* (33), 7625-7635.

79.   Kane, V.; Mulvaney, P., Double-Layer Interactions between Self-Assembled Monolayers of ω-Mercaptoundecanoic Acid on Gold Surfaces. *Langmuir* **1998,** *14* (12), 3303-3311.

80.   Fawcett, W. R.; Fedurco, M.; Kovacova, Z., Double Layer Effects at Molecular Films Containing Acid/Base Groups. *Langmuir* **1994,** *10* (7), 2403-8.

81.   Madueno, R.; Garcia-Raya, D.; Viudez, A. J.; Sevilla, J. M.; Pineda, T.; Blazquez, M., Influence of the solution pH in the 6-mercaptopurine self-assembled monolayer (6MP-SAM) on a Au(111) single-crystal electrode. *Langmuir* **2007,** *23* (22), 11027-11033.

CHAPTER 6

Conformational Changes of Cationized Myoglobin (c-Mb) Tuned by MUA/DT Mixed SAMs: Direct Implications en ET Gating and Catalysis

6. Conformational changes of cationized Myoglobin (c-Mb) tuned by MUA/DT mixed SAMs: Direct implications on ET gating and catalysis Introduction

Electron transfer (ET) reactions involving electron shuttling metalloproteins are of fundamental importance for life. [1-3] Globins are haem-proteins that bind O_2 and thus play an important role in the animal's respiration and oxidative energy production with an unprecedented diversity that has been recently reviewed.[4] In this sense, globins may also have other functions such as the decomposition or production of NO, the detoxification of reactive oxygen species or intracellular signalling.[4] They are typically comprised by around 150 amino acids and arranged into eight α-helical segments (A-H) with a characteristic 3-over-3 α-helical sandwich structure (*i.e. globin fold*) including a haem prosthetic group (*protoporphyrin IX type*) that may bind oxygen or other ligands (Scheme 1). While their overall structures are conserved, globin primary sequences are not. In fact, only the proximal

257

histidine (position 8th at helix F, F8) is present in all globins adjacent to the heme group with most of them stabilized by a phenylalanine in the inter-helical region (CD1). Globins are the best-investigated proteins and represent a prime tool for studying the function and evolution of genes and proteins.

(a)

(b)
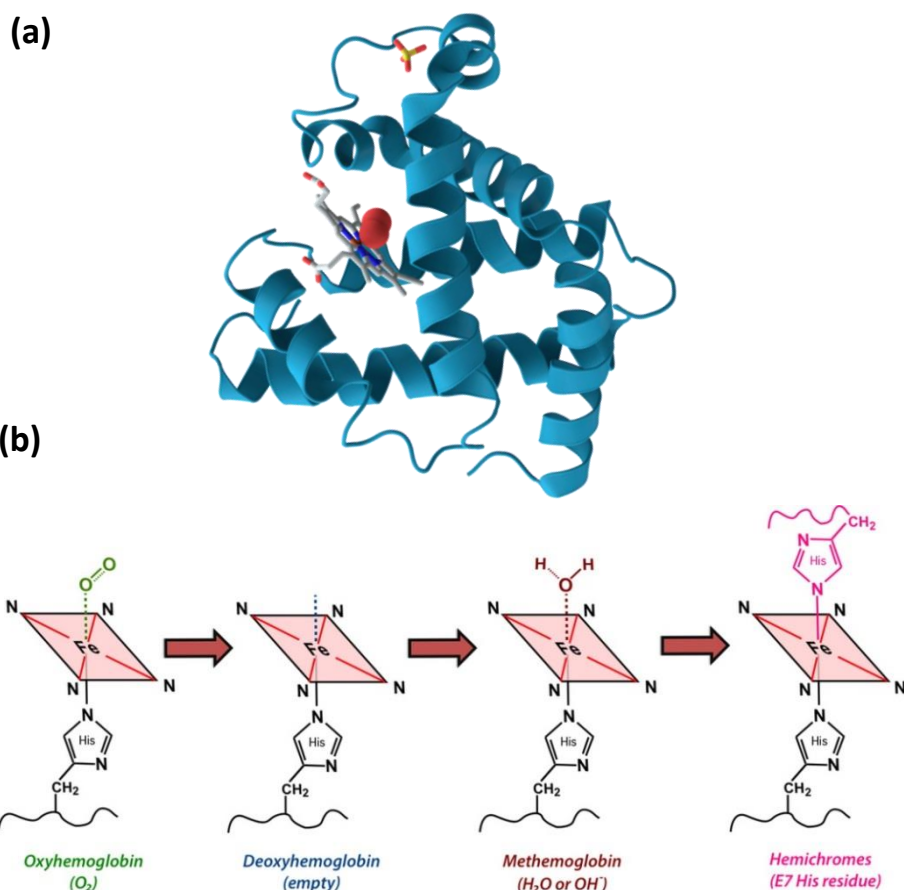
Scheme 1. (a) Native myoglobin structure (Monomeric hemoprotein with a single polypeptide chain of 153 aminoacids). (b) Coordination states of heme group (from left to right): 6C-LS, 5C-HS, 6C-HS, 6C-LS.

The main biological functions of hemoproteins are the electron transport (e.g. cytochromes), oxygen transport and storage (e.g. myoglobin), and the catalysis of redox reactions (e.g. enzymes).[5] Despite the differences in

258

the chemistry, the iron protoporphyrin IX (heme) prosthetic group is present in all the hemoproteins. Likewise, in photosynthesis this cofactor may function either as reaction center (*i.e. charge separation*) or accessory (*i.e. exciton transfer*) pigments in light harvesting. Differences in the apoprotein sequences are not sufficient to explain the drastic different physicochemical properties found for the same cofactor in protein complexes. Then, the different functions must stem from differences in the interaction/coordination and conformational flexibility between the bound cofactor and the substrates which are ultimately determined by the interplay between the redox center and the respective apoprotein structure in addition to hydrogen bonding and electronic effects.[6, 7]

In this sense, the mechanisms by which the protein controls the intrinsic reactivity of the heme are both of theoretical and practical interest. For example, heme-iron can be five- or six-coordinate with the axial ligation strongly related to protein function (Scheme 1). Six-coordination of heme with two strong axial ligands (e.g. His/His) is typical of hemoproteins as electron carriers (*i.e. Low spin state* - 6LS). Penta-coordination or with the sixth position available for substrate binding is usually found in globins and redox enzymes *(i.e.* 5HS or 6HS – *High spin states*). In globins, the imidazole ring of the "proximal" histidine (His) residue provides the fifth iron ligand and the axial position remains available for substrate coordination. Different ligand coordination states are able to modulate the redox potential of the heme iron determining the protein function.

Non-native states induced by changes in the native structure and its interplay with the heme group may help to evolve new functions of the proteins.[8] The relationship between function and structure in non-native hemoproteins is a very important issue to elucidate the role of these macromolecules in biological systems.[8] Thus, protein engineering is arising as a promising research field for the design of different non-native conformations with specific catalytic, ET and photochemical properties.[9, 10] Folded proteins can exist in multiple conformational substates with a distinct structure, where each one reflects a local minimum of free-energy landscape. These substates may represent non-native states of the folded protein. Conformational diversity in proteins may range from fluctuations of side chains and movements of active-site loops to secondary structure changes and rearrangements of the entire protein fold, which confers new functions for the proteins in the non-native states.[11] The mechanisms responsible for the transition from the native protein to its functional non-native conformers is challenging, but ultimately would uncover how proteins execute such variety of biological functions.[12]

In this sense, myoglobin (Mb) is a favorable scaffold protein for rational heme protein design either by genetic and/or chemical modifications that can exhibit novel functions.[13, 14] Even though, X-Ray or NMR structure is not available for non-native Mb states with His-His coordination (6C-LS), molecular modeling has allowed to study the role of the flexibility of the CDE helices in its formation upon introduction of a hydrophilic group (*mutation of Leu29 to Glu29*) in the hydrophobic heme pocket that alters the protein

folding behavior of Mb.[15] Chemical functionalization of protein residues is a sort of engineering of biomolecules that allows generating non-native conformer states and new biomaterials.[16, 17] It has been recently reported that cationized Myoglobin (c-Mb) has been used as a first step to modulate the surface charge of the protein and to build solventless liquids of functional metalloproteins.[18, 19] The cationization of the protein is achieved by the carbodiimide-activate coupling of N,N-dimethyl-1,3-propanediamine (DMPA) molecules to aspartic and glutamic acid residues on the external surface of the native Mb. This chemical modification provokes significant secondary structural changes and rearrangements of the entire protein fold,[18, 19] and consequently the ET, catalytic or substrate transport activities of the Mb are probably affected. Based on this assumption, this chapter will be devoted to get insight into the ET and catalysis behavior of c-Mb at SAM interfaces. The understanding of the influence of the interactions governing the adsorption and conformational orientation of c-Mb onto SAMs is crucial to the proper design of stable bioelectroactive interfaces for sensing applications.

Most of the natural reactions of redox proteins occur at or in membranes under conditions that are distinctly different from those in solution. In this respect, electrochemical interfaces represent a convenient model to mimic the interactions and the charge distribution of the membrane/solution interface specifically upon proper functionalization of the surface of the electrodes.[20, 21] Natural processes can tunnel electrons over nanometric distances, and most redox macromolecules have sufficiently thick protein shells to render the distance between the redox donor and acceptor

sites (*e.g. other biomolecule or an electrode*) so large that the rate of ET could be negligible.[22-24] However, direct ET between biomolecules takes place which is captivating in its own right.[24-26]

Chemically modified electrodes based in self-assembled monolayers (SAMs) appear as ideal platforms to immobilize redox proteins by strategies based on non-covalent or covalent attachment interactions.[21, 27-30] In the particular case of non-covalent attachment, the proteins can adsorb on surfaces by electrostatic, hydrophobic and polar interactions. Which of these intermolecular forces dominate the interaction will depend on the particular protein and surface chemistry involved. This approach leads to protein physisorption resulting in adsorbed protein layers usually heterogeneous and randomly oriented, since each molecule can form many contacts with different orientations by minimizing the repulsive interactions with the surface and the previously adsorbed proteins. However, protein immobilization into monolayer or submonolayer electroactive assemblies provides an adequate platform to elucidate the redox properties and catalytic mechanism of enzymes as well as to elucidate mechanism and kinetics of protein ET where diffusion processes may be not interfering. In this framework, the possibility to facilitate electronic communication, "wiring", between the protein´s redox center and the electrode through SAMs is not only a way to reproduce physiological conditions but has also become an excellent approach to study biophysical fundamentals of their dynamic interactions for better understanding of biological ET processes.[31-36]

ET processes of proteins immobilized on coated electrodes (*i.e. bioelectrochemistry*) can be studied by electrochemical techniques (e.g. protein film voltammetry).[37] The performance has been substantially developed in the last 20 years, to address thermodynamics and dynamics of the redox reactions of protein monolayers. [33, 36, 38-43] Then, the electronic communication between an electrode and the active center of the redox-active protein is instrumentally detected as a current-potential profile having specific features. The analysis of such voltammetric features provides insight into the mechanism of protein interactions with the substrates. In general, the Marcus theory [44] has been demonstrated to be valid to consider the possible contribution of the electrode surface functionality into the ET kinetics, which essentially depends on the electronic coupling between the electrode and redox center (H_{AB}), the reorganization energy ($\lambda = \lambda_{in} + \lambda_{out}$, *sum of the inner and outer-sphere contributions*) and the activation free energy (ΔG_a^*).[36, 42] Thus, the modification of the electrode surface impacts the reorganization energy, λ_{out}, by controlling solvent or protein reorganization at the interface. On the other hand, part of the protein function may be involved in overcoming the reorganization energy for the environment around a buried redox center to stabilize the redox states and the energy barrier, λ_{in}, which is associated with changing bond lengths and angles of the reactant to accommodate the product (*i.e. dynamics*). Finally, λ_{out} may be also lowered by the protein structure upon constraining the coordination geometry of the active site to allow rapid ET reactivity. Additionally, as the redox center cannot be in close contact with the electrode, the ET coupling (H_{AB}) must also account for the molecular structure of the pathway connecting both donor and

acceptor sites. Therefore, the efficiency of such coupling is determined by the 3D protein structure of the intervening medium composed by the peptide matrix, which is ultimately regulating ET. As a consequence, ET will be modulated by the distance and protein structure that is influenced by the specific protein-SAM interactions.

Such interactions can be manipulated by reconstitution of the heme group, changes in the surface coating and the protein´s apparent surface charge, and chemical manipulation of the electron tunneling pathways between the biomolecules and the electrode.[8-10] This sort of protein engineering for bioelectrochemistry can alter the formal potentials of the redox moieties, define different local environments to control the reorganization energy and change electron tunneling pathways between redox center and the electrode.[9] The information provided by electrochemical techniques can be complemented by structural information about the species involved in the ET processes by the use of spectroscopic techniques (FT-IRRAS and Resonance Raman, RR). [45,46]

Many works have focused on determining the parameters that control ET efficiency of redox proteins. Several factors influencing ET such as donor-acceptor distance,[22-24, 36, 47] heme plane orientation,[48] electron transport pathway,[49] conformational changes around the heme group,[50] the reorganization energy involved in spin state changes,[51, 52] environmental conditions (e.g. solvent, pH and ionic strength effects),[53] conformationally gated mechanisms [54] and polarization-relaxation processes of the protein environment have been reported.[55] Among these factors, the ET of redox

proteins immobilized on 2-D assemblies is often coupled to non-faradaic processes such as reorientation and conformational transitions.[40, 56] Non-faradaic processes are modulated by varying the chemical properties of functionalized surfaces, which can directly tune the orientation and/or conformation of protein states,[57-59] and in turn determine the ET properties of the adsorbed proteins.[60]

Different techniques have been used to explore the relationship between the interfacial chemistry of SAMs and the ET properties of immobilized redox proteins. Combining electrochemical techniques with surface vibrational spectroscopies such RR and IRRAS spectroscopies provides a deep understanding of the conformational and structural dynamical changes of the adsorbed proteins associated with changes into the ET process.[45,46] Feng et al.[51] have reported the use of electrochemical and Raman spectroscopy techniques to study native Mb deposited on a Nafion film. They ascribed the fast electron transfer of the adsorbed Mb to a change from high to low spin state of the heme group when the protein was embedded into the film. Similarly, the effect of surfaces properties of hydrophobic and hydrophilic mixed SAMs on the adsorption of BSA and fibrinogen has been also addressed by Quartz Crystal Microbalance (QCM) coupled to grazing angle Fourier transform infrared spectroscopy (GAFTIR) technique.[57] Interestingly, Rocco et al. [61] have recently reported a transition from the low to high spin state at the iron coordination of one heme group at a bacterial di-heme cytochrome C upon protein immobilization on negatively charged

SAMs, as characterized by Cyclic Voltammetry (CV), Resonance Raman (RR) and SERRS spectroscopies.

In this chapter, the electrochemical behavior of c-Myoglobin non-covalently attached to biomimetic surfaces composed of pure and mixed MUA/DT SAMs is addressed based on conformational, structural and orientation changes of non-native states driven by protein-surface interactions. Finally, the electrocatalytic activity of c-Mb/SAMs constructs towards the reduction of hydrogen peroxide has been evaluated. For this purpose, mixed SAMs are built by varying the stoichiometry ratio of hydrophilic 11-mercaptoundecanoic (MUA) to hydrophobic 1-decanethiol (DT) linkers to attain different surface compositions of –COOH moieties: 100%, 92%, 62%, 46%, 16% and 0%, and surface charge densities of deprotonated –COO^- groups ranging approximately from 8% to 80% (at pH=7.6). FT-IRRAS and RR spectroscopic techniques are used to assess the effects of the surface chemistry on the conformational/structural properties of the c-Mb adsorbed. Moreover, the electrochemical behavior of the protein assemblies are characterized by cyclic voltammetry techniques and their surface coverage determined by QCM measurements. CV and chronoamperometric measurements are also carried out showing that c-Mb present excellent electrocatalytic properties that may be applied to the rational design of biosensors.

6.2.   Materials and methods

Chemicals reagents. 11-mercaptoundecanoic acid (COOH-$(CH_2)_{10}$-SH, MUA), 1-decanethiol (CH_3-$(CH_2)_9$-SH, DT), Triton X-100, myoglobin from horse heart (Mb), 3-dimethylamino propylamine (DMAPA), N-(3-dymethylaminopropyl)-N-ethylcarbodiimide hydrochloride (EDC) and semiconductor grade purity potassium hydroxide (KOH) were purchased from Aldrich-Sigma (purity ≥ 99%). The rest of the reagents, 2,5-dihydroxy acetophenone ($(HO)_2C_6H_3COCH_3$), trifluoroacetic acid (CF_3COOH), phosphoric acid (H_3PO_4), hydrochloric acid (HCl), perchloric acid ($HClO_4$), hydrogen peroxide (H_2O_2), potassium chloride (KCl) and potassium nitrate (KNO_3) were from Merck analytical grade. Aqueous solutions were prepared with deionized ultrapure water produced by a Millipore system.

Methods. A three-electrode cell comprising a platinum coil as the counter electrode, a 50 mM KCl calomel electrode as the reference electrode and Au(111) textured surfaces as the working electrode were used. Au(111) surfaces were cleaned and modified with MUA and/or DT as indicated in the protocols described in the Chapter 2 (*Sections 2.3.1. and 2.3.2.*). The adsorption time in lyotropic liquid mixtures was 15 min. Surface compositions of the mixed SAMs were determined as described in Chapters 4 and 5.

The chemical modification protocol for cationization of native Mb (Scheme 2), the characterization of the product, c-Mb, by MALDI-TOF and UV-visible techniques, and the immobilization procedure onto the mixed SAMs are described in detail in the Chapter 2 (*Sections 2.3.3, 2.3.4 and 2.4.3.1.2*). A part

of this work was carried out during a 3-months stay in the Electrochemistry Group headed by David Fermin at the University of Bristol (UK).

a   **b**
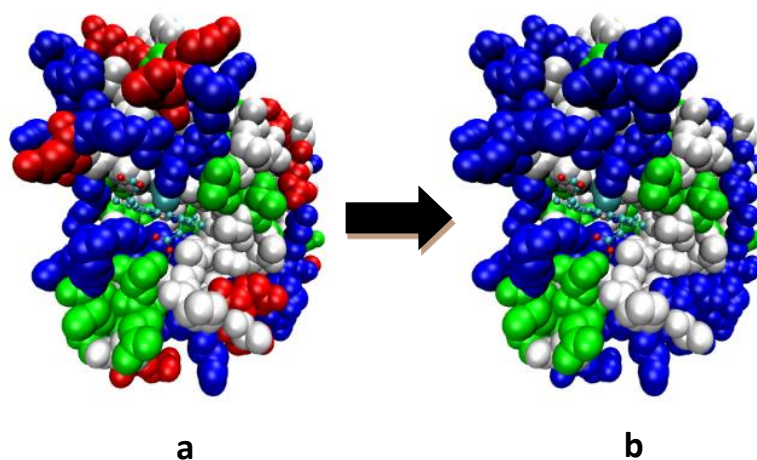
Scheme 2. (a) Native Myoglobin showing negatively (red) and positively (blue) charged regions on the surface structure (b) Cationized Myoglobin prepared by EDC coupling of DMAPA to negatively charged surface residues (Asp and Glu) of Mb.

Electrochemical characterization was carried out accordingly to the specifications and working conditions included, unless otherwise stated, in the Chapter 2 (*Section 2.4.1.*). Characterization of the samples was also performed by FT-IRRAS as previously indicated in Chapter 2 (*Section 2.4.2.1.2*). Raman spectra and QCM measurements were performed following the instructions included in Chapter 2 (*Sections 2.4.2.2.2. and 2.4.3.2.2.*). The reproducibility of the measurements was checked by testing batches of 3-4 samples.

6.3.   Results and Discussion

6.3.1 Structural characterization of c-Mb immobilized on SAMs

6.3.1.1. ATR and FT-IRRAS spectroscopic characterization

Figure 1 shows the ATR spectrum in the amide I band region of the c-Mb in solution. The amide I peak corresponds to the vibrational absorption band of the -C=O stretching mode of the peptide bond. The overall shape and maxima of the amide I peak are directly influenced by the secondary structure of the proteins and consequently used for its conformational study.[62] The peaks in the range of 1654-1660 cm^{-1}, 1640-1650 cm^{-1}, 1670-1680 cm^{-1}, 1610-1637 cm^{-1} and 1680-1691 cm^{-1} have been assigned to the α-helix, random coil, β-turn, β-sheet parallel and antiparallel conformations, respectively.[63]
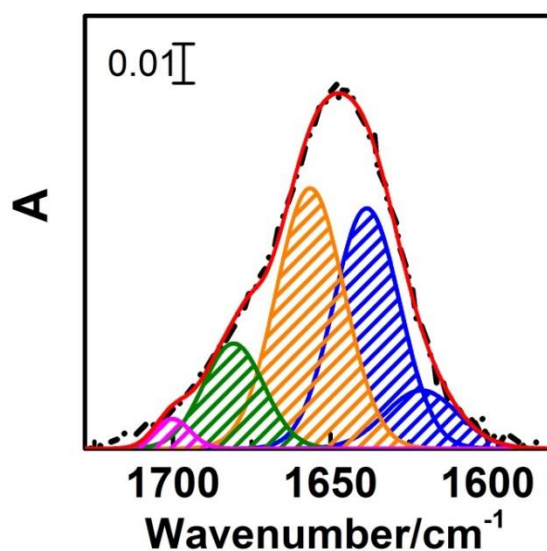

Figure 1. Infrared ATR spectrum of c-Mb in D$_2$O in the Amide I band region (•—•) including the fitting components of the different secondary structure bands deconvoluted: (—) β-sheet and unordered, (—) α-helix, (—) β-turn, (—) β-sheet antiparallel, and (—) convoluted signal.

269

The deconvolution analysis of the amide I signal reveals that the content of α-helical secondary structure of c-Mb in solution decreased drastically to a 39 % compared to that of 75-80% for native Mb (Table 2).[64] This change is associated with an increase in the content of β-sheet, β-turn and unordered domains from 2, 6 and 11% in Mb to 11, 15 and 35% in c-Mb, respectively. These results are in excellent agreement with those reported for c-Mb as determined by circular dichroism (SRCD).[18] Therefore, the significant changes observed on the secondary structure of c-Mb by introducing positive surface charges must be related with the absence of disulphide bridges and the marked dependence of the globular structure of Mb on inter- and intrahelix electrostatic stabilization,[65] which involves glutamic (Glu) and aspartic (Asp) side chains that are modified in the cationization reaction.[66] Such changes in the secondary structure of the non-native state of Mb in solution has a strong effect on the heme environment which is manifested by the transition from a high (6C-HS) to low spin (6C-LS) state of the iron moiety upon cationization (Section 2.3.3.1). In fact, these results are consistent with those reported for c-Mb adducts where spectral changes and circular dichroism measurements have been related to changes in the heme Fe coordination without protein denaturation. [19, 67]

FT-IRRAS is a sensitive and convenient method to obtain structural information about surface-bound proteins. IRRAS measurements have been carried out to assess the conformational states and the possible orientation changes of c-Mb upon adsorption on surfaces modified with different ratios of -CH_3 (hydrophobic) and -COOH (hydrophilic) terminal groups. It is worth

mentioning that, although the amide II region (1500-1600cm) is less sensitive to the conformational changes compared to amide I region (*spectra not shown*), it becomes an useful tool to qualitatively determine the changes in orientation of proteins by changes in the amide I/II peaks intensity ratio.[68, 69] This is based on the following considerations: (i) the dipole moments of amide I and II are approximately perpendicular each other, and (ii) the metal surface selection rules (MSSR), that apply for incident p-polarized radiation at a grazing surface angles used in IRRAS experiments, states that the vibrational transitions with a dipole component perpendicular to the surface are mainly enhanced.

Figure 2 shows the representative examples of the FT-IRRAS spectra for immobilized c-Mb while changing the surface ratio of $-CH_3$/-COOH in the SAMs. The position of the maxima of the amide I and amide II bands together with their intensity ratio are summarized in the table 1 for c-Mb in solution and non-covalently attached to the different MUA:DT SAMs. The shift in the position of the amide I band maxima of the c-Mb in solution upon adsorption in these 2D assemblies shows that the protein undergoes conformational changes in different hydrophobic/hydrophilic environments as a result of the surface interactions. Additionally, the changes in the amide I/II intensity ratio indicates that the protein is also held in different orientations in average depending on the underlying surface chemistry.
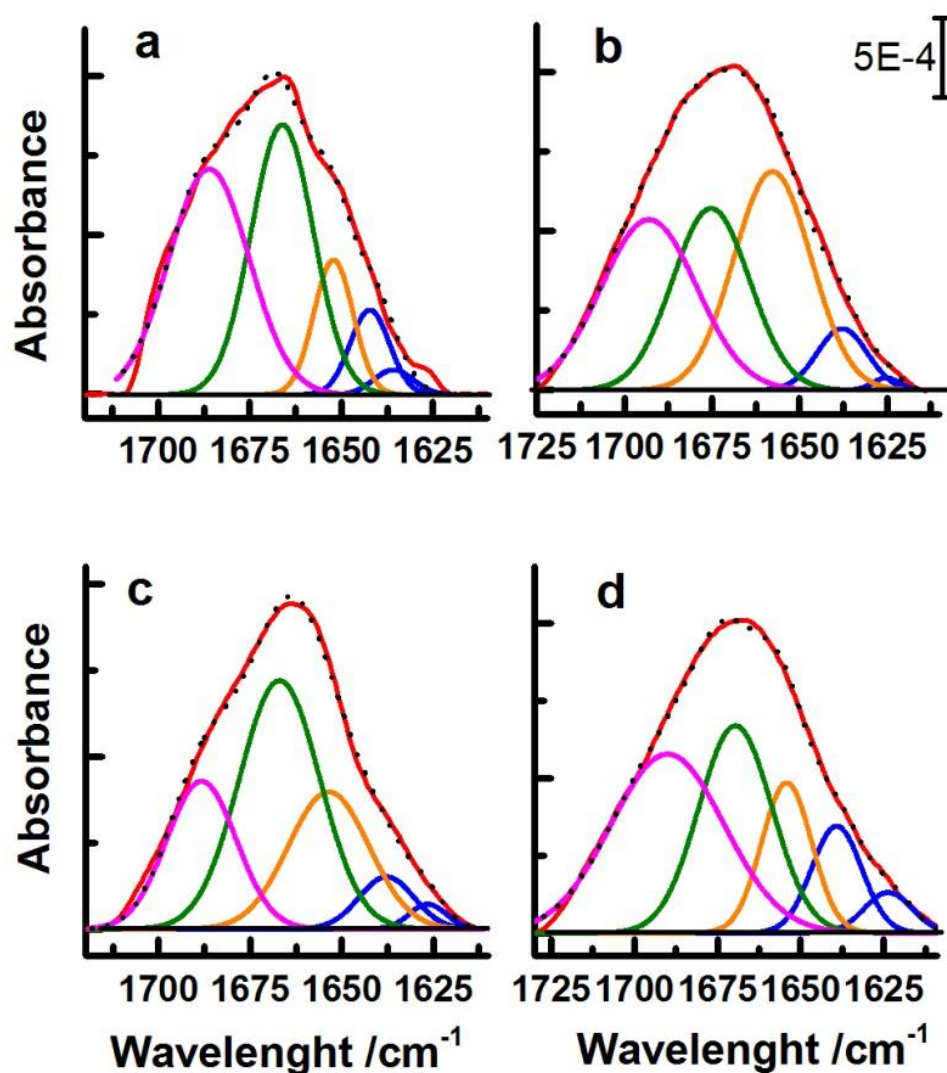
Figure 2. FT-IRRAS spectra of the Amide I region of c-Mb immobilized on mixed MUA/DT SAMs with different surface compositions, X_{MUA}^{Surf} : (a) 1 , (b) 0.9 and 0.76, (c) 0.46, and (d) 0.15 and 0. Experimental Amide I bands (••••) with the fitting components of the different secondary structures deconvoluted are included: (—) β-sheet and unordered, (—) α-helix, (—) β-turn, (—) β-sheet antiparallel, and (—) convoluted signal (*Appendix A*).

Table 1. Infrared data obtained for c-Mb from solution and immobilized on SAMs.

		Amide I máxima (cm^{-1})	Amide II maxima (cm^{-1})	Amide I/II intensity ratio
c-Mb in solution		1651	1535	1.49
cMb on MUA/DT	$X_{MUA}^{Surface}$			
1.00/0.00 **(1)**	1.00	1671	1547	1.48
0.70/0.30 **(2)**	0.90	1671	1545	1.40
0.50/0.50 **(3)**	0.62	1670	1547	1.38
0.45/0.55 **(4)**	0.46	1664	1546	1.17
0.05/0.95 **(5)**	0.16	1670	1545	1.20
0.00/0.00 **(6)**	0.00	1668	1545	1.20

Table 2. Conformational analysis of c-Mb immobilized on MUA:DT SAMs with different ratios.

(% secondary structure)	c-Mb[a]	c-Mb[b]	c-Mb SAM (1)	c-Mb SAMs (2,3)	c-Mb SAM (4)	c-Mb SAMs (5,6)
β-sheet	13	11	34	30	28	52
β-sheet/random	45	46	40 ± 3.5	34 ± 6.6	35 ± 4.9	55 ± 0.7
α-helix	42	39	21 ± 2.8	31 ± 2.9	28 ± 5.7	17 ± 2.1
β-turn	13	15	40 ± 0.7	30 ± 7.8	37 ± 9.9	29 ± 1.4

[a] Data obtained from Synchrotron radiation circular dichroism (SRCD) spectra of c-Mb in water.[18]
[b] Data obtained by the ATR spectra of c-Mb from D$_2$O solution.

Curve fitting analysis of the component bands corresponding to the protein secondary structures reveals that the c-Mb adsorbed on surfaces containing 100%, 16% and 0% –COOH/-COO$^-$ groups shows the more striking conformational changes (Figure 2 and Appendix A). This fact is manifested by

273

a significant reduction of the percentage area of the component band centered at 1655 cm^{-1} (α-helix domains) and a concurrent increase of the β-sheet bands contribution as compared to the protein in solution (Table 1).

Such change in the secondary structure contents suggests that the c-Mb is partially denatured on highly hydrophobic and hydrophilic surfaces, which is consistent with results previously reported for other proteins adsorbed on similar monolayers.[57] The degree of conformational change is mainly dependent on the protein-surface interactions and the internal bonding strengths that hold a particular protein conformation. At hydrophobic surfaces, a significant increment of the entropy should be produced by the loss of water from the c-Mb structure and the monolayer. Therefore, the exclusion of water maximizes the surface-protein interactions and distorts the protein structure allowing the greater conformational changes of the c-Mb. In the case of 100% –COOH/-COO$^-$ surfaces, the adsorption process should be mainly determined by the electrostatic interactions between the carboxylate groups and the positively charged c-Mb surface. Then, the high density of negative charge at the MUA surfaces would induce a strong adsorption of c-Mb which may cause a deformation of the overall protein structure despite the surface-water interaction effects. These results suggest that effective protein-surface interactions rather than hydration contributions are driving the partial protein unfolding in these systems, as it have been also demonstrated by molecular dynamics simulations of the GB1 hairpin peptide on SAM surfaces with different hydrophobicities.[58]

On the other hand, the degree of conformational change for c-Mb deposited onto mixed SAMs with a 90%, 62% and 46% surface content of $-COOH/-COO^-$ groups is less evident than that for the more hydrophobic and hydrophilic layers (Table 1), most likely due to the balance of hydrophobic and hydrophilic short-range interactions. As already commented, a high distribution of different protein orientations is also expected according to the changes in the amide I/II intensity ratios observed for the c-Mb on the SAM surfaces (Table 1). Nevertheless, the most significant overall change in the protein orientation is produced from $-COOH/-COO^-$ enriched-surfaces ($1 \geq X_{MUA}^{Surf} \geq 0.62$) to $-CH_3$ enriched ones ($0.46 \geq X_{MUA}^{Surf} \geq 0$).

6.3.1.2. Resonance Raman (RR) spectroscopic characterization

RR spectroscopy is an especially useful and highly sensitive technique for unravelling the oxidation and spin state, structural features and orientation of the heme iron coordination center of metalloproteins immobilized on surfaces. The heme group of Mb gives rise to two distinct electronic transitions, the so-called Soret (near to 400nm) and α-β bands (500-650 nm). Laser excitation in the Soret and α-β (Q) band regions brings about different enhancements of the Raman vibrational bands via different resonance scattering mechanisms (*Chapter 2 - Section 2.4.2.2.1.*).[70] In a first approximation, the heme cofactor of c-Mb can be considered to be of D_{4h} symmetry. Since the transition dipole moments of the heme groups lie in the porphyrin plane, the RR spectrum of the protein is dominated by the in-plane vibrational modes. Upon Soret-band excitation (~410 nm) the RR spectrum is

preferentially enhanced by the totally symmetric modes (A_{1g}) which gain intensity via the A-term enhancement mechanism. Under these circumstances, due to the enhanced depolarization of the scattering radiation, the RR spectra obtained for the protein at the surface are essentially identical to that obtained in solution in terms of band positions, widths and relative intensities. Although Soret-band excitation measurements provides the highest enhancements are insensitive to protein reorientation.

By contrary, symmetric bands lose intensity upon Q-band (α) excitation (~510-540 nm) while the non-totally symmetric modes (B_{1g}, B_{2g}, A_{2g}) gain intensity via the B-term enhancement mechanism. This much weaker Q-band excitation leads to an intermediate situation, where depolarization of the scattered radiation is still appreciable but not complete. Thus, a reasonable compromise between acceptable enhancement and qualitatively predictable selection rules are still applicable. These selection rules rely on the fact that the individual components of the scattering tensor are influenced by the direction of the electric-field vector and the orientation of the heme plane. Thus, totally symmetric (A_{1g}) and non-totally symmetric (B_{1g}, B_{2g}, A_{2g}) modes display a different surface enhancement of the Raman scattering under pre-resonant excitation (*e.g. 510-540 nm*) depending on the orientation of the heme with respect to the metal surface. Although absolute orientations cannot be accurately determined, changes in the average orientations can be still observed. Therefore, different orientations of the adsorbed protein with respect to the surface are expected to lead the variation of the relative intensity ratio of modes with different symmetry, i.e., A_{1g} vs B_{1g} (e.g.

$v_{10}(B_{1g})/v_4(A_{1g})$). This is especially interesting for direct monitoring of protein dynamics at interfaces.
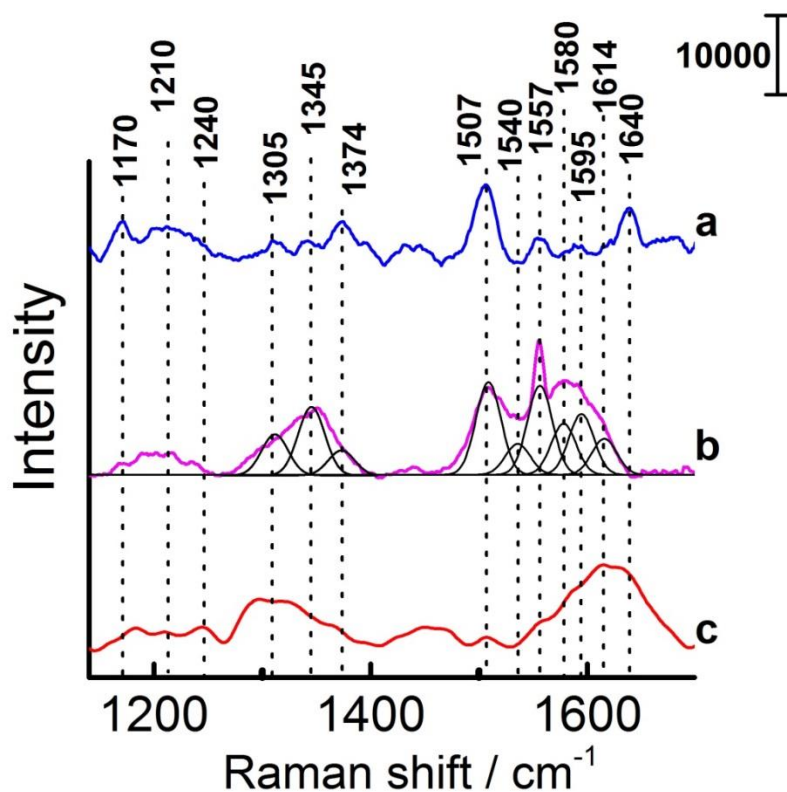

Figure 3. RR spectra of c-Mb in aqueous solution (a) and immobilized on mixed SAMs before (b) and after (c) the addition of a drop of PBS solution (30 mM phosphate buffer at pH=7.6). λ_{ex}= 532nm.

Figure 3 shows the RR spectra of c-Mb in solution and deposited on different mixed SAMs upon excitation at 532 nm in the Q-band region. Most of the vibrational bands originate from C-C and C-H vibrations of the porphyrin macrocycle which are influenced by the conjugated interaction of the π electrons between the central metal ion and the porphyrin ring. The most important bands are labelled in table 3, with some of them directly

277

related with the coordination and spin state of the protein cofactor. It is widely accepted that the peaks at ≈1350-1370 cm^{-1} assigned to C-N vibrations [71, 72] are sensitive to the oxidation state of the heme iron,[70] appearing as a broad band placed at 1374 cm^{-1} for ferric Mb species upon Q-band excitation.[73, 74] Bands at 1610 cm^{-1} and 1640 cm^{-1}, which are attributed to the asymmetrical stretching mode of $C_\alpha C_m$ of the heme (v_{10}),[75] are considered the high and low spin state markers of the heme iron, respectively.[72, 76]

Table 3. Assignment of RR peaks of c-Mb depicted in wavenumbers (cm^{-1}).

Experimental	Reference [74, 75]	Assignment	N°/Symmetry [75, 77]
1640	**Low spin**:1640-1644	$v(C_\alpha C_m)_{asym}$	v_{10} / B_{1g}
1614	**High spin**: 1610-1614	$v(C_\alpha C_m)_{asym}$	v_{10} / B_{1g}
1580	1583	$v(C_\alpha C_m)_{asym}$	v_{19} / A_{2g} v_{37} / E_u
1557	1563	$v(C_\beta C_\beta)$	v_{11} / B_{1g} v_2 / A_{1g}
1540	1544	$v(C_\beta C_\beta)$	v_{11} / B_{1g}
1507	1508	$v(C_\beta C_\beta)$	v_3 / A_{1g} v_{38} / E_u
1374	**Fe^{3+}**: 1370-1375	v(pyr half-ring)$_{sym}$	v_4 / A_{1g}
1345	1341	v(pyr half-ring)$_{sym}$	v_{12} / B_{1g}
1305	1301	$\delta(C_aH=)_2$	v_{21} / A_{2g}
1210	1209	$v(C_mH)$	v_{13} / B_{1g}
1170	1169	v(pyr half-ring)$_{sym}$	v_{30} / B_{2g}

The RR spectrum of the c-MB in solution is shown in Figure 3a. The presence of the bands at 1240, 1374 and 1640 cm^{-1} corroborates that the heme group is in a six-coordinate low spin state (6C-LS) of its ferric form, as previously stated by UV measurements (Chapter 2 – Section 2.3.3.1.). [67] These results indicate that the distal histidine (H64) is strongly attached to the iron center at the sixth position. The RR spectra show remarkable differences when the c-Mb is attached to 2D ordered arrays of MUA:DT molecules (Figure 3b). Interestingly, while the marker band of the oxidation state is maintained at 1374 cm^{-1}, the band at 1640 cm^{-1} disappears with the concurrent appearance of a set of bands at 1614 cm^{-1}, 1580 cm^{-1}, 1557 cm^{-1} and 1540 cm^{-1}, which are representative of a six-coordinated high spin state configuration (6C-HS) typical of MbH_2O structures.[75] This low to high spin state conversion put forward that direct protein-surface interactions provoke structural changes on the His/His ligated heme environment based mainly in the swapping of the axial His ligand with a water molecule.

A similar change in the iron coordination has been recently reported for the electrostatically adsorption of a diheme cytochrome C on carboxyl-terminated monolayers using SERR spectroscopy.[61] Reversible structural changes of the heme coordination pattern have also been reported for cytochrome C adsorbed on Ag coated electrodes when the Met-80 ligand is specifically removed from the sixth coordination site, that remains either vacant (five-coordinated high spin, 5C-HS) or is occupied by a His (six-coordinated low spin, 6C-LS) or a water molecule (6C-HS).[78]
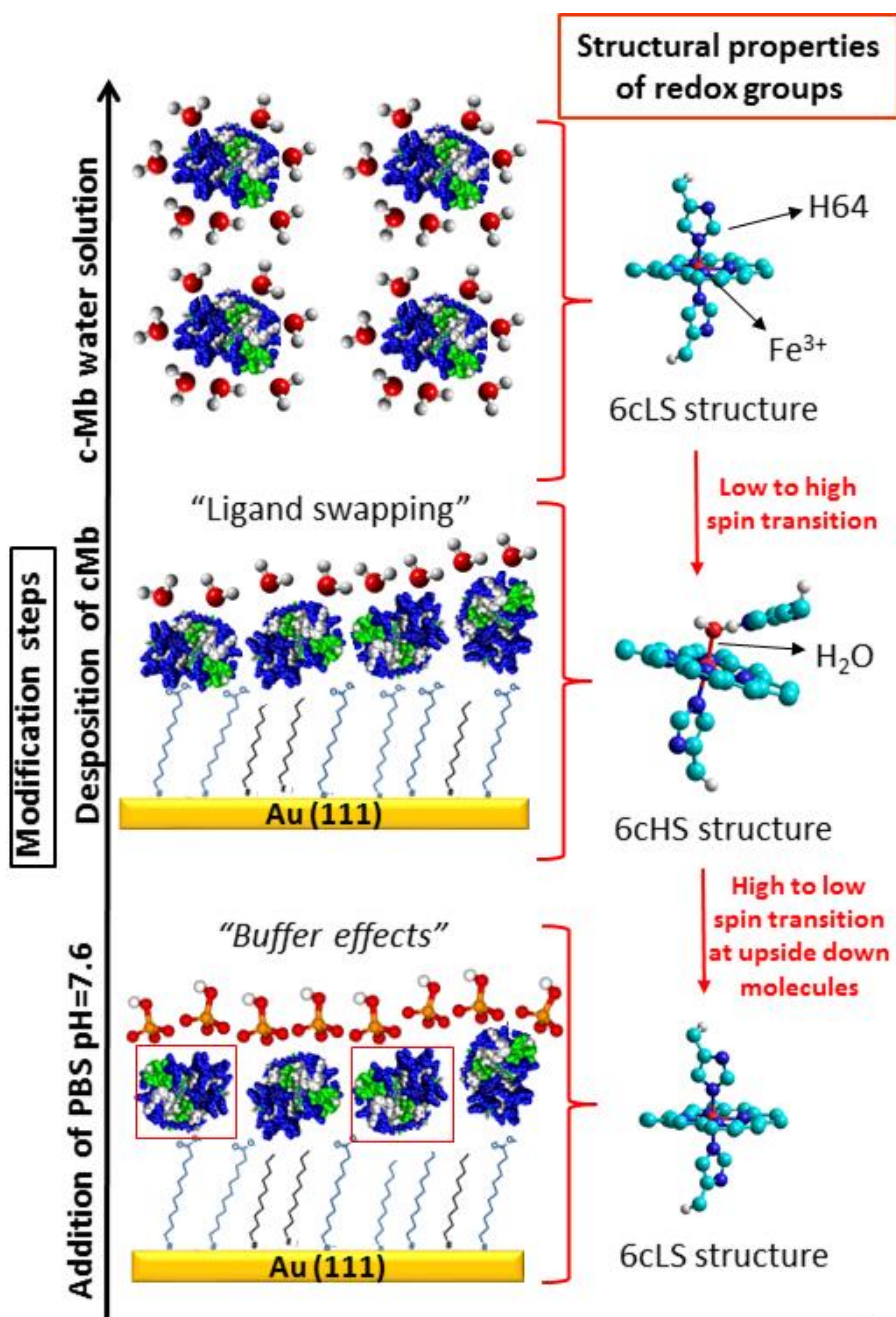
Scheme 3. A general representation of the structural properties of the c-Mb prosthetic group is shown as a function of different experimental conditions.

Upon adsorption of c-Mb, the salt bridges formed by electrostatic interactions between the positively charged regions of the modified Asp and Glu residues and the carboxylate groups on the coated electrode, together with the hydrophobic interactions between the methyl headgroups and hydrophobic aminoacids, may cause a distortion of the heme crevice. This probably leads to the removal of the His64 from the distal position of the heme iron that allows the subsequent incorporation of a water molecule from the surroundings into the prosthetic group structure (Scheme 3).

Remarkably, when the immobilized c-Mb assemblies are exposed to a phosphate buffer solution at pH 7.6, the low spin marker band at 1640 cm^{-1} partially returns to the RR spectra (figure 3c) indicating that a significant population of cationized proteins (6C-HS) swap back to the six-coordinate low spin state (6C-LS) under these experimental conditions. It have been demonstrated that the binding of phosphate anions to positively charged surface domains of cytochrome C located close to the heme pocket may cause significant structural changes in the hydrogen-bonding network of the heme cavity and in turn in the strength of the Fe^{3+}-Met80 bond and its geometry.[79] It is also worth mentioning that in this particular case the relative intensity ratio of the modes with different symmetry, $v_{10}(B_{1g})/v_4(A_{1g})$ increases compared to that of the c-Mb directly immobilized on surfaces from water (*i.e. absence of dissolved ionic species*). Then, this fact is probably related with a change in orientation of the heme of a part of the global population of the immobilized proteins with respect to the surface upon addition of phosphate anions. In this sense, it is proposed that the interaction of phosphate anions in

the close proximity of the prosthetic group is likely facilitated when the proteins are oriented towards the protein/electrolyte interface in an upside down position by making the heme groups accessible to the buffer solution. Such electrostatically-driven binding of phosphate anions to positively charged domains of adsorbed proteins in an upside down orientation should give rise to relevant structural changes in the heme cavity which may involve the strengthening of the Fe-His64 interaction and in turn a high to low state transition of the iron coordination (Scheme 3).

On the basis of these results, it is concluded that c-Mb immobilised on MUA:DT mixed monolayers mainly adopts two heme configuration states linked to different surface orientations when phosphate ions are incorporated: (I) protein populations in a high-spin state configuration (6C-HS) with the heme groups probably facing towards the functional groups of the monolayers which coexists with (II) protein populations in a low-spin state (6C-LS) whose heme groups are probably turned upside down facing towards the solution interface.

6.3.2. Electrochemical response of c-Mb immobilized on SAMs

CV is used to evaluate the redox behavior of the native and c-Mb upon varying the negative charge density at the protein/SAMs interface. Figure 4 shows the ET response of the c-Mb non-covalently immobilized on 2-D assemblies of MUA and DT at different surface mixing ratios. In the case of native Mb, the electrochemical response of the adsorbed protein was absent

for all the experimental conditions and mixed SAMs tested. However, a significant influence of the SAM´s surface composition on the ET behavior of the c-Mb is observed. Three regions could be distinguished according to the electroactive response of the c-Mb adsorbed at the top of the monolayers studied.
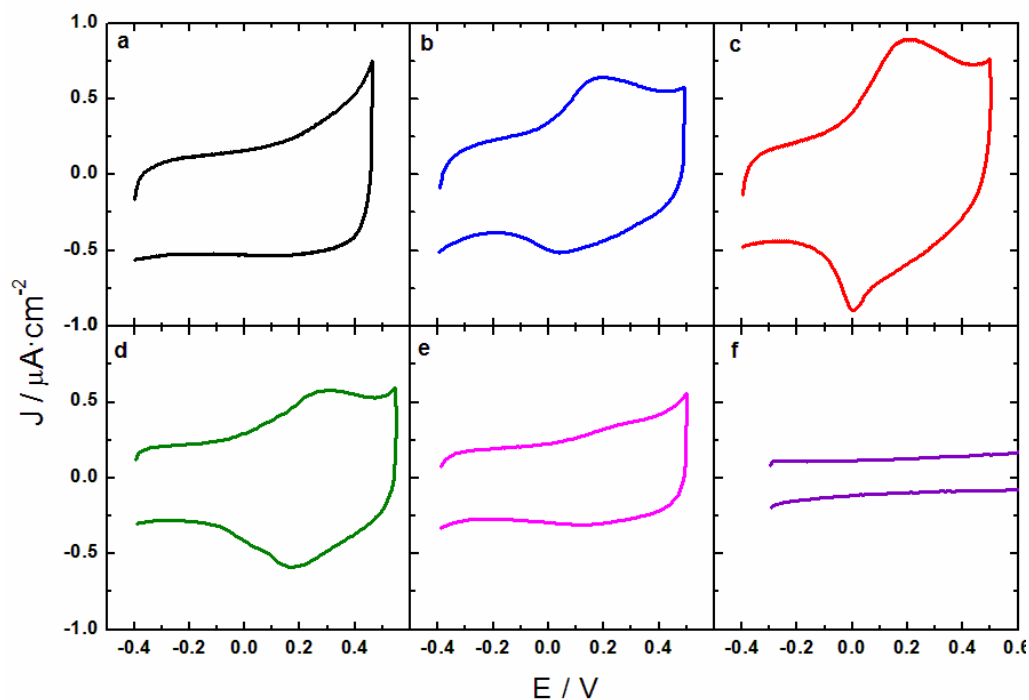

Figure 4. Cyclic voltammograms of c-Mb deposited on MUA:DT mixed SAMs in 30mM phosphate buffer at pH=7.6. MUA:DT surface ratio: (a) 1.00:0.00; (b) 0.90:0.10; (c) 0.62:0.24; (d) 0.46:0.54; (e) 0.30:0.70 and (f) 0.16:0.84 and 0:1. Scan rate: 0.1 V/s.

The first region is constituted by the c-Mb/MUA interface (figure 4a) in which the ET reaction is completely hindered. This behavior seems to contradict that of some authors have reported for the ET response of redox proteins through carboxylic acid-terminated self-assembled monolayers , and

whose native structure is mainly preserved upon immobilization. [49, 54, 55 15,20,21]

However, the lack of electrochemical activity of c-Mb on MUA SAMs can be understood on the light of its significant conformational changes due to the high electrostatic forces between the positively charged protein surfaces and the negatively charged assemblies. Then, it is argued that the partially unfolded architecture of the c-Mb on MUA monolayers may induce the heme center to be displaced from the hydrophobic pocket, thus the electrostatic repulsion between the propionate groups of the prosthetic groups and the − COO⁻ groups of the layers could favor the protein reorientation into non-active ET configurations. This idea would be consistent with those proposed in literature concluding that the electrochemical response of metalloproteins is modulated by the surface charge properties. In this sense, Wang et al.[27, 60] suggested that the poor ET activity of the cytochrome C attached to 6-amino-1-hexanethiol SAMs was linked to a decrease of the content of α-helix domains. Lojou et al. [80] have also claimed that the direct electron transfer (DET) of nickel-iron hydrogenase enzymes can be controlled by the electrostatic interactions through the acidic path of aminoacids that tunes the orientation of the enzymes by adopting upside down configurations as a function of the charge on the electrochemical interface.

In the interval of MUA surface compositions between 90% and 46% (Figure 4 b-d), well-defined voltammetric responses are obtained indicating a better electronic coupling (i.e. "wiring") between the redox center and the metal surface. As it has been previously demonstrated by IRRAS analysis, c-Mb immobilized on these mixed SAMs undergoes the lesser conformational

change as compared to the native structure of the protein in solution. These findings display that the electrochemical properties of the c-Mb can be tuned by the interactions at the protein/surface interface, which directly modulate the conformation and/or orientation promoting the most efficient ET configurations.

At the third region of surface compositions where c-Mb is deposited on $-CH_3$ enriched and pure DT monolayers, the protein electroactivity decays considerably until the disappearance of the current peaks associated to its redox response (Figure 4e,f). In these surfaces, FT-IRRAS measurements showed that the c-Mb structure experienced the greater increase of β-sheet content from 13% in solution to 52 % in the adsorbed state, and the higher reduction of α-helix content from 42% to 17%, respectively. FT-IRRAS and RR results also indicated a significant reorientation of the adsorbed proteins on the surfaces with the highest hydrophobic environments. Then, similarly to what happens on pure hydrophilic surfaces, and taking into account that is generally accepted that α-helix domains are more compact that other secondary structures such as β-sheet, it is expected that a remarkable unfolding of the c-Mb architecture and/or a significant surface reorientation of the proteins would be responsible for the inhibition of the ET function.

The formal redox potential, E°', of c-Mb in solution has been recently reported by spectroelectrochemical measurements.[81] It was observed that a wide distribution of redox potentials landscape of +0.02 V (17%), -0.08 V (38%) and -0.160 V (45%) vs Ag/AgCl$_{sat}$ arises upon cationization of native Mb with DMAPA molecules. Authors argued that such differences in the redox

potential values were due to populations of c-Mb proteins with a different number of DMAPA molecules attached to their surface, and consequently distinct microenvironments on the c-Mb/electrolyte interface were induced in the prosthetic group surroundings. The more positive value of E°' found for the smallest population of proteins (17%) was assigned to native-like Mb unsuccessfully cationized by DMAPA molecules. The shift of E°' to negative potentials corresponding to the largest protein populations (83%) was ascribed to subtle structural changes due to a high to low spin state transition (i.e. 6C-HS to 6C-LS) driven by the insertion of DMAPA moieties in aminoacid residues positioned at the surroundings of the heme pocket.
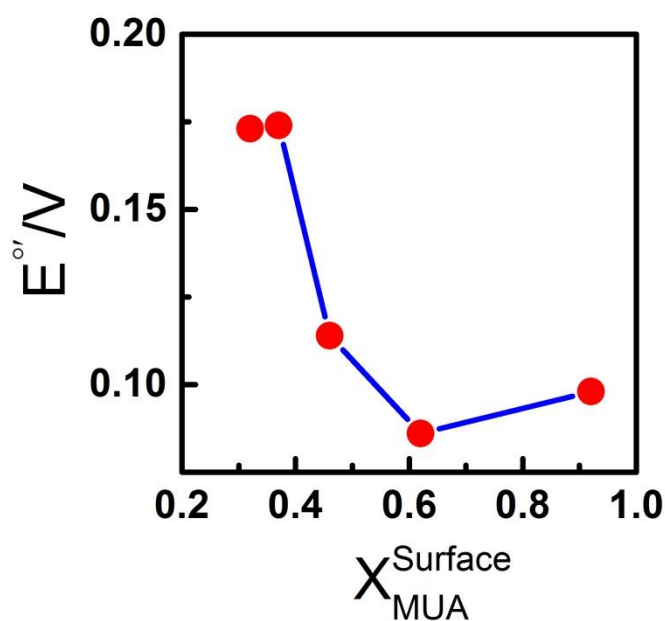

Figure 5. Apparent formal potential, E°', of c-Mb immobilized onto different MUA:DT mixed SAMs/Au(111) surfaces. The potential values are referred to the 0.05M calomel reference electrode ($E_{EC\ 50mM}$ = $E_{Ag/AgCl}$ -0.12 V). Scan rate: 0.1 V/s.

There are several factors that can affect the redox potential of metalloproteins such as changes on the electrostatic potential in the proximities of the heme group, [82] different heme orientation of the heme pocket and conformational or/and structural changes involving the heme area and its surroundings produced by perturbations in the axial ligand or in the orientation of the imidazole plane. [83] Among them, structural changes around the Fe^{3+}-distal ligand bond constitute a key factor that controls the redox potential behavior of the heme group.

Figure 5 shows the apparent formal redox potential, E°′, determined as the midpoint of anodic and cathodic peak potentials of the redox waves of the c-Mb immobilized on the different mixed SAMs. The values obtained display a large positive potential shift approximately of +0.3-0.45V in comparison with both the formal redox potentials of the predominant c-Mb populations at the 6C-LS state and native Mb observed in buffer solutions.[83, 84] A similar remarkable increase in the E°′ has been recently attributed to a coordination transition of the heme center of di-heme cytochrome C from the low to high spin state (6C-LS → 6C-HS) as a result of an adsorption-induced swapping of the axial ligand with a water molecule on carboxyl-terminated SAMs.[61] In fact, these findings have been also supported by molecular dynamics simulations showing that the communication of the heme center with bulk solvent though the opening of cavities/channels at the cytochrome c structure facilitates the increase of E°′ due to the shielding of the negative charges of the heme propionates by water molecules.[85] It is also worth highlighting that His64 residue plays an important role in the binding properties of ligands in the 6C-

HS heme structure of Mb as it forms an H-bond with the H_2O that is coordinated to the Fe(III) form. [86] This interaction creates a highly ordered distal pocket H-bonding "lattice/network" extending to the heme periphery and bulk solvent via N of His64 and Arg45 where the negative charge density of propionate groups is screened. [87] This H-bond makes the ET kinetics of the protein electrochemistry sluggish compared to Mb mutants with the distal pocket in polar environments where H_2O is heme coordinated but non H-bonded to the His64. [87] Consequently, it can be concluded that the population of c-Mb immobilized on the mixed SAMs at the 6C-HS state (i.e. H_2O coordinated and probably non H-bonded) are mainly contributing to the redox response while those at the 6C-LS state (i.e. distal His64 coordinated) would be electrochemically inactive (*Absence of redox response at negative potentials*). c-Mb redox properties seem to be not only determined by the redox couple coordination state, but also likely by the accessibility of the bulk solvent molecules to the heme pocket and the lower reorganization requirements for the ET activation energy of heme Fe(III)-H_2O coordinated excluding H-bonding of solvent molecules near its periphery.

The electrochemically active and total surface coverage of c-Mb immobilized on surface composition-dependent MUA:DT SAMs were determined either from the integrated charge of both cathodic (Q_c) and anodic (Q_a) voltammetric peaks of the surface-confined monoelectronic redox reaction of the c-Mb at low scan rates (10 mV/s) upon background correction by subtraction of the double-layer charge contribution or by QCM measurements, respectively (Figures 6 and 7).
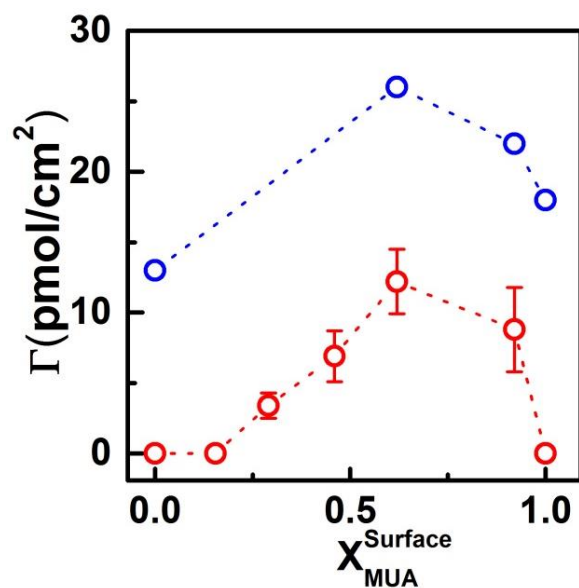
Figure 6. Total (○ —) and electroactive (○ —) surface coverage determined* for c-Mb attached to MUA:DT mixed SAMs of variable composition in 30 mM phosphate buffer at pH=7.6. *Scan rate: 10 mV/s. **Γ_{ET} =Q/nF** (n=1e⁻, F=96484 C/mol e⁻)
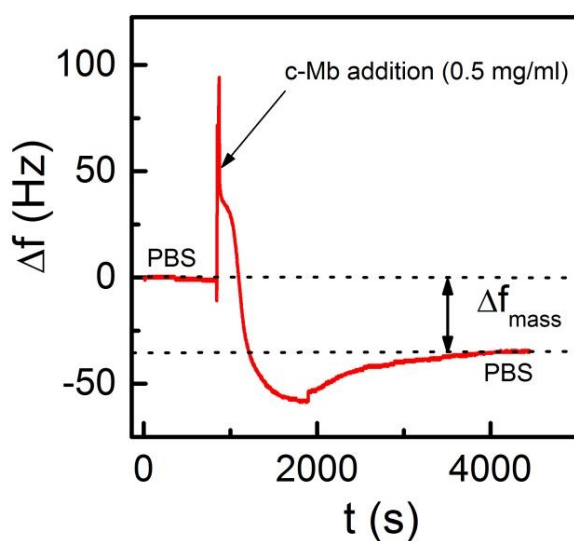

Figure 7. Time resolved frequency changes of a 5 MHz quartz crystal surface covered by gold upon addition of c-Mb to a MUA:DT coated surface with a 0.62:0.38 surface mole ratio.

It is observed that both the electroactive, Γ_{ET}, and the total, Γ_t, surface coverage of c-Mb depends on the surface composition of the layers (Figure 6). Γ_{ET} increases to reach a maximum value of 12 pmol/cm^2 on surfaces with $X_{MUA}^{Surface} = 0.62$, and then decay to zero either drastically or progressively at pure MUA and DT enriched-surfaces ($X_{MUA}^{Surf} < 0.3$), respectively. A similar trend is also observed for the Γ_t values of c-Mb with the surface composition of the layers. The highest Γ_t values are also preferentially obtained at hydrophilic surfaces ($X_{MUA}^{Surf} > 0.50$) where a full monolayer coverage of 26 pmol/cm^2 is reached at $X_{MUA}^{Surface} = 0.62$, instead of hydrophobic ones where Γ_t decay to a value of 13 pmol/cm^2.

Table 4. Electroactive and total surface coverage of c-Mb onto mixed SAMs.[a]

MUA/DT	X_{MUA}^{Surf}	Γ_{ET} [b]	Γ_{total}	Γ_{max} end-on [b,c]	Γ_{max} side-on [b,c]
1.00/0.00	1.00	0	18	26	14
0.70/0.30	0.90	9	22		
0.50/0.50	0.62	12	26		
0.00/1.00	0.00	0	13		

[a] The data included are the average of experimental results obtained for different repetitions. The coverage values are reported in pmol/cm^2 [b] Abbreviations used: Γ_{ET} = electroactive surface coverage, Γ_{max}^{end-on}= theoretical maximum coverage of Mb in edge-on orientation, $\Gamma_{max}^{side-on}$= theoretical maximum coverage of Mb in side-on orientation. [c] Theoretical coverages were obtained from Mb dimensions (4.3 nm X 3.5 nm X 2.3 nm) reported from ref.[88] Similar sizes have been assumed for native and c-Mb.

Therefore, on the basis of the maximum theoretical coverage estimated for the end-on and side-on configurations of c-Mb on surfaces (Table 4) is reasonable to assume that end-on binding models would be compatible for c-Mb at hydrophilic surfaces. On the other hand, side-on

configurations of c-Mb would be more prone in hydrophobic surfaces. It is important to highlight that Γ_t is higher than Γ_{ET} in all the cases, being the difference between both values approximately of 13 pmol/cm^2. This clearly indicates that a significant population of non-active ET configurations of c-Mb is always present at hydrophobic and hydrophilic films. The amount non-electroactive proteins accounts approximately to the total coverage of c-Mb on DT and MUA layers which could be linked to the partial denaturalization of the adsorbed proteins. On the other hand, the total population of c-Mb on mixed monolayers at intermediate surface compositions ($0.9 > X_{MUA}^{Surf} > 0.30$) is composed by distributions of both inactive and active ET configurations that are coexisting.
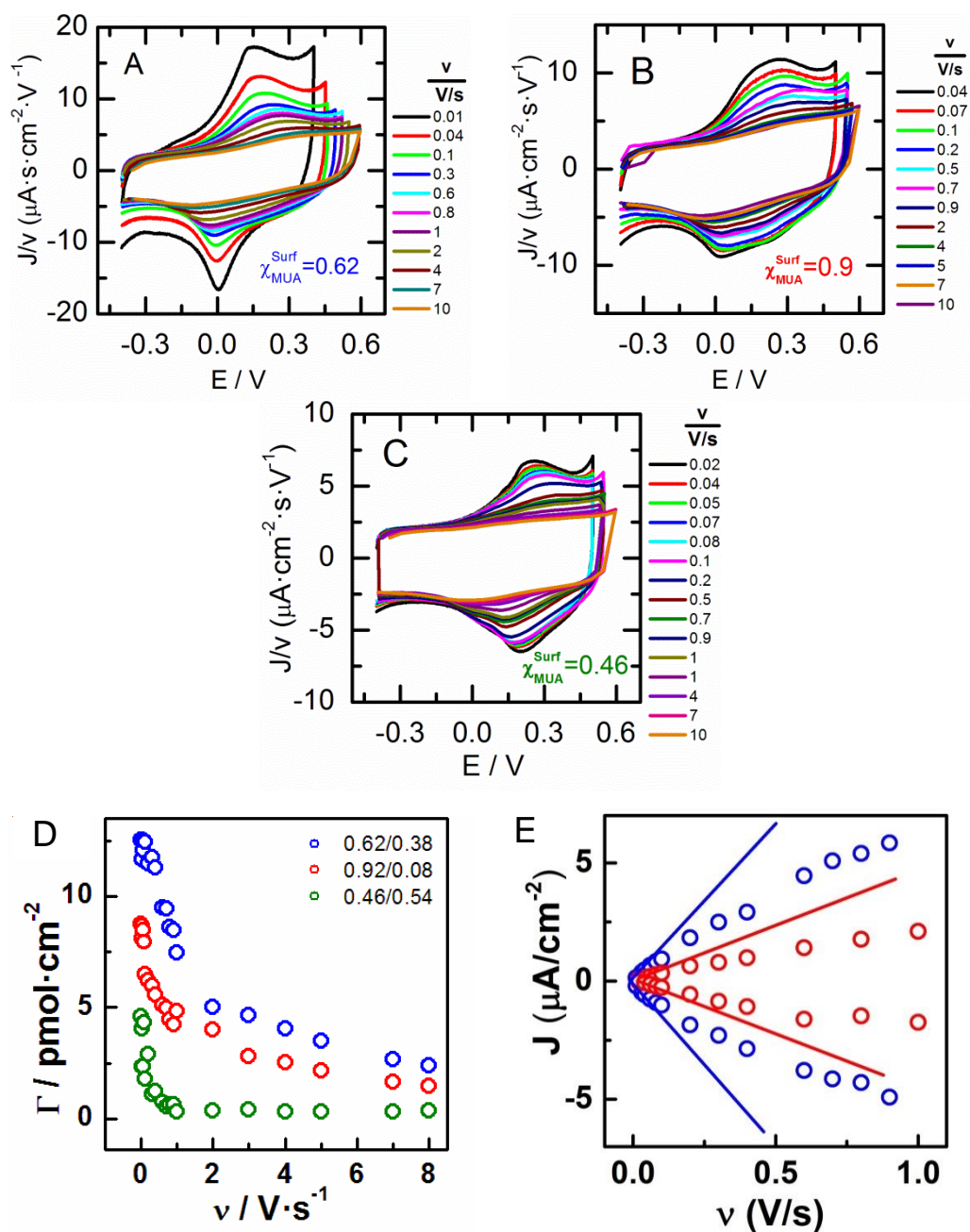
Figure 8. Normalized current density by the scan rate cyclic voltammograms of c-Mb adsorbed onto mixed MUA/DT SAMs with different surface compositions, X_{MUA}^{Surf}: (A) 0.46, (B) 0.9 and (C) 0.46. Dependence of the apparent surface coverage, Γ_{ET}, (D) and current density (E) vs the scan rate of the redox response of immobilized c-Mb.

Figure 8 shows the evolution of the anodic and cathodic peak current and the electroactive surface coverage of the surface-confined redox processes of c-Mb with the scan rate. Unusually, the peak current (i_p) evolution is not linearly dependent on scan rate and the electrochemically active surface coverage of c-Mb display is inversely-dependent on the scan rate. This behavior is qualitatively distinct from that commonly observed for redox molecules, proteins or enzymes involved in surface-confined electrochemical processes, where a linear dependence of the current peak and constant Γ_{ET} values on the scan rate are usually found.[36, 41, 42, 89] The apparent Γ_{ET} of immobilized c-Mb progressively decreases while increasing the scan rate (0.01 to 8 V/s) from a maximum value of 12, 9 and 7 pmol/cm^2 to 2, 1.5 and 0.4 pmol/cm^2 for mixed SAM surface compositions of X_{MUA}^{Surf} =0.62, 0.90 and 0.46 ,respectively (Figure 8a). For the shorter time scales (i.e. higher scan rates) the number of electrochemically active proteins diminishes exponentially upon reaching limiting values approximately of an 5-15% of the maximum electroactive coverage. Then, at the larger time scales of the CV experiments (i.e. lower scan rates) a significant fraction of the population of adsorbed c-Mb that initially appears to be latent in stable binding non-active ET configurations, becomes electrochemically active by its reorientation to more efficient ET configurations. Such behavior strongly suggests that an outstanding fraction of the ET active proteins display a dynamic nature, likely by conformational rearrangements of the c-Mb driven by electric fields at the top of the SAMs.[32, 40] Therefore, it is proposed that kinetics of the ET gating process are essentially controlled by the protein dynamics instead of the non-adiabatic ET tunneling step through the SAMs.
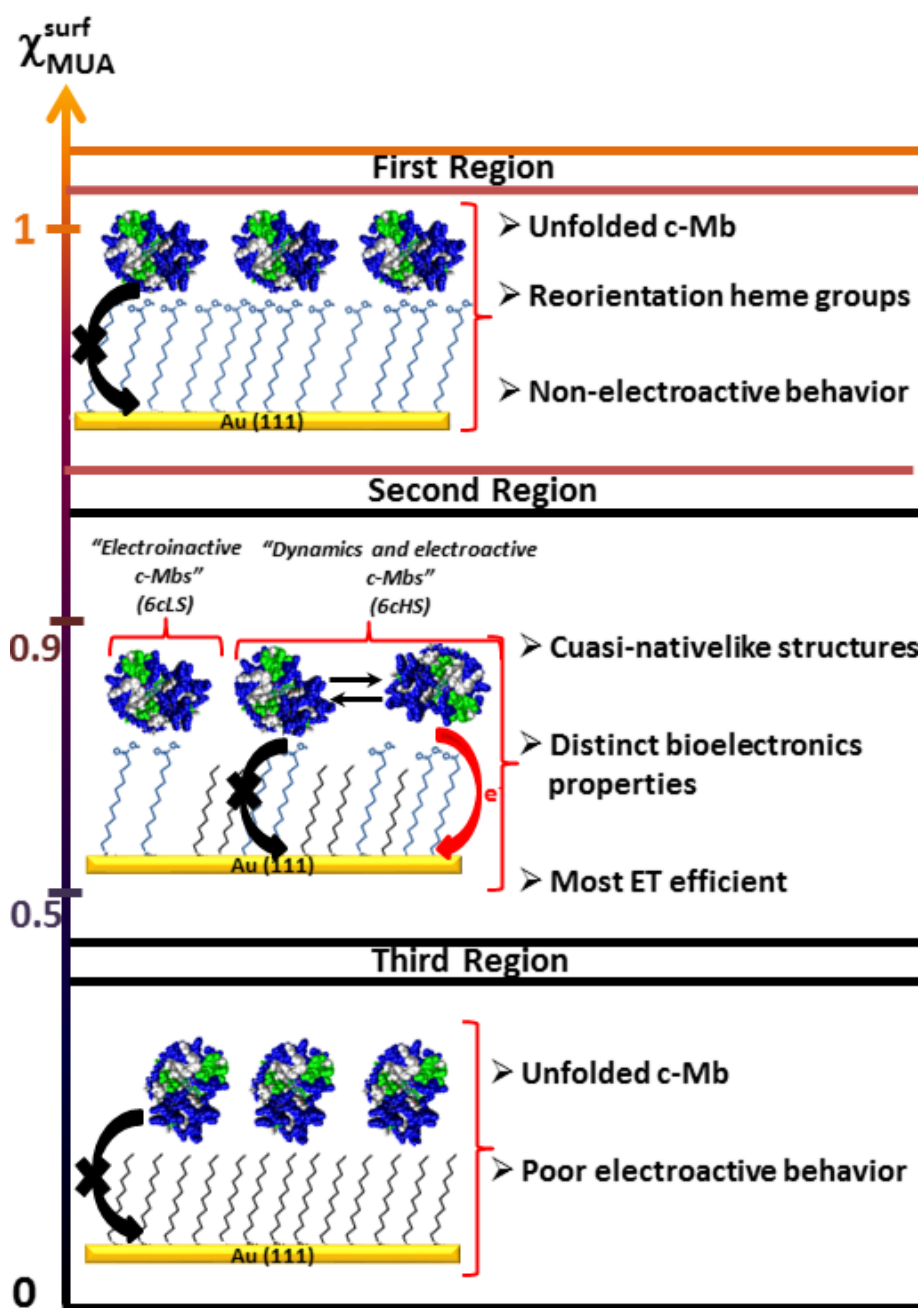
Scheme 4. Relationship between structure and electroactive function of c-Mb attached to MUA:DT mixed SAMs.

Bearing in mind all these ideas and that related with the structural analysis of the interfaces by spectroscopic techniques, the ET behavior of c-Mb on the different SAM constructs can be explained in the basis of the substantial variety of binding orientations of the immobilized proteins that are sorted in three well-defined populations and two different heme iron coordination patterns as follows (Scheme 4):

(1) Electrochemically inactive proteins with the iron center in a six-coordinated low spin state (6C-LS)

(2) Electrochemically active proteins with the iron center in a six-coordinated high spin state (6C-HS)

(3) Conformational/Configurational dynamic proteins in a six-coordinated high spin state (6C-HS) that must reorient from thermodynamically stable but redox-inactive configurations to redox-active ones allowing efficient ET.

As far as we know, there has only been reported a similar behavior to that described here in the voltammetric response of dehaloperoxidase (DHP) adsorbed on –COOH/-OH mixed alkanethiols monolayers. [90, 91] Bowden et al. have proposed a dynamic docking scheme as a model to explain the non-linearity of i_p vs scan rate, and the unusual scan rate dependence of the apparent surface coverage observed at DHP/monolayer interfaces. [90, 91] The electrochemical behavior of immobilized DHP was divided according to three different types of protein populations: a) active, b) dynamic that are able to reorient from inactive to active ET states, and c) inactive ones. The direct correlation between binding and protein function/reactivity has been usually accepted at interprotein ET studies. [92, 93]

295

However, Hoffman et al. [94] have investigated the ET reaction between the Mb and the cytochrome b5 disclosing a new paradigm in protein-protein dynamic interactions designated as Dynamic Docking (DD) landscape, in which reactivity and binding are decoupled due to a large ensemble of weakly bound protein-protein configurations where only a few are ET active. This model can be extrapolated to the scheme of redox proteins tied to biomimetic surfaces by electrostatic binding. Avila et al. [54] have proposed that the gated ET of the cytochrome C attached to ω-carboxyl alkanethiol SAMs is directly tuned by the interconversion rate of 2 configurations: a) thermodynamically stable but ET inactive and b) ET active complexes that are statistically disfavored.

Experimental data of the interfacial ET processes of redox proteins have shown that the redox reaction can be kinetically controlled by two different regimes: (i) Distance-independent gating or (ii) distance-dependent non-adiabatic electron tunneling.[33, 36, 46] In this sense, Murgida et al. [32, 95] have addressed by time-resolved SERR and SEIRA spectroscopies that the average orientation of Cytochrome C in electrostatic complexes with SAM-coated surfaces is dependent on electrode potential and the charge density of the coatings. They argue that protein reorientation is very fast for long alkyl chain carboxyl-terminated SAMs (*i.e. low interfacial electric fields*) but slows down dramatically and becomes ET rate-limiting at shorter distances in SAMs with usually less than 10 methylene units (*i.e. higher interfacial electric fields*). Thus, they ascribed that while the measured ET rates are determined by electron tunneling probabilities at longer distances, the ET reaction kinetics is gated by electric-field-controlled protein dynamics (ET gated) at shorter ones.

The picture emerging from these studies is that local electric fields determine both mean orientation and mobility of Cyt C in electrostatic complexes. Thus, the ET rates represent a convolution of dynamic sampling in search of favorable ET pathways and electron tunneling probabilities at each surface configuration.

Even though c-Mb is linked to MUA and DT SAM surfaces that are 10 methylene units long, it is proposed that the most feasible scenario for ET reaction kinetics is still gating by electric-field-controlled protein dynamics rather than electron tunneling probabilities as described in thinner carboxyl-terminated SAMs surfaces. This is based on the direct observation by CV that the redox processes are clearly controlled by protein dynamics in these assemblies. Moreover, the electrochemically active c-Mb coverage decreases on mixed SAMs while diminishing the –COOH contents, which implies that a significant reduction of the number of $–COO^-$ groups takes place concomitantly, considering that such assemblies display similar surface pK_a values. This fact in turn provokes the interfacial electric field strength to diminish at these SAM/electrolyte interfaces.

Then, the charge densities or local electrical fields should be higher than expected at the top part of the ω-carboxyl substituted C_{10} SAMs in order to explain such results based on ET gating controlled by the c-Mb dynamics. It worth to mention that the ET rate constants values and the onset of the distance-independent gating region for the transition from the "low" to the "high electric field" regime may also vary depending on the intrinsic physicochemical properties of the proteins, such as dipole moments and

distribution of charge at the protein surfaces, as well as other factors related to the coatings and the metallic support.[40, 96, 97]

Electrodes coated with specifically adsorbed sulfate ions or phosphate terminated SAMs have shown a substantial increase of the interfacial charge density and stronger electric fields.[40] In this sense, ET constant rates for Cyt C adsorbed on SO_4-Ag and PO_3-SAM are significantly lower than for COOH-C_nSAMs for comparable distances.[40] Then, an increase of the local concentration of PO_4^{3-} ions at the SAM/electrolyte interface might be driven by the uniformly distributed positive surface charges of the immobilized c-Mb molecules. As a consequence, an increase of the interfacial electric fields would be compatible with the control of conformational/configurational dynamics on ET of the adsorbed c-Mb, even at ω-carboxyl substituted C_{10} SAMs with lower $-COO^-$ surface contents.
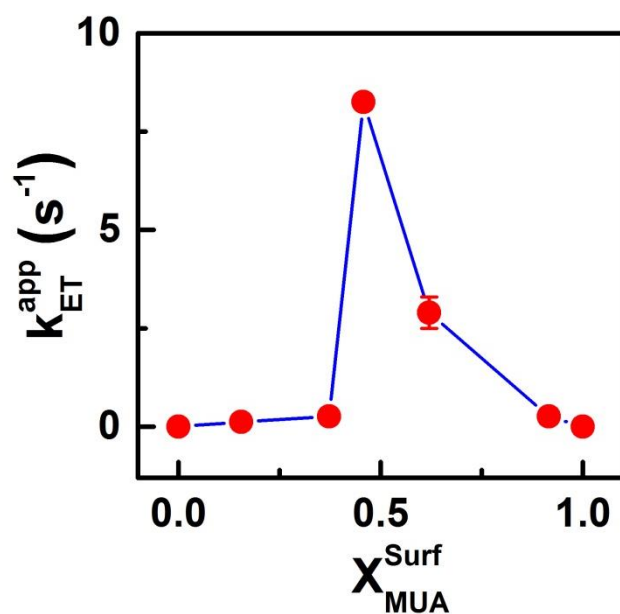
Figure 9. Variation of the apparent ET rate constant versus $X_{MUA}^{Surface}$ for cationized Myoglobin immobilized onto MUA:DT mixed SAMs/Au(111) electrodes.

Table 5. Apparent ET rate constants data for cationized Myoglobin immobilized on different mixed MUA/DT mixed monolayers.[a]

MUA/DT	X_{MUA}[b]	k_{ET}^{app} (s^{-1})
1.00/0.00	1.00	0.00±0.00
0.70/0.30	0.90	0.30±0.29
0.50/0.50	0.62	2.90±0.40
0.45/0.55	0.46	8.30±0.29
0.05/0.95	0.15	0.00±0.00
0.00/0.00	0.00	0.00±0.00

[a] The data included are the average of experimental results obtained for different repetitions. [b] The surface composition of the mixed monolayers was calculated by the potentials of the reductive desorption peaks assuming a simple weighted average from the individual components.[98]

Figure 9 displays the apparent ET rate constants, k_{ET}^{app}, calculated by using the Laviron´s model for c-Mb immobilized on MUA:DT mixed SAMs (Appendix B).[99] The lack of electrochemical response of c-Mb onto the pure MUA and DT SAMs is again justified by conformational changes involving a heme reorientation process on MUA surfaces and by the unfolding of the protein on DT monolayers or hydrophobic-enriched surfaces. The best electronic coupling of c-Mb is attained on SAMs with intermediate MUA molar fractions while ET rates are drastically lowered out this interval (Figure 9 and Table 5). An approximated monotonically increase of the k_{ET}^{app} is appreciated in the range of MUA surface compositions from 92% to 46%, where the adsorbed proteins almost preserve the conformation of its native-like species in solution. This fact would be in accordance with the idea that ET processes of the c-Mb are mainly tuned by its reorientation dynamics and influenced by surface charge density effects at the monolayer/electrolyte interface. Accordingly, within the best coupling ET region, those MUA surface compositions ($X_{MUA}^{Surf} = 0.46$) leading to the lower surfaces charge densities facilitate the mobility of the immobilized proteins and in turn faster reorientation dynamics which may contribute to attaining of the most ET efficient configurations and higher ET rates. However, the influence of redox-state rearrangements in the ET kinetics should not be discarded to occur during the electrochemical experiments. This information could be accessed by time-resolved SERR and SEIRA spectroelectrochemical measurements.

Briefly, it has been confirmed that the non-native states of the Mb and the underlying surface chemistry plays a crucial role on the ET function of the

c-Mb deposited on biomimetic surfaces. The variation in the balance of electrostatic and hydrophobic interactions at the top of the SAMs directly impinges on the control of the surface density coverage of the immobilized proteins, overall protein conformational changes and heme coordination state transitions, and in protein dynamics under interfacial electric fields, which are key factors to determine the direct ET function of the metalloproteins and enzymes in bioelectrochemistry and bioelectronics. [45, 80, 100, 101]

6.3.3 Electrocatalysis of c-Mb adsorbed on mixed SAMs/Au surfaces

The dynamic motion of enzymes during catalytic events is one of the many aspects of protein chemistry that is still in its infancy.[102-104] During the cationization process, Mb changes its global conformation due to the chemical modification of glutamic and aspartic acid chains, which play a key role on inter and intra helix electrostatic stabilization. This kind of non-native state of the Mb is provided with structural flexibility and a considerable increment of the positive charge density at the protein surface. This conformational state may enhance the protein-protein and protein-SAM electrostatic interactions and the capacity of the c-Mb to undergo structural rearrangements and to open of new access pathways/channels for catalytic processes. In fact, native Mb is electrochemically inactive onto the SAMs constructs studied in this work. By contrary, the c-Mb immobilized on the SAM coated surfaces recovers the ET function under the experimental conditions previously described.
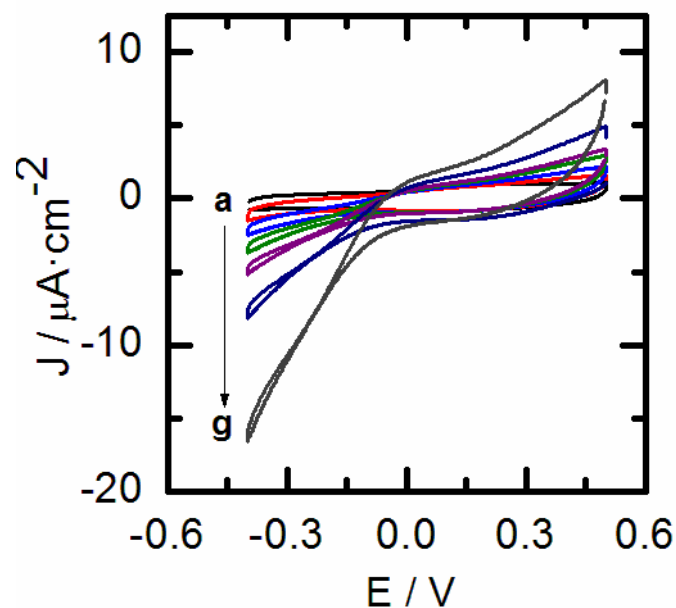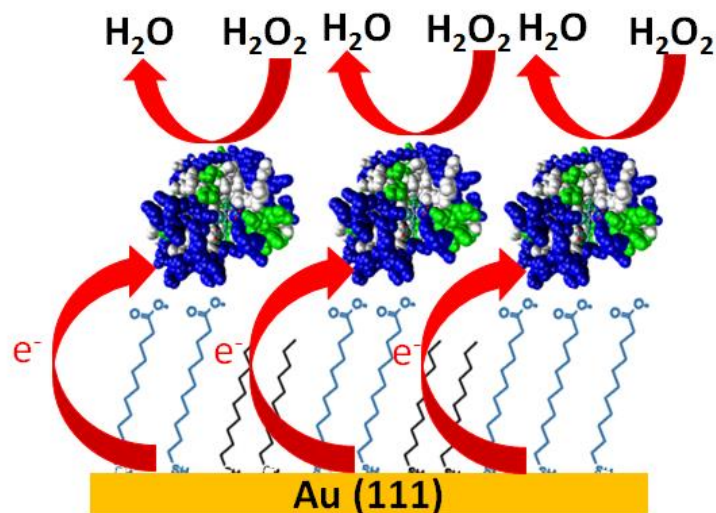
Figure 10. a) CV of c-Mb attached on a mixed monolayer with 0.62:0.38 MUA:DT surface ratio upon successive additions of 1mM of H_2O_2: b) to g). Scan rate: 0.1V/s.

To investigate how the structure and dynamics of the cationized non-native state of the Mb and the heme coordination pattern can affect the electrocatalytic activity towards the reduction of the H_2O_2, the voltammetric response of surface-confined c-Mb/SAM complexes has been investigated at surface compositions (X_{MUA}^{surf}=0.90, 0.62 and 0.46) showing the higher ET rate constants and better wiring efficiency with the electrode (Figure 10). When H_2O_2 is added to the phosphate buffer solution (pH 7.8), the cathodic current sharply increases at negative potentials in contrast to what happens to the anodic current. The c-Mb heme Fe(II)/Fe(III) couple is proposed to participate in the mechanism of catalytic reduction of H_2O_2 as follows (Scheme 5):

$$c\text{-Mb-heme Fe (III)} + H^+ + e^- \longrightarrow c\text{-Mb-heme Fe (II)} \tag{1}$$

$$H_2O_2 + 2H^+ + 2c\text{-Mb-heme Fe (II)} \longrightarrow 2c\text{-Mb-heme Fe (III)} + H_2O \tag{2}$$
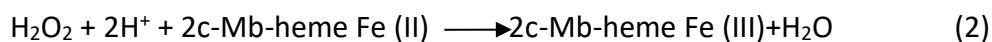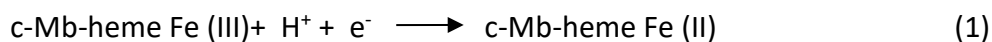
Scheme 5. Representation of the electrocatalytic mechanism of c-Mb attached to mixed monolayers towards reduction of hydrogen peroxide.

In the presence of H_2O_2, Mb–heme Fe(II) would be converted to its oxidized form, Mb–heme Fe(III). Consequently, Mb–heme Fe(III) is reduced at the electrode surface by the direct electron transfer (DET). Noteworthy, the onset of the electrocatalytic response towards hydrogen peroxide is shifted approximately by -200 mV compared to reduction peak of the ET response of the heme group of the immobilized c-Mb. This might be a consequence of the large electrostatic repulsion energy barrier created at the protein-SAM/electrolyte interface by the patches of positive charge at the c-Mb

surface which probably decreases the local concentration of H^+ hindering their accessibility and subsequent reduction of the H_2O_2 to H_2O at the heme group.

The c-Mb/mixed SAMs/Au electrodes have been employed for the chronoamperometric determination of H_2O_2 in solution. The amperometric response of the biosensors was recorded at a fixed potential of -0.35 V upon successive additions of H_2O_2 to the buffer solution at pH 7.8 under continuous stirring (Figure 11A). The fabricated biosensors with mixed SAMs of $X_{MUA}^{surf} =$ 0.90, 0.62 and 0.46 exhibit linear response in the concentration range of 5-800 µM, 5-120 µM and 5-150 µM, respectively. The sensitivity of each sensor was calculated from the slope of the steady-state current versus the H_2O_2 concentration plots (figure 11B) and the values obtained were 0.17, 0.63 and 0.37 $\mu AmM^{-1}cm^{-2}$, respectively. From these calibration curves, the detection limits values were determined to be 3.1, 1.8 and 4.9 µM , based on a signal-to-noise ratio of 3 (Table 6).

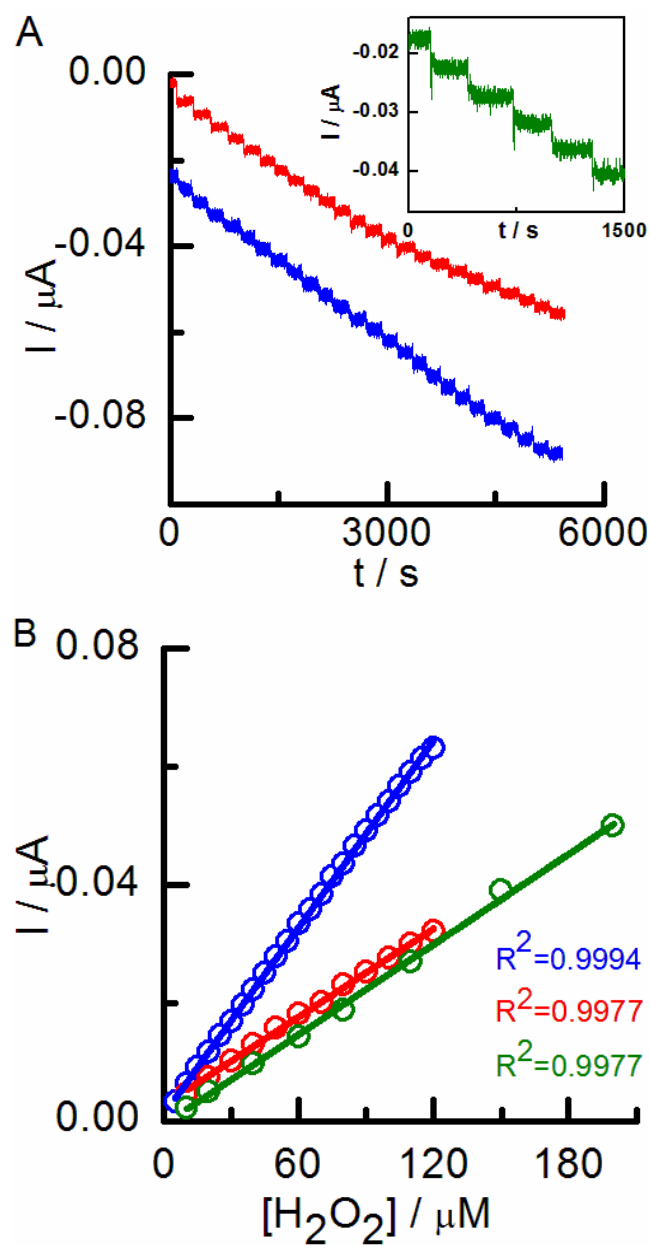**Figure 11.** (A) The amperometric response (A) and the corresponding calibration curves of steady-state currents versus [H_2O_2] (B) of the c-Mb/mixed SAMs modified electrodes: (o —) X_{MUA}^{surf} = 0.90, (o —) X_{MUA}^{surf} = 0.62 and (o —) X_{MUA}^{surf} = 0.46 upon successive additions of 25µl of 10mM of H_2O_2. Applied potential: -0.35V in phosphate buffer pH 7.8.

Table 6. Electroanalytical performance of Mb-biosensors towards the catalysis of H_2O_2

Modified material electrode	Applied Potential (V)	Lineal Range (µM)	Γ_{ET} (pmol/cm^2)	LOD (µM)	k_{ET} (s^{-1})	K_M (mM)	Ref
c-Mb/0.70:0.30	-0.35 vs EC	5-800	11	3.1	0.30	0.6	This work
c-Mb/0.50:0.50	-0.35 vs EC	5-120	16	1.8	2.90	1.4	This work
c-Mb/0.48:0.52	-0.35 vs EC	5-150	4	4.9	8.30	0.3	This work
Mb/Au-PTy-f-MWCNT/GCE	-0.3 (Ag/AgCl)	1-5000	2120	0.01	4.86	0.12	[105]
Mb/ZrO$_2$/MWCNT /GCE	-0.4 (Ag/AgCl)	1-116	136	0.53	1.52	0.085	[106]
Chitosan-MWNTs/Mb/AgNPs/GCE	-0.3 (Ag/AgCl)	25-200	4160	1.02	5.47	0.024	[107]
Mb-CeO$_2$/Indium tin oxide	-0.3 (Ag/AgCl)	200-5000	51	0.6	1.01	3.15	[108]
Nafion/Mb/AuNPs /GCE	-0.45 (SCE)	1.5-90	-	0.5	-	-	[109]
Mb- titanium carbide NPs-Chitosan/GCE	-0.3 (SCE)	0.5-50	586	0.2	3.8	0.07	[110]
Nafion/Mb/ionic liquid/GCE	-0.45 (Ag/AgCl)	1-180	58.9	0.14	-	0.022	[111]
Nafion/f-MWCNTs/MB/Carbon ionic liquid	-	8-196	4640	6	0.332	0.0001	[112]
Clay- [bmim][BF4] / Mb/GCE	-	3.9-259	$4.9 \cdot 10^{11}$	0.73	3.58	0.0176	[113]
Mb-[EMIM][BF4])/GCE	-	110-1600	95.6	0.6	4.21	0.29	[114]

The calibration curves tended to level off at higher concentrations of H_2O_2, which denotes that catalytic current and the concentration of H_2O_2 are related by the Michaelis-Menten kinetics. The apparent Michaelis-Menten constant (K_m), which gives an indication of the enzyme substrate kinetics, can be obtained from the Lineweaver-Burk equation: [115]

$$\frac{1}{I_{ss}} = \frac{1}{I_{max}} + \frac{K_m}{I_{max}C}$$

where I_{ss} is the steady-state current after addition of the substrate, I_{max} is the maximum current measured under saturated substrate conditions and C is the bulk concentration of the substrate. K_m was obtained by analysis of the slope and intercept of the plot of the reciprocals of the steady-state current versus the H_2O_2 concentration. The K_m values of the c-Mb/binary SAMs/Au (111) electrodes were evaluated to be 0.6, 1.4 and 0.3 mM for X_{MUA}^{surf} = 0.90, 0.62 and 0.46, respectively. These results are compared to those reported for other Mb modified electrodes in the table 6. These findings indicate that the c-Mb attached to binary assemblies of MUA and DT molecules retains its electrocatalytic activity and possesses a high biological affinity towards the H_2O_2 catalytic reduction process.

Very low detection limits values of H_2O_2 in biosensors formed by Mb entrapped within nanocomposites of modified multi-walled carbon nanotubes (MWCNTs) have been recently reported for loadings of Mb of 2120 pmol/cm^2. [105] It is worth noting that if the protein surface loading could be also increased up to 2120 pmol/cm^2 while keeping the electroanalytical performance of the c-Mb biosensors, the detection limits might be decreased to the level of 0.01-0.015 µM. This put forwards very efficient electrocatalytic behaviour of the

heme-cMb per unit of concentration without considering other synergistic effects arising in complex nanocomposite materials (see table 6). This efficiency may be related to the structural features of the c-Mb and supported by two main considerations: (i) non-native c-Mb architecture provides to the protein of sufficient flexibility that may allow the conformational gating processes to sample efficient pathways and (ii) the interactions at SAM/protein interfaces for certain MUA:DT compositions may facilitate the dynamic motion of the protein during the catalytic event and the opening of new gates/channels. Both considerations would be compatible with the enhancement of the affinity of the heme group for substrate molecules and the improvement of the "wiring" with the electrode. The ability of ligands to pass through these pathways can be controlled by size discrimination at the molecular scale, geometrical constraints like the curvature of the pathway, and specific molecular interactions such as hydrogen bonds, electrostatic interactions, and hydrophobic interactions with the residues comprising the access pathway.[116]

The stability of the c-Mb biosensors response were also analysed. The operational stabilities of the biosensors were examined with intermittent measuring of the current response to 1mM H_2O_2 additions every 5 days in the period of 1 month. Figure 12 illustrates the remaining activity of c-Mb/film electrodes related to the initial enzyme activity. The results show that the biosensor maintains practically constant activities during a long period of time.
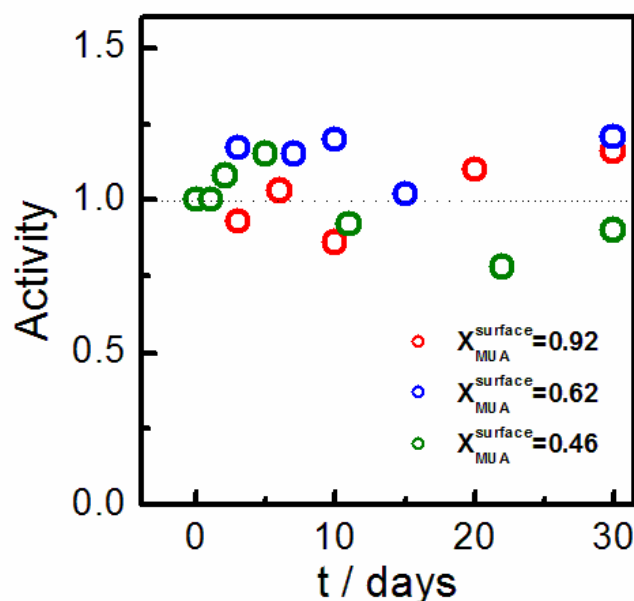
Figure 12. Dependence of the remaining activity to 1mM H_2O_2 in c-Mb biosensors on operational time.

The relative long response times ($\approx$50s) may be ascribed to the large amplitude of the conformational rearrangements of the c-Mb adsorbed onto binary films to achieve optimal catalysis. Finally, the repeatability of the biosensors were also investigated and the relative standard deviation to successive additions of H_2O_2 10 mM were found to be 4.2% (n = 5), 6.6% (n=10) and 3.8% (n=10) for the c-Mb immobilized on monolayers containing X_{MUA}^{surf} =0.90, 0.62 and 0.46, respectively. In general, the biosensors constructed have demonstrated to have good repeatability and stability for electrochemical detection.

6.4.   Conclusions

- The cationization of Mb brings about a non-native Mb state where the content of α-helical secondary structure is drastically reduced to a 39 % and the β-sheet, β-turn and unordered domains increased when compared to native Mb. These results are in excellent agreement with those reported for Mb cationized by similar methodologies.

- The significant changes in the secondary structure of the non-native Mb state in solution has a strong effect on the heme environment which is manifested by the transition from a high (6C-HS) to low spin (6C-LS) state of the iron moiety upon cationization.

- Upon adsorption of c-Mb on SAM coated gold surfaces, proteins are partially denatured on highly hydrophobic and hydrophilic interfaces. Effective protein-surface interactions rather than hydration contributions are proposed to drive such structural rearrangement.

- Less-evident conformational changes are present for c-Mb deposited on mixed SAMs with intermediate surface compositions of –COOH and –CH$_3$ terminal groups, which is likely due to the balance between hydrophobic and hydrophilic short-range interactions at the protein/SAMs interface.

- A significant overall change in the protein orientation is produced from –COOH/-COO- enriched-surfaces ($1 \geq X_{MUA}^{Surf} \geq 0.62$) to –CH$_3$ enriched ones ($0.46 \geq X_{MUA}^{Surf} \geq 0$).

- Independently of the degree of the structural/conformational changes observed for the immobilized c-Mb, a total conversion from 6C-LS to 6C-HS state is shown by RR spectroscopy. Then, direct protein-surface interactions provoke structural changes on the His/His ligated heme environment based on the swapping of the axial His64 ligand with H_2O.

- The contact of the c-Mb surface assemblies with phosphate buffered-solutions causes an additional structural rearrangement to a partial population of confined proteins that swap back again to a 6C-LS heme configuration by strengthening of the Fe-His64 interaction.

- Electrostatically-driven interactions of PO_4^{2-} ions with the positive charge patches in close proximity to the prosthetic group of the protein provoke a heme cavity rearrangement that is likely facilitated when the proteins are oriented in an upside down configuration. Both 6C-HS and 6C-LS heme states coexist probably in differently oriented protein populations, by facing the heme crevice mainly towards either the surface or the electrolyte solution interface, respectively.

- Native Mb deposited on pure and mixed MUA/DT SAMs becomes electrochemically inactive and ET coupling inefficient. Similarly, the redox activity of c-Mb is totally hindered at pure MUA and highly DT-enriched surfaces due to strong protein-surface interactions that induce notable conformational and orientational changes. However, at intermediate –COOH/-CH_3 surface ratios, where the c-Mb native

311

conformation is almost preserved, ET wiring is efficiently promoted between hemeproteins in the 6C-HS state and the electrode.

- A ET gating mechanism driven by conformational dynamics of the c-Mb at the surfaces is directly observed from the CV experiments.

- The analysis in detail of the evolution of different parameters determined from voltammetric features (e.g. E°', Γ_{ET} and k_{ET}) help to draw two main additional conclusions:

  - Three main populations are present at the surfaces:
  - (i) always ET-active proteins 6C-HS coordinated to H_2O
  - (ii) Conformational dynamic proteins 6C-HS that must reorient from thermodynamically stable but redox-inactive configurations to redox-active ones allowing efficient ET
  - (iii) ET non-active proteins 6C-LS coordinated to His64.

  - The influence of interfacial electric fields is compatible with the control of conformational/configurational dynamics on ET of the adsorbed c-Mb depending on the underlying surface chemistry.

- c-Mb shows high efficiency and affinity towards the catalysis of H_2O_2. Again, this fact is directly linked to the c-Mb structure and the dynamic conformational/configurational properties of the protein and the heme group tuned by surface chemistry, which allows promoting efficient pathways contributing to the enhancement of the protein-substrate affinity and the ET rate processes.

312

6.5. Appendix

A. Second derivative/Deconvolution of IRRAS spectra for c-Mb/SAMs
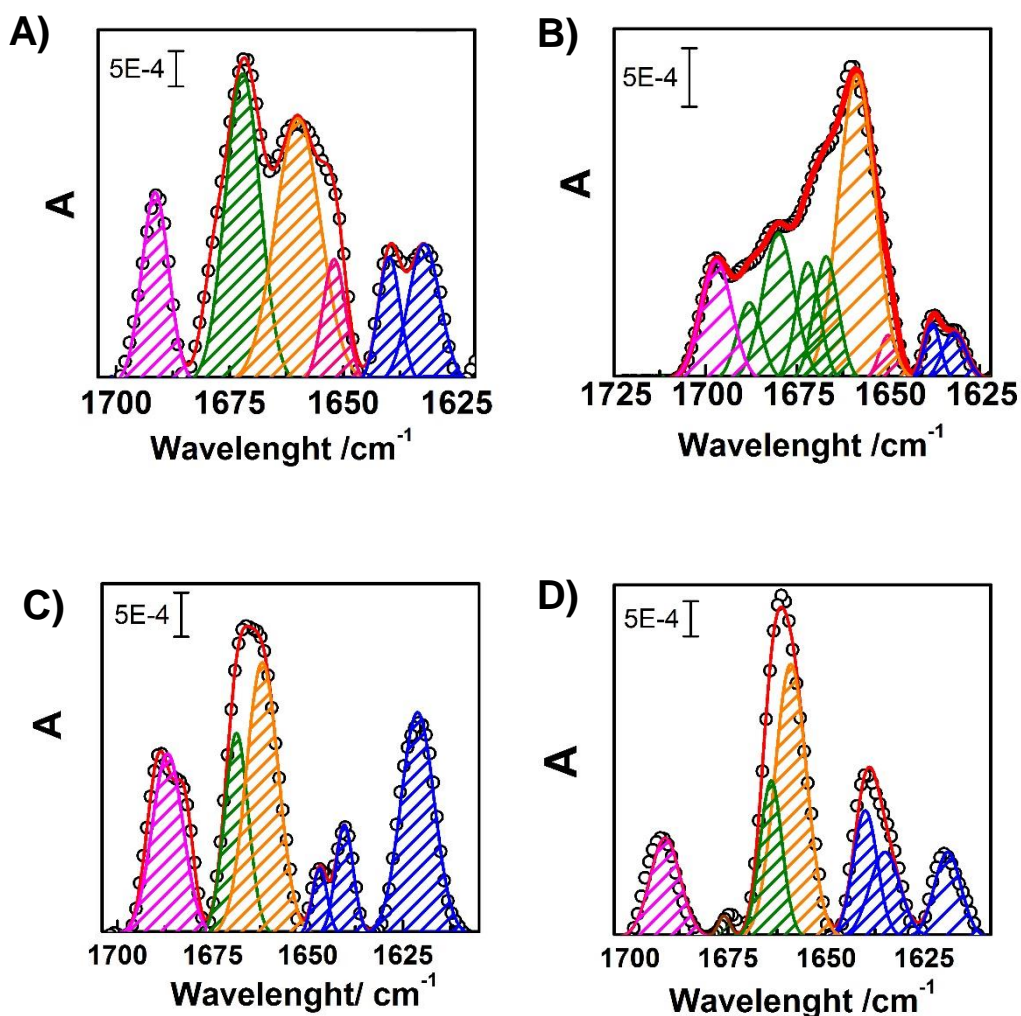
Figure A1. Representative second derivative analysis for the amide I bands of the cationized Myoglobin anchored to MUA:DT mixed monolayers at $X_{MUA/DT}$:A) 1:0, B) 0.90:0.10 and 0.62:0.38, C) 0.46:0.54, and D) 0.16:0.84 and 0:1. Fitting component domains: β-sheet parallel (—), unordered (—), α-helix (—),β-turn bands (—) and β-sheet antiparallel (—). Second-derivative signal values are divided by a factor of 250 for comparison with the absorbance values of the experimental spectra.

Table A1. Full width at half maximum (FWHM) for the fitting Gaussian functions of the individual components used in the second derivative and deconvolution analysis

Secondary structure:	FWHM Amide I [a] Second derivative	FWHM amide I [b] Deconvoluted	Amide I [a] / amide I [b]
α-helix	9	22	2.44
β-sheet	6	15	2.50
β-turn	6	15	2.50
unordered	5.5	15	2.73

The contents of the different protein secondary structures of c-Mb were obtained by following the protocols described in literature. [117,118] Firstly, a linear baseline correction was performed at the amide I band region between 1600-1710 cm^{-1}. Derivative analysis was carried out to separate overlapping bands without arbitrarily choosing deconvolutional parameters. For protein secondary structure determination, the second-derivative spectra were obtained by using a baseline-corrected seven-point Savitsky-Golay derivative function which covers a spectral window region with less than the half-bandwidth at half-height (FWHM) and minor distortion of the amide I components. The data obtained were used to determine the number of bands and their positions in order to resolve the spectra into its components. In a second-derivative spectrum, the peak wavenumber of the components is identical with the original peak frequency while the FWHM is reduced by a factor of 2.7.[117,118] Then, the curve fitting process is mainly determined by the characteristics of the individual components that were fitted with Gaussian/Lorentzian functions and their positions were determined to be in good agreement with those reported in literature. Once the position and FWHM of the bands for each component were set by the best second-

derivative iterative fitting using non-linear least squares, the experimental data were fitted with Gaussian/Lorentzian functions usually with half-bandwidths varying in the range of 15-25 cm^{-1} for each secondary structure element (Table A1). [118] The best fits for the second-derivative analysis of the amide I region are presented at Figure A1 and for the experimental data at the Figure 2 of this chapter. Finally, the band area for each component peak is used to calculate its relative contribution to a particular protein secondary structure.

B. Determination of k$_{ET}$ by Laviron analysis

The Laviron method is widely used for determining the electron transfer rate constant, k$_{ET}$, of species adsorbed to an electrode in many electrochemical systems. [99] This method relies on α, the transfer coefficient, which is a measure of the symmetry of the energy barrier of the redox reaction. Ideally, $\alpha = 0.5$ for all overpotentials, however in many cases deviates from 0.5. Therefore, determination of α is crucial to determine k$_{ET}$. To obtain α, the peak potential E$_p$ is plotted vs. ln v where E$_{pa}$ and E$_{pc}$ are plotted separately to give two branches (figure 10). In our particular case, the values of E$^{\circ\prime}$ were subtracted at each scan rate due to its apparent dependence with this parameter. At higher scan rates where η > 100 mV, the data follow an almost linear dependence where α can be obtained from the slope of cathodic branch by using the Equation B1:

$$\text{slope} = -\frac{2.3RT}{\alpha nF} \tag{B1}$$

Similarly, α can be also determined from the slope of the anodic branch. The values obtained from the experimental results were similar and consistently close to 0.5.

Then, the k_{ET} is determined by the y axis-intercepts of the lines for the anodic and the cathodic branches through the equation B2:

$$E_p = E° - \frac{RT}{\alpha nF} \ln \left(\frac{\alpha nF}{RTk_{ET}} \right) - \frac{RT}{\alpha nF} \ln \upsilon \tag{B2}$$
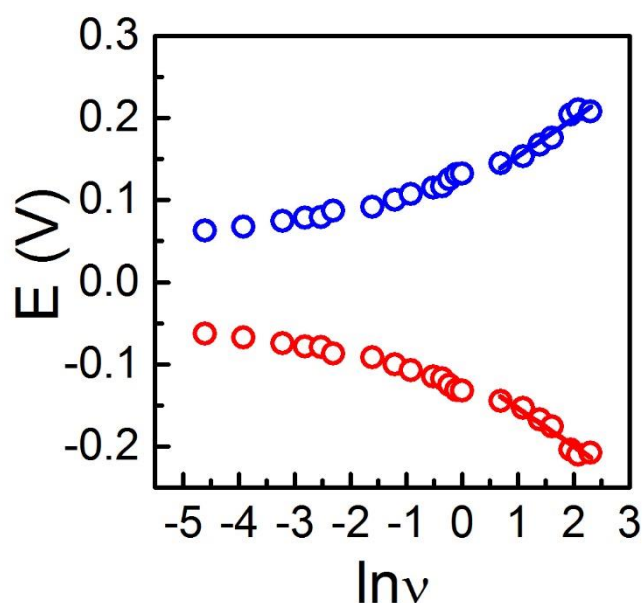

Figure 10. Typical trumpet curve for the variation of the cathodic and anodic peak potentials ($\eta = E_p - E°'$)   vs the logarithm of the scan rate. The data represented corresponds to the case of a c-Mb/mixed SAMs with $X_{MUA}^{Surf} = 0.62$.

The average values obtained by this treatment are included in Table 5 of this chapter.

316

6.6. **References**

1.   Harel, A.; Bromberg, Y.; Falkowski, P. G.; Bhattacharya, D., Evolutionary History of Redox Metal-Binding Domains across the Tree of Life. *Proc. Natl. Acad. Sci. U. S. A.* **2014,** *111* (19), 7042-7047.

2.   Rutherford, A. W.; Osyczka, A.; Rappaport, F., Back-Reactions, Short-Circuits, Leaks and other Energy Wasteful Reactions in Biological Electron Transfer: Redox Tuning to Survive Life in O2. *FEBS Letters* **2012,** *586* (5), 603-616.

3.   Lill, R., Function and Biogenesis of Iron-Sulfur Proteins. *Nature (London, U. K.)* **2009,** *460* (7257), 831-838.

4.   Burmester, T.; Hankeln, T., Function and Evolution of Vertebrate Globins. *Acta Physiol.* **2014,** *211* (3), 501-514.

5.   Williams, R. J. P.; Begley, T. P., Metallo-Enzymes and Metallo-Proteins, Chemistry of. In *Wiley Encyclopedia of Chemical Biology*, John Wiley & Sons, Inc.: **2007**.

6.   Ortiz de Montellano, P. R., Control of the Catalytic Activity of Prosthetic Heme by the Structure of Hemoproteins. *Acc. Chem. Res.* **1987,** *20* (8), 289-94.

7.   Senge, M. O.; MacGowan, S. A.; O'Brien, J. M., Conformational Control of Cofactors in Nature - The Influence of Protein-Induced Macrocycle Distortion on the Biological Function of Tetrapyrroles. *Chem. Commun. (Cambridge, U. K.)* **2015,** *51* (96), 17031-17063.

8.   Lin, Y.-W.; Wang, J., Structure and Function of Heme Proteins iIn Non-Native States: A Mini-Review. *J. Inorg. Biochem.* **2013,** *129*, 162-171.

9.   Akram, M. S.; Rehman, J. U.; Hall, E. A. H., Engineered Proteins for Bioelectrochemistry. *Annu. Rev. Anal. Chem.* **2014,** *7*, 257-274.

10.   Hayashi, T.; Hisaeda, Y., New Functionalization of Myoglobin by chemical Modification of Heme-Propionates. *Acc. Chem. Res.* **2002,** *35* (1), 35-43.

11.   Tokuriki, N.; Tawfik, D. S., Protein Dynamism and Evolvability. *Science* **2009,** *324* (5924), 203.

12.   Henzler-Wildman, K.; Kern, D., Dynamic Personalities of Proteins. *Nature* **2007,** *450* (7172), 964-972.

13.   Lu, Y.; Yeung, N.; Sieracki, N.; Marshall, N. M., Design of Functional Metalloproteins. *Nature* **2009,** *460* (7257), 855-862.

14.   Lu, Y.; Berry, S. M.; Pfister, T. D., Engineering Novel Metalloproteins: Design of Metal-Binding Sites into Native Protein Scaffolds. *Chemical Reviews* **2001,** *101* (10), 3047-3080.

15.   Lin, Y.-W., Structural Insights into a Low-Spin Myoglobin Variant with Bis-Histidine Coordination from Molecular Modeling. *Proteins: Structure, Function, and Bioinformatics* **2011,** *79* (3), 679-684.

16.   Presley, A. D.; Chang, J. J.; Xu, T., Directed Co-Assembly of Heme Proteins with Amphiphilic Block Copolymers toward Functional Biomolecular Materials. *Soft Matter* **2011,** *7* (1), 172-179.

17.   Perriman, A. W.; Coelfen, H.; Hughes, R. W.; Barrie, C. L.; Mann, S., Solvent-Free Protein Liquids and Liquid Crystals. *Angew. Chem., Int. Ed.* **2009,** *48* (34), 6242-6246, S6242/1-S6242/14.

18.   Brogan, A. P. S.; Siligardi, G.; Hussain, R.; Perriman, A. W.; Mann, S., Hyper-thermal Stability and Unprecedented Re-Folding of Solvent-Free Liquid Myoglobin. *Chemical Science* **2012,** *3* (6), 1839-1846.

19.   Perriman, A. W.; Brogan, A. P. S.; Coelfen, H.; Tsoureas, N.; Owen, G. R.; Mann, S., Reversible Dioxygen Binding in Solvent-Free Liquid Myoglobin. *Nature Chemistry* **2010,** *2* (8), 622-626.

20.   Prime, K. L.; Whitesides, G. M., Self-Assembled Organic Monolayers: Model Systems for Studying Adsorption of Proteins at Surfaces. *Science* **1991,** *252* (5009), 1164.

21.   Mrksich, M.; Whitesides, G. M., Using Self-Assembled Monolayers to Understand the Interactions of Man-Made Surfaces with Proteins and Cells. *Annu. Rev. Biophys. Biomol. Struct.* **1996,** *25*, 55-78.

22.   Skourtis, S. S., Review Probing Protein Electron Transfer Mechanisms From the Molecular to the Cellular Length Scales. *Biopolymers* **2013,** *100* (1), 82-92.

23.   Edwards, P. P.; Gray, H. B.; Lodge, M. T. J.; Williams, R. J. P., Electron Transfer and Electronic Conduction Through an Intervening Medium. *Angew. Chem., Int. Ed.* **2008,** *47* (36), 6758-6765.

24.   Cowan, J. A.; Upmacis, R. K.; Beratan, D. N.; Onuchic, J. N.; Gray, H. B., Long-Range Electron Transfer in Myoglobin. *Ann N Y Acad Sci* **1988,** *550*, 68-84.

25.   Winkler, J. R.; Gray, H. B., Electron Flow through Metalloproteins. *Chem. Rev. (Washington, DC, U. S.)* **2014,** *114* (7), 3369-3380.

26.   Davidson, V. L., What Controls the Rates of Interprotein Electron-Transfer Reactions. *Acc. Chem. Res.* **2000,** *33* (2), 87-93.

27.   Jonkheijm, P.; Weinrich, D.; Schroeder, H.; Niemeyer, C. M.; Waldmann, H., Chemical Strategies for Generating Protein Biochips. *Angew. Chem., Int. Ed.* **2008,** *47* (50), 9618-9647.

28.   Arya, S. K.; Solanki, P. R.; Datta, M.; Malhotra, B. D., Recent Advances in Self-Assembled Monolayers Based Biomolecular Electronic Devices. *Biosens. Bioelectron.* **2009,** *24* (9), 2810-2817.

29.   Frasconi, M.; Mazzei, F.; Ferri, T., Protein Immobilization at Gold-Thiol Surfaces and Potential for Biosensing. *Anal. Bioanal. Chem.* **2010,** *398* (4), 1545-1564.

30.   Samanta, D.; Sarkar, A., Immobilization of Bio-Macromolecules on Self-Assembled Monolayers: Methods and Sensor Applications. *Chem Soc Rev* **2011,** *40* (5), 2567-92.

31.   Wei, J.; Liu, H.; Khoshtariya, D. E.; Yamamoto, H.; Dick, A.; Waldeck, D. H., Electron-Transfer Dynamics of Cytochrome C: A Change in the Reaction Mechanism with Distance. *Angew. Chem., Int. Ed.* **2002,** *41* (24), 4700-4703.

32.   Kranich, A.; Ly, H. K.; Hildebrandt, P.; Murgida, D. H., Direct Observation of the Gating Step in Protein Electron Transfer: Electric-Field-Controlled Protein Dynamics. *Journal of the American Chemical Society* **2008,** *130* (30), 9844-9848.

33.   Jeuken, L. J. C., Conformational Reorganisation in Interfacial Protein Electron Transfer. *Biochimica Et Biophysica Acta-Bioenergetics* **2003,** *1604* (2), 67-76.

34.   Khoshtariya, D. E.; Wei, J. J.; Liu, H. Y.; Yue, H. J.; Waldeck, D. H., Charge-Transfer Mechanism for Cytochrome C Adsorbed on Nanometer Thick Films.

Distinguishing Frictional Control from Conformational Gating. *Journal of the American Chemical Society* **2003,** *125* (25), 7704-7714.

35.   Skourtis, S. S.; Waldeck, D. H.; Beratan, D. N., Fluctuations in Biological and Bioinspired Electron-Transfer Reactions. *Annu. Rev. Phys. Chem.* **2010,** *61*, 461-485.

36.   Waldeck, D. H.; Khoshtariya, D. E., Fundamental Studies of Long- and Short-Range Electron Exchange Mechanisms between Electrodes and Proteins. *Mod. Aspects Electrochem.* **2011,** *52* (Applications of Electrochemistry and Nanotechnology in Biology and Medicine I), 105-238.

37.   Armstrong, F. A. In *Voltammetry of Proteins*, Wiley-VCH Verlag GmbH & Co. KGaA: 2002; pp 11, 13-29.

38.   Fedurco, M., Redox Reactions of Heme-Containing Metalloproteins: Dynamic Effects of Self-Assembled Monolayers on Thermodynamics and Kinetics of Cytochrome C Electron-Transfer Reactions. *Coordination Chemistry Reviews* **2000,** *209*, 263-331.

39.   Yue, H.; Waldeck, D. H., Understanding Interfacial Electron Transfer to Monolayer Protein Assemblies. *Curr. Opin. Solid State Mater. Sci.* **2006,** *9* (1-2), 28-36.

40.   Murgida, D. H.; Hildebrandt, P., Redox and Redox-Coupled Processes of Heme Proteins and Enzymes at Electrochemical Interfaces. *Physical Chemistry Chemical Physics* **2005,** *7* (22), 3773-3784.

41.   Leger, C.; Bertrand, P., Direct Electrochemistry of Redox Enzymes as a Tool for Mechanistic Studies. *Chem. Rev. (Washington, DC, U. S.)* **2008,** *108* (7), 2379-2438.

42.   Eckermann, A. L.; Feld, D. J.; Shaw, J. A.; Meade, T. J., Electrochemistry of redox-Active Self-Assembled Monolayers. *Coordination Chemistry Reviews* **2010,** *254* (15-16), 1769-1802.

43.   Gulaboski, R.; Mirceski, V.; Bogeski, I.; Hoth, M., Protein film Voltammetry: Electrochemical Enzymatic Spectroscopy. A Review on Recent Progress. *Journal of Solid State Electrochemistry* **2012,** *16* (7), 2315-2328.

44.   Marcus, R. A., The theory of Oxidation-Reduction Reactions Involving Electron Transfer. I. *J. Chem. Phys.* **1956,** *24*, 966-78.

45.   Murgida, D. H.; Hildebrandt, P.; Todorovic, S. In *Immobilized Redox Proteins: Mimicking Basic Features of Physiological Membranes and Interfaces*, InTech: **2010**; pp 21-47.

46.   Murgida, D. H.; Hildebrandt, P., Disentangling Interfacial Redox Processes of Proteins by SERR Spectroscopy. *Chem. Soc. Rev.* **2008,** *37* (5), 937-945.

47.   Mayo, S. L.; Ellis, W. R., Jr.; Crutchley, R. J.; Gray, H. B., Long-Range Electron Transfer in Heme Proteins. *Science (Washington, D. C., 1883-)* **1986,** *233* (4767), 948-52.

48.   Wang, G.-X.; Bao, W.-J.; Wang, M.; Xia, X.-H., Heme Plane Orientation Dependent Direct Electron Transfer of Cytochrome C at SAMs/Au Electrodes with Different Wettability. *Chem. Commun. (Cambridge, U. K.)* **2012,** *48* (88), 10859-10861.

49.   Fujita, K.; Nakamura, N.; Ohno, H.; Leigh, B. S.; Niki, K.; Gray, H. B.; Richards, J. H., Mimicking Protein-Protein Electron Transfer: Voltammetry of Pseudomonas aeruginosa Azurin and the Thermus thermophilus CuA Domain at ω-Derivatized Self-Assembled-Monolayer Gold Electrodes. *J. Am. Chem. Soc.* **2004,** *126* (43), 13954-13961.

50.   Qian, Y.; Xu, X.; Wang, Q.; Wu, P.; Zhang, H.; Cai, C., Electrochemical Probing of the Solution pH-Induced Structural Alterations around the Heme Group in Myoglobin. *Physical Chemistry Chemical Physics* **2013,** *15* (39), 16941-16948.

51.   Feng, M. L.; Tachikawa, H., Raman Spectroscopic and Electrochemical Characterization of Myoglobin Thin Film: Implication of the Role of Histidine 64 for Fast Heterogeneous Electron Transfer. *Journal of the American Chemical Society* **2001,** *123* (13), 3013-3020.

52.   King, B. C.; Hawkridge, F. M.; Hoffman, B. M., Electrochemical Studies of Cyanometmyoglobin and Metmyoglobin: Implications For Long-Range Electron Transfer in Proteins. *J. Am. Chem. Soc.* **1992,** *114* (26), 10603-8.

53.   Yue, H.; Waldeck, D. H.; Petrovic, J.; Clark, R. A., The Effect of Ionic Strength on the Electron-Transfer Rate of Surface Immobilized Cytochrome c. *J. Phys. Chem. B* **2006,** *110* (10), 5062-5072.

54.   Avila, A.; Gregory, B. W.; Niki, K.; Cotton, T. M., An Electrochemical Approach to Investigate Gated Electron Transfer Using a Physiological Model System:

Cytochrome c Immobilized on Carboxylic Acid-Terminated Alkanethiol Self-Assembled Monolayers on Gold Electrodes. *J. Phys. Chem. B* **2000,** *104* (12), 2759-2766.

55.   Grove, T. Z.; Kostic, N. M., Metalloprotein Association, Self-Association, and Dynamics Governed by Hydrophobic Interactions: Simultaneous Occurrence of Gated and True Electron-Transfer Reactions between Cytochrome f and Cytochrome c6 from Chlamydomonas reinhardtii. *J. Am. Chem. Soc.* **2003,** *125* (35), 10598-10607.

56.   Rivas, L.; Murgida, D. H.; Hildebrandt, P., Conformational and Redox Equilibria and Dynamics of Cytochrome c Immobilized on Electrodes via Hydrophobic Interactions. *J. Phys. Chem. B* **2002,** *106* (18), 4823-4830.

57.   Roach, P.; Farrar, D.; Perry, C. C., Interpretation of Protein Adsorption: Surface-Induced Conformational Changes. *J. Am. Chem. Soc.* **2005,** *127* (22), 8168-8173.

58.   Zerze, G. H.; Mullen, R. G.; Levine, Z. A.; Shea, J. E.; Mittal, J., To What Extent Does Surface Hydrophobicity Dictate Peptide Folding and Stability near Surfaces? *Langmuir* **2015,** *31* (44), 12223-12230.

59.   Peng, C.; Liu, J.; Zhao, D.; Zhou, J., Adsorption of Hydrophobin on Different Self-Assembled Monolayers: The Role of the Hydrophobic Dipole and the Electric Dipole. *Langmuir* **2014,** *30* (38), 11401-11411.

60.   Wang, G.-X.; Wang, M.; Wu, Z.-Q.; Bao, W.-J.; Zhou, Y.; Xia, X.-H., Dependence of the Direct Electron Transfer Activity and Adsorption Kinetics of Cytochrome C on Interfacial Charge Properties. *Analyst (Cambridge, U. K.)* **2013,** *138* (19), 5777-5782.

61.   Di Rocco, G.; Ranieri, A.; Bortolotti, C. A.; Battistuzzi, G.; Bonifacio, A.; Sergo, V.; Borsari, M.; Sola, M., Axial Iron Coordination and Spin State Change in a Heme C upon Electrostatic Protein-SAM Interaction. *Phys. Chem. Chem. Phys.* **2013,** *15* (32), 13499-13505.

62.   Pelton, J. T.; McLean, L. R., Spectroscopic Methods for Analysis of Protein Secondary Structure. *Anal. Biochem.* **2000,** *277* (2), 167-176.

63.   Kakiuchi, T.; Iida, M.; Gon, N.; Hobara, D.; Imabayashi, S.; Niki, K., Miscibility of Adsorbed 1-Undecanethiol and 11-Mercaptoundecanoic Acid Species in Binary Self-Assembled Monolayers on Au(111). *Langmuir* **2001,** *17* (5), 1599-1603.

64.   Goormaghtigh, E.; Cabiaux, V.; Ruysschaert, J.-M., Secondary Structure and Dosage of Soluble and Membrane Proteins by Attenuated Total Reflection Fourier-Transform Infrared Spectroscopy on Hydrated Films. *European Journal of Biochemistry* **1990,** *193* (2), 409-420.

65.   Walker, K. D.; Causgrove, T. P., Contribution of Arginine-Glutamate Salt Bridges to Helix Stability. *J. Mol. Model.* **2009,** *15* (10), 1213-1219.

66.   Ramos, C. H. I.; Kay, M. S.; Baldwin, R. L., Putative Interhelix Ion Pairs Involved in the Stability of Myoglobin. *Biochemistry* **1999,** *38* (30), 9783-9790.

67.   Risbridger, T. A. G.; Watkins, D. W.; Armstrong, J. P. K.; Perriman, A. W.; Anderson, J. L. R.; Fermin, D. J., Effect of Bioconjugation on the Reduction Potential of Heme Proteins. *Biomacromolecules* **2016,** *17* (11), 3485-3492.

68.   Lenk, T. J.; Horbett, T. A.; Ratner, B. D.; Chittur, K. K., Infrared Spectroscopic Studies of Time-Dependent Changes in Fibrinogen Adsorbed to Polyurethanes. *Langmuir* **1991,** *7* (8), 1755-64.

69.   Kim, H. S.; Hartgerink, J. D.; Ghadiri, M. R., Oriented Self-Assembly of Cyclic Peptide Nanotubes in Lipid Membranes. *J. Am. Chem. Soc.* **1998,** *120* (18), 4417-4424.

70.   Spiro, T. G.; Strekas, T. C., Resonance Raman Spectra of Heme Proteins. Effects of Oxidation and Spin State. *Journal of the American Chemical Society* **1974,** *96* (2), 338-345.

71.   Kitagawa, T.; Kyogoku, Y.; Iizuka, T.; Saito, M. I., Nature of the Iron-Ligand Bond in Ferrous Low Spin Hemoproteins Studied by Resonance Raman Scattering. *J. Am. Chem. Soc.* **1976,** *98* (17), 5169-73.

72.   Kitahama, Y.; Egashira, M.; Suzuki, T.; Tanabe, I.; Ozaki, Y., Sensitive Marker Bands for the Detection of Spin States of Heme in Surface-Enhanced Resonance Raman Scattering Spectra of Metmyoglobin. *Analyst* **2014,** *139* (24), 6421-6425.

73.   Rygula, A.; Majzner, K.; Marzec, K. M.; Kaczor, A.; Pilarczyk, M.; Baranska, M., Raman Spectroscopy of Proteins: A Review. *J. Raman Spectrosc.* **2013,** *44* (8), 1061-1076.

74.   Kitahama, Y.; Ozaki, Y., Surface-Enhanced Resonance Raman Scattering of Hemoproteins and Those in Complicated Biological Systems. *Analyst (Cambridge, U. K.)* **2016,** *141* (17), 5020-5036.

75.   Hu, S.; Smith, K. M.; Spiro, T. G., Assignment of Protoheme Resonance Raman Spectrum by Heme Labeling in Myoglobin. *J. Am. Chem. Soc.* **1996,** *118* (50), 12638-12646.

76.   Spiro, T. G.; Stong, J. D.; Stein, P., Porphyrin Core Expansion and Doming in Heme Proteins. New Evidence from Resonance Raman Spectra of Six-Coordinate High-Spin Iron(III) Hemes. *J. Am. Chem. Soc.* **1979,** *101* (10), 2648-55.

77.   Abe, M.; Kitagawa, T.; Kyogoku, Y., Resonance Raman Spectra of Octaethylporphyrinatonickel(II) and Meso-Deuterated and Nitrogen-15 Substituted Derivatives. II. A Normal Coordinate Analysis. *J. Chem. Phys.* **1978,** *69* (10), 4526-34.

78.   Murgida, D. H.; Hildebrandt, P., Heterogeneous Electron Transfer of Cytochrome c on Coated Silver Electrodes. Electric Field Effects on Structure and Redox Potential. *J. Phys. Chem. B* **2001,** *105* (8), 1578-1586.

79.   Shah, R.; Schweitzer-Stenner, R., Structural Changes of Horse Heart Ferricytochrome c Induced by Changes of Ionic Strength and Anion Binding. *Biochemistry* **2008,** *47* (18), 5250-5257.

80.   Ciaccafava, A.; Infossi, P.; Ilbert, M.; Guiral, M.; Lecomte, S.; Giudici-Orticoni, M. T.; Lojou, E., Electrochemistry, AFM, and PM-IRRA Spectroscopy of Immobilized Hydrogenase: Role of a Hydrophobic Helix in Enzyme Orientation for Efficient H2 Oxidation. *Angew. Chem., Int. Ed.* **2012,** *51* (4), 953-956, S953/1-S953/3.

81.   Risbridger, T. A. G.; Watkins, D. W.; Armstrong, J. P. K.; Perriman, A. W.; Anderson, J. L. R.; Fermin, D. J., Effect of Bioconjugation on the Reduction Potential of Heme Proteins. *Biomacromolecules* **2016**, Ahead of Print.

82.   Xue, L.-L.; Wang, Y.-H.; Xie, Y.; Yao, P.; Wang, W.-H.; Qian, W.; Huang, Z.-X.; Wu, J.; Xia, Z.-X., Effect of Mutation at Valine 61 on the Three-Dimensional Structure, Stability, and Redox Potential of Cytochrome b5. *Biochemistry* **1999,** *38* (37), 11961-11972.

83.   Zhou, J.; Zheng, J.; Jiang, S., Molecular Simulation Studies of the Orientation and Conformation of Cytochrome c Adsorbed on Self-Assembled Monolayers. *J. Phys. Chem. B* **2004,** *108* (45), 17418-17424.

84.   Taniguchi, I.; Watanabe, K.; Tominaga, M.; Hawkridge, F. M., Direct Electron Transfer of Horse Heart Myoglobin at an Indium Oxide Electrode. *J. Electroanal. Chem.* **1992,** *333* (1-2), 331-8.

85.   Bortolotti, C. A.; Amadei, A.; Aschi, M.; Borsari, M.; Corni, S.; Sola, M.; Daidone, I., The Reversible Opening of Water Channels in Cytochrome c Modulates the Heme Iron Reduction Potential. *J. Am. Chem. Soc.* **2012,** *134* (33), 13670-13678.

86.   Rohlfs, R. J.; Mathews, A. J.; Carver, T. E.; Olson, J. S.; Springer, B. A.; Egeberg, K. D.; Sligar, S. G., The Effects of Amino Acid Substitution at Position E7 (Residue 64) on the Kinetics of Ligand Binding to Sperm Whale Myoglobin. *J. Biol. Chem.* **1990,** *265* (6), 3168-76.

87.   Van Dyke, B. R.; Saltman, P.; Armstrong, F. A., Control of Myoglobin Electron-Transfer Rates by the Distal (Nonbound) Histidine Residue. *J. Am. Chem. Soc.* **1996,** *118* (14), 3490-2.

88.   Kendrew, J. C.; Bodo, G.; Dintzis, H. M.; Parrish, R. G.; Wyckoff, H.; Phillips, D. C., A Three-Dimensional Model of the Myoglobin Molecule Obtained by X-Ray Analysis. *Nature (London, U. K.)* **1958,** *181*, 662-6.

89.   Paulo, T. d. F.; Diogenes, I. C. N.; Abruna, H. D., Direct Electrochemistry and Electrocatalysis of Myoglobin Immobilized on L-Cysteine Self-Assembled Gold Electrode. *Langmuir* **2011,** *27* (5), 2052-2057.

90.   D'Antonio, E. L.; Chen, T. K.; Turner, A. H.; Santiago-Capeles, L.; Bowden, E. F., Voltammetry of Dehaloperoxidase on Self-Assembled Monolayers: Reversible Adsorptive Immobilization of a Globin. *Electrochemistry Communications* **2013,** *26*, 67-70.

91.   Chen, T. K.; Bowden, E. F., Electrochemical Characterization of Dehaloperoxidase Adsorbates on COOH/OH Mixed Self-Assembled Monolayers. *J. Electroanal. Chem.* **2013,** *703*, 23-28.

92.   Nocek, J. M.; Sishta, B. P.; Cameron, J. C.; Mauk, A. G.; Hoffmann, B. M., Cyclic Electron Transfer within the Zn-Myoglobin, Cytochrome b(5) Complex. *Journal of the American Chemical Society* **1997,** *119* (9), 2146-2155.

93.   Northrup, S. H.; Thomasson, K. A.; Miller, C. M.; Barker, P. D.; Eltis, L. D.; Guillemette, J. G.; Inglis, S. C.; Mauk, A. G., Effects of Charged Amino-Acid Mutations on the Bimolecular Kinetics of Reduction of Yeast Iso-1-Ferricytochrome-C by Bovine Ferrocytochrome-b(5). *Biochemistry* **1993,** *32* (26), 6613-6623.

94.   Liang, Z. X.; Kurnikov, I. V.; Nocek, J. M.; Mauk, A. G.; Beratan, D. N.; Hoffman, B. M., Dynamic Docking and Electron-Transfer between Cytochrome b(5) and a Suite of Myoglobin Surface-Charge Mutants. Introduction of a Functional-Docking Algorithm for Protein-Protein Complexes. *Journal of the American Chemical Society* **2004,** *126* (9), 2785-2798.

95.   Wisitruangsakul, N.; Zebger, I.; Ly, K. H.; Murgida, D. H.; Ekgasit, S.; Hildebrandt, P., Redox-Linked Protein Dynamics of Cytochrome C Probed by Time-Resolved Surface Enhanced Infrared Absorption Spectroscopy. *Phys. Chem. Chem. Phys.* **2008,** *10* (34), 5276-5286.

96.   Yue, H.; Khoshtariya, D.; Waldeck, D. H.; Grochol, J.; Hildebrandt, P.; Murgida, D. H., On the Electron Transfer Mechanism between Cytochrome C and Metal Electrodes. Evidence for Dynamic Control at Short Distances. *J. Phys. Chem. B* **2006,** *110* (40), 19906-19913.

97.   Feng, J.-J.; Murgida, D. H.; Kuhlmann, U.; Utesch, T.; Mroginski, M. A.; Hildebrandt, P.; Weidinger, I. M., Gated Electron Transfer of Yeast Iso-1 Cytochrome c on Self-Assembled Monolayer-Coated Electrodes. *J. Phys. Chem. B* **2008,** *112* (47), 15202-15211.

98.   Gonzalez-Granados, Z.; Sanchez-Obrero, G.; Madueno, R.; Sevilla, J. M.; Blazquez, M.; Pineda, T., Formation of Mixed Mono layers from 11-Mercaptoundecanoic Acid and Octanethiol on Au(111) Single Crystal Electrode under Electrochemical Control. *Journal of Physical Chemistry C* **2013,** *117* (46), 24307-24316.

99.   Laviron, E., General Expression of the Linear Potential Sweep Voltammogram in the Case of Diffusionless Electrochemical Systems. *Journal of Electroanalytical Chemistry* **1979,** *101* (1), 19-28.

100.   Song, Y.-Y.; Jia, W.-Z.; Yang, C.; Xia, X.-H., Template-Synthesized Protein Macroporous Biofilms: Conformational Related Direct Electron Transfer. *Adv. Funct. Mater.* **2007,** *17* (14), 2377-2384.

101.   Chen, D.; Wang, G.; Li, J., Interfacial Bioelectrochemistry: Fabrication, Properties and Applications of Functional Nanostructured Biointerfaces. *Journal of Physical Chemistry C* **2007,** *111* (6), 2351-2367.

102.   Kamerlin, S. C. L.; Warshel, A., At the Dawn of the 21st Century: Is Dynamics the Missing link for Understanding Enzyme Catalysis? *Proteins: Struct., Funct., Bioinf.* **2010,** *78* (6), 1339-1375.

103.   Schwartz, S. D.; Schramm, V. L., Enzymatic Transition States and Dynamic Motion in Barrier Crossing. *Nature Chemical Biology* **2009,** *5* (8), 552-559.

104.   Henzler-Wildman, K. A.; Lei, M.; Thai, V.; Kerns, S. J.; Karplus, M.; Kern, D., A Hierarchy of Timescales in Protein Dynamics Is Linked to Enzyme Catalysis. *Nature (London, U. K.)* **2007,** *450* (7171), 913-916.

105.   Vilian, A. T. E.; Veeramani, V.; Chen, S.-M.; Madhu, R.; Kwak, C. H.; Huh, Y. S.; Han, Y.-K., Immobilization of Myoglobin on Au Nanoparticle-Decorated Carbon Nanotube/Polytyramine Composite as a Mediator-Free H_2O_2 and Nitrite Biosensor. *Scientific Reports* **2015,** *5*.

106.   Liang, R.; Deng, M.; Cui, S.; Chen, H.; Qiu, J., Direct Electrochemistry and Electrocatalysis of Myoglobin Immobilized on Zirconia/Multi-Walled Carbon Nanotube Nanocomposite. *Mater. Res. Bull.* **2010,** *45* (12), 1855-1860.

107.   Li, Y.; Li, Y.; Yang, Y., Direct Electrochemistry and Electrocatalysis of Myoglobin-Based Nanocomposite Membrane Electrode. *Bioelectrochemistry* **2011,** *82* (2), 112-116.

108.   Yagati, A. K.; Lee, T.; Min, J.; Choi, J.-W., An Enzymatic Biosensor for Hydrogen Peroxide Based on CeO_2 Nanostructure Electrodeposited on ITO Surface. *Biosens. Bioelectron.* **2013,** *47*, 385-390.

109.   Yang, W.; Li, Y.; Bai, Y.; Sun, C., Hydrogen Peroxide Biosensor Based on Myoglobin/Colloidal Gold Nanoparticles Immobilized on Glassy Carbon Electrode by a Nafion Film. *Sens. Actuators, B* **2006,** *115* (1), 42-48.

110.   Zhang, H.; Lu, H.; Hu, N., Fabrication of Electroactive Layer-by-Layer Films of Myoglobin with Gold Nanoparticles of Different Sizes. *J. Phys. Chem. B* **2006,** *110* (5), 2171-2179.

111.   Safavi, A.; Farjami, F., Hydrogen Peroxide Biosensor Based on a Myoglobin/Hydrophilic Room Temperature Ionic Liquid Film. *Analytical Biochemistry* **2010,** *402* (1), 20-25.

112.   Sun, W.; Li, X.; Jiao, K., Direct Electrochemistry of Myoglobin in a Nafion-Ionic Liquid Composite Film Modified Carbon Ionic Liquid Electrode. *Electroanalysis* **2009,** *21* (8), 959-964.

113.   Dai, Z.; Xiao, Y.; Yu, X.; Mai, Z.; Zhao, X.; Zou, X., Direct Electrochemistry of Myoglobin Based on Ionic Liquid-Clay Composite Films. *Biosens. Bioelectron.* **2009,** *24* (6), 1629-1634.

114.   Zhang, Y.; Zheng, J., Direct Electrochemistry and Electrocatalysis of Myoglobin Immobilized in Hyaluronic Acid and Room Temperature Ionic Liquids Composite Film. *Electrochem. Commun.* **2008,** *10* (9), 1400-1403.

115.   Kamin, R. A.; Wilson, G. S., Rotating-Ring-Disk Enzyme Electrode for Biocatalysis Kinetic-Studies and Characterization of the Immobilized Enzyme Layer. *Analytical Chemistry* **1980,** *52* (8), 1198-1205.

116.   Gora, A.; Brezovsky, J.; Damborsky, J., Gates of Enzymes. *Chem. Rev. (Washington, DC, U. S.)* **2013,** *113* (8), 5871-5923.

117.   Dong, A.; Huang, P.; Caughey, W. S., Protein Secondary Structures in Water from Second-Derivative Amide I Infrared Spectra. *Biochemistry* **1990,** *29* (13), 3303-8.

118.   Yang, H.; Yang, S.; Kong, J.; Dong, A.; Yu, S., Obtaining Information about Protein Secondary Structures in Aqueous Solution Using Fourier Transform IR Spectroscopy. *Nat. Protoc.* **2015,** *10* (3), 382-396.

CHAPTER 7

Conclusions

Conclusiones

7. Conclusions

Capítulo 3:

1. Se ha llevado a cabo la formación y la caracterización de monocapas autoensambladas de ácido 11-mercaptoundecanoico (MUA-SAMs) sobre superficies de Au(111) mediante tres métodos diferentes de deposición.

2. La organización estructural de dichas SAMs se basa en una disposición vertical de las moléculas formando una superestructura del tipo ($\sqrt{3}$x$\sqrt{3}$) R30º conmensurada con la superficie atómica del oro.

3. La caracterización mediante FT-IRRAS revela que tanto las monocapas formadas a partir de un medio micelar como aplicando un potencial electroquímico presentan un ordenamiento cristalino, mientras que aquellas formadas desde etanol poseen un menor grado de organización molecular.

4. Los cambios en las propiedades ácido-base de la interfase MUA-SAM/electrolito se deben principalmente a las diferencias en la organización estructural de las cadenas alquílicas y de interacción de los grupos carboxilato con iones de carga opuesta. En el caso particular de las monocapas formadas desde etanol, no se puede descartar la posibilidad de que las propiedades ácido/base de la SAM se vean afectadas por la formación de grupos terminales acetilo.

Capítulo 4:

5. Se ha llevado a cabo la caracterización estructural de monocapas mixtas de MUA y decanotiol (DT) sobre Au(111) formadas desde un medio liotrópico a diferentes tiempos de modificación mediante CV, EIS y FT-IRRAS.

6. Dichas monocapas mixtas exhiben un elevado grado de ordenamiento, donde las moléculas se encuentran en una disposición vertical y la adsorción del componente con el grupo terminal más polar (-COOH) desde el medio micelar esta favorecida sobre el sustrato de Au(111).

7. La desorción reductiva de las SAMs mixtas muestran un único pico en los voltamogramas, lo cual es típico de películas cuyas moléculas están distribuidas en la superficie de forma homogénea desde un punto de vista macroscópico.

8. Las técnicas de CV, EIS e IRRAS han puesto de manifiesto un aumento de la homogeneidad en la distribución a nivel molecular de las moléculas de MUA y DT en dichas capas para tiempos de modificación mayores, lo cual se puede atribuir a que en condiciones cercanas a alcanzar el equilibrio termodinámico predominan las interacciones intermoleculares entre componentes distintos (MUA/DT).

9. El grado de miscibilidad, y por tanto la distribución espacial de las moléculas de MUA y DT en la superficie, puede controlarse variando el tiempo de modificación lo que da lugar a dos tipos de patrones:
    a) El primero consiste en pequeños dominios de moléculas del mismo tipo (MUA-MUA o DT-DT) de tamaño nanométrico que se forman probablemente por estados donde ambos componentes quedan atrapados en configuraciones metaestables desde un punto de vista cinético.
    b) El segundo patrón consiste en una distribución homogénea a escala molecular de ambos componentes que está favorecida por la interacción entre moléculas de diferente tipo (MUA-DT).

10. En función del tipo de aplicación que se desee ambos patrones resultan de gran interés, bien sea en el diseño de interfases de contacto a escala nanométrica para su utilización en el estudio del transporte electrónico y de carga moleculares (Ejemplo: Electrónica molecular) o en el diseño de plataformas que mimetizan interfases biológicas mediante la inmovilización de biomoléculas de forma específica en superficies (Ejemplo: Diseño de biosensores, biomateriales y nanomateriales biocompatibles).

Capítulo 5:

11. Los experimentos realizados mediante EIS indican que los grupos –COOH ionizables de la interfase SAM/disolución no contribuyen significativamente a que la capacidad, C, varíe con el pH. Se ha determinado la composición superficial de ambos componentes (MUA y DT) en las SAM mixtas a partir de los valores promedio de C obtenidos, estando dichos resultados en concordancia con los obtenidos por el método de desorción reductiva (Capítulo 4).

12. Los cambios en los valores de resistencia de transferencia de carga, R_{CT}, y las curvas de valoración de las bandas de IR en función del pH reflejan claramente la ionización y el cambio en el grado de disociación de los grupos –COOH terminales, lo cual permite la determinación de los valores de $pK_{1/2}$ superficial aparentes tanto en SAMs puras de MUA como mixtas de MUA/DT.

13. El valor de $pK_{1/2}$ determinado para las monocapas de MUA con ordenamiento cristalino es mayor que el predicho por el modelo teórico basado exclusivamente en el campo electrostático. Por lo tanto, es necesario asumir que existe una influencia adicional en el proceso de ionización debida a efectos asociados con la formación de enlaces por puente de hidrógeno, solvatación de iones e hidrofobicidad en la vecindad de los grupos carboxy-terminales.

14. El comportamiento ácido-base de las interfases de MUA/DT-SAMs se corresponde con el típico de mezclas homogéneas de dos componentes. No obstante, dicho comportamiento depende del grado de homogeneidad en la distribución espacial de las moléculas de MUA y DT según su organización en distintos patrones superficiales.

15. Para las monocapas mixtas con composiciones superficiales de MUA $\chi_{MUA}^{surf} > 0.3$ (t=15 min) y $\chi_{MUA}^{surf} > 0.60$ (t=18 h) se produce una disminución progresiva de los valores de $pK_{1/2}$, pK_a, y el parámetro de interacción, $\beta\bar{E}$ (para un valor de pK_a fijado), los cuales son obtenidos a partir de los mejores ajustes del modelo 1-pK a los resultados experimentales, a medida que se diluye la cantidad de MUA en la superficie con DT. Esto es consistente con el efecto predominante de la disminución de las interacciones repulsivas que se establecen entre los grupos –COO⁻ terminales. En ambos casos, las curvas de valoración se caracterizan por la presencia de un único $pK_{1/2}$, lo que se relaciona con la presencia de grandes dominios de grupos -COOH que experimentan similares microambientes al de un capa de MUA pura.

16. Por el contrario, para composiciones de $\chi_{MUA}^{surf} < 0.3$ (t=15 min) y $\chi_{MUA}^{surf} < 0.60$ (t=18 h), los valores de $pK_{1/2}$ aumentan varias unidades de pH cuando la cantidad de MUA en la superficie de estas capas se diluye aún más. En este caso, predomina el efecto local de la disminución de la constante dieléctrica en la ionización de grupos –COOH vecinos.

17. En el caso de las SAMs formadas a bajos tiempos de modificación, la heterogeneidad en la distribución de tamaños de los dominios de MUA determina la aparición de dos valores de $pK_{1/2}$ superficiales aparentes. Así pues, los grupos –COOH coexisten en distintos microambientes en función de su ubicación en nanodominios de diferente tamaño. Los nanodominios de MUA de menor tamaño y aquellas moléculas de MUA situadas en los límites de dominios en contacto con DT se desprotonan a valores de pK_a más elevados debido a la disminución

significativa que experimenta la constante dieléctrica en la vecindad de los grupos -COOH. Por el contrario, aquellos grupos –COOH que se encuentran en el interior de dominios de MUA lo suficientemente grandes como para no experimentar localmente el ambiente hidrofóbico de los grupos –CH$_3$ son los responsables de la aparición de un pK$_a$ a valores más bajos dentro de la misma curva de valoración.

18. En las SAMs formadas a altos tiempos de inmersión, los grupos -COOH parecen distribuirse homogéneamente prácticamente a nivel molecular. En este caso, solamente aparece un único pK$_{1/2}$ a valores altos. Eso puede explicarse por el microentorno hidrofóbico similar que experimentan los grupos –COOH una vez alcanzada una relación de composición crítica de MUA/DT en la superficie, a partir de la cual se puede asumir que las moléculas de MUA se asocian en dominios muy pequeños, dímeros o que incluso están aisladas individualmente.

19. La formación de interacciones por puente de hidrógeno entre moléculas de MUA se observa tras la reorganización estructural de las SAMs. Se sugiere que la asociación más probable entre moléculas vecinas de MUA es mediante la formación de especies diméricas (-COOH···HCOO-), tanto dentro de nanodominios de mayor extensión (SAMs formadas a bajos tiempos) como para mezclas homogéneas de dímeros ya preexistentes (SAMs formadas a altos tiempos).

20. Las monocapas mixtas formadas a 15 minutos son las más adecuadas para el estudio de su interacción con biomoléculas a pH fisiológico ~7, ya que permiten disponer de un intervalo más amplio de proporciones de grupos -COO$^-$ y –COOH en la superficie (8-45%) para evaluar el efecto de las interacciones electrostáticas (*influencia de los campos electrostáticos interfaciales*) y por puentes de hidrógeno, así como del efecto de las interacciones hidrofóbicas al poder controlar la inserción de grupos –CH$_3$ ajustando su porcentaje entre un 10-85%.

Capítulo 6:

21. Al cationizar la Mb se forma un estado no nativo donde el contenido de estructura secundaria α-hélice se reduce significativamente hasta un 39 % junto con el aumento del de láminas β, giros β y dominios desordenados. Estos resultados concuerdan perfectamente con los publicados para metodologías similares de cationización de la Mb.

22. Los cambios estructurales que se producen en la Mb cationizada (c-Mb) en relación con la Mb nativa son tan importantes que provocan un efecto en el ambiente y la coordinación del grupo hemo, lo cual se refleja en la transición desde el estado de alto spin (6C-HS) presente en la Mb nativa al de bajo spin (6C-LS) para la c-Mb en disolución.

23. La inmovilización de c-Mb en superficies de oro modificadas con SAMs exclusivamente con grupos hidrofílicos (MUA) o hidrofóbicos (DT) provoca su desnaturalización parcial. Este cambio estructural se achaca al efecto predominante que ejercen las interacciones efectivas proteína/superficie en lugar de la solvatación o hidratación de la proteína en la interfase.

24. Aunque también se producen cambios conformacionales en la c-Mb depositada en SAM mixtas con composiciones superficiales intermedias de grupos –COOH y –CH$_3$ son de menor extensión. Esto se debe probablemente al balance adecuado entre las interacciones hidrofóbicas e hidrofílicas de corto alcance presentes en la interfase proteína/SAM.

25. Se produce un cambio significativo global en la orientación de la proteína desde las superficies enriquecidas con COOH/-COO$^-$ ($1 \geq$ X$_{MUA}^{Surf} \geq 0.62$) hasta las enriquecidas con –CH$_3$ ($0.46 \geq$ X$_{MUA}^{Surf} \geq 0$).

26. Independientemente del grado del cambio estructural/conformacional observado para la c-Mb inmovilizada, ésta sufre una conversión total en la coordinación del grupo prostético desde un estado 6C-LS en disolución a 6C-HS en superficie, según se demuestra mediante

espectroscopia Raman (RR). Este resultado se explica considerando que las interacciones proteína-superficie provocan un cambio estructural de forma que una de las histidinas ligadas al grupo hemo (His64) se intercambia por una molécula de H_2O.

27. Cuando los ensamblajes de proteínas ya inmovilizadas se ponen en contacto con disoluciones de tampón fosfato se producen alteraciones estructurales adicionales que permiten que una parte de la población de proteínas adsorbidas cambie de nuevo a una configuración del grupo hemo 6C-LS, como consecuencia de un fortalecimiento de las interacciones Fe-His64.

28. Las interacciones impulsadas electrostáticamente entre los iones PO_4^{2-} y las regiones cargadas positivamente de la proteína colocadas en las proximidades del grupo protésico inducen un reordenamiento de la cavidad del grupo hemo, lo cual es probable que se facilite cuando las proteínas se orienten con la hendidura del grupo redox hacia la disolución. Ambos estados de spin, 6C-HS y 6C-LS, coexisten probablemente en poblaciones de la proteína orientadas de manera diferente, bien con la cavidad del grupo hemo orientada hacia la superficie de las SAMs o hacia la disolución, respectivamente.

29. Las proteínas de Mb nativa depositadas sobre SAMs puras o mixtas no dan en ningún caso una respuesta electroquímica. De la misma forma, la actividad redox de la c-Mb inmovilizada se suprime completamente en SAMs de MUA puras o enriquecidas con DT, lo que se achaca a los cambios notables observados en su conformación y orientación. Sin embargo, en superficies con composiciones intermedias de –COOH/-CH_3, donde la que la c-Mb conservaría prácticamente su conformación nativa, la transferencia electrónica se promueve de forma eficiente entre las hemoproteínas en el estado 6C-HS y el electrodo.

30. Mediante medidas electroquímicas es posible observar directamente la presencia de un mecanismo de transferencia electrónica (TE) interrumpida ("gated"), el cual está regulado por la dinámica conformacional de la c-Mb.

31. A partir del análisis de la evolución de diferentes parámetros con la velocidad de barrido obtenidos a partir de los perfiles voltamétricos ($E°'$, Γ_{ET} y k_{ET}) es posible concluir lo siguiente:

- Hay tres tipos de poblaciones en la superficie:

(iv) Proteínas que son siempre electroactivas con una configuración del grupo hemo 6C-HS.
(v) Proteínas dinámicas desde un punto de vista conformacional en un estado 6C-HS, las cuales debe reorientarse desde configuraciones termodinámicamente estables pero inactivas electroquímicamente hasta configuraciones activas electroquímicamente que favorecen la TE de forma efectiva.
(vi) Proteínas no electroactivas con una configuración 6C-LS.

- El control de la dinámica conformacional sobre la transferencia electrónica de la c-Mb es compatible con la influencia ejercida por el campo eléctrico interfacial en función de la química superficial subyacente.

32. La c-Mb presenta una alta eficiencia hacia la catálisis de H_2O_2. Este hecho está directamente relacionado con las propiedades de la dinámica conformacional de la proteína y del grupo hemo que son controlados a su vez por la química superficial de las SAMs, y que promueve caminos más eficientes que contribuyen a favorecer la afinidad proteína/sustrato y los procesos de transferencia electrónica.
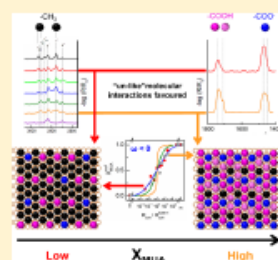
ANEXO

Publicaciones y Comunicaciones Científicas

Formation of 2-D Crystalline Intermixed Domains at the Molecular Level in Binary Self-Assembled Monolayers from a Lyotropic Mixture

Alain R. Puente Santiago, Teresa Pineda, Manuel Blázquez, and Rafael Madueño*

Institute of Fine Chemistry and Nanochemistry. Department of Physical Chemistry and Applied Thermodynamics, University of Cordoba, Campus Rabanales, Ed. Marie Curie 2a Planta, E-14014 Córdoba, Spain

ABSTRACT: The organization and intermolecular interactions of mixed self-assembled monolayers (SAMs) of 1-decanethiol (DT) and 11-mercaptoundecanoic acid (MUA) formed on Au(111) from a lyotropic medium have been studied by cyclic voltammetry (CV), electrochemical impedance spectroscopy (EIS), and infrared reflection–absorption spectroscopy (IRRAS) as a function of their surface composition. The presence of a single reductive desorption peak in the voltammograms and thiol surface coverages close to 7.6×10^{-10} mol/cm^2 reveal the formation of homogeneous mixtures of both molecules in an upright configuration in the mixed SAMs. Despite this fact, two different distributions of the individual components have been found in these MUA-enriched SAMs according to their different electron transfer blocking behavior and conformational order shown by EIS and IRRAS results. At short modification times, MUA–MUA and DT–DT homomolecular interactions prevail during the assembly process, and nanodomains of like molecules are probably formed by kinetically trapped metastable states. On the other hand, MUA–DT heteromolecular interactions are predominant in the layers formed at the higher immersion time, leading to a crystalline-like conformational order of molecularly intermixed domains. A discussion based on the Bragg–Williams thermodynamic approach and on the role of the spatial distribution and charge state of the carboxyl terminal groups in the SAMs' organization is performed.

■ INTRODUCTION

The control of the spatial confinement of individual functional molecules and nano-objects on surfaces is a highlight topic in studying single-molecule properties, such as reactivity and kinetics, and provides new insights into the design of molecular switches and motors, opening new applications in the field of biochemical sensors, molecular electronics, catalysis, and surface material chemistry.[1−7]

Of particular importance is the building up of multifunctional architectures on solid substrates to make their active functional groups accessible and to create molecular recognition sites that can act either as receptors or favoring the specific adsorption of different kind of biomolecules, such as proteins. Among the different methodologies proposed to achieve the assembly of functional molecules on solid substrates, the chemisorption of self-assembled monolayer (SAMs) on gold has been widely studied.[8] Particularly, the strategy of building up mixed monolayers by the dilution of ω-functionalized alkanethiols in a homogeneous two-dimensional array is a way for tailoring the surface properties of these SAMs. However, in many cases a true mixing of the components is not reached at the molecular level, and phase segregation in single-component domains is usually observed.[9−11] To achieve this goal, the control of determined factors affecting the balance of the intermolecular interactions during the self-assembly process, such as different molecular chain length, nature of the functional groups, and solvent, is crucial for obtaining binary SAMs with the expected mixing properties.

Developing of these strategies requires understanding of the intrinsic phase behavior of the mixed thiol monolayers. In this sense, Folkers et al., by using the Bragg–Williams model, described the behavior of binary alkanethiolate SAMs at gold surfaces.[12] They concluded that only one phase consisting of a homogeneous mixture of both alkanethiolates would exist under equilibrium conditions, being the strength of the interactions between neighboring molecules the factor that determines the actual composition of the phase. Consequently, it can be inferred that it would be possible to obtain fully miscible and crystalline intermixed domains of two-component SAMs favoring heteromolecular interactions.

Electrochemical and infrared spectroscopy techniques have emerged as useful tools to elucidate the phase behavior in multicomponent SAMs systems from a macroscopic point of view.[11,13,14] Although macroscopic in nature, these techniques afford to get also valuable information related with the feasible nanoscopic scheme of the monolayer organization. In this sense, it has been reported that a mixed monolayer with domains containing 50 molecules exhibits two-dimensional bulk properties[15] which has been used to infer a complete mixing in these quasi-two-dimensional systems.[11,14]

Most of the studies carried out to explore phase segregation of binary SAMs formed from molecules of similar chain length and intermolecular interactions have been based on SAMs built

El Vicerrector de Estudios de Posgrado y Formación Continua y Coordinador de la Escuela Multidisciplinar de Doctorado de la Universidad de Córdoba

ACREDITA que:

ALAIN RAFAEL PUENTE SANTIAGO

ha presentado la **comunicación oral** que lleva por título :

"ESTUDIO ELECTROQUÍMICO DE NANOESTRUCTURAS FORMADAS POR AU/MONOCAPAS AUTOENSAMBLADAS DE TIOLES/NPS AU."

en el **III Congreso Científico de Investigadores en Formación de la Universidad de Córdoba** celebrado los días 9 y 10 de abril de 2013.

Y para que así conste, se expide y firma este certificado en Córdoba, a 10 de abril de 2013

Fdo: JOSE CARLOS GÓMEZ VILLAMANDOS
Vicerrector de Estudios de Posgrado y Formación Continua
Coordinador de la Escuela Multidisciplinar de Doctorado ED-UCO

Rectorado de la Universidad de Córdoba – Avd. Medina Azahara 5, 14071 CÓRDOBA

NANOUCO IV
Encuentro sobre Nanociencia y Nanotecnología de Investigadores Andaluces

Córdoba, 7 y 8 de Febrero 2013

UNIVERSIDAD D CÓRDOBA

IV Workshop
NANO UCO

El Comité Científico del IV Encuentro sobre Nanociencia y Nanotecnología de Investigadores Andaluces, celebrado en Córdoba los días 7 y 8 de febrero de 2013,

HACE CONSTAR

Que D. Alain Rafael Puente Santiago ha participado en el citado evento presentando la siguiente comunicación oral invitada:

"Estudio electroquímico de nanoestructuras formadas por Au/Monocapas autoensambladas/Nanopartículas de Au"

Córdoba, 8 de febrero de 2013.

Fdo: Luis Camacho Delgado
Presidente del Comité Científico

Fdo: Rafael Madueño Jiménez
Secretario del Comité Científico

CARACTERIZACIÓN ELECTROQUÍMICA DE LA FORMACIÓN DE ENLACES DISULFURO EN MONOCAPAS DE 1,10-DECANODITIOL SOBRE Au(111), Au(100) Y Au(110).

Alain R. Puente-Santiago, Teresa Pineda, Rafael Madueño, Manuel Blázquez.

Departamento de Química Física y T. A., Facultad de Ciencias, Univ. de Córdoba, 14014-Córdoba.

La formación de monocapas autoensambladas (SAMs) sobre sustratos de oro a partir de la adsorción espontánea de organotioles desde disolución es un método simple y conveniente para la preparación de interfases funcionalizadas[1]. No obstante, la necesidad de obtener monocapas con propiedades reproducibles para que sean útiles en posibles aplicaciones, hace que se investiguen métodos de preparación que permitan un control adecuado de su organización superficial. Durante la formación existen factores que pueden afectar al proceso de ensamblado y a la propia estructura de la SAM resultante así como a su velocidad de formación. Tanto la estructura superficial del sustrato como la elección del disolvente son factores que pueden afectar de manera significativa a dicho proceso. En este sentido, la formación de SAMs de alcanoditioles con alta calidad y reproducibilidad, de manera que las moléculas se adsorban en una configuración aproximadamente perpendicular a la superficie, exponiendo un grupo –SH a la disolución, ha mostrado ser muy dependiente de la naturaleza del disolvente empleado para la formación.[2-4]
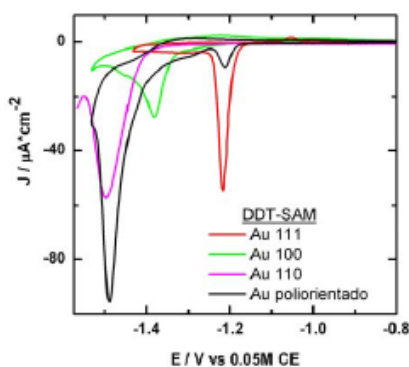

Figura 1. Voltagramas cíclicos de la desorción reductiva de DDT-SAM en KOH 0.1M. t_{mod}=2h

En este trabajo se recoge un estudio de la formación de SAMs de 1,10-decanoditiol (DDT) sobre sustratos monocristalinos de Au de bajo índice, Au(111), Au(100) y Au(110), mediante adsorción espontánea desde un medio micelar (Tritón X-100/H_2O). Bajo todas las condiciones experimentales ensayadas se obtienen capas con una cierta organización y compacidad, como lo ponen de manifiesto los resultados obtenidos mediante técnicas electroquímicas: voltametría cíclica, curvas de capacidad diferencial de la doble capa y espectroscopía de impedancia. En la Figura 1 se muestran voltagramas cíclicos de la desorción reductiva de una SAM de DDT sobre distintos sustratos de oro. La obtención de monocapas reproducibles de SAMs de alcanoditioles requiere la utilización de atmósfera inerte durante el proceso de deposición (ausencia total de oxígeno disuelto) para evitar la formación oxidativa de enlaces S-S, inter o intramoleculares[5].

En este sentido, cuando la adsorción de DDT se lleva a cabo desde el medio micelar, la DDT-SAM que se obtiene es altamente organizada y prácticamente libre de defectos sin necesidad de usar atmósfera inerte. Sin embargo, se establece que mientras sobre Au(111) la monocapa de DDT se organiza exponiendo grupos –SH en la interfase, las superficies de Au(100) y Au(110) juegan un papel crucial en la formación de enlaces S-S intramoleculares en la organización de dichas monocapas.

Referencias.

[1] Love, J.C.; Estroff, L.A.; Kriebel, J.K.; Nuzzo, R.G.; Whitesides, G.M. Chem. Rev. 105 (2005) 1103
[2] García-Raya, D.; Madueño, R.; Sevilla, J. M.; Blazquez, M.; Pineda, T. Electrochim. Acta 53 (2008) 8026.
[3] García-Raya, D.; Madueño, R.; Blázquez, M.; Pineda, T. J. Phys. Chem. C 114 (2010) 3568.
[4] García-Raya, D.; Madueño, R.; Blázquez, M.; Pineda, T. Langmuir 26 (2010) 11790.
[5] Esplandiu, M.J.; Carot, M.L.; Cometto, F.P.; Macagno, V.A.; Patrito, E.M. Surf. Sci. 600 (2006) 155

Influencia de un disolvente micelar en la composición superficial de monocapas mixtas de decanotiol y ácido mercaptoundecanoico sobre Au(111).

Alain Rafael Puente Santiago, Guadalupe Sánchez, José Manuel Sevilla, Teresa Pineda, Manuel Blázquez, Rafael Madueño

Dpto. de Química Física y Termodinámica Aplicada, Universidad de Córdoba, Ed. Marie Curie 2ª Planta, Campus de Rabanales 14014 Córdoba, Tfno: +34 957 212423

La formación espontánea de monocapas autoensambladas (SAMs) sobre sustratos metálicos a partir de alcanotioles ω-sustituidos es una aproximación particularmente interesante a la hora de controlar sus propiedades interfaciales [1]. La utilización de distintos grupos funcionales en SAMs, así como su organización estructural, confiere diferentes propiedades químicas y físicas a estas superficies. El estudio de la influencia que tiene la interacción superficial de estas SAMs en fenómenos como adhesión, corrosión, fricción, biocompatibilidad (adsorción y reconocimiento de proteínas o material biológico) o transferencia electrónica es importante para el diseño de dispositivos nanoestructurados (MEMs), electrónicos (interruptores moleculares, etc.) o biosensores. Dependiendo de la naturaleza del grupo funcional presente en la SAM, éste puede introducir desorden en su estructura. Una estrategia para evitar este inconveniente es la formación de SAMs mixtas. De esta manera, la dilución de un grupo funcional superficial se consigue al insertar otra molécula en su estructura. En este sentido, la relación de concentraciones de cada molécula en disolución, el tipo de sustrato, disolvente, la temperatura y el tiempo de modificación son factores esenciales para controlar la proporción y distribución de grupos funcionales superficiales, bien formando dominios separados de moléculas [2-3] o de forma homogénea [4-6]. Dicha composición determinará el tipo de aplicación [7].
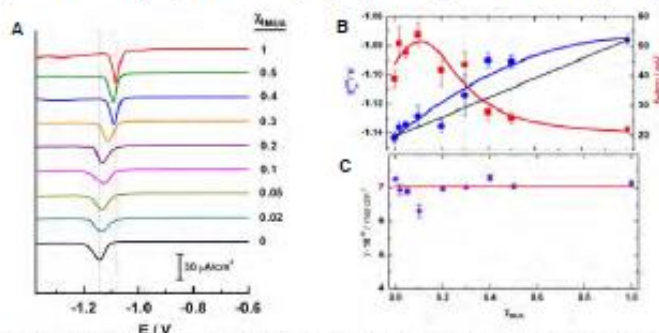

Figura 1. (a) Voltagramas de la desorción reductiva de SAMs mixtas formadas desde un medio micelar (Tritón X-100: H$_2$O) en KOH 0.1M, a diferentes proporciones de DT (X_{DT}) y MUA (X_{MUA}). C_{total} =1mM y t_{mod}=15 min. v=20 mV/s. **(b-c)** Representaciones de la evolución del potencial de pico, semianchura y recubrimiento superficial de las SAM mixtas formadas vs X_{MUA}.

En el presente trabajo se lleva a cabo un estudio de la formación de SAMs mixtas de ácido mercaptoundecanoico (HOOC-(CH$_2$)$_{10}$-SH-MUA) y decanotiol (CH$_3$-(CH$_2$)$_{10}$-SH-DT) cambiando su concentración en un medio micelar. La naturaleza de las SAMs formadas se ha estudiado a través de su desorción reductiva mediante voltametría cíclica (VC). Las moléculas de MUA y DT tienen una longitud similar, y por tanto forman SAMs puras de estructura y estabilidad similar. Las SAMs mixtas no presentan picos voltamétricos separados, indicando que la mezcla de grupos –COOH y –CH$_3$ es homogénea (*Figura 1a*). Al aumentar la relación de DT/MUA, se pone de manifiesto la inserción progresiva de DT al producir un desplazamiento del pico a valores más negativos de potencial (E$_p$). No obstante, puede concluirse a partir del análisis de la evolución de E$_p$, su semianchura y el recubrimiento superficial (*Figura 1b-c*) que existe una proporción superficial de MUA mayor a la que cabría esperar según la relación DT/MUA en el medio. Este hecho indica una influencia del disolvente en la adsorción preferencial de MUA frente a DT. Finalmente, la caracterización de estas capas se ha llevado a cabo mediante medidas de VC y espectroscopía de impedancia electroquímica (EIS) de la transferencia electrónica de sondas redox, obteniéndose información de la influencia del tiempo de modificación y de la disociación del grupo –COOH.

Bibliografía.
[1] A. Ulman, Chem. Rev. 96 (1996) 1533
[2] J. P. Folkers, P.E. Laibinis, G.M. Whitesides, Langmuir 8 (1992) 1330
[3] J. P. Folkers, P.E. Laibinis, G.M. Whitesides, J. Phys. Chem. 98 (1994) 563-571 W.
[4] P.E. Laibinis, G.M. Whitesides, JACS 114 (1992) 1990
[5] P. Gupta, A. Ulman, J. Fanfan, A. Korniakov, K. Loos, JACS 127 (2005) 4
[6] F.T. Oyerokun, R.A. Vaia, J.F Maguire, B.L. Farmer, Langmuir 26 (2010) 11991
[7] F. Rissner, D.A. Egger, L. Romaner, G. Heimel, E. Zojer, ACS Nano 4 (2010) 6735

XXXV MEETING OF ELECTROCHEMISTRY OF THE SPANISH
ROYAL SOCIETY OF CHEMISTRY
1ST E3 MEDITERRANEAN SYMPOSIUM:
ELECTROCHEMISTRY FOR ENVIRONMENT AND ENERGY

July 14th – July 16th, 2014
University of Burgos
Burgos (Spain)

CERTIFICATE

ALAIN RAFAEL PUENTE SANTIAGO

has presented the communication entitled "*ELECTROCHEMICAL AND RAIRS STUDY OF 11-MERCAPTOUNDECANOIC ACID MIXED SAMS ON Au(111)*" as ORAL COMMUNICATION at the XXXV MEETING OF ELECTROCHEMISTRY OF THE SPANISH ROYAL SOCIETY OF CHEMISTRY AND 1ST E3 MEDITERRANEAN SYMPOSIUM: "ELECTROCHEMISTRY FOR ENVIRONMENT AND ENERGY", held from July 14th to July 16th, 2014 in Burgos (Spain)

Co-authors: Guadalupe Sánchez; Miguel Blázquez; Teresa Jimenez; Rafal Madueño

July 16th, 2014

Burgos (Spain)

Mª Julia Arcos Martinez
President of the Organizing Committee

UNIVERSIDAD DE BURGOS

Estudio electroquímico y espectroscópico de mioglobina cationizada inmovilizada sobre monocapas mixtas en Au(111)

Alain R. Puente Santiago [a], Thomas Risbridger [b], David Fermin, Teresa Pineda, Manuel Blázquez [a,*], Rafael Madueño [a].

[a] Dpto. de Química Física y T.A , Universidad de Cordoba, E-14014, Cordoba, España.
[b] School of Chemistry, University of Bristol, BS8 1TD, Cantocks Close, United Kingdom.
[a,*] mblazquez@uco.es

El estudio de la transferencia electrónica (TE) de proteinas con grupos redox abre la posibilidad de una mejor comprensión de procesos biológicos reales, así como del desarrollo de dispositivos bioelectrónicos como biosensores y celdas de combustible[1]. Los electrodos modificados químicamente ofrecen una plataforma ideal para su adecuada inmovilización y la investigación de los posibles mecanismos de TE [2].
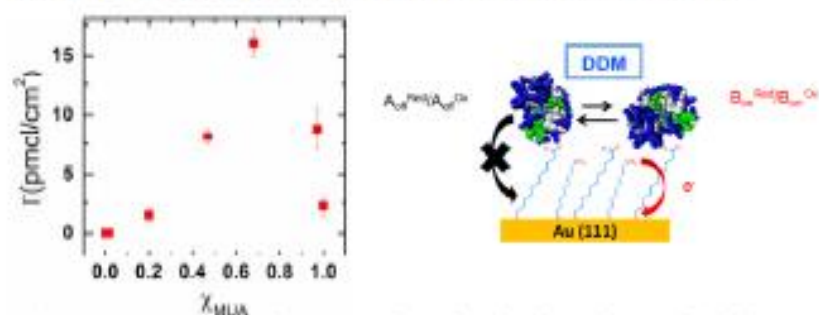

Figura 1. Concentración electroactiva de c-Mb vs fracción molar superficial de MUA

En este trabajo se ha logrado inmovilizar exitosamente mioglobina cationizada (c-Mb) sobre monocapas mixtas de ácido 11-mercaptoundecanoico (MUA) y decanotiol en Au (111), variando su concentración superficial y por tanto, la hidrofilicidad y el potencial eléctrico interfaciales. El comportamiento electroquímico de la c-Mb adsorbida se ha examinado mediante voltametría cíclica y FT-IRRAS. La respuesta electroactiva de la proteína varía con la concentración superficial de MUA (Figura 1), lo cual es debido probablemente a cambios inducidos en su orientación [3,4].

Palabras clave: Autoensamblaje, Transferencia electrónica, Mioglobina cationizada

Referencias

[1]   C. Leger and P. Bertrand, *Chem. Rev.* 108 (2008), 2379-2438
[2]   D. Samanta and A. Sarkar, *Chem. Soc. Rev.*, 40, (2011) 2567-2592
[3]   G.-X. Wang, W.-J. Bao, M. Wang and X.-H. Xia, *Chem.Commun.*,48, (2012) 10859-10861
[4]   A. Kranich, H. K. Ly, P. Hildebrandt, and D. H. Murgida, *J. Am. Chem.Soc.*, 130, (2008) 9844-9848.

Respuesta electrocatalítica de mioglobina cationizada inmovilizada sobre monocapas mixtas en Au(111)

Alain R. Puente Santiago[a], Thomas Risbridger[b], David Fermín[b], Teresa Pineda[a], Manuel Blázquez[a], Rafael Madueño[a]

[a] Instituto de Química Fina y Nanoquímica, Dpto. Química Física y T. A. Universidad de Córdoba, Campus Rabanales, Ed. Marie Curie 2ª Planta, E-14014 Córdoba, España
[b] School of Chemistry, University of Bristol, BS8 1TD, Cantocks Close, United Kingdom
z02pusaa@uco.es

El diseño de biosensores electroquímicos basados en el uso de proteínas redox o enzimas es de interés por su alta sensibilidad y biocompatibilidad. La respuesta electroquímica de proteínas redox viene determinada por el transporte electrónico desde los grupos electroactivos hasta el electrodo. Desde un punto de vista fundamental es esencial el estudio de los factores que afectan a la transferencia electrónica (TE). En este sentido, la optimización de la respuesta en reacciones electrocatalizadas puede depender del tipo de inmovilización, de posibles cambios conformacionales y/u orientación de las proteínas inmovilizadas así como de la utilización de nanomateriales que promuevan eficientemente la TE con el electrodo [1-3].
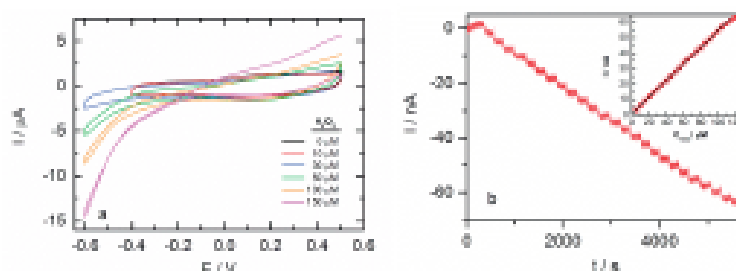

Figura 1: (a) Voltamperogramas c-Mb inmovilizada en MUA/DT SAMs en ausencia y presencia de H_2O_2. (b) Curvas cronoamperométricas y dependencia de la corriente con la $[H_2O_2]$

En este trabajo se estudia la respuesta electrocatalítica del H_2O_2 en un electrodo de oro formado por mioglobina cationizada (c-Mb) inmovilizada electrostáticamente sobre diferentes monocapas mixtas autoensambladas (SAMs) de decanotiol (DT) y ácido 11-mercaptoundecanoico (MUA). Dicho estudio se centra en determinar si existe relación entre la respuesta electroactiva de la c-Mb y la reacción electrocatalítica en función de su interacción con dichas SAMs.

Bibliografía:

[1] Wu, H., Wang, X., Mengxia, Q., Zhang, H., Sensor and Actuator B, 221 (2015) 694-699.
[2] Karimi Shervedani, R., Samiei Foroushani ,M. , Electrochimica Acta, 187 (2016) 646-654.
[3] Canbaya, E., Sahin, B., Kıran, M., Akyilmaz, E., Bioelectrochemistry, 101 (2015) 126-131.